

Investigations of the non-adiabatic photophysics of Cu(I)-phenanthroline complexes

THÈSE N° 6966 (2016)

PRÉSENTÉE LE 19 AVRIL 2016

À LA FACULTÉ DES SCIENCES DE BASE

LABORATOIRE DE SPECTROSCOPIE ULTRARAPIDE

PROGRAMME DOCTORAL EN CHIMIE ET GÉNIE CHIMIQUE

ÉCOLE POLYTECHNIQUE FÉDÉRALE DE LAUSANNE

POUR L'OBTENTION DU GRADE DE DOCTEUR ÈS SCIENCES

PAR

Gloria CAPANO

acceptée sur proposition du jury:

Prof. L. Helm, président du jury
Prof. M. Chergui, Dr I. Tavernelli, directeurs de thèse
Prof. G. Worth, rapporteur
Prof. T. A. Wesolowski, rapporteur
Prof. C. Corminboeuf, rapporteuse



ÉCOLE POLYTECHNIQUE
FÉDÉRALE DE LAUSANNE

Suisse
2016

To my lovely family...

Acknowledgements

Behind the scene of a scientific research project and the compilation of a thesis, there is many people's hard work. Over the past 4 years, I learnt what doing research means by working in close contact with wonderful supervisors and collaborators.

First and foremost, I want to sincerely thank Dr. Thomas Penfold. It has been an honour to be his first Ph.D. This thesis would never have existed without his support and his ideas. He has been a tremendous advisor and his contagious enthusiasm motivated and encouraged me in any situation. Dr. Ivano Tavernelli is one of those rare inspiring scientists: every conversation with him is a precious moment of very good science. I want to thank him for being such a good teacher and supporter. I am deeply grateful to Prof. Majed Chergui for being my doctoral supervisor. His curiosity and his will to deeply explore the physical world spurred me to give the best. I am also thankful for kindly hosting me in his laboratory and allowing me to work in the best conditions.

I would also like to thank my committee members, Prof. Clémence Corminboeuf, Prof. Lothar Helm, Prof. Tomasz Wesolowski, and Prof. Graham Worth for making my private defense an enjoyable moment, rich of brilliant comments and suggestions.

I thank Prof. Ursula Röthlisberger, the head of the Computational Chemistry and Biochemistry Laboratory, in which I spent the first two years of my Ph.D. research. I enjoyed working and spending time with former and present people of her group.

The members of Chergui group, LSU, have contributed immensely to my personal and professional time at EPFL. I have found not only competent colleagues but also a bunch of wonderful friends that make me feel to belong to a big family. They welcomed and supported me during the toughest and final period of my studies. Among them, I want especially thank my collaborators Roberto and Jose, my climbing mate Lars, my very patience officemates Thomas and Enrico, the sweet painter Mahsa, the eclectic Malte, the latino dancer Janina, the cheering Fabio, the engineer (almost physicist) Edoardo, the chef Luca, the exuberant Chris, the joyous Tania, the fiery Andre, the willing Jacob, the "one-man-lab" Frank and the seriously playful Dominik.

In the CECAM group, I thank Felipe, colleague and friend, for the helpful and funny conversations and for the nice moments spent together.

Doing research at EPFL is extremely pleasant, due also to the perfect organization provided by our efficient secretaries. I want to acknowledge Anne-Lene, from the doctoral school, Karin from LCBC, and Monique and Annissa from LSU.

My long Ph.D. life would have been much harder without the many EPFL friends. In particular,

Acknowledgements

I want to thank Sandro, Michele, Lorenzo, Davide, Gabriele and Riccardo for the exciting and fun activities we did together. My time at EPFL was also enriched by the Association Universitaire de Musique de Chambre at EPFL. I want to express my special thanks to Thomas, Arnaud, and Mandira for our amazing music sessions. I am in debt with Fernando for all those times he comforted me with sweet smiles.

Finally, my heartfelt thanks go to my family for all their love and for encouraging me to keep pushing in pursuing my dreams. Thank you.

Lausanne, 7 April 2016

G. C.

Abstract

Cu(I)-phenanthrolines are an important class of metal-organic molecules that exhibits much promise for solar energy harvesting and solar-driven catalysis applications. Although many experimental studies have been performed calling for high-level simulations to elucidate their photophysics, a complete picture is still missing. This is the goal of the present thesis. On the ultrafast (femtosecond) timescale we studied the non-adiabatic relaxation of a prototypical Cu(I)-phenanthroline, $[\text{Cu}(\text{dmp})_2]^+$, by performing excited state simulations using two approaches: quantum dynamics and trajectory surface hopping. These simulations help to identify several mechanisms, internal conversion, pseudo Jahn-Teller distortion, intersystem crossing, occurring in the subpicosecond time scale. Surprisingly, we have found that intersystem crossing does not take place between the lowest singlet and triplet excited states, as previously proposed, but between the lowest singlet and higher triplet states. Moreover, we observed the initial stages (< 100 fs) of the solvent reorganization due to the electronic density changes in the excited state. This leads to an energy stabilization of the excited states that is associated with an increase of the non-radiative decay rate.

The quantum dynamics simulations allowed us to provide indications for performing additional spectroscopy measurements by using the recently developed X-ray Free Electron Lasers (X-FELs). This technology can monitor both electronic and structural changes with an unprecedented time resolution of tens of femtoseconds and, therefore, is capable of revealing the aforementioned processes. In addition, we questioned the feasibility of such experiments and calculated the signal strengths for XAS and XES transient spectra.

Finally, we analyzed the luminescence quenching, which has been observed for all Cu(I)-phenanthroline complexes when they are dissolved in strongly donating solvents. By performing Molecular Dynamics calculations we showed that, in contrast with the previously accepted model based on the formation of an exciplex (a species formed by two molecules, one in the excited state and one in the ground state), no stable exciplex is formed and that quenching is due to electrostatic solute-solvent interactions. In addition, we investigated how the geometry configuration can affect the luminescence lifetime in these molecules. We found a correlation between rigidity of the copper complex - inhibition of the pseudo-Jahn-Teller distortion - and lifetime of the emission. The more the metal complex retains the ground state structure (large substituents), the longer its lifetime. This effect is attributed to a higher energy gap (excited state minus ground state energy) due to the reduction of relaxation.

Our research reveals important insights into the relaxation mechanism and the complex

Acknowledgements

interplay between geometry and electronic structure in Cu(I)-phenanthroline. These results can be exploited for guiding the synthesis of complexes with the desired physical properties.

Key words: quantum dynamics, non-adiabatic dynamics, MCTDH, TSH, internal conversion, intersystem crossing, spin-orbit coupling, pseudo Jahn-Teller distortion, Cu(I)-phenanthroline, XAFS, XES

Compendio

I complessi di rame(I) e 1,10-fenantrolina costituiscono una importante classe di composti metallorganici, promettenti per lo sviluppo di celle solari e di catalizzatori fotoattivati. Nonostante numerosi studi sperimentali e simulazioni teoriche abbiano cercato di fare luce sulla loro fotofisica, una descrizione completa è ancora mancante.

Utilizzando due diversi metodi computazionali, la dinamica quantistica e la traiettoria balzante tra superfici, abbiamo investigato il rilassamento non adiabatico di un complesso tipico, $[\text{Cu}(\text{dmp})_2]^+$. Questo rilassamento, definito come ultraveloce, avviene nella scala di tempo dei femtosecondi. Grazie a queste simulazioni siamo stati in grado di identificare diversi meccanismi ultraveloci di rilassamento come la conversione interna, la distorsione di Jahn-Teller e l'incrocio intersistema. In particolare, abbiamo osservato che l'incrocio intersistema non avviene tra il più basso stato di singoletto eccitato e il più basso stato di tripletto, come proposto da altri autori, ma tra il suddetto stato di singoletto e gli stati di tripletto a più alta energia. Inoltre, è stato anche possibile osservare i primi passi della reorganizzazione del solvente (< 100 fs), indotta dal cambiamento della distribuzione elettronica nello stato eccitato. Questo processo porta a una stabilizzazione degli stati eccitati con conseguente aumento della velocità di decadimento non radiativo.

Le simulazioni effettuate con dinamica quantistica ci hanno permesso di ottenere informazioni su indicazioni sulle misure di spettroscopia da effettuare utilizzando laser X-ray ad elettrone libero (X-FELs). Questa nuova tecnologia consente di monitorare cambiamenti strutturali ed elettronici con una risoluzione temporale di alcune decine di femtosecondo. Tale vantaggio permette di osservare i fenomeni ultrarapidi descritti precedentemente. Per valutare la praticabilità di questi esperimenti abbiamo la forza del segnale degli spettri di assorbimento e di emissione, XAS e XES.

Infine, abbiamo analizzato lo smorzamento della luminescenza osservato per tutti i complessi di rame-fenantrolina dissolti in solventi donori. Questo smorzamento è stato attribuito alla formazione di un eccipletto, una specie termodinamicamente stabile composta da una molecola in uno stato elettronico eccitato e un'altra nel suo stato fondamentale. Effettuando simulazioni di Dinamica Molecolare, abbiamo mostrato che non si forma nessun eccipletto e che lo smorzamento della luminescenza è generato da interazioni elettrostatiche fra solvente e soluto. Inoltre, abbiamo analizzato come la forma della fenantrolina possa indurre modificazioni nel tempo di vita della luminescenza. A questo proposito, abbiamo trovato che esiste una correlazione tra la rigidità del complesso metallorganico e il tempo di vita. Infatti, complessi che sono affetti da una piccola distorsione di Jahn-Teller sono caratterizzati da un

Compendio

maggiore energia degli stati eccitati.

La nostra ricerca ha fatto chiarezza sui meccanismi di rilassamento dei complessi di rame-fenantrolina e sulle interazioni reciproche fra la loro geometria e la struttura elettronica. Questi risultati sono importanti allo scopo di guidare la sintesi di complessi con le proprietà fisiche desiderate.

Parole chiave: dinamica quantistica, dinamica non adiabatica, MCTDH, TSH, conversione interna, incrocio intersistema, accoppiamento spin orbita, distorsione di Jahn-Teller, rame(I)-1,10-fenantrolina, XAFS, XES

Contents

Acknowledgements	i
Abstract (English/Italian)	iii
Introduction	1
1 Investigation of the photophysics of metal-organic complexes	3
1.1 Photophysical processes	3
1.1.1 Timescale of photophysical processes	5
1.2 Investigation of the photoinduced dynamics	6
1.2.1 Spectroscopy	6
1.2.2 Computational methods	11
1.3 Cu(I)-phenanthroline complexes	14
1.3.1 Phosphorescence and Fluorescence	15
1.3.2 Solvent dependence	17
1.3.3 Ultrafast relaxation kinetics	19
2 Molecular dynamics methods	23
2.1 Time dependent Schrödinger equation for a molecular system	23
2.1.1 Born-Huang expansion	24
2.1.2 Adiabatic representation	25
2.1.3 Diabatic representation	27
2.1.4 Group Born-Oppenheimer approximation	28
2.2 A short overview of the MCTDH method	28
2.2.1 The MCTDH <i>ansatz</i>	29
2.2.2 Vibronic Coupling Hamiltonian expansion	33
2.3 Trajectory surface hopping	36
2.3.1 Equations of motion	37
2.3.2 Tully's fewest switches algorithm	39
2.3.3 Intersystem crossing	40
2.3.4 Hybrid scheme - QM/MM	41
2.3.5 LR TDDFT applied to Trajectory Surface Hopping	42
2.4 Ground state dynamics	44
2.4.1 <i>Ab-initio</i> Born-Oppenheimer MD	45

Contents

2.4.2	Car-Parrinello method	45
2.4.3	Classical molecular dynamics	46
3	Non-adiabatic ultrafast relaxation of photoexcited [Cu(dmp)₂]⁺	47
3.1	Ultrafast spectroscopic studies	47
3.2	Building the Vibronic Coupling Hamiltonian	49
3.2.1	Zeroth order expansion coefficients	49
3.2.2	First order expansion coefficients	51
3.2.3	Second order expansion coefficients	52
3.2.4	Spin orbit coupling coefficients	53
3.3	Wavepacket propagation	54
3.3.1	The singlet non-adiabatic dynamics	55
3.3.2	The effect of intersystem crossing	58
3.4	Discussion	61
3.5	Conclusions	63
4	Feasibility of ultrafast time-resolved X-ray spectroscopy	65
4.1	Introduction	65
4.2	Theory and computational details	67
4.2.1	Quantum Dynamics of [Cu(dmp) ₂] ⁺	67
4.2.2	Simulations of the time-resolved spectra	67
4.3	Results	68
4.3.1	EXAFS	68
4.3.2	Pre-edge X-ray Absorption	71
4.3.3	X-ray emission	72
4.3.4	Numerical Examples: Feasibility of Probing Wavepacket Dynamics	74
4.4	Conclusions	77
5	TSH within QM/MM: a study of the dynamical solvent effects	79
5.1	Introduction	79
5.2	Computational details	81
5.3	Trajectory Surface Hopping	81
5.3.1	Analysis of the electronic state character during the photoexcited dynamics	84
5.3.2	Photophysics of [Cu(dmp) ₂] ⁺ : Internal Conversion and Intersystem Crossing dynamics	87
5.3.3	Solvent effects on the dynamics of [Cu(dmp) ₂] ⁺	90
5.4	Derivation of collective modes for MCTDH dynamics from TSH trajectories	92
5.4.1	PCA of the TSH trajectories	93
5.4.2	Application to the MCTDH dynamics of [Cu(dmp) ₂] ⁺	94
5.5	Discussion and Conclusions	97

6	Study of the emission properties of Cu(I)-phenanthroline complexes	101
6.1	Introduction	102
6.2	Computational Details	104
6.2.1	Electronic structure calculations	104
6.2.2	Molecular dynamics simulations	105
6.3	Results	105
6.3.1	Quantum chemistry: The geometric and electronic structure and contribution of spin orbit coupling	106
6.3.2	Molecular dynamics	114
6.4	Discussions	124
6.5	Conclusions	126
7	Unravelling the photophysics of two long-living Cu(I)-phenanthrolines	129
7.1	Introduction	129
7.2	Computational details	131
7.3	Results	131
7.4	Discussion and conclusion	137
	Conclusions	141
A	Electronic structure	143
A.1	The Hohenberg-Kohn theorems	143
A.2	Exchange-correlation functionals	145
A.3	Basis sets and Pseudopotential	148
B	TDDFT in a Nutshell	151
B.1	The foundation theorems	151
B.2	Linear response TDDFT	151
B.3	Casida formalism	154
B.4	Sternheimer formalism	155
	Bibliography	157
	Curriculum Vitae	173

Introduction

Humans have long been fascinated by the bright colours of metal-organic complexes. Red madder lake, composed of aluminum alizarin and purpurin complexes, was used as textile dyes by Persians and Egyptians [1]. Notably, it was found on Pre-dynastic Egyptian mummies (prior to 3,100 BC). The red uniforms of the British Army soldiers, “Red Coats”, were also dyed with madder, as decreed by Henry II. Leonardo da Vinci wrote many of his manuscripts using iron-gall ink [2], a complex composed of iron and gallic acid, produced with a recipe that dates back to Plinius Maior and described in his *Naturalis Historia*. The mesmeric Vincent van Gogh’s “Starry Night” would not have been the same without Prussian blue, whose nuances are created by Iron(II,III) hexacyanoferrate(II,III) complexes.

The XVIIIth century started with the early discoveries and accidental preparations [3] of metal-organic complexes. The interest arisen around these new systems lead to the inception of a new research area. These efforts were rewarded with the synthesis of the first metal-organic industrial dye, a compound derived from the red madder, in 1868 [1]. The discovery of the Grignard reactions (Nobel Prize in Chemistry, 1912) was a crucial milestone for the recognition of the chemical importance of metal-organic complexes. Over the same period, the concept of catalysis was developed, first by Berzelius in 1835 and Ostwald (Nobel Prize in Chemistry, 1909), and later by Sabatier who distinguished between homogeneous and heterogenous catalysis (Nobel Prize in Chemistry, 1912). Metal complexes soon proved to be excellent candidates as catalysts, as demonstrated by the success of the Ziegler-Natta catalyst (Nobel Prize in Chemistry, 1963).

Since then a myriad of complexes has been synthesized for many different applications. Notably, due to their unique optical and electronic properties combined with a huge design flexibility, metal-organic complexes have attracted increasing interest for optoelectronic devices, such as solar cells, light-emitting diodes, chemical sensors, photodetectors and field-effect transistors [4, 5, 6]. Finding the best candidate, by tuning the physical properties and changing the molecular architecture, is one of the primary tasks of applied research. However, this can not be achieved without a deep knowledge of the fundamental processes occurring in these molecules under operative conditions.

For this purpose, spectroscopic techniques are valid tools because they can investigate the electronic and geometric structures of a system both in equilibrium and non-equilibrium

states [7]. As an example, optical spectroscopy can determine the electronic ground state of a molecule and, by performing the same experiment using a pump/probe setup, one can monitor the relaxation mechanism governing the excited states decay, induced by an external electromagnetic field, to the lower states or the ground state of the system (see Sec. 1.2). Nonetheless, the large amount of data obtained from these experiments makes it difficult to understand the underlying phenomena, which, in the majority of the cases, are further complicated by their mutual interaction.

Computational methods, based on theoretical models, provide a complementary approach to the observation of nature. As for spectroscopy, computational experiments are carried out under controlled conditions, chosen by the user in order to be the closest possible to those of the experiment to compare. The overlap of the computational output data and the experimental observables can lead to a valid interpretation of the physical and chemical mechanisms examined. However, the potentialities of computer simulations are not fully expressed by the mere support to the enlightenment of experimental observations. Computational science has deeper and fundamental objectives. First, it can predict properties of molecules that have never been synthesized thus accelerating the selection process and guiding the experimental study only to the promising species. In the same way, it can simulate phenomena that are not detectable with the current technology and therefore propose innovative experiments. Finally, but not less importantly, it can assess in advance the feasibility of an experiment, guiding experimentalists in the choice of the system to investigate and the best technique to employ.

The aim of my research, presented in this thesis, is to understand the mechanisms occurring in a special class of metal-organic complexes, Cu(I)-phenanthrolines, upon photoexcitation with visible light. An introduction to the photophysical decay processes and to these molecules is given in Chapter 1. In order to accomplish this study, I used different computational techniques, described in Chapter 2, and I compared my results with experimental observables obtained by time-resolved optical and X-ray spectra. In particular, I investigated the ultrafast (fs-ps) non-adiabatic dynamics of $[\text{Cu}(\text{dmp})_2]^+$ utilizing both quantum dynamics, Multi-Configurational-Time-Dependent-Hartree (MCTDH), and classical trajectory, Trajectory Surface Hopping (TSH), methods. The results are presented, respectively, in Chapter 3 and 5. The variability of the luminescence lifetime of a set of Cu(I)-phenanthroline in solution was inspected through electronic structure methods and ground state dynamics as shown in Chapter 6 and 7. The development in the X-ray spectroscopy domain of X-ray free electron lasers (X-FELs) has offered exciting opportunities to trace electronic and structural evolution with the unprecedented time resolution of the order of tens of femtoseconds. However, it is still not clear if weak changes of the transient spectra can be detected with a reasonable integration time. This is examined in Chapter 4 for time-resolved X-ray absorption and emission spectroscopy of the photoexcited $[\text{Cu}(\text{dmp})_2]^+$.

1 Investigation of the photophysics of metal-organic complexes

This chapter gives a short introduction to the photophysics of metal-organic complexes (Sec. 1.1) and to the most common spectroscopic techniques and computational methods used in order to investigate them (Sec. 1.2). In the last section a special class of metal-organic complexes, Cu(I)-phenanthroline, is introduced.

1.1 Photophysical processes

The variety of colours shown by metal-organic complexes is a fingerprint of their peculiar photophysics and photochemistry. Owing to their strong absorption in the UV-visible region of the spectrum and to their long-lived excited states, transition metal complexes have become a central component of photocatalysts [8, 9], dye-sensitized solar cells (DSSCs) [10] and optical light emitting devices (OLEDs) [11, 12, 13]. Their widespread use for such applications has been the main driving force for a large research effort aimed at understanding their fundamental photophysical and photochemical properties [7]. Central to this are the fate and decay mechanisms of the initially excited state that usually occurs on the femtosecond timescale and which provide critical insight into their suitability and efficiency for a particular application. Herein we give a general description of the photophysical processes occurring in a molecule upon electronic excitation. This portrayal applies also to metal-organic complexes.

Let us consider a molecule, at equilibrium, in the electronic ground state. For initiating a photophysical process, an electromagnetic field, with a frequency that corresponds to the energy difference between a given excited vibronic state and the initial vibronic ground state, has to be applied to the molecule. As a consequence, an oscillating electronic (or magnetic) moment, is generated. The probability of transition, from the ground to the excited state, is given by the square of the amplitude of this electronic moment, the so-called transition moment. The absorption of a photon is so fast (10^{-15} s) compared to the motion of the nuclei (10^{-13} s) that they are considered frozen during the electronic transition (Franck-Condon principle [14, 15]). In this approximation, the probability of transitions can be rewritten in

Chapter 1. Investigation of the photophysics of metal-organic complexes

terms of electronic and vibrational selection rules.

Usually, immediately after photoexcitation, the system is, due to the electronic structure changes, in a non-equilibrium state. Therefore, the excess energy is released through radiative and non-radiative relaxation mechanisms. In the photon absorption process, due to momentum conservation laws, only some vibrational “active modes” are excited. Subsequently, the energy can be distributed among different vibrational degrees of freedom in a process called intramolecular vibrational redistribution (IVR). As a result of the excitation, the vibrational temperature of the system can be very high: the thermal equilibrium with the environment can be established through vibrational cooling. When other electronic states lie close to the photoexcited one, other non-radiative mechanisms take place. If the system decays to electronic states with same spin multiplicity, the process is named internal conversion (IC); if there is a change of spin multiplicity, intersystem crossing (ISC).

An additional non-radiative mechanism, which plays an important role in the dynamics of metal-organic complexes in solution, is the reorganization of the solvent, triggered by the charge redistribution following photoexcitation. When a metal complex absorbs a photon, an electron from a metal-like (ligand-like) molecular orbital may be promoted to an orbital with ligand-like (metal-like) character giving rise to metal-to-ligand-charge-transfer (ligand-to-metal-charge-transfer) states, indicated with the acronym MLCT (LCMT)¹. These excitations are characterized by a large change of the electron distribution following photoexcitation, inducing an immediate dipole in the solvent to which the solvent molecules respond. The motion of the solvent molecules is slower than the formation of the induced dipole: non-diffusive processes, such as rotations, take place in tens to hundreds of femtosecond whereas diffusive processes are solvent dependent and occur on a timescale of the order of few picoseconds [16, 17].

The molecule can relax also through radiative (emission of a photon) processes. If the emission takes place between a singlet excited state and the ground state², the emission is called fluorescence [18, 19] and the decay is very fast (fs-ns timescale); if the excited state is a triplet, the emission, phosphorescence [20], may be very long and even last for days. The energy of the first singlet excited state is always larger than the corresponding first triplet excited state due to exchange term of the electron-electron repulsion.

These processes are usually represented by the Jablonski diagram [21], which depicts the electronic states of a molecule and the radiative and non-radiative transitions among them. Figure 1.1 shows a typical Jablonski diagram for the photoexcitation and the relaxation pathways of a molecular system.

¹In other cases the electron can be excited from a metal-like orbital to another metal-like orbital, metal-centered (MC), or from a ligand-like orbital to a ligand-like orbital, ligand-centered (LC).

²In the majority of the cases, the ground state of a molecular system has singlet multiplicity

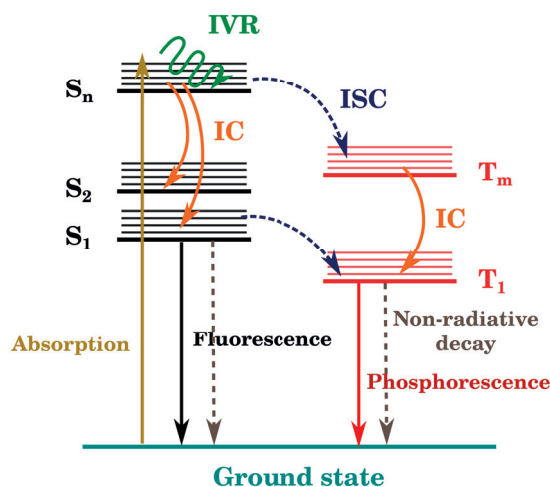


Figure 1.1: Jablonski scheme for the most common radiative and non-radiative processes occurring in a molecule upon absorption of a photon (yellow line) to a singlet excited state: intramolecular vibrational redistribution (IVR), internal conversion (IC) to the lowest singlet excited states, intersystem crossing (ISC) to states with different multiplicity, e.g. triplet states, non-radiative decay to the ground state and fluorescence and phosphorescence emissions.

1.1.1 Timescale of photophysical processes

As previously described, upon photoexcitation different vibrational and electronic mechanisms take place before complete relaxation of the system into the ground state. Time-resolved spectroscopy has shed light on the nature but also on the timescale of these events.

By using ultrafast techniques, it was found that IVR may occur on a time scale shorter than vibrations (10^{-14} - 10^{-12} s) [7] whereas vibrational cooling is a slower process that is completed in tens of picoseconds.

Internal conversion, the transfer of the wavepacket from two excited states with the same multiplicity, is a non-adiabatic process, meaning that it can occur only when two or more electronic states are coupled to each other through the nuclear motion, e.g. vibrations. IC may be extremely fast (< 10 fs) if the coupling between the electronic states is large or if the nuclear wavepacket crosses regions containing conical intersections or avoided crossings [22]. For more details about non-adiabatic processes, see Chapter 2.

Intersystem crossing, like IC, is a non-adiabatic process, which reveals the relativistic nature of the atoms. The ISC rate depends on the atomic number of the atoms composing the molecule [23] (relativistic effects are larger for heavy atoms), on the character of the excited state involved [13], on the density of electronic states [24] and, in some cases, as recently found, on the solvent (if the molecule is in solution) [20]. Like IC, ISC may be very fast if the nuclear wavepacket explores regions where potential energy surfaces of different multiplicity

are degenerate and the coupling is large [25]. Ultrafast ISC, < 40 fs, has been measured for Ru- and Fe-polypyridine [19, 18]. Since many aspects contribute to the determination of the ISC process, its characteristic time cover a time range from tens of femtosecond to millisecond.

1.2 Investigation of the photoinduced dynamics

1.2.1 Spectroscopy

Spectroscopy is the standard technique for investigating the electronic structure and the geometry of a system. Depending on the wavelength of the probing pulse, electrons with different energies are excited. In particular, optical spectroscopy, which employs light in the visible and in the near infrared to ultraviolet regions, promotes electrons from the highest occupied orbitals into the lowest unoccupied ones, giving information about the valence electronic structure. On the other side, core-spectroscopy is element-selective and can deliver information both the electronic (coordination number, valence states) and geometrical (bond length, nature of atoms) structures by exciting, with X-ray radiation, electrons from the inner levels into the continuum. Two different operative setups, static and time-resolved, can be employed.

Static spectroscopy is commonly used in order to gain insight into the nature of the Franck-Condon state and to determine the lowest-energy emitting excited states. In addition, it is a useful tool for preliminary studies before setting the parameters for carrying out time-resolved measurements.

Time-resolved spectroscopy makes it possible to observe the dynamical changes occurring upon the application of an external perturbation. With the advent of pulsed lasers, it was possible to observe photophysical processes with pico/femtosecond resolution [26]. opening a new area in the investigation of the myriad of ultrafast mechanisms (IVR, IC, ISC, charge transfer, etc.) occurring from the photoexcitation to the complete relaxation of the system into the ground state. Notably, the combination of optical and X-ray spectroscopies allows us to follow both the electronic and geometrical changes occurring during a photophysical or photochemical process [27].

Optical spectroscopy

Under the name of optical spectroscopy, different techniques, which operate in the visible, infrared and near ultraviolet region of the spectrum are collected. The variety of methods allows us to examine distinct phenomena. Herein we focus on absorption and fluorescence spectroscopies.

1.2. Investigation of the photoinduced dynamics

Absorption spectroscopy Static absorption spectra are obtained by irradiating the sample and collecting with a detector, either the transmitted or the reflected light. By plotting the intensity as a function of the energy, one can extract information about the electronic structure of the system. Notably, due to the selection rules, only some transitions are allowed. These states are the starting point for the following decay and therefore, their identification is of prime importance.

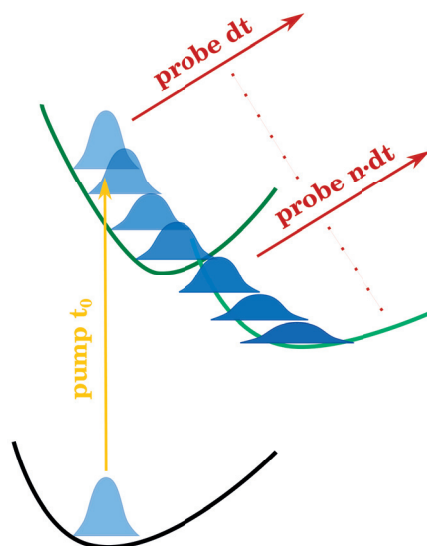


Figure 1.2: Scheme of a pump-probe experiment. The pump pulse excites the system transferring the nuclear wavepacket in the photo-excited state. The probe pulse, at different time delay, samples the motion of the wavepacket.

Transient Absorption (TA) Spectroscopy, focuses on the changes of the absorption coefficient, after photoexcitation, by using the so-called pump-probe scheme. Briefly, a first pulse, the pump, photoexcites the system triggering a cascade of photophysical and photochemical events. Following the Franck-Condon principle, the ground state nuclear wavepacket is transferred, vertically, to the photoexcited electronic state. A second pulse, the probe, delayed with respect to the first, inspects the motion of the nuclear wavepacket on the excited states by absorption to higher states or by stimulated emission. At each step, a single delayed picture is obtained. In order to reconstruct the whole relaxation path, many “snapshots” have to be collected at different time delays. A scheme of a pump-probe experiment is depicted in Fig. 1.2. The collected spectra are called “transient spectra” and are defined as the difference between the pumped signal, multiplied by the quantum yield of the excitation, $\Phi(t)$, minus the unpumped signal:

$$\Delta I(E, t) = \Phi(t) \left(I_{\text{pumped}}(E) - I_{\text{unpumped}}(E) \right). \quad (1.1)$$

Quantum yield, which corresponds to the percentage of excited molecules, and unpumped signal are obtained by a static measurement of the sample, by using only the probe pulse.

Several mechanisms can be tracked by using TA, such as IVR, IC, ISC and vibrational cooling. However, the TA spectrum contains contributions from the excited-state absorption (ESA), stimulated emission (SE), and ground state bleaching (GSB), negative signal given by the depopulation of the ground state, making the analysis and the interpretation of the signal complicated [28].

Fluorescence spectroscopy Emission spectra deliver information not only about the electronic structure but also about the presence of radiative states, the nature of intermolecular interaction and the spatial configuration of molecules. The study of the luminescence, thus, gives direct access to the mechanisms occurring in the excited states.

According to the Kasha rule, static emission spectra are dominated by luminescence of the lowest energy excited state because the relaxation processes are very fast, in the subpicosecond timescale. As a consequence, luminescence arising from higher excited states does not give any relevant contribution. Temperature dependent measurements may reveal the presence of multiple emitting states, which are populated, due to the Boltzmann distribution, only at higher temperature.

Time-resolved fluorescence spectroscopy can probe the population rate of the emitting excited states, defined as

$$\frac{dN(t)}{dt} = -k_R N(t) \quad (1.2)$$

where $N(t)$ is the state population and k_R the radiative transition rate. The intensity of the luminescence, $I(t)$ is proportional to the population $N(t)$ of the emitting state and it decreases exponentially,

$$I(t) = I(t_0)e^{-t/\tau_R}, \quad (1.3)$$

with $\tau_R = 1/k_R$ the characteristic emission time of the state. If the same excited state can decay also through non-radiative pathway with rate, k_{NR} , the total depopulation rate is given by the sum of all rates, $k_{tot} = k_R + k_{NR}$. Subsequently, the characteristic decay time shortens:

$$\frac{1}{\tau_{tot}} = \frac{1}{\tau_R} + \frac{1}{\tau_{NR}}; \quad \tau_{tot} < \tau_R. \quad (1.4)$$

In order to achieve femtosecond resolution, fluorescence up-conversion spectroscopy is commonly used. This technique is based on a non-linear optical phenomenon, sum frequency generation, exhibited by some materials, such as KDP or BBO crystal. In specific conditions, two incident photons, with equal or difference frequencies ω_1 and ω_2 , can give rise to a photon with frequency equal to the sum of the two frequencies, $\omega = \omega_1 + \omega_2$. In a fluorescence up-conversion experiment, the sample is excited with a pulse at time t_0 .

1.2. Investigation of the photoinduced dynamics

The emitted fluorescence is focused with a gate pulse, at a delayed time, onto a non-linear optical crystal. Sum frequency photons are generated only when the gate pulse is inside the crystal, which acts like a “light gate”. These photons are then collected by a detector. The time evolution of the fluorescence is traced by varying the time delay of the gate. This technique is complementary to TA as it does not suffer from overlapping signals problem. Moreover, the time resolution is limited by the time duration of the pulse width [29] and thus allows to observe very short-lived excited singlet states [7].

X-ray spectroscopy

Optical spectroscopy can probe the evolution of the electronic structure but is not sensitive to changes of the nuclear geometry of molecules. This limitation can be overcome with the use of X-ray spectroscopy techniques, which are site-selective and can provide information about local nuclear and electronic structures [30]. At present third-generation synchrotrons, such as the Swiss Light Source at PSI, allow performing pump-probe experiments with a time resolution of 50-100 ps. In this time scale, it is possible to observe stable or metastable states such as photoproducts or long-lived relaxed excited states [31, 32] with impressive accuracy.

The development of X-ray Free Electron Lasers (X-FEL), such as the SwissFEL currently under construction at the PSI, will achieve a time resolution of 10 fs with extremely high brightness (10^9 larger than synchrotron sources) [33]. This technology, already available in Japan (SACLA), United States of America (LCLS) and Italy (FERMI), enables to follow experimental observables with unprecedented time resolution, opening new avenues in the study of the excited state dynamics of ultrafast physical and chemical processes [34, 35, 36].

Ultrafast X-ray absorption spectroscopy The advent of the X-ray absorption spectroscopy (XAS) has made it possible to obtain information about the local geometric and electronic structure of molecules in solution. Following its extension into time-domain experiments using an optical pump/X-ray probe scheme, it has had a strong impact in advancing the research to elucidate the mechanisms of photoexcited systems. An X-ray Absorption spectrum (XAS) marks the absorption of a core electron to the continuum. Depending on the excited core electron, the edges are labeled with different names: K for the $1s$ electron, L_1 for $2s$, L_2 for $2p_{1/2}$, L_3 for $2p_{3/2}$, etc.

The distinct spectral resonances, which occur around the absorption edge of XAS, deliver information about the geometric structure, electronic and vibrational properties of a material [38]. The spectrum, as shown in Fig. 4.4 is conventionally divided into two principal regions: the Extended X-ray Absorption Fine Structure (EXAFS) region, with energy from ~ 50 eV above the edge, and the X-ray absorption Near Edge Structure (XANES) region in the proximity of the transition edge until 50 eV above it. The EXAFS spectrum is characterized by weak oscillatory modulations arising from the interference between the outgoing pho-

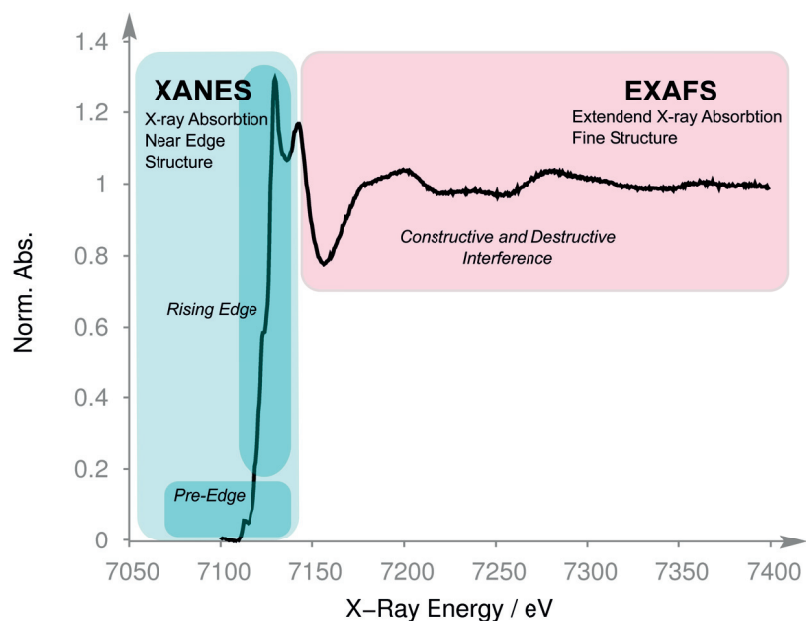


Figure 1.3: X-ray fine structure spectrum of Fe K-edge of $[\text{Fe}(\text{bpy})_3]^{+2}$, from Ref. [37]: the two main regions, XANES and EXAFS, are highlighted.

photoelectron wave with its backscattered wave from neighboring atoms. In this region, single scattering events dominate the spectrum. The photoelectron mean free path depends on the coordination number and the internuclear bond distances of the nearest neighbors around the absorbing atom. The XANES spectrum can be divided into two regions: i) below the absorption edge resonances arise from bound-bound transition into the valence molecular orbitals below the ionization potential (IP) ii) above the edge new features arise from scattering of the photoelectron. The low kinetic energy of the photoelectron in the XANES region results in large scattering amplitudes increasing the probability of multiple-scattering events. As a consequence, the XANES region delivers details about both the electronic structure, such as the occupancy of valence orbitals, oxidation state, orbital delocalization, and the nuclear arrangement of the system such as bond distances and angles. Since the XANES spectrum is strongly influenced by the geometrical structure around the absorber and by the electronic structure, many effects contribute to the signal. These effects, combined with the fact that several approximations are needed for its theoretical description, makes the quantitative interpretation of the XANES spectrum a challenge.

In its time-domain extension, the XAS signal is recorded at different time delay after exciting the system with visible or ultraviolet light. The scheme adopted is very similar to the pump/probe used in TA but with an X-ray pulse as probe.

X-ray emission spectroscopy The excitation of a core-electron, by absorption of X-ray radiation, leaves a hole that is filled in very short time, $\sim 10^{-15}$ s, by electrons from higher

1.2. Investigation of the photoinduced dynamics

occupied orbitals. The de-excitation mechanism produces electrons and photons. This latter are collected when a X-ray emission spectroscopy experiment is performed. The energy of this fluorescence is a fingerprint of the electronic structure of the occupied orbitals. If the incident photon creates a hole in the K shell (1s orbital), the X-ray emission spectrum exhibits many features arisen due to transitions from different electronic states. Fig. 1.4 shows the K shell emission of copper in CuO [39]. The most intense lines, called K_{α} , are produced from transitions from another core level, $2p$. Due to strong spin-orbit coupling of the core-electrons, K_{α} is shifted in two lines, labeled as K_{α_1} and K_{α_2} , which are originated by the $2p_{3/2}$ and $2p_{1/2}$ levels. At higher emission energy, transitions from the $3p$ shell generate the $K_{\beta_{1,3}}$ lines, almost one order of magnitude weaker than the K_{α} lines. This region is sensitive to the oxidation state of the system. Finally, transitions from the valence electrons, are responsible for very weak and high energy emission lines, $K_{\beta''}$ and $K_{\beta_{2,5}}$. These latter provide information about the chemical environment of the scattering atom, in particular chemical bonds and local coordination [40, 41].

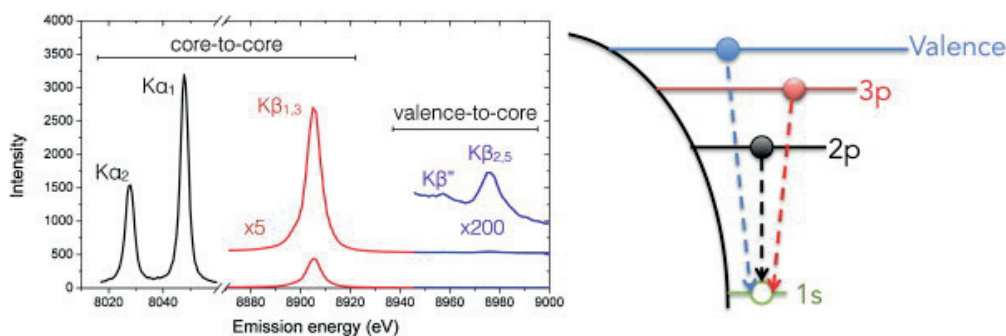


Figure 1.4: Right) The K shell emission spectrum of CuO [39]. Left) Scheme of the transitions. The most intense peaks, K_{α_1} and K_{α_2} , correspond, respectively, to transitions from the $2p_{3/2}$ and $2p_{1/2}$ levels (black). Transitions from the $3p$ levels give rise to the $K_{\beta_{1,3}}$ lines (red). Filling of the hole from valence electrons generates the $K_{\beta''}$ and $K_{\beta_{2,5}}$ peaks. Reproduced with permission from Ref. [40], Copyright (2014 Elsevier B.V.)

1.2.2 Computational methods

Computational tools are essential for the complete interpretation of the experimental spectra. Such analysis can be performed by using a variety of computational methods that can provide information of different photophysics aspects of a molecular system and deliver insight into the ultrafast photoinduced dynamics of a molecular system.

Electronic structure methods First of all, electronic structure methods, give insight into the nature of the Franck-Condon state, the initial electronic ground state. We can, for example, adopt Density Functional Theory (DFT) for retrieving the optimized structure of the metal complex of interest and its ground state electronic structure. In the same manner, we can determine the nature of the lowest excited state, if the multiplicity of the system

changes. Time-Dependent DFT (TDDFT) can be used for the identification of the excited states, and for the calculation of absorption spectra, both in gas phase and in solvent.

Simulation of spectra X-ray Simulation of X-ray absorption spectra required the combination of many techniques because at different absorption energies peculiar processes are activated. The EXAFS region, due to the high kinetic energy of the photoelectron, is dominated by single scattering events. The EXAFS fine structure function, $\chi(E)$, is defined as

$$\chi(E) = \frac{\mu(E) - \mu_0(E)}{\Delta\mu_0(E)}, \quad (1.5)$$

where $\mu(E)$ is the measured absorption coefficients, $\mu_0(E)$ the smooth absorption function of an isolated atom, and $\Delta\mu_0$ the difference of absorption coefficients at the edge, can be described by a scattering path expansion [42], in the $k = \sqrt{\frac{2m(E-E_0)}{\hbar^2}}$ space,:

$$\chi(k) = \sum_{\gamma} \frac{N_{\gamma} S_0^2 |f_{eff}(k)|}{k R_{\gamma}^2} e^{-2R_{\gamma}/\lambda_{tot}(k)} e^{-2\sigma^2 k^2} \sin(2kR_{\gamma} + \phi_{\gamma}), \quad (1.6)$$

where N_{γ} is the number of equivalent γ paths, S_0^2 is an overall amplitude reduction factor, which takes in account the many-body effects due to the relaxation of the system in response to the creation of the core hole, R_{γ} is defined as the half-path distance and $f_{eff}(k) = |f(k)e^{i\phi(k)}|$ is the complex back-scattering amplitude for each path γ . The oscillatory structure arises from the destructive and constructive interference, is determined by the $\sin(2kR)$ term. The backscattering amplitude, which depends on the nature and the number of neighboring atoms, is related to the strength of the reflected waves. In the formula two decay terms are present: $e^{2R_{\gamma}/\lambda_{tot}(k)}$ takes into account the mean free path of the photoelectron and the Debye-Waller factor, $e^{2s^2 k^2}$, which accounts for thermal effects and structural disorder.

Although Eq. 1.6 can accurately simulate the EXAFS spectrum, the most complex origin of the near edge (XANES) region means that this approach is no longer valid. The most widely used approach for the calculation of the final state is based on the Multiple-Scattering Theory (MST)[38]. This has the merit of a very low calculation cost, but does require that the potential around each scattering center is described as non-overlapping spheres, namely the muffin-tin approximation, for which the space is divided into non-overlapping atomic regions where the potential is spherical and in an interstitial intranuclear region where it is flat. An alternative method based on the so-called Finite-Difference-Method (FDM) [43] was proposed [44] in order to overcome the limitations of the muffin-tin potential in describing real potentials. Within this method, the potential is described by the Local Density Approximation (LDA). Extrinsic and intrinsic losses are taken into account by broadening the spectrum with a Lorentzian convolution function. The broadening of the spectrum, induced by extrinsic and intrinsic losses, is reproduced with the use of a Lorentzian convolution

1.2. Investigation of the photoinduced dynamics

function, $\Gamma_f(\omega) = \Gamma_{hole} + \gamma(\omega)$, which includes the natural finite lifetime of the core-hole and the spectral width of the final state due to inelastic scattering processes, $\gamma(\omega)$.

Transitions from the core to the valence orbitals, below the ionization threshold, can be simulated by using TDDFT or the Linear-Response TDDFT formalism. The standard formulation of TDDFT, within the adiabatic approximation [45] is based upon pure density functionals, and therefore, it can only yield one of the triplet states, namely the transition, which maintains the spin quantum number. Recently the non-collinear (spin-flip) TDDFT scheme [46, 47] has been extended for core-hole excitations [48]. Alternatively, the Restricted Open-shell Single excitation Configuration Interaction (ROCS) method have been proposed [49]. In this approach a restricted open-shell HF or an open-shell Kohn-Sham orbitals function reference is expanded with five excitation classes. Finally, it is important to note that in the cases when multiplet effects are important, a full treatment of electron correlation effects is important to guarantee the correct description of the spectra. Towards this goal Josefsson et al. [50] have recently implemented an approach based upon RASSCF and RASPT2. However, these calculations are a significant challenge for larger systems.

In the case of heavier elements, relativistic effects are important. For K-edges the spin-orbit coupling (SOC) constant of the 1s levels is zero meaning that only scalar relativistic effects need to be accounted for. This can be efficiently achieved using, for example, the Zero Order Relativistic approximation (ZORA) [51, 52]. However, for the simulation of L-edge spectra, it is necessary to consider also multiplet effects and a detailed treatment of the strong 2p Spin-Orbit Coupling (SOC).

X-ray emission spectra can be computed by performing a DFT calculation and approximating the orbital energy difference to the transition energy [53, 54].

Molecular dynamics The advent of ultrafast spectroscopic techniques has opened up the possibility of tracing the motion of the nuclear wavepacket from photoexcitation to the complete relaxation into the lowest emitting states.

Computationally, the most common approach to address such problems is by calculating energy profiles along viable reaction and/or decay pathways. While useful, the resulting picture is static and lacks the dynamical information important for obtaining a complete understanding. In particular, because excited state dynamics is characterized by the breakdown of the Born-Oppenheimer approximation [55, 56], these simulations must not only describe the profile of the excited state surfaces but also, accurately incorporate the effects of the coupling between the different states, which leads to multiple non-adiabatic relaxation channels and effects such as wavepacket bifurcation.

Couplings between excited states can be distinguished into two principal groups, internal conversion (IC) and intersystem crossing (ISC). While the first is wavepacket population transfer between two states of the same spin multiplicity, the latter arises from the spin-orbit

coupling (SOC) interaction between states of different multiplicity. For transition metal complexes, accurately describing ISC is often important.

In order to describe the dynamics of excited molecules, several non-adiabatic dynamics schemes have been developed. In general non-adiabatic dynamics can be classified into two classes depending on the way the nuclei are described. The first is quantum wavepacket dynamics, in which the nuclei are represented as a nuclear wavepacket propagating on pre-calculated potential energy surface according to the time-dependent Schrödinger equation. An example is the Multi Configuration Time-Dependent Hartree (MCTDH)[57] method (see Sec. 2.2). This method is very accurate, especially if combined with high-level post-Hartree-Fock methods but limited to a small number of nuclear degrees of freedom. For medium to large size system, it is necessary to evaluate *a priori* the relevant normal modes to be included in the electronic Hamiltonian. The second approach treats the nuclei as classical particles moving on an effective potential energy surface, Ehrenfest dynamics [58], or on multiple potential energy surfaces, Trajectory Surface Hopping (TSH)[59] (see Sec. 2.3). The advantage of the methods, based on the classical description of the nuclei, is the possibility to compute the electronic properties *on-the-fly* allowing the system to span freely the multidimensional phase space.

However, non-adiabatic dynamics is computationally expensive and the dynamics is limited to a few ps. Once the system is relaxed into a long-lived excited state, non-adiabatic coupling terms may become negligible. However, other effects, for example, solvent reorganization or structural changes, take place over a longer time. In this case, molecular dynamics (MD) based on the Born-Oppenheimer approximation can be used. All nuclear quantum effects are neglected and the nuclear wavepacket is replaced by a single classical trajectory. The advantage is to drastically reduce the computational effort and to access longer time scale (from tens of ps to ns). Depending on the method used for describing the electronic degree of freedom of the system, many schemes have been developed, namely *ab-initio* MD, Car-Parrinello MD, or Classical MD (see Sec. 2.4).

1.3 Cu(I)-phenanthroline complexes

Photocatalysts seeking to exploit solar radiation to produce chemical fuels, such as hydrogen, represents a promising approach to meet growing energy demands [60, 61, 62]. In recent years, various steps towards efficient systems have been undertaken, although no example having the desired properties of stability and economic viability has been discovered. Many examples of molecular catalysts, composed of a sensitiser, reduction catalyst and sacrificial donor have been reported with some of them exhibiting incredible performances [63, 64]. However, molecular sensitisers tend to be based on ruthenium(II) derivatives coordination chemistry complexes, and in the interest of long-term sustainability, a preferable scenario is one for which these complexes containing rare transition metals are replaced with earth-abundant ones.

To achieve this, photosensitisers based on d^{10} Cu(I)-phenanthroline complexes have received significant attention [65]. In this regard, they have many properties, which are similar to the ruthenium polypyridines [66]. However, they exhibit a lower coordination number of 4 which, while offering greater flexibility to fine tune their photophysical properties, also leads to strongly structure-dependent energetics and a susceptibility to solvent effects, which has so far hampered their use. In addition, these molecules are characterized by an intense absorption in the visible region of the spectrum. Unfortunately, many of these complexes exhibit excited state lifetimes (ps-ns) that are incommensurate with the prolonged timescales required to facilitate photocatalytic reactions. This kinetic discrepancy hinders the realization of efficient photocatalytic devices for fuel production [62].

In general, the ground state of these complexes adopts a pseudo-tetrahedral geometry with the two ligands being orthogonal [67]. The highest occupied orbitals of Cu(I)-phenanthroline complexes have a predominant d-character, due to the metal contribution. Cu(I) has formally the $3d^{10}$ electronic configuration. Upon photoexcitation an electron, from d orbitals, is formally promoted into a π^* orbital, localized on one of the two phenanthroline ligands, leaving a hole at the metal center that becomes Cu(II). The resulting excited state is a metal-to-ligand-charge-transfer (MLCT) state. The π^* electron is weakly bound and can easily oxidize other species. In contact with n-type semiconductor surfaces, thin films of copper complexes can inject electrons from the MLCT state into the conduction band. The system relaxes through non-radiative electronic processes (IC, ISC, IVR) into the lowest MLCT triplet state. Due to the change of oxidation state of the metal center, Cu(I) \rightarrow Cu(II), the structure twists from a perpendicular to a flattened geometry (pseudo Jahn-Teller distortion) (see Fig. ??). As a result, the lowest triplet and singlet states are characterized by a double-minimum potential energy surface, in which each minimum corresponds to one of the two symmetric flattened geometries. The emission exhibits a large Stokes shift and its lifetime is strongly solvent dependent [68, 69, 70]. Notably, for $[\text{Cu}(\text{dmp})_2]^+$, luminescence lifetime is 90 ns in a non-donating solvent, dichloromethane??, and it decreases to less than 2 ns in a donating one, acetonitrile??. Such luminescence quenching was ascribed to the formation of an exciplex, a stable complex composed of a molecule in the excited state, Cu(I)-phenanthroline, and by a molecule in the ground state, solvent, promoted by the flattening of the metal complex, which creates an additional coordination site where a nucleophile can be accommodated. This model, as discussed in Subsec. 1.3.2, was not confirmed by recent time-resolved XAS measurements.

1.3.1 Phosphorescence and Fluorescence

The emission properties of Cu(I)-phenanthroline molecules have been investigated since the end of the 70's, in the pioneering studies of McMillin and coworkers [71, 72, 73, 74, 75]. By performing temperature dependent measurements they found that the luminescence arises from a two-level system [76]. Fig. 1.6 shows the decay time of the emission maximum of $[\text{Cu}(\text{dmp})_2]^+$ in CH_2Cl_2 at 25 and -30C. The two states are separated by an energy gap of

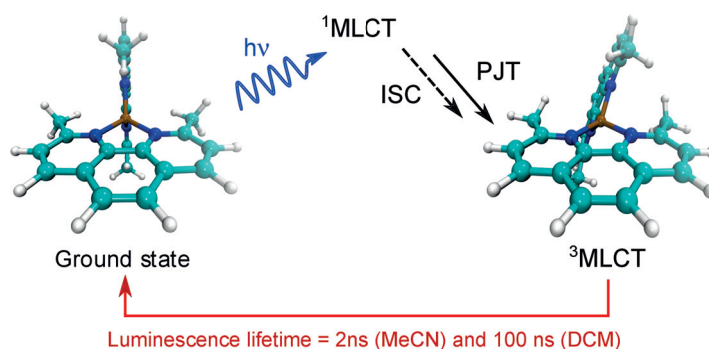


Figure 1.5: General schematic of the excited state dynamics of $[\text{Cu}(\text{dmp})_2]^+$. MeCN = acetonitrile and DCM = dichloromethane.

$\Delta E \approx 1800\text{cm}^{-1}$ and the radiative rates were estimated as $k_{1r} \approx 2 \times 10^7\text{s}^{-1}$ and $k_{2r} \approx 1 \times 10^3\text{s}^{-1}$, which lead the authors to conclude that the higher-lying energy one is a singlet $^1\text{MLCT}$ state and the other a triplet $^3\text{MLCT}$ state. Similar results have been reported for other Cu(I)-phenanthroline complexes [77, 78].

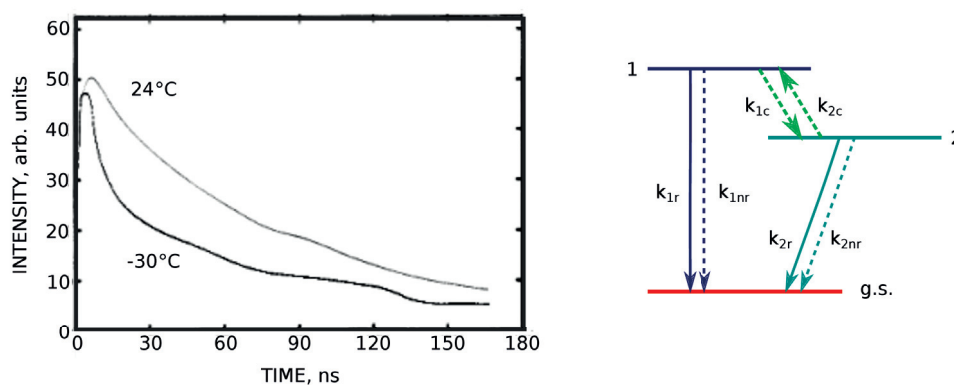


Figure 1.6: Left) Emission decay for $[\text{Cu}(\text{dmp})_2]^+$ dissolved in CH_2Cl_2 at 24 and -30°C . Data from Ref. [76]. The emission at low temperature is red-shifted, less intense, and has a shorter decay time. Right) Scheme of two emitting states, 1 and 2, respectively, with radiative constant, k_{1r} and k_{2r} , and nonradiative constant, k_{1nr} and k_{2nr} . The conversion mechanisms from state 1 to state 2, and vice-versa, have rate of k_{1c} and k_{2c} .

The transfer of population from $^1\text{MLCT}$ to $^3\text{MLCT}$, shown in Fig. 1.6, is ruled by the intersystem crossing mechanism. The downward process, from $^1\text{MLCT}$ to $^3\text{MLCT}$, induced by spin-orbit coupling, is fast. However, due to the small energy separation $\Delta E(^1\text{MLCT} - ^3\text{MLCT})$, also the opposite upward process, from $^3\text{MLCT}$ to $^1\text{MLCT}$ is effective at room temperature. As a result, the emission to the ground state, g.s., is governed by a Boltzmann distribution:

$$\frac{\text{Int}(^1\text{MLCT} \rightarrow \text{g.s.})}{\text{Int}(^3\text{MLCT} \rightarrow \text{g.s.})} = \frac{k_r(^1\text{MLCT} \rightarrow \text{g.s.})}{k_r(^3\text{MLCT} \rightarrow \text{g.s.})} \cdot \exp\left(-\frac{\Delta E_{1\text{MLCT}-3\text{MLCT}}}{k_B T}\right) \quad (1.7)$$

where $\text{Int}({}^1\text{MLCT} \rightarrow \text{g.s.})$ and $\text{Int}({}^3\text{MLCT} \rightarrow \text{g.s.})$, $k_r({}^1\text{MLCT} \rightarrow \text{g.s.})$ and $k_r({}^3\text{MLCT} \rightarrow \text{g.s.})$ represent the fluorescence and phosphorescence intensities and the corresponding radiative rates, respectively, k_B is the Boltzmann constant and T the absolute temperature [13]. This luminescence mechanism is known as thermally activated delayed fluorescence (TADF).

1.3.2 Solvent dependence

In the mid-'80s, McMillin and co-workers observed [68] that the luminescence quantum yields of $[\text{Cu}(\text{dmp})_2]^+$ is strongly reduced in donating solvents, i.e. those behaving as Lewis bases, such as acetonitrile, ethanol, and water. In these solvents, of each 1000 absorbed photon, only one is emitted (quantum yields $\sim 10^{-4}$). In addition, it was found that the emission lifetime in donating solvents, such as acetonitrile (~ 2 ns), ethylene glycol (~ 2 ns) [79] or tetrahydrofuran (< 10 ns) [70] is significantly shortened compared with non-donating solvents such as dichloromethane (~ 100 ns) and toluene (~ 100 ns) [80]. This pronounced difference, observed for all the class of Cu-phenanthroline molecules, was attributed to the formation of a metastable complex formed by the interaction of one solvent molecule and the metal center of the photoexcited molecule. The formation of an exciplex generates additional non-radiative decay channels reducing the luminescence lifetime and quantum yields. In addition, the interaction between the Cu(II) atom and the electron-rich donor molecule is thought to stabilize the excited species, reducing the energy gap between excited and ground state. As a consequence, the non-radiative decay rate increases [81]. This implies that to a longer emission wavelength corresponds a shorter emission lifetime. $[\text{Cu}(\text{dmp})_2]^+$ and other related Cu(I)-phenanthroline complexes seem to support this trend.

The exciplex model achieved resounding success because it could explain the luminescence lifetime trend of different Cu-phenanthroline complexes. It was observed that complexes with cumbersome substituents at the positions 2,9 of the phenanthroline (see Fig. 6.2 for the number nomenclature) have a longer lifetime in both donating and non-donating solvent (see Table 1.1). Among them, an outstanding long lifetime and large quantum yield were measured for $[\text{Cu}(\text{dsbtmp})_2]^+$ (dsbtmp = 2,9-di(sec-butyl)-3,4,7,8-tetramethyl-1,10-phenanthroline) by Castellano and al. [82, 83]. Large substituents, in fact, may act as protector groups around the metal center preventing the formation of the exciplex and thus increasing the lifetime [70, 69, 84]. However, some important exceptions make it difficult to clarify the role of the donating solvent, emission wavelength or steric impediment in governing these trends. Notably, $[\text{Cu}(\text{phen})_2]^+$ (phen=1,10-phenanthroline), the only Cu(I)-phenanthroline without any phenanthroline substituents, exhibit shorter lifetimes than expected in both acetonitrile (16 ps) and dichloromethane (140 ps) [85]. Another example, $[\text{Cu}(\text{detp})_2]^+$ (detp=3,8-di(ethynyltrityl)-1,10-phenanthroline) has bulkier and extended ligands, which are supposed to prevent exciplex formation. However, its emission lifetime is very short, similar to that of $[\text{Cu}(\text{phen})_2]^+$, but it was still attributed to complexation at the metal center [85]. $[\text{Cu}(\text{dbp})_2]^+$ and $[\text{Cu}(\text{dbtmp})_2]^+$, respectively (dbp=2,9-di(butyl)-1,10-phenanthroline) and (dbp=tetra(methyl)-2,9-di(butyl)-1,10-phenanthroline), have the same

Chapter 1. Investigation of the photophysics of metal-organic complexes

Table 1.1: Room-temperature Solvent-Dependent Excited-State Lifetimes (τ) and Emission Wavelengths of a Series of Cu-Phenanthroline Complexes. ^a [79], ^b [70], ^c [69], ^d [86], ^e [78], ^f [85], ^g [87], ^h . Table from Ref. [88].

Complex	Acetonitrile		Dichloromethane		Tetrahydrofuran		Solid	
	τ (ns)	λ_{max}^{em} (nm)	τ (ns)	λ_{max}^{em} (nm)	τ (ns)	λ_{max}^{em} (nm)	τ (ns)	λ_{max}^{em} (nm)
[Cu(dmp) ₂] ⁺	1.6 ^a	700 ^b	90 ^b	690 ^b	<10 ^{b3}	700 ^b		650 ^h
[Cu(dnpp) ₂] ⁺	100 ^b	685 ^b	260 ^b	665 ^b	140 ^b	675 ^b		670 ^h
[Cu(dpp) ₂] ⁺	120 ^c	740 ^c	270 ^c	720 ^c	190 ^c	730 ^c	780 ^g	670 ^g
[Cu(tfp) ₂] ⁺			165 ^d					
[Cu(dmdp) ₂] ⁺			80 ^d					
[Cu(dbp) ₂] ⁺	35 ^b (35 ^c)	690 ^b (730 ^c)	150 ^b (150 ^c)	670 ^b (715 ^c)	50 ^b (50 ^c)	680 ^b (725 ^c)		620
[Cu(dbtmp) ₂] ⁺	440 ^c	690 ^c	920 ^c	670 ^c	630 ^c	670 ^c		
[Cu(tpp) ₂] ⁺			230 ^e	745 ^e				
[Cu(dpdmp) ₂] ⁺			310 ^c	720 ^c				
[Cu(dbdmp) ₂] ⁺			145 ^c	710 ^c				
[Cu(dptmp) ₂] ⁺	260 ^c	735 ^c	480 ^c	715 ^c	350 ^c	725 ^c		
[Cu(detp) ₂] ⁺	0.014 ^f		0.20 ^f					
[Cu(phen) ₂] ⁺	0.016 ^f		0.14 ^f					
[Cu(bcp) ₂] ⁺			80 ^e	770 ^e				690 ^g
[Cu(tmbp) ₂] ⁺			18 ^e	775 ^e				
[Cu(tmp) ₂] ⁺			20 ^d					700 ^g

substituents at the positions 2,9 that are thought to be important for the fifth coordination site. Nonetheless, [Cu(dbp)₂]⁺ exhibits a lifetime shortening of a factor of five in a donating solvent and a larger quenching than [Cu(dbtmp)₂]⁺.

Although the exciplex model can explain a variety of behaviours, no clear evidence of its formation was provided. To verify this hypothesis, several studies were performed using transient X-ray absorption spectroscopy. According to the model, the formation of an exciplex, and thus the presence of a solvent molecule close to the copper atom, will modify the geometric and the electronic structure of the system. XAS is the ideal technique to shed light on this issue as it can unravel the local geometric and electronic structure around the Cu atom and therefore it can eventually provide evidence for the formation of the exciplex. In particular, the $1s \rightarrow 4p$ feature of the Cu K-edge was proved to be a sensitive probe of the coordination [90]. In particular, the intensity of the signal from a tetracoordinated species is expected to be twice compared to pentacoordinated ones. Chen et al. [91, 92] measured a loss of intensity for this transition for [Cu(dmp)₂]⁺ in both acetonitrile and toluene, concluded that both solvents form exciplexes. This interpretation was reinforced by the structural characterization performed by Smolentsev *et al.* [93, 94], which found that the transient XANES spectrum of the system can be fitted assuming one acetonitrile molecule coordinated to the copper. Importantly they found the nitrogen of the acetonitrile was only

$\sim 2.0 \text{ \AA}$ from the copper atom and, therefore, was indistinguishable from the nitrogens of the diimine ligands. However, no justification for this model has been obtained from theoretical simulations, and a geometry optimisation of a $[\text{Cu}(\text{dmp})_2]^+ \cdots \text{HCN}$ adduct reported that the acetonitrile nitrogen is more than $\sim 3.0 \text{ \AA}$ away from the copper [91]. Indeed, in a recent work by Chergui and co-workers [88] the exciplex interpretation was not confirmed. They found, performing transient XAS of $[\text{Cu}(\text{dmp})_2]^+$ in acetonitrile (donating) and dichloromethane (non donating) that the spectra are remarkably similar, invalidating the exciplex model. Fig. 1.7 shows, on the right, the experimental static and transient spectra of $[\text{Cu}(\text{dmp})_2]^+$ in acetonitrile and, on the left, the same transient spectra in acetonitrile plotted with the one obtained in dichloromethane. Such results question the long established exciplex model. The authors, using quantum chemical calculations and molecular dynamics simulations, ascribed the quenching of the luminescence to the weak electrostatic interaction between the complex and the first solvation shell. More details about this topic for $[\text{Cu}(\text{dmp})_2]^+$ and other related Cu(I)-phenanthroline can be found in Chapter 6 and 7.

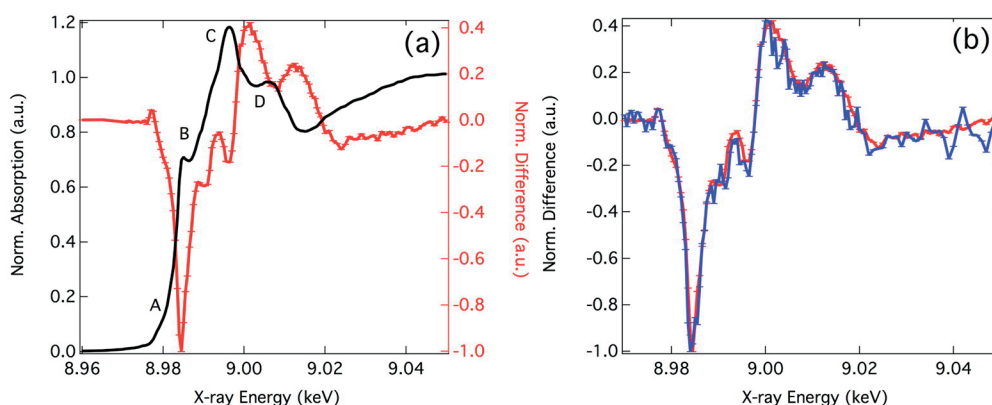


Figure 1.7: (a) Static (black) and transient (red, at 50 ps) Cu K-edge XANES spectra of $[\text{Cu}(\text{dmp})_2]^+$ in acetonitrile. (b) Transient XANES spectrum (at 50 ps) of $[\text{Cu}(\text{dmp})_2]^+$ in acetonitrile (red) and dichloromethane (blue). In all cases the transient spectra have been normalized to the largest difference.

1.3.3 Ultrafast relaxation kinetics

In the previous section, we summarised the studies characterizing the effect of the electronic and geometric structure and the role of the solvent on the photophysical properties. Here we focus on those processes occurring in the ultrafast (femtosecond) timescale after light absorption. Such processes have been studied by a number of groups employing time-resolved optical (absorption and fluorescence) and time-resolved X-ray absorption spectroscopies [79, 95, 96, 97, 98]. Their works revealed that these initial steps are completed within a few tens of picosecond and are broadly equivalent for all of the complexes. However, nature and characteristic time of the ultrafast processes are still unclear and the full dynamic description of the relaxation processes remains elusive.

Chapter 1. Investigation of the photophysics of metal-organic complexes

The ultrafast dynamics of $[\text{Cu}(\text{dmp})_2]^+$, which is considered the prototypical Cu(I)-phenanthroline complex, was first studied by Chen et al. [91], using time-resolved optical absorption. The mechanism proposed by the authors consists in a photoexcitation of the optically bright $^1\text{MLCT}$ followed by sub-picosecond internal conversion into the lowest singlet state. Notably, they found two characteristic time decays, 500-700 fs and 10-20 ps, which were assigned, respectively, to intersystem crossing and Jahn-Teller distortion. This assignment was revised by Tahara and co-workers [99], which probed the excited state dynamics using femtosecond fluorescence up-conversion. They measured an ultrafast IC (45 fs) followed by two processes occurring in 660 fs and 7.4 ps. Contrary to what was proposed by Chen and co-workers, they assigned the fast component to the structural distortion and the long one to ISC. In a later study, Chen et al. [79], by performing both time-resolved absorption spectroscopy and ultrafast fluorescence up-conversion, found similar results and, in agreement with Tahara and co-workers, assigned the slow component to ISC. Finally, Tahara and co-workers [99], upon excitation of the lowest $^1\text{MLCT}$, were able to observe wavepacket motion along the Jahn-Teller distortion coordinates, concluding that structural distortion occurs since the earliest times.

These experiments pointed out that Cu(I)-phenanthroline does not exhibit ultrafast ISC. This is partially supported by computational studies [100, 67] showing that the spin-orbit coupling matrix element between the lowest singlet and triplet excited states, S_1 and T_1 is very small at the distorted geometry $\sim 30 \text{ cm}^{-1}$ and, therefore, ISC occurs on the timescale of tens of picosecond. However, the same studies mention that at the Franck-Condon geometry, spin-orbit coupling is an order of magnitude larger, $\sim 300 \text{ cm}^{-1}$ [100] and other triplet states are packed close to S_1 [67], meaning that $S_1 \rightarrow T_1$ is not the only ISC channel.

In conclusion, Fig. 1.8 shows the scheme for a photoexcited Cu(I)-phenanthroline. After photon absorption, the system is in an optically allowed singlet state before complete relaxation into the triplet state minima. Such relaxation is completed in a few picoseconds but the nature of the processes (IC, ISC, and PJT), is still unknown. The lowest singlet and triplet states are characterized by a double-minimum structure, originated by the flattening of the ligands that can take place in two opposite and symmetric directions. Both states can decay radiatively to the ground state, via fluorescence and phosphorescence. However, the rate of the emission is strongly reduced when the complex is dissolved in a donating solvent.

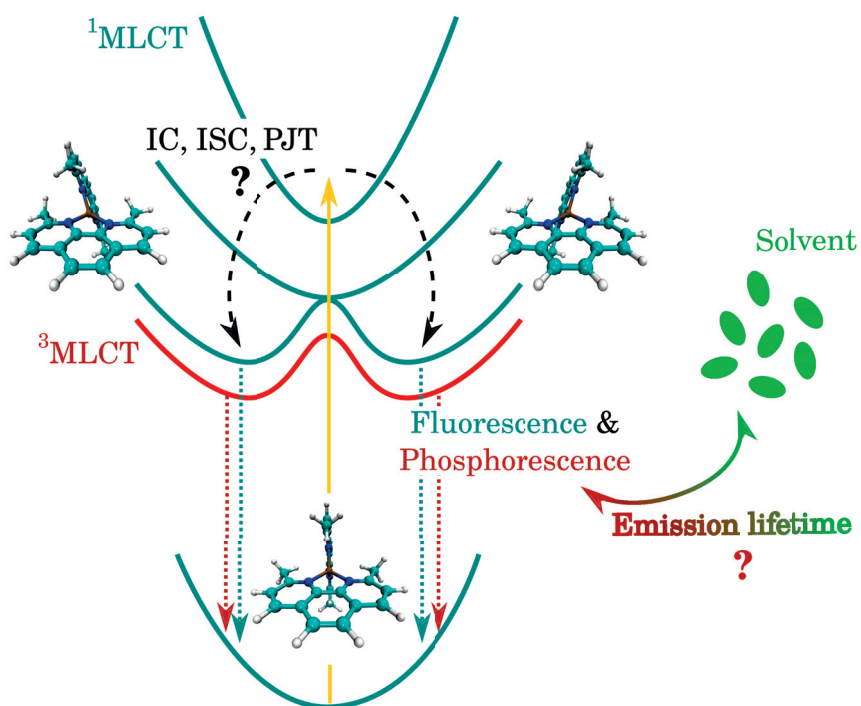


Figure 1.8: Scheme of the relaxation processes of a photoexcited Cu(I)-phenanthroline. Upon photoexcitation to the optical allowed $^1\text{MLCT}$ electronic state, yellow arrow, the system relaxes through non-adiabatic mechanisms such as IC, ISC, and PJT distortion (black dashed lines) to the lowest emitting $^1\text{MLCT}$ and $^3\text{MLCT}$ states. These two states are characterized by two degenerate minima, which corresponds to the two symmetric distortions of the ligands. Interaction with the solvent leads to a solvent dependency of the luminescence lifetime. See main text for details.

2 Molecular dynamics methods

This chapter provides an overview of the most important theoretical methods developed for solving the time-dependent Schrödinger equation (TDSE) of a molecular system. In Section 1, the nuclear TDSE is derived using the Born-Huang expansion of the wavefunction, and the non-adiabatic coupling operators are defined. In Section 2, the quantum wavepacket dynamics is introduced with an explanation on the MCTDH method. Section 3 focuses on the non-adiabatic classical trajectories dynamics introducing the trajectory surface hopping (TSH) methods within the Time-Dependent Density Functional Theory (TDDFT) formalism for the electronic structure. The final sections, 4 and 5, describe the approaches used to study the ground state dynamics.

2.1 Time dependent Schrödinger equation for a molecular system

Studying the time evolution of a molecular system means solving the time-dependent Schrödinger equation [101]:

$$i\hbar \frac{\partial}{\partial t} \Psi = \hat{H} \Psi, \quad (2.1)$$

where Ψ is the molecular wavefunction and \hat{H} the Hamiltonian of the system. A molecular system composed by n_N nuclei and n_e electrons can be described by a set of nuclear coordinates $\mathbf{R}_1, \dots, \mathbf{R}_N \equiv \mathbf{R}$ and a set of electronic coordinates $\mathbf{r}_1, \dots, \mathbf{r}_N \equiv \mathbf{r}$. The corresponding molecular Hamiltonian, in absence of an external field, has the following form:

$$\hat{H}(\mathbf{r}, \mathbf{R}) = \hat{T}_N(\mathbf{R}) + \hat{T}_e(\mathbf{r}) + \hat{V}_{ee}(\mathbf{r}) + \hat{V}_{NN}(\mathbf{R}) + \hat{V}_{eN}(\mathbf{r}, \mathbf{R}) \quad (2.2)$$

where \hat{T}_N and \hat{T}_e are the nuclear and electronic kinetic operators,

$$\hat{T}_N(\mathbf{R}) = \sum_{\alpha}^{n_N} \frac{\hat{p}_{\alpha}^2}{2M_{\alpha}} = - \sum_{\alpha}^{n_N} \frac{\hbar^2}{2M_{\alpha}} \nabla_{\alpha}^2, \quad (2.3)$$

$$\hat{T}_e(\mathbf{r}) = \sum_i^{n_e} \frac{\hat{p}_i^2}{2m_e} = - \sum_i^{n_e} \frac{\hbar^2}{2m_e} \nabla_i^2 \quad (2.4)$$

where $\nabla_\alpha = \frac{\partial}{\partial \mathbf{R}_\alpha}$ and $\nabla_i = \frac{\partial}{\partial \mathbf{r}_i}$. The other three terms of Eq. 2.2 are the electron-electron interaction,

$$\hat{V}_{ee}(\mathbf{r}) = \frac{e^2}{4\pi\epsilon_0} \sum_i^{n_e-1} \sum_{j>i}^{n_e} \frac{1}{|\mathbf{r}_i - \mathbf{r}_j|}, \quad (2.5)$$

nuclear-nuclear interaction,

$$\hat{V}_{nn}(\mathbf{R}) = \frac{e^2}{4\pi\epsilon_0} \sum_\alpha^{n_N-1} \sum_{\beta>\alpha}^{n_N} \frac{Z_\alpha Z_\beta}{|\mathbf{R}_\alpha - \mathbf{R}_\beta|}, \quad (2.6)$$

and electron-nuclear interaction,

$$\hat{V}_{en}(\mathbf{R}, \mathbf{r}) = - \frac{e^2}{4\pi\epsilon_0} \sum_i^{n_e} \sum_\alpha^{n_N} \frac{Z_\alpha}{|\mathbf{r}_i - \mathbf{R}_\alpha|}. \quad (2.7)$$

In the previous formulas, M_α and Z_α are the nuclear mass and atomic number of atom α , m_e , e , and ϵ_0 are respectively electronic mass, electronic charge, and permittivity of the vacuum. All the terms that depend on the electronic coordinates \mathbf{r} can be gathered in an electronic Hamiltonian, $\hat{H}_e(\mathbf{r}; \mathbf{R})$.

2.1.1 Born-Huang expansion

The molecular Hamiltonian can, thus, be written as a sum of the nuclear kinetic operator and the electronic Hamiltonian, which depends parametrically on the nuclear positions \mathbf{R} ,

$$\hat{H}(\mathbf{r}, \mathbf{R}) = \hat{T}_N(\mathbf{R}) + \hat{H}_e(\mathbf{r}; \mathbf{R}). \quad (2.8)$$

The total molecular wavefunction can be represented by means of the Born-Huang expansion [102, 103]:

$$\Psi(\mathbf{r}, \mathbf{R}, t) = \sum_i^\infty \chi_i(\mathbf{R}, t) \psi_i(\mathbf{r}; \mathbf{R}) \quad (2.9)$$

where the time-independent electronic wavefunctions $\psi_i(\mathbf{r}; \mathbf{R})$ depend parametrically on the nuclear coordinates \mathbf{R} and form an orthonormal basis set $\langle \psi_i | \psi_j \rangle = \delta_{ij}$. The time-dependent coefficients, $\chi_i(\mathbf{R}, t)$, are functions of \mathbf{R} and are called “nuclear wavefunctions”. Their square norm, $|\chi_i(\mathbf{R}, t)|^2$, represents the state probability (population) of the corresponding electronic state $\psi_i(\mathbf{r}; \mathbf{R})$. By inserting Eq. 2.14 in Eq. 2.1, multiplying the left-hand side by $\psi_j^*(\mathbf{r}; \mathbf{R})$,

2.1. Time dependent Schrödinger equation for a molecular system

and integrating over the electronic coordinates \mathbf{r} , one obtains the Schrödinger equation for the nuclear motion:

$$i\hbar \frac{\partial}{\partial t} \chi_i(\mathbf{R}, t) = \left[\hat{T}_N(\mathbf{R}) + H_{ii}^e(\mathbf{r}; \mathbf{R}) - \sum_{\alpha} \frac{\hbar^2}{2M_{\alpha}} \mathbf{G}_{ii}^{\alpha} \right] \chi_i(\mathbf{R}, t) + \sum_{j \neq i} \left[H_{ij}^e - \sum_{\alpha} \frac{\hbar^2}{2M_{\alpha}} \left(2\mathbf{F}_{ij}^{\alpha} \cdot \frac{\partial}{\partial \mathbf{R}_{\alpha}} + \mathbf{G}_{ij}^{\alpha} \right) \right] \chi_j(\mathbf{R}, t) \quad (2.10)$$

where the matrix elements for the electronic Hamiltonian are defined as

$$H_{ij}^e = \langle \psi_i | \hat{H}_e | \psi_j \rangle. \quad (2.11)$$

$\mathbf{F}_{ij}^{\alpha}(\mathbf{R})$ and $\mathbf{G}_{ij}^{\alpha}(\mathbf{R})$ are, respectively, the first and second order non-adiabatic coupling matrix element arisen from the application of the nuclear kinetic operator to the electronic wavefunctions:

$$\mathbf{F}_{ij}^{\alpha}(\mathbf{R}) = \langle \psi_i | \nabla_{\alpha} | \psi_j \rangle, \quad \mathbf{G}_{ij}^{\alpha}(\mathbf{R}) = \langle \psi_i | \nabla_{\alpha}^2 | \psi_j \rangle. \quad (2.12)$$

Importantly, the non-adiabatic coupling operators are nonlocal operators. Eq. 2.10 is composed of two parts: the first one describes the motion of the nuclear wavepacket on the electronic state i , while the second one takes into account the population transfer between electronic states. The nuclear motion depends on the nuclear kinetic energy, the potential energy surface (PES) of the electronic state i , H_{ii}^e , and a small correction term \mathbf{G}_{ii}^{α} . This last term disappears if the electronic wavefunctions ψ_i are real functions. The transfer term, which is fundamental to describe radiationless transitions, contains the off-diagonal terms of the electronic matrix and the non-adiabatic coupling elements that describe the transfer of nuclear amplitude between two different potential energy surfaces with the same spin multiplicity, which leads to the wavepacket splitting.

2.1.2 Adiabatic representation

The total molecular wavefunction can be represented, as seen in the previous subsection, by using the Born-Huang expansion (Eq. 2.9) of an orthonormal set of electronic basis function ψ_i . Let's assume that $\psi_i(\mathbf{r}; \mathbf{R})$ and $\epsilon_i(\mathbf{R})$ are, respectively, the eigenstates and eigenvalues of the electronic Hamiltonian $\hat{H}_e(\mathbf{r}; \mathbf{R})$:

$$\hat{H}_e(\mathbf{r}; \mathbf{R}) \psi_i(\mathbf{r}; \mathbf{R}) = \epsilon_i(\mathbf{R}) \psi_i(\mathbf{r}; \mathbf{R}). \quad (2.13)$$

The eigenstates $\psi_i(\mathbf{r}; \mathbf{R})$ are called ‘‘adiabatic electronic states’’ and form a complete infinite basis set, which satisfies the orthonormal relations. For the sake of clarity, we call ψ_i^{adia} and χ_i^{adia} the electronic and nuclear functions in the adiabatic representation. The total

wavefunction is expanded as

$$\Psi(\mathbf{r}, \mathbf{R}, t) = \sum_i \chi_i^{\text{adia}}(\mathbf{R}, t) \psi_i^{\text{adia}}(\mathbf{r}; \mathbf{R}) \quad (2.14)$$

and Eq. 2.10 becomes

$$i\hbar \frac{\partial}{\partial t} \chi_i^{\text{adia}}(\mathbf{R}, t) = [\hat{T}_N(\mathbf{R}) + \epsilon_i(\mathbf{R})] \chi_i^{\text{adia}}(\mathbf{R}, t) + \quad (2.15)$$

$$\sum_{j \neq i} \left[-\sum_{\alpha} \frac{\hbar^2}{2M_{\alpha}} \left(2\mathbf{F}_{ij}^{\alpha} \cdot \frac{\partial}{\partial \mathbf{R}_{\alpha}} + \mathbf{G}_{ij}^{\alpha} \right) \right] \chi_j^{\text{adia}}(\mathbf{R}, t), \quad (2.16)$$

which can be written in matrix form:

$$i\hbar \frac{\partial}{\partial t} \boldsymbol{\chi}^{\text{adia}}(\mathbf{R}) = \left[\hat{T}_N \mathbf{I} + \boldsymbol{\epsilon}(\mathbf{R}) - \frac{\hbar^2}{2\mathbf{M}} (2\mathbf{F}(\mathbf{R}) \cdot \nabla + \mathbf{G}(\mathbf{R})) \right] \boldsymbol{\chi}^{\text{adia}}(\mathbf{R}, t). \quad (2.17)$$

The adiabatic nuclear wavefunction, $\boldsymbol{\chi}^{\text{adia}}$, evolves over the adiabatic PES, defined by Eq. 2.13 for each nuclear configuration \mathbf{R} . The electronic Hamiltonian matrix \hat{H}_e is diagonal and the transition of the nuclear amplitude from one surface to another is described just by the non-adiabatic coupling operators \mathbf{F} and \mathbf{G} . The first order non-adiabatic coupling operator is antihermitian, namely $\mathbf{F} + \mathbf{F}^{\dagger} = 0$, whereas for the second order non-adiabatic operator the relation, $\mathbf{G} + \mathbf{G}^{\dagger} = 2\mathbf{F} \cdot \mathbf{F}$, holds. As consequence, the divergence of \mathbf{F} is

$$\nabla \cdot \mathbf{F} = \mathbf{G} - \mathbf{F} \cdot \mathbf{F}. \quad (2.18)$$

Substituting Eq. 2.18 into Eq. 2.17, and explicitly expressing $\hat{T}_N = -\frac{\hbar^2}{2\mathbf{M}} \nabla^2$, one gets

$$i\hbar \frac{\partial}{\partial t} \boldsymbol{\chi}^{\text{adia}}(\mathbf{R}, t) = \left[-\frac{\hbar^2}{2\mathbf{M}} (\nabla + \mathbf{F}(\mathbf{R}))^2 + \boldsymbol{\epsilon}(\mathbf{R}) \right] \boldsymbol{\chi}^{\text{adia}}(\mathbf{R}, t), \quad (2.19)$$

in which the nuclear kinetic energy operator is replaced by a *dressed* kinetic energy operator, $-\frac{\hbar^2}{2\mathbf{M}} (\nabla + \mathbf{F}(\mathbf{R}))^2$ [56]. In the adiabatic representation, the first order non-adiabatic coupling matrix elements, in the adiabatic representation, can be written as

$$\mathbf{F}_{ij}^{\alpha} = \langle \psi_i^{\text{adia}} | \nabla_{\alpha} | \psi_j^{\text{adia}} \rangle = \frac{\langle \psi_i^{\text{adia}} | \nabla_{\alpha} \hat{H}_e | \psi_j^{\text{adia}} \rangle}{\epsilon_j - \epsilon_i} \text{ for } i \neq j, \quad (2.20)$$

which shows that \mathbf{F} depends inversely on the energy gap between different electronic PESs. When the gap diminishes, the coupling increases prevailing on the effect of the mass. In the limit of avoided crossings or degeneracy of two electronic states ($\epsilon_i = \epsilon_j$), i.e. conical intersections, the non-adiabatic coupling \mathbf{F}_{ij}^{α} becomes infinite.

2.1. Time dependent Schrödinger equation for a molecular system

2.1.3 Diabatic representation

In order to overcome this problem, one can use, instead of adiabatic electronic wavefunctions, diabatic orthonormal electronic wavefunctions,

$$|\psi_j^{\text{adia}}(\mathbf{r}; \mathbf{R})\rangle \rightarrow |\psi_j^{\text{dia}}(\mathbf{r}; \mathbf{R}_0)\rangle, \quad (2.21)$$

which depend on a set of nuclear coordinates for a single fixed point in the configurational space, \mathbf{R}_0 :

$$\hat{H}_e(\mathbf{r}; \mathbf{R}_0)\psi_i^{\text{dia}}(\mathbf{r}; \mathbf{R}_0) = \epsilon_i(\mathbf{R}_0)\psi_i^{\text{dia}}(\mathbf{r}; \mathbf{R}_0). \quad (2.22)$$

The total wavefunction of the system becomes

$$\Psi(\mathbf{r}, \mathbf{R}, t) = \sum_i^{\infty} \chi_i^{\text{dia}}(\mathbf{R}, t)\psi_i^{\text{dia}}(\mathbf{r}; \mathbf{R}_0), \quad (2.23)$$

which replaced in Eq.2.10, after multiplying the left-hand side by $\psi_j^{*\text{dia}}(\mathbf{r}; \mathbf{R})$, and integrating over the electronic coordinates \mathbf{r} , leads to the following nuclear Schrödinger equation:

$$i\hbar \frac{\partial}{\partial t} \chi_i^{\text{dia}}(\mathbf{R}, t) = \hat{T}_N(\mathbf{R})\chi_i^{\text{dia}}(\mathbf{R}, t) + \sum_j W_{ij}\chi_j^{\text{dia}}(\mathbf{R}, t) \quad (2.24)$$

that expressed in matrix notation becomes

$$i\hbar \frac{\partial}{\partial t} \boldsymbol{\chi}^{\text{dia}}(\mathbf{R}, t) = [\hat{T}_n \mathbf{I} + \mathbf{W}(\mathbf{R})] \boldsymbol{\chi}^{\text{dia}}(\mathbf{R}, t), \quad (2.25)$$

where $\mathbf{W}(\mathbf{R})$ is the diabatic potential matrix, whose matrix elements are defines as

$$W_{ij} = \langle \psi_i^{\text{dia}}(\mathbf{r}; \mathbf{R}_0) | \hat{H}_e(\mathbf{r}; \mathbf{R}) | \psi_j^{\text{dia}}(\mathbf{r}; \mathbf{R}_0) \rangle. \quad (2.26)$$

The diabatic potential matrix has only local potential-like terms. In addition, all coupling terms between electronic states are included in $\mathbf{W}(\mathbf{R})$. More importantly, at conical intersection points and avoided crossing regions, by using diabatic electronic states [104, 105], the calculation is not longer affected by singularity [106, 107], inherent to the adiabatic representation. Fig. 2.1 shows a schematic drawn of two electronic states, ψ_1 and ψ_2 , in the adiabatic and diabatic representation. The adiabatic picture provides a sets of energy-ordered potential energy surfaces. In contrast, in the diabatic picture each potential energy surface is related to a specific electronic configuration. Notably, as the surfaces in the diabatic picture are smooth they can often be described by a low-order Taylor expansion.

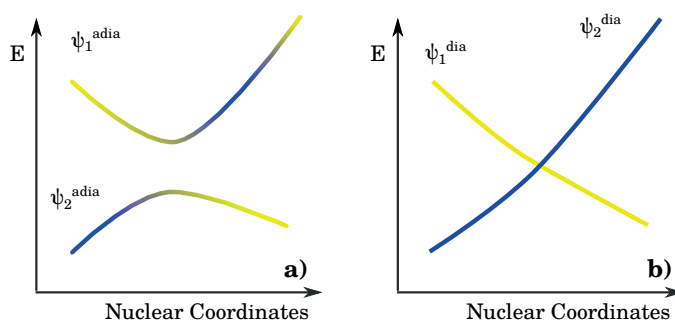


Figure 2.1: Adiabatic and diabatic states for the two level systems, along a single nuclear degrees of freedom. Colors referred to the character of the state. In the adiabatic representation the states have mixed characters; on the other hand, in the diabatic representation, each diabatic state conserves its own character.

2.1.4 Group Born-Oppenheimer approximation

Since the matrix elements of the non-adiabatic coupling operators depend inversely on the energy difference of the electronic states, only adiabatic electronic states that are close in energy couple significantly to each other. The sum over all the adiabatic states (Eq. 2.14) can be restricted to a small number of discrete states n to include only a relevant group:

$$\Psi(\mathbf{r}, \mathbf{R}, t) \approx \sum_i^n \chi_i(\mathbf{R}, t) \psi_i(\mathbf{r}; \mathbf{R}). \quad (2.27)$$

This approximation takes the name of “Group Born-Oppenheimer approximation” and it is used in all non-adiabatic dynamics simulations. The more familiar Born-Oppenheimer approximation [108, 103] corresponds to the extreme case in which a single electronic state is taken in consideration (usually the electronic ground state). Additionally, the adiabatic approximation, can be applied by setting all the non-adiabatic coupling matrix elements to zero. As a consequence, all electronic states decouple and nuclei move on a single electronic potential energy surface.¹

2.2 A short overview of the MCTDH method

The solution of the nuclear equation of motion, Eq. 2.10, due to presence of a large number of matrix elements to be computed, it requires significant CPU and memory resources. Exact time-dependent methods remain prohibitive when more than few (2-4) nuclear degrees of freedoms (DOFs) are included. An intuitive trick is to restrict the dynamics along the relevant DOFs of the system.

¹Often “Born-Oppenheimer” and “adiabatic approximations” are used as interchangeable terms.

The normal approach for solving TDSE is the propagation of nuclear wavepacket expressed in a time independent basis set, $\{\varphi_{j_k}^{(k)}(R_k)\}$, with time dependent coefficients, $c_j(t)$,

$$\chi(\mathbf{R}_1, \dots, \mathbf{R}_f, t) = \sum_{j_1=1}^{n_1} \dots \sum_{j_f=1}^{n_f} c_{j_1 \dots j_f}(t) \prod_{k=1}^f \varphi_{j_k}^{(k)}(\mathbf{R}_k) \quad (2.28)$$

where n_f are the number of basis used for the f -th degree of freedom and R_k the nuclear coordinates along the k -th degree of freedom. The memory required to store the wavefunction and the integrals used for the propagation scales as $\sim n^f$, making this approach prohibitive for a large number of DOFs. It is clear that approximated methods are required in order to study real molecular systems. The easiest one, called time-dependent Hartree, describes the nuclear wavefunction as a single Hartree product of time-dependent basis functions, $\{\varphi^{(k)}(R_k, t)\}$, one for each degree of freedom, multiplied by a single time-dependent coefficient, $c(t)$. Although the number of coefficients and basis function is drastically decreased, this method suffers from lack of correlation among DOFs. This can be problematic in regions of the potential energy surfaces such as crossing points or avoided crossing regions [109]. The method can be systematically improved by adding configurations [110] and producing multi-configurational *ansatz*.

Among them, the most successful is the Multi-Configurational Time-Dependent Hartree (MCTDH) [111, 57, 112, 113]. In this formalism, the nuclear wavefunction is written as a linear combination of Hartree products and it propagates in a reduced configurational space span by the most relevant coordinates of the system. The Hamiltonian is obtained through a fit of the electronic potential energy surfaces along the selected coordinates.

This chapter overviews, in Section 2.2.1, the MCTCH method, describing the nuclear wavepacket *ansatz* and deriving the equations of motion. Section 2.2.3 is devoted to the Vibronic Coupling Hamiltonian model and how the relevant DOFs of a system are selected.

2.2.1 The MCTDH *ansatz*

Performing a quantum molecular dynamics simulation means solving the Schrödinger equation (TDSE) for the nuclear wavefunction moving on coupled electronic states from some specified initial conditions $\chi(t=0)$:

$$i\hbar \frac{\partial}{\partial t} \chi(\mathbf{R}, t) = \hat{\mathbf{H}} \chi(\mathbf{R}, t). \quad (2.29)$$

In the Multi-Configurational Time-Dependent Hartree (MCTDH) method [111, 57, 56], the nuclear wavefunction of a system with f degrees of freedom (DOF) is expressed using a

linear combination of Hartree products:

$$\chi(\mathbf{R}_1, \dots, \mathbf{R}_f, t) = \sum_{j_1=1}^{n_1} \dots \sum_{j_f=1}^{n_f} A_{j_1 \dots j_f}(t) \prod_{k=1}^f \varphi_{j_k}^{(k)}(\mathbf{R}_k, t) \quad (2.30)$$

where $\mathbf{R}_1, \dots, \mathbf{R}_f$ are the nuclear coordinates, $A_{j_1 \dots j_f}(t)$ are the time-dependent expansion coefficients and $\varphi_{j_k}^{(k)}$ are the n_k time dependent expansion functions for each nuclear degree of freedom κ , known as single particle functions (SPFs). The SPFs are a set of orthonormal functions and are represented as a linear combination of the primitive basis ζ_{i_k} :

$$\varphi_{j_k}^{(k)}(\mathbf{R}_k, t) = \sum_{i_k=1}^{N_k} c_{i_k, j_k}^{(k)}(t) \zeta_{i_k}^{(k)}(\mathbf{R}_k). \quad (2.31)$$

Usually ζ_{i_k} are replaced by a Discrete Variable Representation (DVR), such as harmonic oscillator functions (HO). By using composite indexes $J = j_1 \dots j_f$, the A coefficients and SPFs can be written as:

$$A_J = A_{j_1, \dots, j_f}, \quad \Phi_J = \prod_{k=1}^f \varphi_{j_k}^{(k)}, \quad (2.32)$$

which lead to a short version of Eq. 2.30:

$$\chi(\mathbf{R}_1, \dots, \mathbf{R}_f, t) = \sum_J \mathbf{A}_J \Phi_J. \quad (2.33)$$

It is useful, at this point, to define the single-hole function of the κ -th DOF:

$$\chi_l^{(k)} = \langle \varphi_l^{(k)} | \chi \rangle = \sum_{j_2=1}^{n_2} \dots \sum_{j_f=1}^{n_f} A_{l j_2 \dots j_f} \varphi_{j_2}^{(2)} \dots \varphi_{j_f}^{(f)} = \sum_{J^k} A_{J_l^k} \Phi_{J^k}. \quad (2.34)$$

The single-hole function can be used for introducing the mean-field matrix

$$\langle H \rangle_{jk}^{(k)} = \langle \chi_j^{(k)} | \hat{H} | \chi_l^{(k)} \rangle \quad (2.35)$$

and the density matrix

$$\rho_{kl}^{(k)} = \langle \chi_j^{(k)} | \chi_l^{(k)} \rangle = \sum_{J^k} A_{J_k}^* A_{J_l^k}. \quad (2.36)$$

The equations of motion The equations of motion for the MCTDH *ansatz* can be derived by applying the Dirac-Frenkel variational principle [114, 115]², the time-dependent equivalent

²The Dirac-Frenkel principle guarantees that, given an hermitian and time-independent Hamiltonian and a model wavefunction in a finite-dimensional space of the full Hilbert space, the equations of motion derived are an approximate variational solution of the original problem, and both norm and energy are conserved.

of the variational principle

$$\langle \delta \chi | \hat{H} - i \frac{\partial}{\partial t} | \chi \rangle = 0. \quad (2.37)$$

After defining the MCTDH projector

$$P^{(k)} = \sum_{j=1}^{n_k} |\varphi_j^{(k)}\rangle \langle \varphi_j^{(k)}|, \quad (2.38)$$

and splitting the Hamiltonian into f single degrees of freedom Hamiltonians $\hat{h}^{(\kappa)}$ and a correlation part \hat{H}_{corr}

$$\hat{H} = \sum_{\kappa} \hat{h}^{(\kappa)} + \hat{H}_{corr} \quad (2.39)$$

we obtain a coupled set of equations that describe the time evolution of the coefficients and of the single particle functions:

$$i \dot{A}_J = \sum_L \langle \Phi_J | \hat{H} | \Phi_L \rangle A_L - i \sum_{k=1}^f \sum_{l=1}^{n_k} g_{j_k l}^{(k)} A_{J_l^k} \quad (2.40)$$

$$i \dot{\varphi}^{(k)} = (\hat{g}^{(k)} \mathbf{1}) \varphi^{(k)} + (1 - P^{(k)}) \{ \boldsymbol{\rho}^{(k)-1} \langle \hat{\mathbf{H}} \rangle^{(k)} - \hat{g}^{(k)} \mathbf{1} \} \varphi^{(k)} \quad (2.41)$$

where $\varphi^{(\kappa)} = (\varphi_1^{(\kappa)} \dots \varphi_{n_\kappa}^{(\kappa)})^T$ is the SPF vector and $g^{(k)}$ is called the ‘‘constraint operator’’.

The constraint operator The MCTDH *ansatz* is not unique because it is possible to represent the same wavefunction in different ways. For example one can write

$$\chi = \sum_{l_1 \dots l_f} \tilde{A}_{l_1 \dots l_f} \tilde{\varphi}_{j_1} \dots \tilde{\varphi}_{j_f}, \quad (2.42)$$

which is connected to the previous one, Eq. 2.30, through a linear transformation of the SPFs and an inverse transformation on the coefficients A :

$$\begin{aligned} \tilde{\varphi}_{j_k}^{(k)} &= \sum_{l_k} U_{j_k l_k}^{(k)} \varphi_{l_k}^{(k)}, \\ \tilde{A}_{j_1 \dots j_f} &= \sum_{l_1 \dots l_f} A_{l_1 \dots l_f} (U^{(1)})_{l_1 j_1}^{-1} \dots (U^{(f)})_{l_f j_f}^{-1}. \end{aligned}$$

For this reason, it is necessary to choose an arbitrary constraint operator $g^{(k)}$ defining an unique transformation matrix.

The equations of motion can be simplified by a wise choice of the constraint operator: common options are $\hat{g}^{(k)} \equiv 0$ and $\hat{g}^{(k)} \equiv \hat{h}^{(k)}$, which give two sets of equations of motion. The first one leads to

$$i\dot{A}_J = \sum_L \langle \Phi_J | \hat{H} | \Phi_L \rangle A_L, \quad (2.43)$$

$$i\dot{\varphi}^{(k)} = (1 - P^{(k)}) \boldsymbol{\rho}^{(k)-1} \langle \hat{\mathbf{H}} \rangle^{(k)} \varphi^{(k)}, \quad (2.44)$$

and the second holds to

$$i\dot{A}_J = \sum_L \langle \Phi_J | \hat{H} | \Phi_L \rangle A_L, \quad (2.45)$$

$$i\dot{\varphi}^{(k)} = h^{(k)} \mathbf{I}_{n_k} (1 - P^{(k)}) \left[\boldsymbol{\rho}^{(k)-1} \langle \hat{\mathbf{H}} \rangle^{(k)} \right] \varphi^{(k)}. \quad (2.46)$$

Multistate In the study of photo-relaxation processes, multiple electronic states are involved, coupled together by non-adiabatic coupling terms. In order to describe multistate systems it is possible to use the 'single-set' formulation³. The MCTDH equations of motion have an extra degrees of freedom, k_e , that represents the electronic manifold:

$$\chi(\mathbf{R}_1, \dots, \mathbf{R}_{f-1}, \alpha, t) = \sum_{j_1=1}^{n_1} \dots \sum_{j_f=1}^{n_{f-1}} A_{j_1 \dots j_f}(t) \prod_{\kappa=1}^{f-1} (\varphi_{j_\kappa}^{(k)}(\mathbf{R}_\kappa, t)) \varphi_{j_f}^{(f)}(\alpha, t). \quad (2.47)$$

Advantages of MCTDH ansatz The MCTDH *ansatz*, besides the inclusion of correlation among the DOFs, has other useful advantages: i) the norm of the *ansatz* is conserved, by fulfilling the Dirac-Frenkel principle, ii) the wavefunction converges monotonically to the exact one by increasing n_k , iii) the effective number of DOFs can be decreased by defining multi-dimensional SPFs. A multi-dimensional SPFs is defined by a collective variable $\tilde{\mathbf{R}}_k = (\mathbf{R}_i, \mathbf{R}_j, \dots)$ and the ansatz is rewritten as:

$$\chi(\mathbf{R}_1, \dots, \mathbf{R}_p, t) = \sum_{j_1=1}^{\tilde{n}_1} \dots \sum_{j_p=1}^{\tilde{n}_p} A_{j_1 \dots j_p}(t) \prod_{k=1}^p \varphi_{j_k}^{(k)}(\tilde{\mathbf{R}}_p, t) \quad (2.48)$$

where p is the d combined degrees of freedom, such that $p = f/d$.

In addition, also the memory required for storing the wavefunction scales slower by comparing the one needed for the standard method, which is proportional to n^f . The MCTDH method scales as $\sim f n N + n^f$ where n is the number of SPFs, f is the number of DOFs, and

³Also there exists a 'multi-set' formulation, in which different sets of SPFs are used for each electronic state. The equations of motion are derived with an extra label for the electronic states.

N the number of grid points. The two terms are, respectively, the memory to store the SPF and the A coefficients representation. In the case of multi-dimensional SPFs the memory required becomes $\sim p \tilde{n} N^d + \tilde{n}^p$. More details about the computational effort can be found in Ref. [57].

2.2.2 Vibronic Coupling Hamiltonian expansion

The potential energy surfaces expressed using the diabatic potential have the peculiarity to be smoother than their adiabatic counterparts. Moreover, the potential operator \mathbf{W} is a matrix of functions depending on position \mathbf{R} . The Hamiltonian, thus, can be Taylor-expanded, around a point of interest \mathbf{R}_0 ⁴. For example, in order to simulate the de-excitation processes after photoexcitation, usually the Franck-Condon (FC) point, which is the ground state equilibrium geometry, is chosen. The n interacting electronic states, expressed as an $n \times n$ matrix, takes the name of Vibronic Coupling Hamiltonian (VCH) model and is written as:

$$\mathbf{H} = \mathbf{H}^{(0)} + \mathbf{W}^{(0)} + \mathbf{W}^{(1)} + \mathbf{W}^{(2)} + \dots \quad (2.49)$$

The first term, $\mathbf{H}^{(0)}$, includes the diagonal kinetic energy operator and a term representing the ground state Hamiltonian, usually within the harmonic approximation:

$$H^{(0)} = \sum_{\alpha} \frac{\omega_{\alpha}}{2} \left(\frac{\partial^2}{\partial R_{\alpha}^2} + R_{\alpha}^2 \right) \quad (2.50)$$

with the vibrational frequencies ω_{α} . For convenience, \mathbf{R}_0 can be chosen as the nuclear configuration at which the diabatic basis set is equal to the adiabatic basis set. The zero-order matrix is diagonal and corresponds to the diagonal matrix of the electronic eigenvalues in the adiabatic basis:

$$\mathbf{W}^{(0)} = \epsilon(\mathbf{R}_0), \quad (2.51)$$

which represents the vertical excitation at \mathbf{R}_0 . The first order matrix elements can be expressed in the adiabatic basis, as

$$W_{\alpha,ij}^{(1)} = \langle \psi_i | \frac{\partial \hat{H}_e}{\partial R_{\alpha}} | \psi_j \rangle R_{\alpha}, \quad (2.52)$$

where α indicates one of the component of Q , the displacement vector relative to \mathbf{R}_0 , and \hat{H}_e is the standard clamped-nucleus electronic Hamiltonian. In the last formulation, the diagonal terms are the derivative of the adiabatic PES with respect to the coordinates R_{α} and correspond to the adiabatic forces acting on the nuclei. The off-diagonal terms are related to the derivative of the coupling and are the first-order non-adiabatic coupling terms. The quantities within the Dirac brackets, the expansion coefficients of the linear term $\mathbf{W}^{(1)}$, are

⁴Usually, instead of the nuclear coordinates, the dimensionless (mass-frequency scaled) normal mode coordinates can be used.

Chapter 2. Molecular dynamics methods

called $\kappa_\alpha(i)$ (on-diagonal) and $\lambda_\alpha(i, j)$ (off-diagonal). Higher order terms can be included in the same manner [116]: for example, the second-order on-diagonal terms,

$$W_{\alpha,\beta,i,i}^{(2)} = \langle \psi_i | \frac{\partial \hat{H}_e}{\partial R_\alpha \partial R_\beta} | \psi_i \rangle R_\alpha R_\beta, \quad (2.53)$$

can play an important role. The quantity within the Dirac brackets is referred to as $\gamma_{\alpha,\beta}(i)$. When $R_\alpha = R_\beta$, the coupling occurs within a nuclear DOF and, depending on the sign causes a blue or red shift of the frequency of the excited state. If $R_\alpha \neq R_\beta$, each resulting bilinear term couples two nuclear degrees of freedom and is responsible for intramolecular vibrational redistribution. In some cases, where the harmonic approximation fails, the ground state potential can be customized using Morse, or quartic potentials:

$$V_{morse} = D_0 e^{[\alpha(R-R_0)-1]^2} + E_0, \quad (2.54)$$

or quartic potentials,

$$V_{quad} = \frac{1}{2} \omega^2 R^2 + \kappa_1 R + \frac{1}{2} \kappa_2 R^2 + \frac{1}{24} \kappa_3 R^4. \quad (2.55)$$

Spin-orbit Coupling So far we have discussed the non-relativistic molecular Hamiltonian. In certain instances, relativistic effects are important, e.g. for describing intersystem crossing processes during photo-relaxation of a molecular system. Intersystem crossing is ruled by Spin-Orbit Coupling (SOC) between states of different spin multiplicity. The inclusion of these effects can be achieved using a relativistic Hamiltonian but the computational cost of solving the relativistic equations make this approach unpractical.

Since relativistic effects are usually small, an alternative is to treat them as a perturbation of the non-relativistic Hamiltonian:

$$\hat{H}_{TOT} = \hat{H} + \hat{H}_{SOC} \quad (2.56)$$

where for \hat{H}_{SOC} one can use the Breit-Pauli Spin-Orbit Operator [117]:

$$\hat{H}_{SOC} = \frac{e^4}{32\pi^2 \epsilon_0^2 \hbar^2 c^2} \left[\sum_\alpha \sum_i \frac{Z_\alpha}{r_{\alpha,i}^3} (\hat{\mathbf{l}}_{\alpha,i} \cdot \hat{\mathbf{s}}_i) \right] - \frac{e^4}{32\pi^2 \epsilon_0^2 \hbar^2 c^2} \sum_{i \neq j} \left[\frac{1}{r_{i,j}^3} (\hat{\mathbf{r}}_{i,j} \times \hat{\mathbf{l}}_i) \cdot (\hat{\mathbf{s}}_i + 2\hat{\mathbf{s}}_j) \right] \quad (2.57)$$

where $\mathbf{r}_{\alpha,i}$ is the distance between the nucleus α and the electron i , $\hat{\mathbf{l}}_{\alpha,i}$ is the electron angular momentum with respect to the nucleus α , $\hat{\mathbf{s}}_i$ is the spin operator of the electron i . spin-orbit coupling elements, defined for example for a singlet, $|\psi_{S_i}\rangle$, and a triplet state, $|\psi_{T_j}\rangle$,

$$H_{S_i, T_j}^{SOC} = \langle \psi_{S_i} | \hat{H}_{SOC} | \psi_{T_j} \rangle \quad (2.58)$$

are included in the Vibronic Coupling Hamiltonian in the same way as non-adiabatic cou-

pling elements [118].

Choice of the active modes As discussed previously, the cost of quantum dynamics simulations grows quickly with the number of nuclear degrees of freedom, thus, quantum dynamics simulations have to be performed within a *subspace* of relevant coordinates. The choice of these modes results from the synergy of two different approaches: symmetry constraints and quadratic expansion of the Hamiltonian matrix.

Symmetry constraints allow to determine, *a priori*, the normal modes that may give non-zero adiabatic electronic coupling. For the linear terms, $W_{\alpha,ij}^{(1)}$, the expansion coefficients $\lambda_{\alpha}(i, j)$ are non-zero only if the product between the irreducible representation of the electronic states i and j and the nuclear degrees of freedom \mathbf{R}_{α} is totally symmetric:

$$\Gamma_i \times \Gamma_j \times \Gamma_{\mathbf{R}_{\alpha}} \supset \Gamma_A \quad (2.59)$$

The second-order terms, $\gamma_{\alpha,\beta}(i)$, may be non-zero only if:

$$\Gamma_i \times \Gamma_{\mathbf{R}_{\alpha}} \times \Gamma_{\mathbf{R}_{\beta}} \supset \Gamma_A. \quad (2.60)$$

For electronic states with different multiplicity, singlet and triplet e.g., one has to include also the symmetry of the electronic states. For linear terms:

$$\Gamma_{\text{Singlet}} \times \Gamma_{\text{SOC}} \times \Gamma_{\text{Triplet}} \times \Gamma_{\mathbf{R}_{\alpha}} \in A. \quad (2.61)$$

The quadratic expansion of the Hamiltonian matrix is a complementary approach [119] that allows to spot the “photoactive modes”, namely those along which there are conical intersection seams or avoided crossings. Along photoactive modes, the energy difference between two electronic states decrease (see Fig. 2.2.left). On the contrary, along photoinactive modes the energy difference increases and when it does not change significantly one has the so-called bath modes (Fig. 2.2 center and right). The nuclear wavepacket, after photoexcitation at the FC point to an higher energy state, following the derivative of the potential energy surfaces, will spread along photoactive modes and contract along photoinactive modes. The width of the wavepacket does not change along bath mode and thus they can be neglected in the dynamics.

In the past years other approaches, such as *ab-initio* multiple spawning (AIMS) [120, 121, 122], variational Multi-Configurational Gaussian wavepacket (vMCG) [123, 124, 119, 125] and Gaussian MCTDH (G-MCTDH) [126], have been developed in order to better sample the configurational space and not to limit the dynamics to an *a priori* choice of the subspace. They are based on constructing the nuclear wavefunction using Gaussian functions, whose centers follow Newton’s equation of motion. Electronic properties and non-adiabatic coupling terms are computed *on the fly*. The advantage of this new generation of quantum

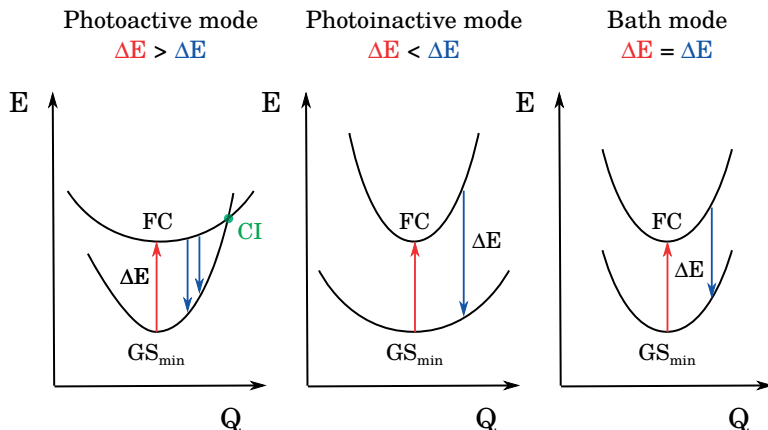


Figure 2.2: Classification of normal modes based on projected energy-difference Hessian [119]: photoactive mode (left), photoinactive mode (center); bath mode (right).

wavepacket dynamics is that the system is free to explore the whole configurational space.

Fitting of the Vibronic Coupling Hamiltonian Following the choice of the configurational *subspace*, in order to build the VCH one needs the energy of the adiabatic electronic states and the coupling terms, as shown previously. Practically, one can compute the adiabatic potential energy surfaces of a molecular system using electronic structure codes already available. The calculations can be performed for fixed configurations along the selected DOFs and along the diagonal of two DOFs. The values thereby obtained are the V^{exact} that will be fitted by the VCHAM algorithm. During the fitting procedure, the weighted error, Δ^2 , is minimized:

$$\Delta^2 = \sum_{j1=1}^{N_i} \dots \sum_{jf=1}^{N_f} (V_{i_1, \dots, i_f}^{exact} - V_{i_1, \dots, i_f}^{approx})^2 \omega_{i_1, \dots, i_f}^2, \quad (2.62)$$

where ω_{jk} is a weight function. Weight functions allow one to minimize differently the error depending on the regions. Usually one wants to have very accurate potential close to minima or relevant topological points such as Jahn-Teller crossings and transition states. On the other side it is possible to reach less accuracy in regions that are not visited by the wavepacket (high potential). Since many coefficients have to be optimized, the process is iterative. It is also possible to define constraints and choose which parameters have to be optimized.

2.3 Trajectory surface hopping

Quantum wavepacket dynamics, although is it able to capture quantum nuclear effects, is limited to the study of systems composed by few atoms and it requires, in the majority of the

cases, the *a priori* determination of the important regions of the PESs and the calculations of all couplings within these regions. An interesting alternative is offered by non-adiabatic dynamics based on classical trajectories. Here the nuclei are not represented by a nuclear wavepacket but are treated like classical particles moving according to Newton's equation of motion. The computation of the quantities, electronic energy, non-adiabatic coupling, can be performed *on-the-fly* leaving the system to sample the whole configurational space.

Different methods have been developed within this scheme. They differ in how the nuclear motion is coupled to the electronic degrees of freedom. The two most common variants are the Ehrenfest or mean-field [58, 127] and the trajectory surface hopping (TSH) [58, 128] approaches. Briefly, in the former the atoms evolve on an effective potential arising from a mixture of adiabatic states. In the latter the nuclear wavepacket is substituted by an ensemble of trajectories. Each trajectory is independent and moves on a single electronic state with the possibility, ruled by the non-adiabatic coupling terms, of instantaneous transitions to other electronic states. Since mean-field is not one of the subject of this thesis, the interested reader can find a comprehensive treatment in Refs. [58, 129]. Trajectory surface hopping is described in more details in the following two subsections.

2.3.1 Equations of motion

Trajectory surface hopping (TSH) is able to overcome some of the limitation of mean-field dynamics. Notably, it is very efficient in describing breaching processes [130]. The nuclear wavepacket is substituted by a swarm of independent trajectories evolving on the adiabatic potential energy surfaces. Each trajectory has the possibility to *hop* to other adiabatic states. The number of trajectories for each adiabatic state i is proportional to the state probability $|C_i(t)|^2$. In the original formulation by Tully [131] transitions to other states were allowed in specific region defined *a priori*. Tully, in 1990 [132], proposed a generalization of the *hopping* algorithm allowing switches at any point of the configurational space explored by the system during the dynamics. The Tully's fewest switching (FS) algorithm has found an increasing approval over years and it has been decisive for the resounding success of TSH method.

As previously derived, writing the total molecular wavefunction by using the Born-Huang expansion and the adiabatic representation of the electronic wavefunctions (Eq. 2.9), the time-dependent Schrödinger equation becomes:

$$i\hbar \frac{\partial}{\partial t} \chi_i(\mathbf{R}, \mathbf{t}) = [\hat{T}_N(\mathbf{R}) + \epsilon_i(\mathbf{R})] \chi_i(\mathbf{R}, \mathbf{t}) + \sum_j \sum_\alpha \frac{\hbar^2}{2M_\alpha} G_{ij}^\alpha(\mathbf{R}) - \sum_{j \neq i} \sum_\alpha \frac{\hbar^2}{M_\alpha} F_{ij}^\alpha(\mathbf{R}) \nabla_\alpha \chi_j(\mathbf{R}, \mathbf{t}) \quad (2.63)$$

where F and G are the first and second order non-adiabatic coupling terms (Eqs. 2.12). The

nuclear wavefunction can be written in the polar representation:

$$\chi_i(\mathbf{R}, t) = A_i(\mathbf{R}, t) \exp\left[\frac{i}{\hbar} S_k(\mathbf{R}, t)\right] \quad (2.64)$$

where $A_i(\mathbf{R}, t)$ and $S_{ki}(\mathbf{R}, t)/\hbar$ are the real amplitude and the phase respectively. Inserting Eq. 2.64 in Eq. 2.63 we get a set of coupled equations:

$$\begin{aligned} \frac{\partial S_i(\mathbf{R}, t)}{\partial t} &= \sum_{\alpha} \frac{\hbar^2}{2M_{\alpha}} \frac{\nabla_{\alpha}^2 A_i}{A_i} - \sum_{\alpha} \frac{1}{2M_{\alpha}} (\nabla_{\alpha}^2 S_i)^2 - \epsilon_i(\mathbf{R}) \\ &\quad - \sum_j \sum_{\alpha} \frac{\hbar^2}{2M_{\alpha}} G_{ij}^{\alpha}(\mathbf{R}) \frac{A_j(\mathbf{R}, t)}{A_i(\mathbf{R}, t)} \left[e^{\left(\frac{i}{\hbar}(S_j(\mathbf{R}, t) - S_i(\mathbf{R}, t))\right)} \right] \\ &\quad + \sum_{j \neq i} \sum_{\alpha} \frac{\hbar^2}{2M_{\alpha}} F_{ij}^{\alpha}(\mathbf{R}) \frac{\nabla_{\alpha} A_j(\mathbf{R}, t)}{A_i(\mathbf{R}, t)} \left[e^{\left(\frac{i}{\hbar}(S_j(\mathbf{R}, t) - S_i(\mathbf{R}, t))\right)} \right] \end{aligned} \quad (2.65)$$

$$\begin{aligned} \hbar \frac{\partial A_i(\mathbf{R}, t)}{\partial t} &= \sum_{\alpha} \frac{\hbar}{M_{\alpha}} \nabla_{\alpha} A_i(\mathbf{R}, t) \nabla_{\alpha} S_i(\mathbf{R}, t) - \sum_{\alpha} \frac{\hbar}{2M_{\alpha}} A_i \nabla_{\alpha}^2 S_i + \\ &\quad + \sum_j H_{ij}(\mathbf{R}) A_j(\mathbf{R}, t) \left[e^{\left(\frac{i}{\hbar}(S_j(\mathbf{R}, t) - S_i(\mathbf{R}, t))\right)} \right] \\ &\quad - \sum_{j \neq i} \sum_{\alpha} \frac{\hbar}{M_{\alpha}} F_{ij}^{\alpha} A_j(\mathbf{R}, t) \nabla_{\alpha} S_j(\mathbf{R}, t) \left[e^{\left(\frac{i}{\hbar}(S_j(\mathbf{R}, t) - S_i(\mathbf{R}, t))\right)} \right] \end{aligned} \quad (2.66)$$

These two equations describe, the nuclear dynamics over different adiabatic electronic states (Eq. 2.65) and the amplitude transfer of the nuclear wavefunction from one electronic state to another (Eq. 2.66). Importantly, they are a different representation of the exact time-dependent Schrödinger equation (Eq. 2.1). Solving this set of coupled equation is computationally very expensive since it requires to compute many trajectories coupled together.

As already mentioned above, in TSH the nuclear wavepacket is substituted by a swarm of independent classical trajectories evolving on the adiabatic potential energy surfaces. This approximation implies that the nuclei evolve as classical particle and each trajectory is independent from the other neglecting the quantum correlation effects. In the classical limit $\hbar \rightarrow 0$ Eq. 2.65 becomes

$$\frac{\partial S_i(\mathbf{R}, t)}{\partial t} = -\frac{1}{2} \sum_{\alpha} \frac{1}{M_{\alpha}} (\nabla_{\alpha}^2 S_i)^2 - \epsilon_i(\mathbf{R}) \quad (2.67)$$

which is known as the ‘‘Hamilton-Jacobi’’ equation of classical mechanics. It describe the motion of classical particles (the nuclei) moving on the i -th electronic potential energy surface. Using the relation $\nabla_{\gamma} S_i = P_{i,\gamma}$ where $P_{i,\gamma}$ is the momentum the following Newton-like

equation is obtained:

$$M_\alpha \mathbf{R}_\alpha = -\ddot{\nabla}_\gamma \epsilon_i(\mathbf{R}). \quad (2.68)$$

2.3.2 Tully's fewest switches algorithm

The transfer between electronic states, described by Eq. 2.66, is described by a stochastic procedure that can be done by adopting the fewest switching (FS) algorithm. This is based on two assumptions: 1) minimisation of the number of hops, 2) the fraction of trajectories in each state α , at each time t , is proportional to the quantum state probability $|C_i^\alpha(t)|^2$, in absence of classically forbidden transitions. $C_i^\alpha(t)$ are complex-valued expansion coefficients that replace the nuclear wavefunction $\chi_i(\mathbf{R}, t)$:

$$\chi_i(\mathbf{R}, t) \sim \frac{1}{M_\alpha} \sum_\alpha \int_{t=0}^{\infty} dt' |C_i^\alpha(t)|^2 \delta(\mathbf{R} - \mathbf{R}^\alpha(t')) \delta(t - t'). \quad (2.69)$$

As for quantum wavepacket dynamics it is possible to choose between adiabatic and diabatic basis sets but usually, since the majority of molecular dynamics and electronic structure codes were developed for electronic adiabatic states, these are the most used. Moreover, the adiabatic representation allows to compute the adiabatic basis functions and corresponding eigenvalues *on-the-fly* during the simulation. At each time step t , these quantities together with the non-adiabatic coupling terms are calculated for the corresponding nuclear configuration. In the adiabatic representation, non-adiabatic coupling terms are easy to evaluate because they just involve the direct calculation of derivatives of the Hamiltonian with respect to the nuclear coordinates [133]. The adiabatic surface can switch at any given time t based on how the quantum probabilities $|C_i(t)|^2$ are changing with time. The rate of change of $|C_i(t)|^2$ is given by:

$$\dot{C}_i(\mathbf{R}, t) = -i\hbar C_i(\mathbf{R}, t) \epsilon_i - \sum_{j \neq i} C_j(\mathbf{R}, t) \dot{\mathbf{R}}^\alpha \cdot \mathbf{F}_{ij}^\alpha, \quad (2.70)$$

and probability to ‘‘hop’’ from the electronic state i to j is computed as

$$g_{ji}^\alpha(t, t + dt) \approx -2 \int_t^{t+dt} d\tau \frac{\text{Re} [C_i(\tau) C_j^*(\tau) \dot{\mathbf{R}}^\alpha \cdot \mathbf{F}_{ij}^\alpha]}{C_j(\tau) C_j^*(\tau)}. \quad (2.71)$$

The ‘‘hop’’ is accepted if and only if

$$\sum_{k \leq i-1} g_{jk}^\alpha < \zeta < \sum_{k \leq i} g_{jk}^\alpha \quad (2.72)$$

with ζ a random number in the interval $[0 : 1]$. Whenever a hop takes place, the velocity is adjusted in the direction of the non-adiabatic coupling vector \mathbf{F}_{ij}^α to ensure conservation of energy [134]. If there is not enough velocity in that direction to maintain energy conservation,

then the transition is classically forbidden and is not allowed to occur. In this case the component of the velocity along the non-adiabatic coupling vector may be reversed [134] or keep unchanged [135].

The above-mentioned FS algorithm ensures that, for a statistical relevant number of trajectories, the fraction of trajectories in each electronic state at each time is identical to the quantum state probability in the absence of classically forbidden transitions. Classically forbidden transitions lead to an inconsistency between the quantum and the TSH probability [135]. Increasing the size of the quantum system can help in avoiding this problem but often this solution is not practical. An alternatives has been proposed to allow them to reverse the direction of the nuclear velocity vectors [134], to not change the velocity, to adjust the velocity taking energy by other components or to delay the transition until the system recovers enough kinetic energy [135]. The usual scheme adopted nowadays is to avoid classically forbidden transitions [135, 136] and to compute the population only from the fraction of trajectories on each state and not from the state probabilities.

As each trajectory is independent, the non-adiabatic coupling depends only on the current nuclear configuration making it difficult to capture quantum coherence and de-coherence effects. Moreover, due to the classical nature of the nuclear motion, TSH is not able to simulate nuclear tunneling and dephasing processes. However, variations of TSH schemes can partially correct these problems [137, 138, 139].

2.3.3 Intersystem crossing

In the original formulation, non-adiabatic coupling terms are computed only between states of same multiplicity and therefore, trajectory surface hopping has been used for studying internal conversion mechanisms. By including spin-orbit coupling, one can expand to include intersystem crossing processes.

The easiest way to proceed is to identify the crossing points between singlet and triplet states obtained from a TSH dynamics performed in the singlet states manifold. At the singlet-triplet crossing points, spin-orbit couplings are then computed together with the corresponding ISC probabilities. Depending on the outcome, a new ‘branching’ trajectory can then be continued from that point evolving on the triplet manifold. This scheme proposed for the first time in the mid-'70s [140], is still in use, in particular for the description of metal-organic systems [25, 141].

A more elegant approach consists in adding to the electronic non-relativistic molecular Hamiltonian \hat{H}_{el} , an additional term, \hat{H}_{rel} , that describes the relativistic effects:

$$\hat{H}_{el}^{tot} = \hat{H}_{el} + \hat{H}_{rel}. \quad (2.73)$$

This extra term, which described the spin-orbit coupling between states with different

multiplicity, can be approximated by the Breit-Pauli operator (Eq. 2.57). The dynamics can be carried out in two different schemes. In the first case, one uses the eigenstates of the non-relativistic Hamiltonian, \hat{H}_{el} , which commutes with the total spin, \hat{S}^2 , and spin projection, \hat{S}_z , operators and treats spin-orbit as a perturbation [142]. The nuclear dynamics, hence, evolves on PESs with defined spin-multiplicity (defined spin quantum numbers s and m_s) and spin-orbit coupling matrix elements (Eq. 2.58) are computed at each time step, or in the proximity of crossing regions, for the evaluation of the intersystem crossing probability. These electronic eigenstates are usually referred to as “spin-diabatic” states [143]. At the crossing points, probability of intersystem crossing can be computed according to Landau-Zener theory:

$$P_{LZ} = 1 - e^{-2pG} \quad (2.74)$$

with

$$G = \frac{(H_{S_i, T_j}^{\text{SOC}})^2}{\hbar \frac{d}{dt} |E_{T_j} - E_{S_i}|}. \quad (2.75)$$

Here $H_{S_i, T_j}^{\text{SOC}}$ is the spin-orbit coupling matrix element between the singlet state S_i and the triplet state T_j as defined in Eq. 2.58, and $|E_{T_j} - E_{S_i}|$ is the energy gap between the two states.

The other possibility is to solve for the eigenstates of the total electronic Hamiltonian, $\hat{H}_{el}^{\text{tot}}$, which are called “spin-adiabatic” states. The total Hamiltonian does not commute either with the total spin or the spin projection. As a consequence, the “spin-adiabatic” states can not be labeled by the spin quantum numbers s and m_s and the dynamics is performed on “mixed-spin” states, depending on the time-dependent molecular structure. Coupling between the states is described by off-diagonal terms of the total Hamiltonian (Eq. 2.8). Since spin-orbit coupling is directly included in the description of the electronic states, it affects the shape of the PESs, and hence, the forces acting on the nuclei. The ISC probabilities can be evaluated using Tully’s algorithm, in analogy to the TSH scheme used for electronic states with same spin-multiplicity.

2.3.4 Hybrid scheme - QM/MM

Although quantum mechanics calculations can describe the evolution of the electronic and geometrical changes of a system during dynamical processes, such as photo-relaxation, this approach is limited to molecular and crystalline structures composed of tens up to hundred of atoms.

The Quantum mechanics/Molecular mechanics (QM/MM) approach [144] was born from the general idea that a large system can be partitioned into an important region, which requires a quantum chemical treatment, and a remainder, that only acts in a perturbative fashion and can be described using classical mechanics. By reducing the size of the quantum

system and treating the environment at a classical MD level it is possible reduce substantially the computational cost and the memory storage capacity required. In the additive scheme used here, the QM/MM Hamiltonian is defined as [145, 146]:

$$\hat{H}_{\text{total}} = \hat{H}_{\text{QM}} + \hat{H}_{\text{MM}} + \hat{H}_{\text{QM/MM}} \quad (2.76)$$

where \hat{H}_{QM} indicates the Hamiltonian for the quantum system, \hat{H}_{MM} for the classical environment and $\hat{H}_{\text{QM/MM}}$ is the interaction potential between the two regions. $\hat{H}_{\text{QM/MM}}$ describes the polarization of the electronic density of the QM system due to the MM region. However, the effect of the QM system to the MM region is not taken into account. The interaction energy $E_{\text{QM/MM}}$ can be written as

$$\begin{aligned} E_{\text{QM/MM}} = & \sum_{\alpha} q_{\alpha} \int v_{\text{SC}}(|\mathbf{R}_{\alpha} - \mathbf{r}|) n_0(\mathbf{r}) d\mathbf{r} + \sum_{\alpha, \beta} \frac{Z_{\beta} q_{\alpha}}{|\mathbf{R}_{\beta} - \mathbf{R}_{\alpha}|} \\ & + \frac{1}{2} \sum_{\beta} \sum_{\alpha} 4\epsilon_{\alpha\beta} \left(\left(\frac{\sigma_{\alpha\beta}}{|\mathbf{R}_{\beta} - \mathbf{R}_{\alpha}|} \right)^{12} - \left(\frac{\sigma_{\alpha\beta}}{|\mathbf{R}_{\beta} - \mathbf{R}_{\alpha}|} \right)^6 \right). \end{aligned} \quad (2.77)$$

The first and the second terms describe the interaction between the QM system with density n_0 and nuclear charge Z_{β} with the point charge of the MM region q_{α} while the third one represents the van der Waals interactions between QM and MM atoms. v_{SC} is a screened Coulomb potential generated by the atom at \mathbf{R}_{α} . The MM region is described by a force field (see Sec. 2.4.3).

2.3.5 LR TDDFT applied to Trajectory Surface Hopping

Trajectory Surface Hopping can be easily coupled to DFT and TDDFT methods for the calculations of the ground state and excited states energy with the advantage of making non-adiabatic calculations feasible for system composed of tens of atoms. In particular the LR TDDFT-based TSH scheme derived by Tavernelli et al. [59] allows us to include an unlimited number of excited states and easy compute both electronic energies and forces [147, 148, 149]. Excited state energy, within LR TDDFT are exact up to first order [150]. They can be obtained using the LR TDDFT Sterneheimer formalism solving the non-Hermitian eigenvalue problem

$$\sum_{ij}^{N_o} (H^{KS} \delta_{ij} - \epsilon_i) |\phi_j^{\pm}\rangle + \delta V^{SCF}(\pm\omega) |\phi_i\rangle = \mp\omega |\phi_i^{\pm}\rangle \quad (2.78)$$

where KS orbitals $\{\phi_i\}$ and energies ϵ_i are obtained by a ground state calculation; $\{\phi_i^{\pm}\}$ are the linear response orbitals, used to express the response of the density to a periodic perturbation with frequency ω and amplitude δV^{\pm} , H^{KS} is the KS Hamiltonian, and $\delta V^{SCF}(\pm\omega)$ is the response of the effective potential to the first order (linear approximation) change in

the electronic density

$$\delta V^{SCF}(\pm\omega) = \int d\mathbf{r}' \left(\frac{1}{|\mathbf{r}-\mathbf{r}'|} + \frac{\delta^2 E_{xc}}{\delta n(\mathbf{r})\delta n(\mathbf{r}')} \Big|_{n=n_0} \right) \delta n(\mathbf{r}, \pm\omega). \quad (2.79)$$

The response of the density to a periodic perturbation with frequency ω and amplitude δV^\pm can be expressed using the linear response orbitals $\{\phi_i^\pm\}$:

$$\delta n(\mathbf{r}, \pm\omega) = \sum_i^{N_{occ}} \phi_i(\mathbf{r})(\phi_i^\pm)^*(\mathbf{r}) + \phi_i^\pm(\mathbf{r})\phi_i^*(\mathbf{r}). \quad (2.80)$$

Applying the Tamm-Dancoff approximation (TDA) [151, 147], which neglects the linear response associated with the orbital $\{\phi^+\}$, the problem is approximated by a Hermitian eigenvalue problem. Tully's probability can be computed using an auxiliary wavefunction

$$|\Phi_k(\mathbf{r}; \mathbf{R})\rangle \approx \sum_{o=1}^{N_o} \sum_{v=N_o+1}^{N_o+N_v} C_{ov}^k \hat{a}_v^\dagger \hat{a}_o |\Phi_0((\mathbf{r}; \mathbf{R}))\rangle = \sum_{o=1}^{N_o} \sum_{v=N_o+1}^{N_o+N_v} C_{ov}^k |\Phi_0^v((\mathbf{r}; \mathbf{R}))\rangle \quad (2.81)$$

where \hat{a}_i^\dagger and \hat{a}_i are, respectively, the creation and the annihilation operator acting on the i -th KS orbital and ground state wavefunction is the single Slater determinant of the occupied KS orbitals; the indexes o, v refer to the occupied and the unoccupied orbitals, respectively. The expression $\hat{a}_v^\dagger \hat{a}_o |\Phi_0((\mathbf{r}; \mathbf{R}))\rangle$ indicates singly excited Kohn-Sham determinants. The expansion coefficients C_{ov}^k for the excited state are obtained by projecting the LR orbitals on a subset of N_v unoccupied KS orbitals $\{\phi_i\}$

$$C_{ov}^k = \sqrt{\frac{\epsilon_{vv} - \epsilon_{oo}}{\omega_I}} \langle \phi_o^- | \phi_v \rangle. \quad (2.82)$$

The TD many electrons wavefunction $\Psi(\mathbf{r}; \mathbf{R}(t))$ can be expressed as a linear combination of the stationary KS-SDs Φ_o^v

$$|\Psi(t)\rangle = C_0(t)|\Phi_0\rangle + \sum_{j=1}^{\infty} C_j(t) \sum_{o,v} c_{o,v}^j |\Phi_o^v\rangle. \quad (2.83)$$

Substituting into the Tully surface hopping equations for the amplitudes, and using

$$\sigma_{kj} = \langle \Phi_k | \frac{\partial \Phi_j}{\partial t} \rangle = \dot{\mathbf{R}} \cdot \mathbf{F}_{kj} \quad (2.84)$$

for the scalar non-adiabatic coupling elements (NAC), the first order differential equation

for the amplitudes $C_j(t)$ becomes

$$i\hbar\dot{C}_k(t) = \sum_{j=0}^n \{C_k(t)V_{kj} - i\hbar C_j(t)\sigma_{kj}\} \quad (2.85)$$

where the sum is truncated after n adiabatic states. Importantly, in the adiabatic representation the potential matrix $V_{kj} = \langle \Phi_k | H | \Phi_j \rangle$ is diagonal and the term V_{jj} can be replaced by relative energies $\tilde{V}_{jj} = V_{jj} - \langle \Phi_0 | H | \Phi_0 \rangle$ where H is the Hamiltonian of the interacting system and \tilde{V}_{jj} the TDDFT excitation energies ω_j . Finally, the expansion coefficients can be simplified into

$$i\hbar\dot{\tilde{C}}_k(t) = \tilde{C}_k(t)\omega_k - i\hbar \sum_{j=0}^{N_{ad}} \tilde{C}_j(t)\sigma_{kj}. \quad (2.86)$$

As a consequence, the coefficients $C_j(t)$ are substituted by a new set of coefficients $\tilde{C}_j(t)$ that are used to calculate the switching probability. The calculation of the NAC term σ_{kj} is done by finite differences

$$\sigma_{kj}(t + \Delta t/2) = \frac{1}{2\Delta t} [\langle \Phi_k(\mathbf{r}; \mathbf{R}(t)) | \Phi_j(\mathbf{r}; \mathbf{R}(t + \Delta)) \rangle - \langle \Phi_k(\mathbf{r}; \mathbf{R}(t + \Delta)) | \Phi_j(\mathbf{r}; \mathbf{R}(t)) \rangle]. \quad (2.87)$$

The NAC terms are used for evaluating Eq. 2.82 for the pair of electronic states Φ_k and Φ_j , taken at subsequent classical time steps t and $t + \Delta$. The calculation of the switching probability g_{kj} between states k and j in the interval of time $[t, t + \Delta]$ is computed from the solution of Eq. 2.86:

$$g_{kj}(t + \Delta) \approx -2 \int_t^{t+\Delta} d\tau \frac{\text{Re} [\tilde{C}_j(\tau)\tilde{C}_k^*(\tau)\sigma_{jk}(\tau)]}{\tilde{C}_k(\tau)\tilde{C}_k^*(\tau)}. \quad (2.88)$$

2.4 Ground state dynamics

So far we have discussed methods for studying the dynamics of a molecular system when more than one electronic states are involved. As we have seen, electronic states can couple through nuclear motion and the nuclear wavepacket can spread over different electronic potential energy surfaces. For systems in which a single PES is well separated (energetically) from all other PESs one can invoke the adiabatic (or Born-Oppenheimer) approximation. This is especially the case when dealing with ground state dynamics in which the energy gap with the first excited state is large enough, meaning that the non-adiabatic coupling is negligibly small. Different efficient schemes based on the classical treatment of the nuclear degrees of freedom have been developed to deal with the adiabatic dynamics.

2.4.1 *Ab-initio* Born-Oppenheimer MD

The *Ab-initio* Born-Oppenheimer (BO) Molecular Dynamic (MD) combines atomistic molecular dynamics with internuclear forces obtained from electronic structure calculations performed "on the fly" as the simulation proceeds. The central point is that quantum nuclear effects are neglected and the wavepacket is replaced by a single trajectory on the ground state potential energy surface.

Using the Born-Oppenheimer approximation, which neglects the coupling between electronic and nuclear degrees of freedom, the temporal evolution of the nuclear wavefunction ($\chi(\mathbf{R}, t)$), within the Born-Huang expansion, can be expressed as:

$$i\hbar \frac{\partial}{\partial t} \chi(\mathbf{R}, t) = [\hat{T}_N(\mathbf{R}) + \epsilon_0(\mathbf{R})] \chi(\mathbf{R}, t) \quad (2.89)$$

where $\epsilon_0(\mathbf{R})$ is the ground state potential energy surface, eigenvalue of the time-independent electronic Schrödinger equation for the ground state adiabatic electronic wavefunction ψ_0 :

$$\hat{H}_e(\mathbf{r}; \mathbf{R}) \psi_0(\mathbf{r}; \mathbf{R}) = \epsilon_0(\mathbf{R}) \psi_0(\mathbf{r}; \mathbf{R}), \quad (2.90)$$

As derived in the previous section, the nuclear wavefunction can be written using the polar representation, and in the classical limit, a Newton-like equation is obtained. In this case, for the ground state dynamics, one gets the following relationship for the nuclear forces:

$$M_\alpha \ddot{\mathbf{R}}_\alpha = -\nabla_\alpha \min_{\psi_0(\mathbf{r}; \mathbf{R})} \{ \langle \psi_0 | \hat{H}_e | \psi_0 \rangle \}. \quad (2.91)$$

where ψ_0 is the ground state wavefunction that minimizes the expectation value of the electronic Hamiltonian \hat{H}_e .

In practice, at each time step t , Eq. 2.90 is solved for the given nuclear configuration, and the ground state PES is computed. Applying Eq. 2.91, one calculates the nuclear forces as the gradient of the adiabatic PES, which are used to obtain the new nuclear configuration at the following time step, $t + \delta t$.

2.4.2 Car-Parrinello method

BO MD is limited by time and CPU resources required for solving Eq. 2.90. An elegant and efficient alternative scheme, capable of reducing the computational effort of a BO MD, was proposed by Car and Parrinello [152], based on the following Lagrangian:

$$\mathcal{L} = \sum_l \frac{\mu}{2} \int dr^3 |\dot{\psi}_l|^2 + \frac{1}{2} \sum_I M_I |\dot{R}_I|^2 - \epsilon[\{\psi_l\}, \{R_I\}] \quad (2.92)$$

where μ is a fictitious electronic mass, $\epsilon[\{\psi_l\}, \{R_I\}]$ the Kohn-Sham energy density functional and ψ_i the one-electron Kohn-Sham orbitals. The use of the Lagrangian ensures the

conservation of the total energy. In addition, it guarantees that the fictitious kinetic energy is conserved and, thus, there is no exchange of energy between the electronic and the nuclear part [153]. From this Lagrangian two equations of motion, one for the electronic degree of freedom and one for the nuclei, are derived:

$$\mu\ddot{\psi}_I = -\hat{H}_{el}\psi_I + \sum_k \Lambda_{Ik}\psi_I, \quad (2.93)$$

and

$$M_I\ddot{\mathbf{R}}_I = -\nabla_I E[\{\psi_I\}, \{\mathbf{R}_I\}]. \quad (2.94)$$

Eq. 2.93 describes the motion of the fictitious electronic system, where Λ_{Ik} is the Lagrange multiplier introduced for assuring the orthogonality of the wavefunctions ψ_I . In order to enforce the adiabatic approximation, the forces acting on the fictitious electrons have to be small, meaning that μ should be small. Increasing μ , the electronic wavefunction oscillates faster around the bottom of the Born-Oppenheimer ground state potential. In the limit of $\mu \rightarrow 0$, the Born-Oppenheimer dynamics is recovered. Typical values of μ are 300-600 times the electronic mass [154, 155]. Car-Parrinello dynamics, avoiding the calculation of the ground state potential energy ϵ_0 is faster than the BO method.

2.4.3 Classical molecular dynamics

Classical molecular dynamics is characterized by the complete absence of quantum chemistry calculations, and the potential energy surface is parameterized, making it possible to access longer time-scales. Within this approach all bonds, angles, and dihedrals are replaced by springs and the potential is written as a sum of harmonic classical potentials. In this thesis, the AMBER force field was used for sampling the solvent structure around a set of Cu-Phenanthroline molecules. The expression, as implemented in the AMBER code [156, 157] is:

$$V(r^N) = \sum_{\text{bonds}} k_b(l - l_0)^2 + \sum_{\text{angles}} k_a(\theta - \theta_0)^2 + \sum_{\text{torsions}} \frac{1}{2} V_n [1 + \cos(n\omega - \gamma)] \\ + \sum_{j=1}^{N-1} \sum_{i=j+1}^N \left\{ \epsilon_{i,j} \left[\left(\frac{r_{0ij}}{r_{ij}} \right)^{12} - 2 \left(\frac{r_{0ij}}{r_{ij}} \right)^6 \right] + \frac{q_i q_j}{4\pi\epsilon_0 r_{ij}} \right\} \quad (2.95)$$

where the first three terms describe, respectively, the harmonic potential along the bonds, the angles and the dihedrals of the molecule and the latter two take into account the van der Waals and the electrostatic forces. The force constants k_b and k_a , the equilibrium distances l_0 , the equilibrium angles θ_0 , the half-height potential barrier V_n , the degeneracy γ , the equilibrium dihedrals ω , the well depth ϵ_0 , the van der Waals radius of the atoms and the charges q_i are the parameters that determine the so-called Force Field.

3 Non-adiabatic ultrafast relaxation of photoexcited $[\text{Cu}(\text{dmp})_2]^+$

The ultrafast non-adiabatic relaxation processes of $[\text{Cu}(\text{dmp})_2]^+$, despite numerous ultrafast spectroscopy studies, has not been still fully understood. Quantum nuclear dynamics, within the framework of the Multi-Configurational Time-Dependent Hartree (MCTDH) method, is able to describe ultrafast non-adiabatic phenomena such as internal conversion and intersystem crossing or wavepacket bifurcation.

The chapter is based on the following publications:

G. Capano, T.J. Penfold, U. Röthlisberger, I. Tavernelli, "A Vibronic Coupling Hamiltonian to Describe the Ultrafast Excited State Dynamics of a Cu (I)-Phenanthroline Complex", *CHIMIA*, 68 (4), 220-230, 2014

G. Capano, M. Chergui, T.J. Penfold, U. Röthlisberger, I. Tavernelli "A Quantum Dynamics Study of the Ultrafast Relaxation in a Prototypical Cu (I)-Phenanthroline", *The Journal of Physical Chemistry A*, 118 (42), 9861-9869, 2014

3.1 Ultrafast spectroscopic studies

Unravelling the ultrafast processes occurring upon photoexcitation is of primary importance for synthesizing Cu(I)-phenanthroline complexes that maximize the electron injection into inorganic substrates (see Chapter 1). Despite numerous ultrafast spectroscopic studies, a full description of the ultrafast excited state dynamics of $[\text{Cu}(\text{dmp})_2]^+$ remains elusive. One of the first time-resolved spectroscopic studies of $[\text{Cu}(\text{dmp})_2]^+$ was performed by Chen et al. [91]. Following photoexcitation of the optically bright S_3 state¹, they used time-resolved absorption spectroscopy and reported two principal dynamical processes occurring in 500-700 fs and 10-20 ps. On the basis of the ultrafast ISC of $[\text{Ru}(\text{bpy})_3]^{2+}$ [158, 17, 159, 19], they

¹Note that S_3 in this chapter is sometimes referred to as S_2 in other works. This is because at the previously assigned D_{2d} symmetry, S_1 and S_2 are degenerate. However, we find that the lowest energy structure has a D_2 symmetry, which breaks the degeneracy.

assigned the first process to ultrafast ISC and the second to the structural relaxation, i.e. the pseudo Jahn-Teller (PJT) distortion. At the same time Nozaki and co-workers [100] suggested that the 10-20 picosecond relaxation reported by Chen is due to ISC, which is relatively slow due to a strong effect of the structural rearrangements on the magnitude of the Spin-Orbit Coupling (SOC) matrix elements. Indeed, at the Frank-Condon (FC) geometry, the SOC between S_1 and T_1 was estimated to be $\sim 300 \text{ cm}^{-1}$, but at the distorted excited state geometry, expected to be more important on the timescale of tens of picosecond, it is only $\sim 30 \text{ cm}^{-1}$. However, the authors also concluded that the quantum yield of the lowest singlet state in the PJT relaxed geometry (S_1^{PJT}) was ~ 0.1 , and suggested that this pathway competes with the ultrafast ISC to the $^3\text{MLCT}$ occurring at the FC geometry, which is, therefore, the dominant relaxation channel.

Later, Tahara and co-workers [99] probed the excited state dynamics using femtosecond fluorescence up-conversion. Following photoexcitation at 420 nm they found three principal time components. An initial strong fluorescence, which decayed with a time constant of $\sim 45 \text{ fs}$, was attributed to the decay of the initially populated excited state via IC. This was followed by two time components of 660 fs and 7.4 ps, assigned to the PJT distortion and ISC, respectively. Later, Chen and co-workers [79], reported similar time-components, 80 fs, 510 fs and 10-15 ps and they concluded, in agreement with Tahara and co-workers, that the longer timescale was ISC and assigned the shortest time constant to the PJT distortion. Finally, Tahara and co-workers [96], investigated the dynamics following excitation at 550 nm by using transient absorption spectroscopy. This transition corresponds to the lowest singlet MLCT state (S_1), which is dipole forbidden but gains intensity through vibronic coupling with the main absorption band. They observed distinct wavepacket dynamics corresponding to the structural rearrangement (PJT distortion), and were able to obtain a low-frequency vibrational spectrum of the relevant modes. As the damping time for the oscillations was similar to that of the structural change, the authors concluded that the wavepacket dynamics arises from the coherent nuclear motion of the S_1 state before the structural change. They proposed the presence of a small but finite potential barrier between the perpendicular and flattened S_1 states, which using TDDFT was found to be of 0.002 eV [96]. However, this is at odds with the spontaneous structural instability usually associated with PJT effects and the reported barrier is well below the accuracy of TDDFT and an order of magnitude smaller than $k_b T$ at 300 K.

These latter studies [96, 99, 98, 79] would appear to rule out ultrafast ISC. However, the analysis of these experiments only considered SOC between the S_1 and T_1 states and as pointed out by Zgierski [67], there are four closely spaced triplet states in close proximity to S_1 , and therefore the S_1/T_1 coupling may be not the only relaxation channel into the triplet states.

Consequently, it is apparent that a complete and consistent rationalization of the initial dynamics reported by Chen et al. [91, 79] and Tahara et al. [99] is still missing. To shed new light on these dynamics and provide a complete picture of the photophysical processes

of $[\text{Cu}(\text{dmp})_2]^+$, we used quantum nuclear wavepacket dynamics within the framework of the Multi-Configurational-Time-Dependent-Hartree (MCTDH) method described in the previous chapter.

3.2 Building the Vibronic Coupling Hamiltonian

$[\text{Cu}(\text{dmp})_2]^+$ has 57 atoms and therefore 168 normal modes, and consequently, calculating a full potential energy surface is unrealistic. To decrease the computational effort we use a first principles model Hamiltonian including only the electronic states in an energy range of interest and the vibrational degrees of freedom (DOF) most important for the ultrafast dynamics. In fact, while this approximated Hamiltonian will be unable to capture longer time effects, such as vibrational cooling (~ 10 ps [79]), the approximations made will have little influence on the dynamics during the first ps. In particular, we identified, using the magnitude of the linear coupling constants, 8 normal modes. Although this clearly represents a significant reduction in the dimensionality of the potential, the modes included closely correspond to those identified in the femtosecond transient absorption study of Ref. [96].

The expansion coefficients expressed in Eqs 2.52 and 2.53 were obtained by performing a fit of quantum chemistry points calculated at nuclear geometries along the important normal modes. Couplings between the vibrational degrees of freedom are included as bilinear terms, calculated using diagonal cuts through two normal modes. These normal modes were calculated using DFT as implemented in Gaussian09 [160] within the approximation of the M06 functional [161], which gave good agreement with the experimental vibrational modes reported in Ref. [96]. The ground and excited state energies were obtained using DFT/TDDFT within the approximation of the B3LYP exchange and correlation functional. For all the calculations the TZVP basis set was used for the copper atom and an aug-SVP basis set for N, C and H. The fit was performed using the VCHAM program, distributed with the Heidelberg MCTDH [57] package. The quality of the fit was evaluated with the root mean square standard deviation (RMSD) between the model surfaces and the ab initio points which was < 0.025 eV for all degrees of freedom.

3.2.1 Zeroth order expansion coefficients

The zero order expansion coefficients ($\hat{W}^{(0)}$) correspond to the vertical excitation energies at the equilibrium ground state geometry (FC geometry). They are reported in Tab. 3.1. All of these states are composed of an excitation from a metal d-orbital to a ligand π^* orbital (Fig. 3.2) and are therefore MLCT states [67]. The lowest four triplet states are all below the S_1 state and all lie in a close energy range of ≈ 0.1 eV. The lowest two singlet states (S_1 and S_2) have excitation energies of 2.44 and 2.51 eV, respectively, at the ground state optimized geometry. In previous simulations, which constrained the structure to a D_{2d} symmetry [79, 67], these states are degenerate. However, no such constraints were used in this study and we find that

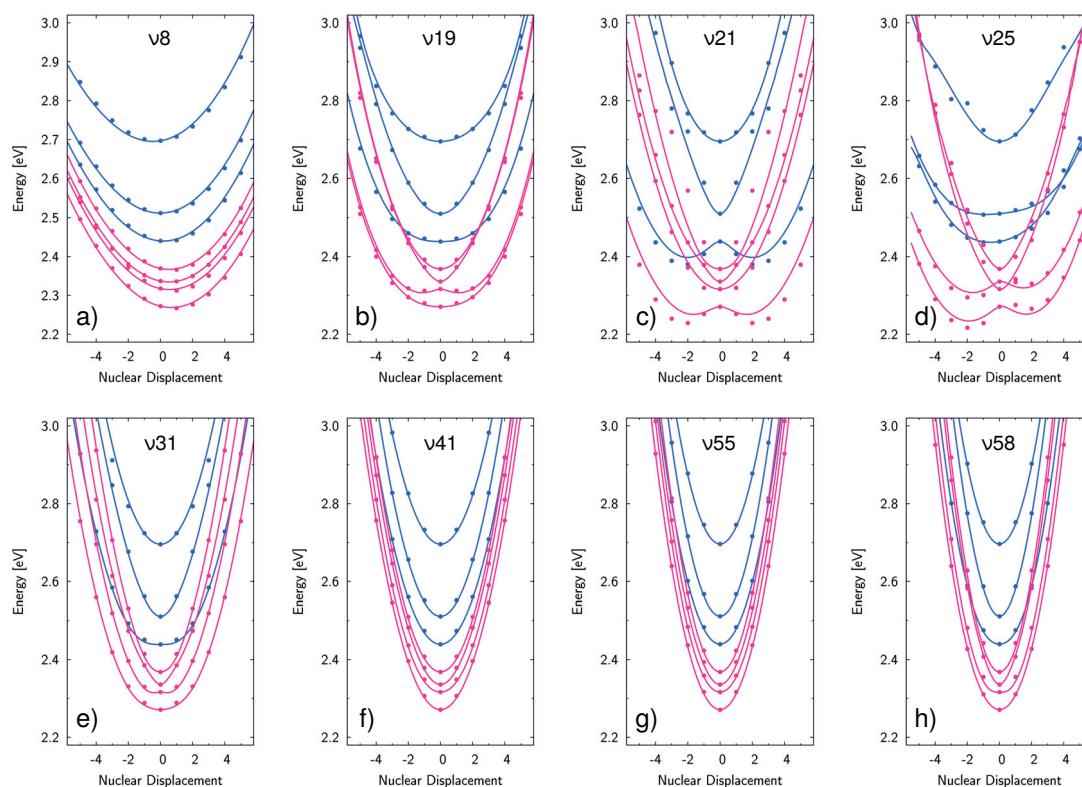


Figure 3.1: Cuts through the PES along a) ν_8 , b) ν_{19} , c) ν_{21} , d) ν_{25} , e) ν_{31} , f) ν_{41} , g) ν_{55} , and h) ν_{58} . The dots are results from the quantum chemistry calculations for the singlet (blue) and triplet (pink) states. The lines correspond to their fit from which the expansion coefficients are determined.

the lowest energy structure has D_2 symmetry, giving rise to a small but sizable splitting of these states. The S_3 state, whose transition from the ground state is dipole-allowed, has an energy of 2.70 eV and closely corresponds to the maximum observed in the experimental absorption spectra of $[\text{Cu}(\text{dmp})_2]^+$, 2.73 eV [100].

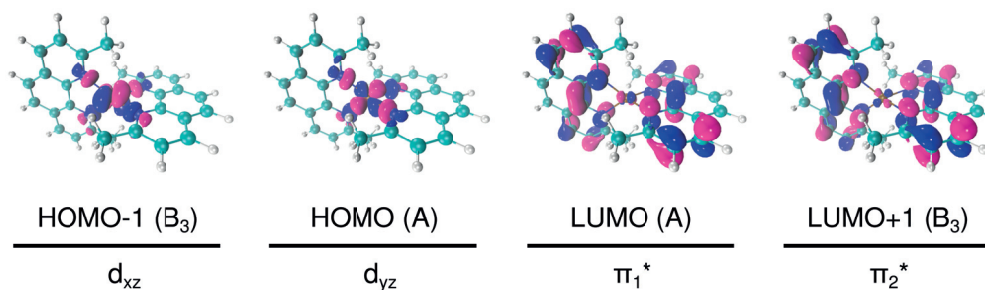


Figure 3.2: Molecular orbital diagram and characteristics of the HOMO-1, HOMO, LUMO, and LUMO+1 orbitals involved in the low lying excited states of $[\text{Cu}(\text{dmp})_2]^+$. Contour levels drawn at 0.02 a.u.

3.2. Building the Vibronic Coupling Hamiltonian

Table 3.1: Excitation energies (eV) and oscillator strength of the singlet and triplet states of $[\text{Cu}(\text{dmp})_2]^+$ at the ground-state equilibrium geometry calculated using TD-DFT with the B3LYP functional.

State	Symmetry	Energy [eV]	Osc. Strength	Description ²
S ₁	¹ B ₃	2.44	0.0006	$d_{yz} \rightarrow \pi_1^*$, $d_{xz} \rightarrow \pi_2^*$
S ₂	¹ A	2.51	0.0000	$d_{yz} \rightarrow \pi_2^*$, $d_{xz} \rightarrow \pi_1^*$
S ₃	¹ B ₃	2.70	0.1608	$d_{xz} \rightarrow \pi_1^*$, $d_{xz} \rightarrow \pi_2^*$
T ₁	³ A	2.27	-	$d_{yz} \rightarrow \pi_2^*$
T ₂	³ A	2.31	-	$d_{yz} \rightarrow \pi_1^*$
T ₃	³ B ₃	2.33	-	$d_{xz} \rightarrow \pi_1^*$
T ₄	³ B ₃	2.37	-	$d_{xz} \rightarrow \pi_2^*$

3.2.2 First order expansion coefficients

Table 3.2: Symmetry and frequency (cm^{-1}) of the selected normal modes. The experimental values are taken from Ref. [96]

Mode	Symmetry	Calc. (cm^{-1})	Exp. (cm^{-1})	Description
ν_8	<i>a</i>	99.156	125	Breathing
ν_{19}	<i>b</i> ₃	193.608	191	Rocking
ν_{21}	<i>b</i> ₃	247.610	240	Rocking
ν_{25}	<i>a</i>	270.848	290	Twist
ν_{31}	<i>b</i> ₃	420.770	438	Bending
ν_{41}	<i>b</i> ₃	502.649	-	Bending
ν_{55}	<i>b</i> ₃	704.750	704	Rocking
ν_{58}	<i>b</i> ₃	790.762	-	Rocking

As shown in Eq. 2.52, the first order coupling terms arise from coupling of the electronic states to a nuclear DOF. Based on the magnitude of the linear coupling constants we have identified 8 low frequency normal modes, which are likely to be dominant in the initial photoexcited dynamics (Tab. 3.2). Although this clearly represents a significant reduction in the dimensionality of the potential, the modes include closely correspond to those identified in the femtosecond emission study of Ref. [96]. Cuts through the potential energy surfaces of the selected important modes are depicted in Fig. 3.1. Along the x-axis, 0 corresponds to the FC geometry.

Importantly, owing to symmetry, *a*, only modes ν_8 and ν_{25} can yield non-zero on-diagonal linear coupling coefficients (κ). Indeed, both these modes exhibit excited state minima that are shifted from the ground state equilibrium position (an effect of on-diagonal linear coupling). For ν_8 , this shift of the S₁ and S₂ states reflects a strengthening of the Cu-N bonds in these excited states which is supported by experiment [91, 79] and previous DFT [96, 67, 100] calculations and is due to the π back-donation character of the pyridine ligand and the

enhanced electrostatic interaction between metal center and ligands resulting from the charge transfer. To correctly describe the anharmonicity of this mode a morse potential (Eq. 2.54) was used (Tab. 3.4).

Along ν_{25} , the S_1 and S_2 states also exhibit a shortening of the Cu-N bonds. However, rather contrastingly the triplet states exhibit a profile more reminiscent of a pseudo Jahn-Teller distortion with an asymmetric double-minimum structure for which the lowest energy minimum corresponds to a contracted Cu-N bond distance. This behaviour compared with the singlet manifold is due to the symmetry of the electronic states involved. T_1 and T_2 have both A symmetry and can, therefore, may couple along the totally symmetry mode ν_{25} . The same is true for T_3 and T_4 which both have symmetry B_3 . Finally, as shown in Tab. 3.3 we also find an off-diagonal expansion coefficient (γ) along ν_{25} coupling the S_3 and S_1 states. This offers the possibility for the wavepacket to relax directly from the initially populated state into the lowest singlet state. However, given the large energy separation and the strong coupling between the S_1 and S_2 states, this pathway will likely provide only these a minor contribution to the overall dynamics.

The mode ν_{19} and ν_{21} have b_3 symmetry and correspond a flattening motion of the two ligands and an off center movement of the central Cu(I) atom, respectively. The on-diagonal linear coupling coefficients (κ) are always zero by symmetry, however, the off-diagonal expansion coefficients (γ) can be non-zero between states S_3 and S_2 and/or S_2 and S_1 . As shown in Tab. 3.3, these modes strongly couple the S_2 and S_1 surfaces and are responsible for the pseudo-Jahn-Teller effects in $[\text{Cu}(\text{dmp})_2]^+$. This is strongest in ν_{21} where both the lowest singlet and triplet states are strongly characterized by a double-minimum profile located symmetrically with respect the ground state equilibrium position, and which arises from the aforementioned coupling. The effect is weaker for ν_{19} .

Finally, the potential energy surfaces along ν_{19} and ν_{25} were described using a quartic potential (Eq. 2.55): parameters can be found in Tab. 3.5.

3.2.3 Second order expansion coefficients

All of the modes considered in this work require some small on-diagonal second order coupling terms (Tab. 3.6), which account for a change of frequency of the excited state potentials compared to the ground state. However, we find that they are all relatively small, meaning that their effect is expected to be negligible.

In addition, small bilinear terms were also fitted between each pair of modes. These terms, which are responsible for redistribution of vibrational energy formed during the electronic relaxation, were found to be smaller than <0.005 eV. Although these terms will have an important role for long time dynamics associated with vibrational cooling, such effects are beyond the scope of our investigation since their effect on the short time dynamics, <1 ps, is expected to be small.

3.2. Building the Vibronic Coupling Hamiltonian

Table 3.3: On-diagonal (κ) and off-diagonal (λ) linear coupling constants in eV for the selected vibrational mode of $[\text{Cu}(\text{dmp})_2]^+$. ν_8 is not reported because it is described by a Morse potential.

	ν_{19}	ν_{21}	ν_{25}	ν_{31}	ν_{41}	ν_{55}	ν_{58}
κ_{S_1}	-	-	0.0053	-	-	-	-
κ_{S_2}	-	-	0.007	-	-	-	-
κ_{S_3}	-	-	-0.0031	-	-	-	-
λ_{S_1,S_2}	0.027	0.0695	-	0.0463	0.0156	0.0218	0.0417
λ_{S_1,S_3}	-	-	0.0275	-	-	-	-
λ_{S_2,S_3}	0.052	0.0178	-	0.0145	0.0077	-	-0.002
λ_{S_1,S_2}	0.027	0.0695	-	0.0463	0.0156	0.0218	0.0417
λ_{S_1,S_3}	-	-	0.0275	-	-	-	-
λ_{S_2,S_3}	0.052	0.0178	-	0.0145	0.0077	-	-0.002
λ_{T_1,T_2}	-	-	0.0491	-	-	-	-
λ_{T_1,T_3}	-0.0033	0.0512	-	0.0243	0.0086	0.0136	0.0136
λ_{T_1,T_4}	0.0267	0.0137	-	0.0243	0.0073	0.0126	0.031
λ_{T_2,T_3}	0.0296	0.0051	-	0.0323	0.0115	0.0107	0.0342
λ_{T_2,T_4}	0.0011	0.0006	-	0.009	0.0068	0.0137	0.0042
λ_{T_3,T_4}	-	-	0.0441	-	-	-	-

Table 3.4: Morse parameters for normal mode ν_8 .

	D_0 (ev)	$k \cdot 10^{-4}(a.u.)$	Q_0
S_1	99.00	266.81	0.186
S_2	99.00	154.43	-0.111
S_3	99.00	112.62	-0.465
T_1	99.00	244.24	0.672
T_2	99.00	253.72	0.573
T_3	99.00	270.79	0.537
T_4	99.00	309.13	0.544

3.2.4 Spin orbit coupling coefficients

To probe the role of ISC, the singlet and triplet manifolds are coupled by SOC. The SOC matrix elements at various geometries along the potential energy surface were computed with the perturbative approach developed by Wang and Ziegler [162] as implemented within ADF [163, 164, 165]. A TZP basis set was used for all atoms and scalar relativistic effects were included using ZORA [166, 167]. Once calculated, the SOC matrix elements were fitted with either linear or Gaussian functions and incorporated in the Hamiltonian in the same manner as the non-adiabatic coupling terms. During the dynamics, all three components (x, y, and z) of the triplet states were treated as a single state and the SOC terms are the square root of the sum of the squares of the three couplings. The parameters and of the SOC matrix elements

Table 3.5: Quartic potential in eV for the vibrational mode ν_{19} and ν_{25}

	ν_{19}			ν_{25}		
	k_1	$k_2 \cdot 10^{-3}$	$k_2 \cdot 10^{-2}$	$k_1 \cdot 10^{-2}$	$k_2 \cdot 10^{-2}$	$k_2 \cdot 10^{-2}$
S ₁	0.000	0.9820	0.1819	0.7056	-1.5675	0.3473
S ₂	0.000	0.4151	0.2107	0.4185	-0.8371	0.1813
S ₃	0.000	-2.9245	0.2328	0.0073	-0.2200	-0.8078
T ₁	0.000	0.0134	0.1521	1.2592	-0.9915	0.0238
T ₂	0.000	0.4145	0.2039	-0.9463	-0.3467	0.4169
T ₃	0.000	0.7161	0.1924	0.9546	-0.7923	-0.0507
T ₄	0.000	0.9709	0.3100	-0.5965	-0.3626	0.2300

Table 3.6: On-diagonal (γ) second-order coupling constants in eV for the selected vibrational modes of $[\text{Cu}(\text{dmp})_2]^+$.

	ν_8	ν_{19}	ν_{21}	ν_{25}	ν_{31}	ν_{41}	ν_{55}	ν_{58}
γ_{S_1}	0.0027	0.0010	0.0035	-0.0183	0.0124	0.0020	0.0024	0.0034
γ_{S_2}	0.0015	0.0004	0.0032	-0.0069	-0.0011	0.0027	-	0.0035
γ_{S_3}	-0.0011	-0.0029	0.0054	0.0067	-0.0029	0.0017	0.0020	0.0029
γ_{T_1}	-	-	-0.0009	-0.0099	0.0016	0.0020	0.0020	0.0021
γ_{T_2}	-	-0.0041	0.0038	-0.0035	0.0022	0.0021	0.0016	0.0047
γ_{T_3}	-	0.0007	-0.0006	-0.0079	0.0027	0.0022	0.0021	0.0018
γ_{T_4}	-	0.0001	0.0051	-0.0036	0.0051	0.0020	0.0016	0.0052

along the important modes are shown in Tab. 6.4 and 3.8.

3.3 Wavepacket propagation

The dynamics were performed using two model Hamiltonians. The first (model A) includes the three lowest singlet states and the second (model B) also incorporates the four lowest triplet states. The computational details for the quantum dynamics simulations are shown in Tab. 3.9 and ensured convergence of the dynamics for 1 ps of the wavepacket propagation. For each simulation, the initial wavefunction in the ground state, built using one-dimension harmonic oscillator functions with zero initial momentum, was vertically excited into the S₃ state at the Franck-Condon geometry, $Q = 0$.

In the following subsection, the non-adiabatic dynamics after photoexcitation into the optically bright S₃ state are reported. Initially, by neglecting the SOC matrix elements only the dynamics within the singlet manifold are considered. In the second subsection, these are included and the influence and rate of ISC are assessed.

3.3. Wavepacket propagation

Table 3.7: The spin orbit coupling matrix elements between the important singlet and triplet states at the Franck-Condon and ³MLCT state geometry

State		SOC (cm ⁻¹)	
Singlet	Triplet	FC geom.	Ex. geom.
S ₁	T ₁	336	43
S ₁	T ₂	240	0
S ₁	T ₃	0	28
S ₁	T ₄	0	0
S ₂	T ₁	0	0
S ₂	T ₂	0	116
S ₂	T ₃	298	39
S ₂	T ₄	345	87
S ₃	T ₁	254	9
S ₃	T ₂	358	11
S ₃	T ₃	0	0
S ₃	T ₄	0	15

Table 3.8: Spin orbit coupling between S₁ and T₁, T₂ and T₃.

$$m_1 = 10 \text{ cm}^{-1}, m_2 = -30 \text{ cm}^{-1},$$

$$SO_1 = 237 \text{ cm}^{-1}, SO_2 = 169 \text{ cm}^{-1}, SO_3 = -263 \text{ cm}^{-1}, SO_4 = -250 \text{ cm}^{-1}, SO_5 = -108 \text{ cm}^{-1}, SO_6 = -276 \text{ cm}^{-1},$$

$$\sigma_1 = 2.0684, \sigma_2 = 1.6905, \sigma_3 = 0.6962, \sigma_4 = 0.7128, \sigma_5 = 0.5511, \sigma_6 = 1.1825, \sigma_7 = 0.8812,$$

$$q_1 = 0.3155, q_2 = 0.2666$$

Mode	S ₁ -T ₁	S ₁ -T ₂	S ₁ -T ₃
ν_8	$m_1 q_{\nu_8} + SO_1$	$m_2 q_{\nu_8} + SO_2$	0
ν_{19}	$SO_1 \times \exp[-q_{\nu_{19}}^2 / 2\sigma_1^2]$	$SO_2 \times \exp[-q_{\nu_{19}}^2 / 2\sigma_2^2]$	$SO_3 \times \exp[-q_{\nu_{19}}^2 / 2\sigma_3^2] - SO_3$
ν_{21}	$SO_1 \times \exp[-q_{\nu_{21}}^2 / 2\sigma_4^2]$	SO_2	$SO_4 \times \exp[-q_{\nu_{21}}^2 / 2\sigma_3^2] - SO_4$
ν_{25}	$SO_1 \times \exp[-(q_{\nu_{25}} - q_1)^2 / 2\sigma_4^2]$	$SO_5 \times \exp[-(q_{\nu_{25}} - q_2)^2 / 2\sigma_3^2] - SO_6$	0
ν_{31}	SO_1	SO_2	0
ν_{41}	SO_1	SO_2	0
ν_{55}	SO_1	SO_2	0
ν_{58}	SO_1	SO_2	0

3.3.1 The singlet non-adiabatic dynamics

We now consider the dynamics following photoexcitation into S₃, focusing upon the first 1 ps of the dynamics. Fig. 3.3.a shows the relative diabatic state populations during the first picosecond after photoexcitation. After only a few femtoseconds IC from S₃ to the S₂ and S₁ states is observed. The population of these states occurs almost simultaneously due to the strong coupling between S₁ and S₂. The electronic energy of the wavepacket on S₃ is then converted into kinetic energy on the lower states, resulting in an incoherent distribution of

Table 3.9: Computational details for the MCTDH simulations of the 3-state singlet model (model A). The 7-state intersystem crossing model (model B). N_i, N_j are the number of primitive harmonic oscillator discrete variable representation (DVR) basis functions used to describe each mode. n_i are the number of single-particle functions used to describe the wavepacket on each state.

	Modes	N_i, N_j	$n_{S_1}, n_{S_2}, n_{S_3}, n_{T_1}, n_{T_2}, n_{T_3}, n_{T_4}$
Model A	ν_8, ν_{25}	60,60	30,30,20
	ν_{19}, ν_{21}	60,60	30,30,20
	ν_{31}, ν_{41}	60,60	30,30,20
	ν_{55}, ν_{58}	60,60	30,30,20
Model B	ν_8, ν_{25}	60,60	25,25,15,25,25,15,15
	ν_{19}, ν_{21}	60,60	25,25,15,25,25,15,15
	ν_{31}, ν_{41}	60,60	25,25,15,25,25,15,15
	ν_{55}, ν_{58}	60,60	25,25,15,25,25,15,15

vibrationally hot levels. Initially (up to 200 fs) the two states can be said to be in equilibrium; however as the dynamics proceeds, the wavepacket increasing populates the S_1 state. At later times ($t > 200$ fs), population transfer between these two states still occurs, especially as each time the wavepacket on S_1 returns to the FC region, the strong coupling between the two states causes some re-crossing to S_2 . Eventually, vibrational cooling and energy transfer to the solvent will completely relax the wavepacket into S_1 ; however, this occurs on a longer timescale than presented here [79].

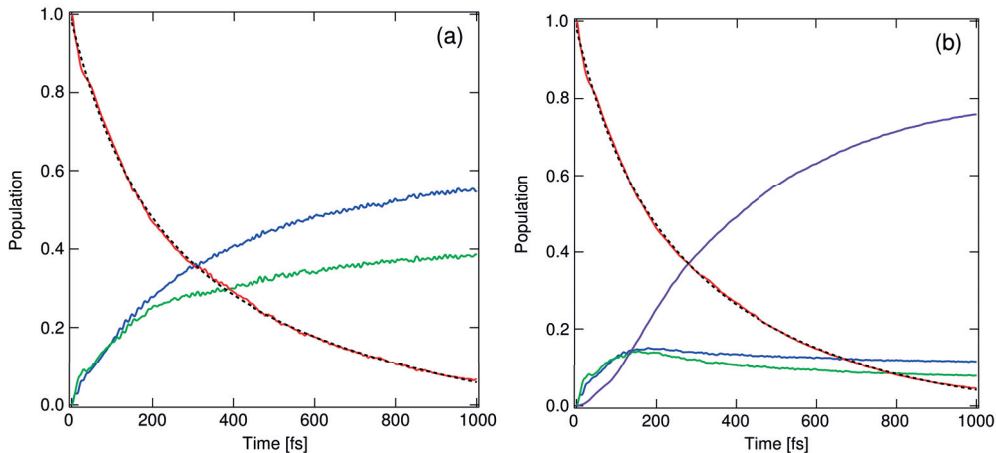


Figure 3.3: (a) Relative diabatic state populations of S_1 (blue), S_2 (green) and S_3 (red) for 1 ps following photoexcitation. (b) Relative diabatic state populations of S_1 (blue), S_2 (green), S_3 (red), the triplet (T_{1-4}) states (purple), for 1 ps following photoexcitation. The black dashed line is the biexponential fit of the S diabatic state populations.

A more detailed insight into the dynamics may be obtained from the position and width of the wavepacket along the important modes during the dynamics. This is shown in Fig. 3.4

for the totally symmetric (ν_8) and PJT (ν_{21}) modes. In the S_3 state (Fig. 3.4.a,d), the dominant motion is that of the totally symmetric ν_8 mode that oscillates around $Q = -0.5$, with a vibrational period of 300 fs. This displacement from the FC point, i.e. $Q = 0$, corresponds to an elongation of the Cu-N bond distance, which is the initial motion in the photoexcited dynamics and enables population transfer into the lower states. Along ν_{21} no significant dynamics are observed in S_3 due to the harmonic nature of the potential.

In the S_2 (Fig. 3.4.b,e), and S_1 (Fig. 3.4.c,f), the wavepacket motion are somewhat similar, due to their strong coupling. We observe, in contrast to the dynamics in S_3 , that the motion along ν_8 corresponds to a contraction of the Cu-N bond distance, i.e. $\langle q \rangle$ oscillates around values > 0 , consistent with time-resolved X-ray experiments [88]. Along ν_{21} the population in neither the S_2 nor the S_1 (Fig. 3.4.b,c), appears to exhibit any significant displacement from the FC geometry. Instead, due to the vibrational hot system, in these states the dynamics are reflected in the width of the wavepacket dq rather than in its position. Here, at early times, we observe a large increase in the width of the wavepacket along ν_{21} (Fig. 3.4.e,f). At later times a gradual decrease in this width is observed, highlighting the beginning of vibrational relaxation.

To compare these simulations to the experimentally observed dynamics, we fit the decay of S_3 population with a biexponential. The best fit in Fig. 3.3.a was obtained with a two decay times of $\tau_1 \sim 113$ fs and of $\tau_2 \sim 600$ fs. The first corresponds to the Internal Conversion (IC) from S_3 to S_2 and S_1 . While tempting to simply assign the second to the PJT distortion, we found this is not strictly the case. Although this component does include the dynamics associated with PJT distortion it also contains the dynamics of the other modes which contributed to the later time population transfer. Indeed, the diabatic basis as presented thus far would not show a PJT distortion, and therefore, for the dynamics associated with this component, we must transform it into the adiabatic representation.

Fig. 3.5.a shows the adiabatic populations of the S_1^{ad} (blue), S_2^{ad} (green), and S_3^{ad} (red) obtained by a unitary transformation of the diabatic state populations presented in Fig. 3.3. For clarity, we have added an ad to denote the adiabatic state. Here, S_3^{ad} shows a decay similar to that observed in the diabatic representation; however, we now observe that, due to the strong coupling between the states, S_2^{ad} acts as a doorway for population transfer into S_1^{ad} .

To obtain the timescale for the PJT distortion and enable comparison to the experimental timescales, in Fig. 3.5.b we plot the portion of the wavepacket in a distorted geometry on S_1^{ad} , which is obtained by integrating for $Q < -1.0$ and $Q > 1.0$ along the PJT mode (see Fig. 3.1 and 3.5.b inset). This shows an exponential rise and at 1 ps, just over 50% of the total wavepacket population in the S_1^{ad} state is in the PJT configuration. The black line in Fig. 3.5.b shows the fit of this population, which yields a time constant of 400 fs. Although faster than the time reported for $[\text{Cu}(\text{dmp})_2]^+$ in dichloromethane, this is in close agreement with the time constant for the PJT distortion t reported in lower viscosity solvents [99]. As expected, because the present quantum dynamics simulations do not incorporate the frictional effects

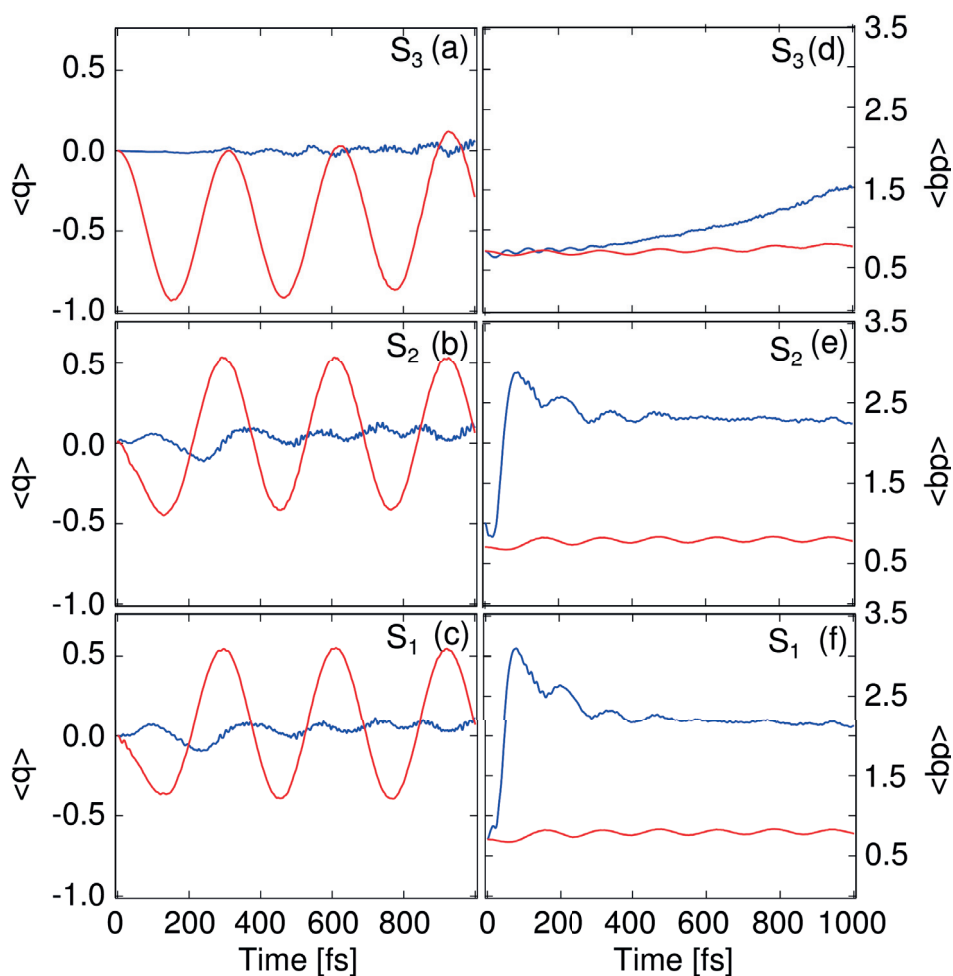


Figure 3.4: Expectation value of the position and of the width of the wavepacket in the excited singlet states: a) and d) S_3 , b) and e) S_2 , c) and f) S_1 . Red: ν_8 , blue: ν_{21} .

of the environment and, therefore, the time scale extracted represents the lower limit of the experimentally observed time constants.

3.3.2 The effect of intersystem crossing

Here we repeat the dynamics performed in the previous section, but including the SOC matrix elements, which permits ISC. Fig. 3.3.b shows the relative diabatic singlet and triplet state populations during the first picosecond. It shows that the decay of S_3 is slightly faster than Fig. 3.3.a. However, the largest difference is observed in the population of the S_1 and S_2 states which, due to the presence of new triplet relaxation channels do not exceed a relative population of 0.2. Significantly, during the first picosecond we observe a total of 80% of the wavepacket populating the triplet states consistent with ultrafast ISC. This observation disagrees with the conclusions by Tahara et al. [99, 96], but agrees with the

3.3. Wavepacket propagation

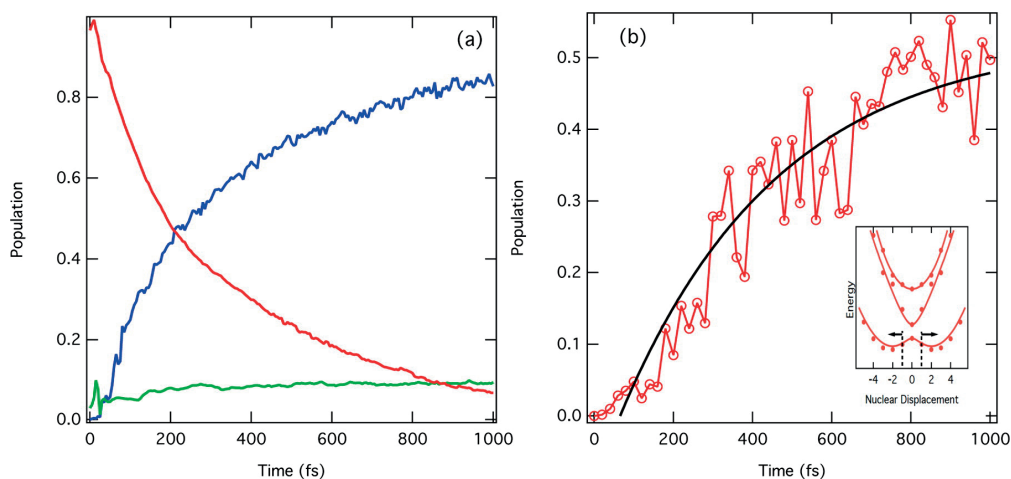


Figure 3.5: (a) Relative adiabatic population of S_1^{ad} (blue), S_2^{ad} (green), and S_3^{ad} (red) for 1 ps following photoexcitation. (b) Population of the wavepacket in the adiabatic S_1^{ad} in the distorted PJT minimum (red). The black dashed line corresponds to a single exponential fit with a time constant of 400 fs.

original interpretation of Chen and co-workers [91] and Siddique et al. [100].

The biexponential fit of the S_3 population decay was again performed and in this case the first decay, $\tau_1=103$ fs, becomes only slightly faster than in the previous section. The slower component is shorter, $\tau_2=416$ fs, because the presence of triplet states opens new relaxation channels. The time scale for the PJT distortion remains, as found in the previous section, ~ 400 fs, but, due to the presence of the ISC, exhibits a significantly smaller population.

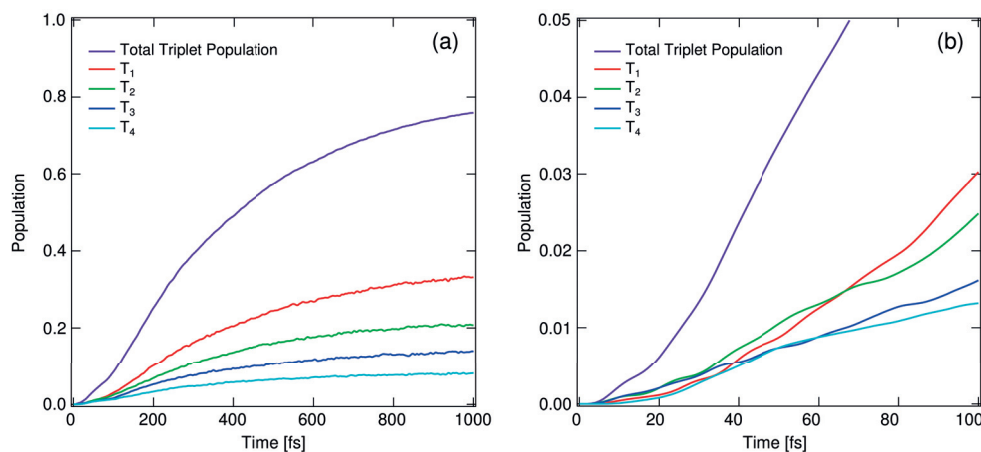


Figure 3.6: a) The relative population of the triplet states T_1 (red), T_2 (green) and T_3 (dark blue) and T_4 (light blue) for 1 ps following photoexcitation. b) Zoom of the first 100 fs.

Fig. 3.6.a shows the population of the individual triplet states during the dynamics. Due to the strong vibronic coupling within the triplet manifold and the small energy gap between the states we see a distribution of the wavepacket across all of the triplets. This population

distribution will remain until, at later times, vibrational cooling relaxes the wavepacket into the flattened geometry of the T_1 state. To understand the mechanism of the ISC process, Fig. 3.6.b zooms into the first 100 fs. This shows that ISC initially occurs via the $S_1 \rightarrow T_2$ and $S_1 \rightarrow T_3$, due to the strong spin-orbit coupling and degeneracies of these three states along the PJT (ν_{21}) mode (see Fig. 3.1b). Indeed, at this point, it is important to note that in all of the previous studies the S_1/T_1 ISC was considered the only relaxation channel to the lowest triplet state. The present simulations demonstrate that in fact, ISC occurs via a dynamical effect by traversing a region where the coupled singlet and triplet states are degenerate leading to efficient and multiple ultrafast ISC channels.

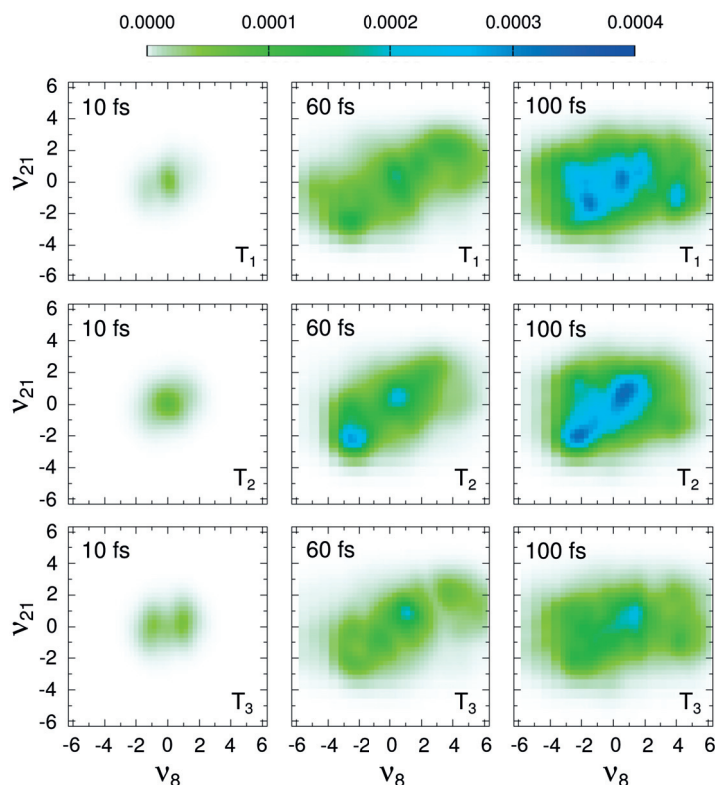


Figure 3.7: Snapshots of the wavepacket density in the triplet states projected along ν_8 and ν_{21} at time delays of 10, 60 and 100 fs after photoexcitation.

This is highlighted in Fig. 3.7, which shows snapshots of the wavepacket density in the triplet states projected along ν_8 and ν_{21} at time delays of 10, 60 and 100 fs. After 10 fs, we observe a very small population of the triplet states in the T_2 and T_3 states only. As expected, this occurs at $Q \sim \pm 1$ along ν_{21} , where the T_1 is degenerate with the T_2 and T_3 states. At later times, as observed in Fig. 3.6, the triplet states become increasingly populated and, due to the strong vibronic coupling, the majority of the wavepacket resides in T_1 . However, for the timescales shown here, as the electronic energy of the wavepacket is converted into kinetic energy giving rise to an incoherent superposition of vibrationally hot levels distributed among the triplet states.

3.4 Discussion

In the previous section, we have presented first-principles quantum dynamics simulations which have been used to identify the key mechanistic steps during the excited state non-adiabatic dynamics of $[\text{Cu}(\text{dmp})_2]^+$. A summary of the time scales extracted from this work compared to recent experiments is shown in Tab. 3.10. As observed, these results compare favorably to recent experimental measurements [99, 91], and clarify an important point, which has been widely disputed within the literature. Our simulations demonstrate that $\sim 80\%$ of the wavepacket crosses into the triplet states within the first picosecond. The majority of this occurs near the FC geometry where the S_1 is degenerate with both the T_2 and T_{23} . This confirms that ISC occurs on the sub picosecond time scale in $[\text{Cu}(\text{dmp})_2]^+$. In this section, we discuss and interpret our results in relation to recent experimental findings [99, 79], especially concerning the observed ultrafast ISC.

Table 3.10: Time Constants (ps) of the Key Mechanistic Processes Extracted from the Quantum Dynamics Compared to Recent Experimental Conclusions. ¹Due to the longer time constant of this component, it is not addressed in this work. However, although existence of this component observed in previous experiments is undeniable, our simulations point to an additional relaxation channel and a strong branching of the population kinetics between the $S_1^{\text{FC}} \rightarrow S_1^{\text{PJT}}$ and $S_1^{\text{PJT}} \rightarrow T_2^{\text{FC}}, T_3^{\text{FC}}$ pathways.

	this work	Ref. [91]	Ref. [100]	Ref. [79]	Ref. [99]
$S_3 \rightarrow S_2, S_1$	0.10			0.08	0.045
$S_1^{\text{FC}} \rightarrow S_1^{\text{PJT}}$	0.40	10-20		0.10	0.34-0.70
$S_1^{\text{FC}} \rightarrow T_x^{\text{FC}}$	0.45	0.5-0.7			
$S_1^{\text{PJT}} \rightarrow T_x^{\text{PJT}}$	1		13-16	10-15	7.40

Using either femtosecond emission [99] or absorption spectroscopy [79] the fastest components of the dynamics exhibit time-constants of ~ 45 or ~ 80 fs, respectively. In both cases, this was assigned to the decay of the initially excited S_3 state via IC (see (a) in Fig. 3.8). This is in good agreement with the ~ 100 fs decay component identified in this work, especially considering the 45 fs component was extracted using a 200 fs temporal resolution of the experimental setup reported in Ref. [99]. Our dynamics confirms this assignment of population transfer from S_3 to the S_2 and S_1 states. In particular, the strong coupling between the latter two gives rise to a cascade relaxation process, and the rapid nature of this decay is because the population transfer occurs near to or at the FC region, meaning that very little nuclear dynamics is required. Besides IC, the authors of Ref. [99] also reports that the overall quantum yield of this transition is 0.7. They concluded that the remaining portion of the wavepacket passes directly from the S_3 to the T_1 state on the nanosecond timescale. Although this latter observation is not directly addressed in this work, this conclusion is consistent with our SOC calculations presented in Tab. 6.4, which shows that there is SOC between S_3 and T_1 at the FC geometry ($\sim 250 \text{ cm}^{-1}$), but also between the S_3 and T_2 ($\sim 360 \text{ cm}^{-1}$) providing two possible relaxation channels. Though these SOC matrix elements are

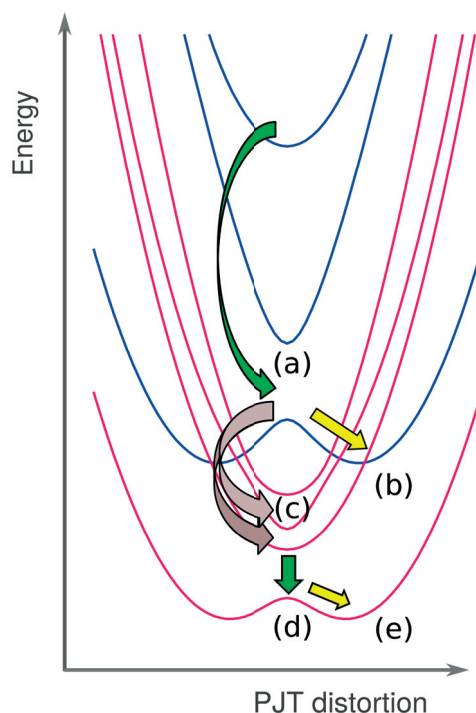


Figure 3.8: Schematic representation of the key dynamical steps occurring within the ultrafast non-adiabatic dynamics of $[\text{Cu}(\text{dmp})_2]^+$ studied here. (a) Internal conversion from S_3 to S_2 and S_1 : $\tau = 45$ and 80 fs [99, 79]. (b) Vibrational relaxation from S_1^{FC} to S_1^{PJT} , $\tau = 340 - 700$ fs [99], 400 fs. (c) Ultrafast ISC from S_1^{FC} to T_2^{FC} and T_3^{FC} , $\tau = 450$ (d) IC within the triplets from $T_{2,3}^{\text{FC}}$ to T_1^{FC} and (e) Vibrational relaxation from T_1^{FC} to T_1^{PJT} .

of similar magnitude to those between the S_1 and the T_2/T_3 states, the ISC occurs on the nanosecond timescale in this case due to the large energy gap between the coupled states.

Tahara and co-workers [99] reported that the second dynamical process has a time constant between 340 - 700 fs. In contrast to the previous decay component, this time constant exhibits a slight dependence on the viscosity of the solvent and consequently it was assigned to the flattening dynamics associated with the PJT structural distortion. Indeed, the simulations here presented confirms this assignment and at these longer times we observe the wavepacket increasingly populate the S_1 minimum (Fig. 3.5). The time constant extracted from our simulations (~ 400 fs) represents the lower limit of these experimental time scales as the effect of the friction mechanism imparted by the solvent is not incorporated in our present model.

As previously stated, while these two previous dynamical components agree closely with recent experimental conclusions, upon inclusion of ISC (Fig. 3.3.b), we observe that $\sim 80\%$ of the population is transferred into the triplet states within the first picosecond. This is contrary to the conclusions of Refs [99, 79, 96, 98], which have instead reported that ISC only occurs after 10 ps at the flattened PJT geometry. However, the interpretations of all of

these studies were crucially based on the assumption that SOC is only important between the S_1 and T_1 states. Our present simulations point to a strong branching of the wavepacket between the $S_1^{\text{FC}} \rightarrow S_1^{\text{PJT}}$ (see **(b)** in Fig. 3.8) and $S_1^{\text{FC}} \rightarrow T_{2,3}^{\text{PJT}}$ (see **(c)** in Fig. 3.8) pathways, which favours the latter. Importantly, they show that ISC initially occurs via the $S_1 \rightarrow T_2$ and T_3 , due to the strong coupling and degeneracies of these states along the PJT (ν_{21}) mode. This strong branching ratio in favour of ultrafast ISC is in close agreement with the conclusions of Ref. [100], and although this is contrary to the model proposed by Tahara and co-workers [99], who assumed a unity quantum yield from $S_1^{\text{FC}} \rightarrow S_1^{\text{PJT}}$, they also acknowledged the likelihood of a sizable error.

3.5 Conclusions

In conclusion, we have applied the vibronic coupling Hamiltonian and quantum dynamics within the framework of the MCTDH method to study excited state non-adiabatic dynamics of $[\text{Cu}(\text{dmp})_2]^+$. Including the dominant nuclear and electronic degrees of freedom, we have obtained excited state decay components which agree with those observed experimentally. Our present simulations lead us to the following description of the excited state dynamics. Following photoexcitation into the optically bright S_3 state, the system rapidly decays into S_2 at the Franck-Condon geometry. At this location and due to the strong coupling between the almost degenerate S_1 and S_2 states, IC into the S_1 state occurs almost simultaneously. This initial population decay is dominant for the first ~ 150 - 200 fs of the dynamics and corresponds to the decay component of the S_3 state population of ~ 100 fs (45 fs experimentally [99]). We, therefore, assign this to the internal conversion from the optically bright transition (S_3) to the S_2 , S_1 states in the perpendicular geometry in agreement with Ref. [99]. Vibrational relaxation into the PJT geometry occurs in ~ 400 fs, in both the lowest singlet S_1 and triplet T_1 states. Experimentally this process is slowed down, 340-700 fs, due to solvent friction effects. Finally, the strong spin orbit coupling between singlet and triplet manifolds combined with the degeneracy of the S_1 , T_2 and T_3 states near the FC structure gives rise to a multiple ISC channels, which is the driving force behind the occurrence of ultrafast ISC. This finding of ultrafast ISC has significant implications if one wishes to apply these complexes to solar energy conversion. Indeed, Huang et al. [168] recently demonstrated that, when a related Cu(I)-phenanthroline complex is attached to TiO_2 , charge injection from the $^1\text{MLCT}$ is 2 orders of magnitude faster than that from the $^3\text{MLCT}$. Consequently, for efficient charge injection one needs to restrict ISC.

4 Feasibility of ultrafast time-resolved X-ray spectroscopy

The advent of X-ray Free Electron Lasers (X-FELs) is providing new opportunities for probing ultrafast excited state dynamics using structurally sensitive techniques. Herein we use excited state wavepacket dynamics of a prototypical Cu(I)-phenanthroline complex, $[\text{Cu}(\text{dmp})_2]^+$ (dmp = 2,9-dimethyl-1,10-phenanthroline) to investigate how femtosecond vibrational and electronic relaxation is translated into transient X-ray absorption (XAS) and emission (XES). Using realistic experimental parameters we also derive the anticipated signal strengths for these transient features. This indicates that although recording a signal capturing the strongest transient (i.e. excited state - ground state) changes will be possible for all cases, only with X-ray Absorption Near-Edge Structure (XANES) and Extended X-ray Absorption Fine Structure (EXAFS) will it be possible to resolve the details associated with the wavepacket dynamics within realistic experimental acquisition times.

This chapter is largely based on the following publication “*Probing Wavepacket Dynamics using Ultrafast X-ray Spectroscopy*” by G. Capano, C. J. Milne, M. Chergui, U. Röthlisberger, I. Tavernelli and T. J. Penfold, *J. Phys. B: At. Mol. Phys.* 48 (21), 214001, 2015

4.1 Introduction

Probing ultrafast non-equilibrium dynamics became possible with the advent of ultrafast time-resolved linear and non-linear optical spectroscopies [169, 170]. However, because optical spectroscopy consists of transitions between delocalised valence states, the link between the spectroscopic observable and structure is ambiguous for systems of more than one nuclear degree of freedom, i.e. >2 atoms. To overcome this, the last decades have witnessed a significant research effort aimed at exploiting short wavelength probe pulses to achieve direct structural sensitivity in time-resolved pump-probe experiments. This has led to the development of time-resolved diffraction methods using X-rays [171, 172, 173] or electrons [174, 30] and core level spectroscopies using either X-rays [175, 176, 177, 40] or electrons [178, 179].

Chapter 4. Feasibility of ultrafast time-resolved X-ray spectroscopy

For the implementation of time-resolved X-ray spectroscopy, the focus of the work presented in this chapter, third generation light sources are most suited because of their wide tuneability, stability, and high photon flux. However, for normal operational modes, the X-ray pulses from these light sources have a temporal width of 50-100 ps. They are therefore unable to probe the initial ultrafast dynamics that can often be critical in determining the outcome of non-equilibrium dynamics. While this can, to a certain extent, be overcome using the laser-slicing scheme [180] which has been used to demonstrate femtosecond X-ray spectroscopy [181, 182, 183], these experiments are extremely challenging due to low photon counts. With an X-ray flux per pulse that is typically 10-11 orders of magnitude higher than the laser-slicing scheme, X-ray Free electron lasers (X-FELs) [184] offer new perspectives for performing ultrafast X-ray experiments. Indeed, femtosecond X-ray spectroscopy at X-FELs has been demonstrated for photoexcited $[\text{Fe}(\text{bpy})_3]^{2+}$ [185, 186], $[\text{Fe}(\text{phen})_2(\text{NCS})_2]$ [187], $[\text{Fe}(\text{C}_2\text{O}_4)_3]^{3-}$ [188] and $\text{Fe}(\text{CO})_5$ [189].

These studies have been used to shed light on the evolving electronic structure, changing spin states and overall structural changes occurring after photoexcitation. However, none of these studies have probed the nuclear wavepacket dynamics, which is commonly elucidated from femtosecond optical spectroscopy [190, 191]. Indeed directly observing signatures of (coherent) vibrational dynamics, electronic relaxation, intramolecular energy redistribution and vibrational cooling can shed important insight into how a particular system dissipates the energy after photoexcitation. Consequently, the absence of these dynamics in any time-resolved X-ray spectroscopic experiment reported to date poses a number of questions: i) What is the sensitivity of X-ray spectroscopic techniques to wavepacket dynamics? ii) What is the measurement sensitivity and therefore number of photons required to successfully observe these dynamics? iii) What is the best X-ray spectroscopic technique to observe these dynamics?

To address these questions, in this work we use first principles quantum dynamics simulations of a prototypical Cu(I)-phenanthroline complex, $[\text{Cu}(\text{dmp})_2]^+$ (dmp = 2,9-dimethyl-1,10-phenanthroline) described in the previous chapter, initiated after photoexcitation into the optically bright metal-to-ligand charge-transfer (MLCT) state to investigate how femtosecond nuclear wavepacket dynamics are reflected in X-ray spectroscopic signals. This is achieved by studying the Extended X-ray Absorption Fine Structure (EXAFS), pre-edge X-ray Absorption Near-Edge Structure (XANES), $K_{\alpha_{1,2}}$, $K_{\beta_{1,3}}$ and $K_{\beta_{2,5}}$ (sometimes referred to as valence-to-core) X-ray emission (XES) spectra. Subsequently, using realistic experimental parameters we derive the anticipated signal strengths for these transient (i.e. excited state - ground state) features. For the present complex, these simulations show that while recording a signal capturing the strongest transient changes is possible for each spectroscopic method, only for XANES and EXAFS will it be possible to resolve the fine details associated with wavepacket dynamics within realistic experimental acquisition times.

4.2 Theory and computational details

4.2.1 Quantum Dynamics of $[\text{Cu}(\text{dmp})_2]^+$

In this work we derive ultrafast X-ray spectroscopic signals from the quantum dynamics of a prototypical Cu(I)-phenanthroline complex, $[\text{Cu}(\text{dmp})_2]^+$ described in the previous chapter. The ultrafast dynamics of $[\text{Cu}(\text{dmp})_2]^+$ have previously been well characterised using optical absorption and emission spectroscopies [91, 79, 100, 99, 96, 98]. The general picture that emerges from these studies indicates that following photoexcitation, the complex relaxes into the lowest singlet excited state in 100 fs. This is followed by a structural distortion (flattening of the dihedral angle between the ligands), and intersystem crossing (ISC) to the lowest triplet state T_1 [98]. Of particular relevance to the present work, Tahara and co-workers [99, 96, 98] have demonstrated the presence of distinct wavepacket dynamics occurring in the excited state. These coherent vibrational dynamics were dominated by a vibrational mode with frequency 125 cm^{-1} (period of 300 fs), which was assigned to a breathing mode of the complex that causes a symmetric stretching of the four Cu-N bonds [96].

The quantum dynamics used herein are presented in detail in the previous Chapter and were performed using the Heidelberg Multi Configuration Time Dependent Hartree (MCTDH) package [192, 57]. The Hamiltonian was described using the vibronic coupling model [193]. It included 8 nuclear degrees of freedom, the three lowest singlet states and the four lowest triplet states. After photoexcitation, which populates the S_3 state, the population rapidly decays into the S_2 and S_1 states. Due to a degeneracy of these states with the lowest lying triplet states, there is rapid intersystem crossing into the triplet manifold (red line in Fig. 3.3) and after 1 ps 80% of the wavepacket is in the triplet states. Of this population, just under half is in the T_1 state. Further details of the quantum dynamics simulations can be found in Chapter 3.

4.2.2 Simulations of the time-resolved spectra

The X-ray spectrum of the non-stationary wavepacket is calculated as the weighted sum of the spectra calculated at each grid point used to describe the nuclear wavepacket. The weighting corresponds to the magnitude of the nuclear wavepacket at that grid point. For the EXAFS spectra, a sum over each electronic state was also performed, thus achieving a description of the full nuclear wavepacket. All of the other spectra (pre-edge XANES and XES) considered only the wavepacket, and thus the dynamics, on the T_1 state. This is because, in contrast to EXAFS spectra, the valence electronic structure is expected to influence the spectrum, meaning that for the excited states (i.e. S_1 , S_2 , S_3 , and T_2 , T_3 , T_4), one must directly simulate the core-level spectrum of each excited state. At present, the most rigorous approach of simulating the core-level spectra of the electronically excited states is Restricted Active Space Self Consistent Field (RASSCF) method [50]. However, since these calculations are extremely computationally intensive (1000 hrs per calculations) they are unrealistic to

describe the time-evolution of a nuclear wavepacket. Consequently, this approach is best applied to probe selected important points of the dynamics, as recently demonstrated in the study of photoexcited $\text{Fe}(\text{CO})_5$ [189]. An alternative approximate way to address the excited state is using a SCF approach, such as the maximum overlap method (MOM) [194]. However, this requires that the excited state is well described by a single electron excitation, such as a HOMO-LUMO transition. Unfortunately, this is not the case for the present system. In addition, the character of the excited states changes along the main reaction path making it impossible to assign a single configuration to represent each of the excited states.

The EXAFS spectra at each grid point were calculated with the FEFF9 package [195] using the path expansion multiple scattering approach and a self-consistent field (SCF) potential. All scattering pathways shorter than 6 Å were included. The XAS and XES spectra were computed within the one-electron approach [54] as implemented in the ORCA [49] quantum chemistry package. Computations used the BP86 functional [196, 197] and the def2-TZVP basis set [198, 199]. All of the calculations included spin orbit coupling (SOC), for which the SOC operator is approximated by the spin-orbit mean-field method (SOMF) [200]. A Lorentzian lifetime broadening with full-width half maximum (FWHM) of 1.89 eV was applied to the pre-edge XANES, while a Lorentzian broadening with FWHM of 2.5 eV was used for the XES spectra.

Finally, for both the XAS and XES spectra, the relative energies of the calculated transition are generally well reproduced compared to experiment. However, it is well documented that the absolute transition energies are usually in poor agreement [201]. This failure stems from the approximate exchange description within the exchange-correlation functionals and is associated with the self interaction error (SIE) [194]. This is usually corrected by applying a constant shift to the spectrum a posteriori [202, 37]. In this case, as these spectra are not directly compared to experimental data, these shifts have not been included.

4.3 Results

In the following sections, we present the simulations of the EXAFS, pre-edge XANES and XES spectra. Then, using the calculated signal magnitudes, we derive the anticipated feasibility of these techniques to probe the wavepacket dynamics.

4.3.1 EXAFS

The ground state EXAFS spectrum of $[\text{Cu}(\text{dmp})_2]^+$ [88] compared to the spectrum simulated using the ground state wavepacket is shown in Fig. 4.1. Although the simulated spectrum is slightly more structured than the experimental spectrum, fairly good agreement between the two is observed with the main features, especially those at low k , well captured. As previously reported, this EXAFS spectrum is largely dependent on the Cu-N distance, which is 2.09 Å in the ground state.

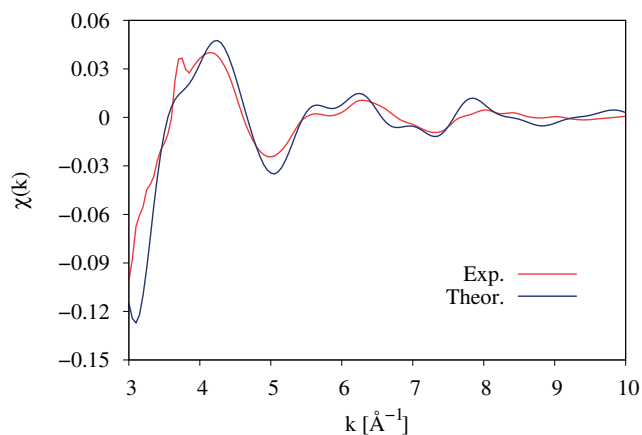


Figure 4.1: Experimental ground state Cu K-edge EXAFS spectrum (red line) compared to the spectrum simulated using the ground state wavepacket (blue line). The experimental data has been taken from T. J. Penfold et al. J. Phys. Chem. A, 117:4591-4601, 2013.

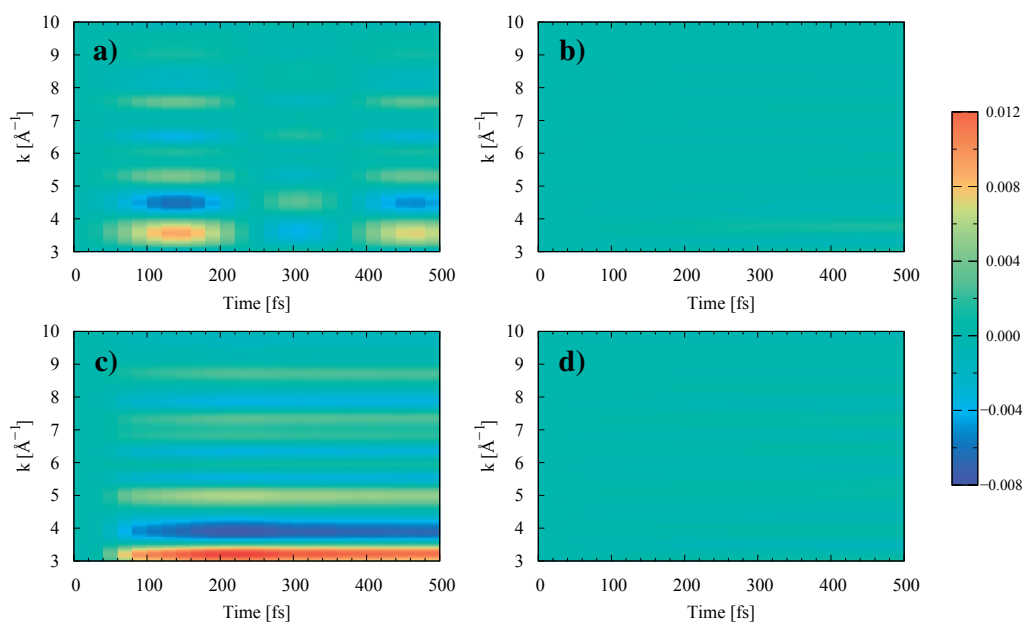


Figure 4.2: The simulated transient Cu K-edge EXAFS spectrum, $\Delta\chi$, of $[\text{Cu}(\text{dmp})_2]^+$ for the first 500 fs after photoexcitation. In each case the spectra are calculated using the nuclear wavepacket dynamics along one degree of freedom; ν_8 (a), ν_{19} (b), ν_{21} (c), ν_{25} (d).

Fig. 4.2 shows the transient EXAFS spectrum for the first 500 fs of the photoexcited dynamics projected along 4 (ν_8 , ν_{19} , ν_{21} , ν_{25}) of the 8 nuclear degrees of freedom included in the model Hamiltonian. This shows that two modes, ν_8 and ν_{21} , would be expected to dominate the

transient features in the EXAFS spectrum. The other two modes, ν_{19} , ν_{25} have a weak signal as they are not strongly displaced from their ground state configuration during the dynamics. Of the two active modes, ν_8 is the totally symmetric breathing mode responsible for the contraction of the Cu-N distance in the excited state. This shows an oscillation, caused by a phase shift in the transient EXAFS spectrum, with a period of 300 fs which is in good agreement with the wavepacket dynamics reported by Tahara et al. [89]. In contrast, ν_{21} , which is the mode associated with the pseudo Jahn-Teller (PJT) distortion, exhibits a strong transient signal that is out of phase with the features occurring in the ground state EXAFS spectrum (Figure 3), pointing to a damping of the EXAFS features in the excited state. It occurs because the excited state potential along this mode is flatter than the ground state, leading to a nuclear wavepacket that is more spread in the excited state. This additional width has the same dampening effect on the EXAFS spectrum as a Debye-Waller term [203].

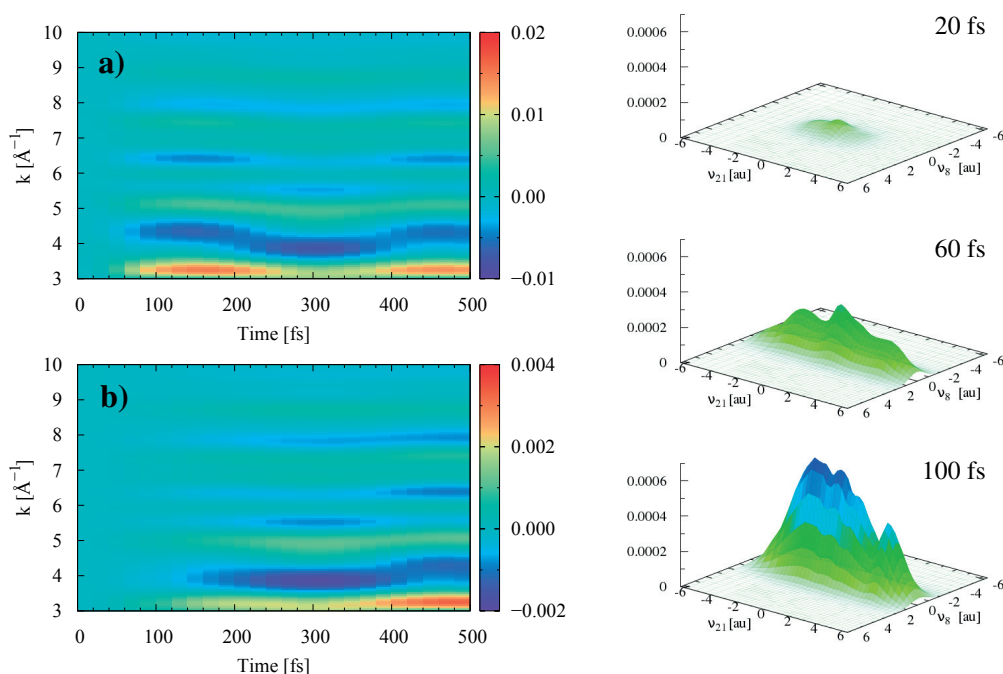


Figure 4.3: The simulated transient Cu K-edge EXAFS spectrum of $[\text{Cu}(\text{dmp})_2]^+$ for the first 500 fs after photoexcitation calculated using the nuclear wavepacket dynamics occurring in the 2D nuclear coordinate space of ν_8 and ν_{21} . (a) The spectrum for the full nuclear wavepacket (b) The spectrum for the wavepacket dynamics in only the lowest triplet (T_1) state. The right-hand side shows snapshots of the nuclear wavepacket in the T_1 along the two modes at 20, 60 and 100 fs.

Figure 4.3a shows the simulated transient EXAFS spectrum using the nuclear wavepacket dynamics projected in a 2D nuclear coordinate space of ν_8 and ν_{21} . This shows a transient that has its main features out of phase with the ground state spectrum, but which is superimposed with the 300 fs oscillation associated with the wavepacket motion along ν_8 . Due to the

simplicity of the first coordination sphere, which is the dominant contribution to the EXAFS spectrum, this general structure is repeated at larger photoelectron energies (k), meaning that the experimental spectrum only needs to be recorded to $\sim 5 \text{ \AA}^{-1}$ ($\sim 9080 \text{ eV}$, $\sim 100 \text{ eV}$ above the absorption edge). However, it is noted that in more complicated systems, with a less symmetric first coordination shell around the absorbing atom, different dynamics may well be reflected at different photoelectron energies, especially in the presence of heavier elements that scatter at larger k [204, 205].

As discussed in section 2.2, simulations of the EXAFS spectrum for the different excited states requires only the nuclear geometry. However, the same cannot be said for the pre-edge region of the XAS spectrum and for the XES spectrum. For these cases, we investigate the ultrafast dynamics on the T_1 state only. Consequently to assess the effect of this approximation, Figure 3b shows the transient EXAFS spectrum using nuclear wavepacket in the 2D nuclear coordinate space of ν_8 and ν_{21} , for which only the wavepacket on the T_1 has been considered. Importantly, the same wavepacket dynamics are observed, although the signal is a factor of ~ 5 weaker. This is due to the smaller ($< 30\%$) population (see Figure 1) of the T_1 state.

4.3.2 Pre-edge X-ray Absorption

Fig. 4.4.a shows the ground and T_1 states (from 0 to 500 fs after photoexcitation) of the Cu K-edge pre-edge XANES spectrum calculated in 2D nuclear coordinate space of ν_8 and ν_{21} . The transient spectra simulated every 20 fs between $\tau=0$ to 500 fs are shown in Fig. 4.4.b. Ideally, one would wish to simulate the entire XANES regions of the spectrum. However, as a result of the difficulties associated with a quantitative description of the transient features in this region of the spectrum [38], a quantitative agreement between the experimental spectrum recorded at a time-delay of 50 ps and the corresponding simulations [88] could not be achieved. Consequently, we focus upon the pre-edge region of the spectrum.

As reported in Ref. [88], the transient spectrum (Fig. 4.4.a) shows the 2 main features, a weak positive feature 8747 eV that corresponds to a $1s \rightarrow 3d$ transition, and a strong negative feature that corresponds to a loss of intensity of the $1s \rightarrow 4p$ transition in the ground state spectrum. This latter feature is due to the blue shift of the absorption edge due to the oxidation state change of the metal center upon population of the metal-to-ligand charge transfer state. The spectral changes in the transient pre-edge XANES spectra are dominated by the oxidation shift of the absorption edge and the change of the population of the T_1 (Fig. 4.4.b). As a consequence, they do not exhibit any distinct changes associated with the wavepacket dynamics. To remove these two effects, Fig. 4.4.c shows the transient changes occurring in the T_1 state only, i.e. $T_1(\tau \text{ fs}) - T_1(20 \text{ fs})$. Time traces at specific energies are shown in Fig. 4.4.d. Importantly, the time-trace at 8753.5 eV, corresponding to just below the $1s \rightarrow 4p$ transition in the ground state spectrum, captures the oscillatory dynamics observed in the EXAFS spectra and exhibits a signal change $\sim 1\%$. While, given the energy range considered here, we also cannot rule out these changes also occurring at higher energies in the XANES region of the

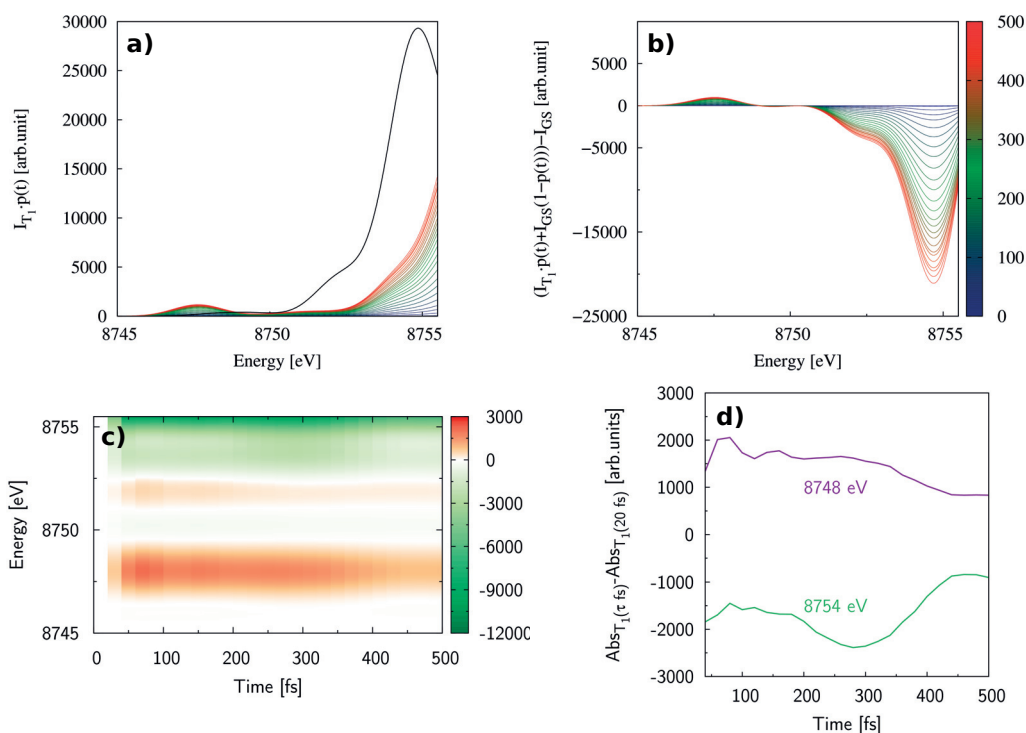


Figure 4.4: The simulated Cu K-edge pre-edge XANES spectra for the dynamics in the lowest triplet T_1 state. (a) The ground state spectrum and b) transient spectrum of the wavepacket in the lowest triplet state from 0 to 500 fs after photoexcitation (c) the transient changes in the lowest triplet state calculated using $T_1(t \text{ fs}) - T_1(20 \text{ fs})$ (d) time traces of (b) at 8745.5 and 8753.5 eV.

spectrum, these will be significantly smaller than the transient change associated with the $1s \rightarrow 4p$ transition and much closer to those of the EXAFS region.

4.3.3 X-ray emission

Fig. 4.5.a shows the ground state, from 0 to 500 fs, of the $K_{\alpha_{1,2}}$ XES spectra calculated in 2D nuclear coordinate space. This shows that the changes are small ($\sim 10\%$) and dominated by a shift in the emission energy associated with the change of spin state compared to the ground state [206]. The transient spectra calculated every 20 fs between $\tau=0$ to 500 fs are shown in Fig. 4.5.b. This dominance of changing spin state is not surprising, as this core to core ($2p \rightarrow 1s$) transition is not very sensitive to small changes in the molecular structure or valence electronic structure. Fig. 4.5.c and d again shows the transient changes in the T_1 state and time traces at 7825 eV and 7844 eV. In this case, we do not observe any variations that can be associated with the nuclear wavepacket dynamics.

Fig. 4.6 shows the corresponding plots for the $K_{\beta_{1,3}}$ XES spectra. As this concerns transitions from $3p \rightarrow 1s$, it is likely to be more sensitive to the structural and valence electronic structural

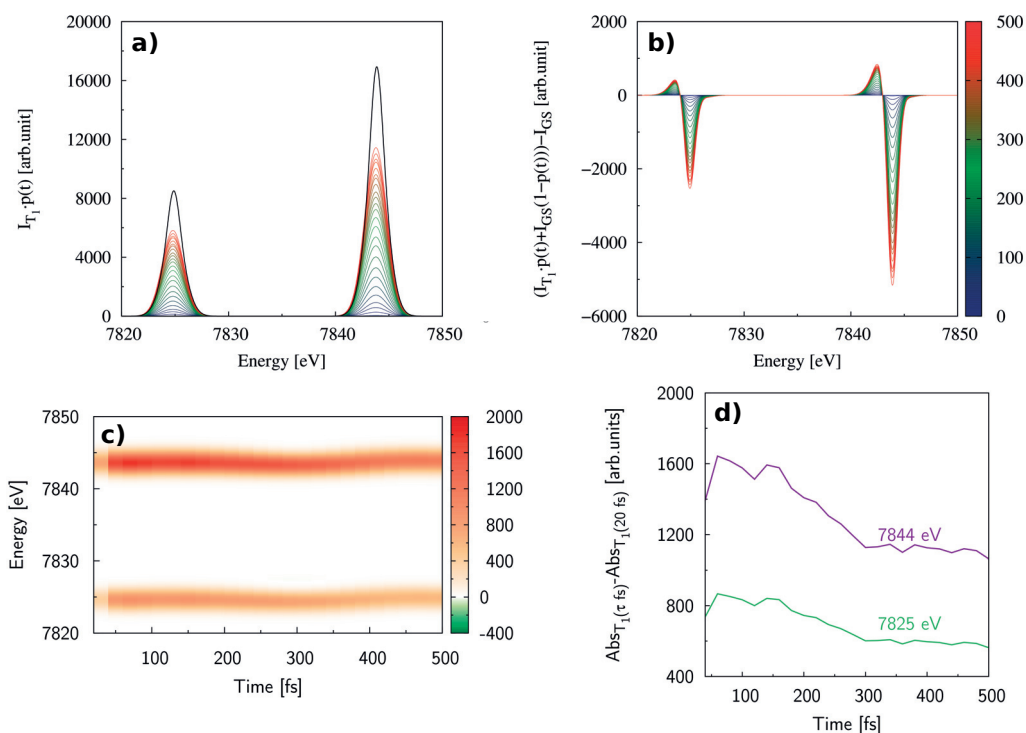


Figure 4.5: The simulated Cu $K_{\alpha_{1,2}}$ XES spectra for the dynamics in the lowest triplet T_1 state. (a) The ground state spectrum and b) transient spectrum of the wavepacket in the lowest triplet state from 0 to 500 fs after photoexcitation (c) the transient changes changes in the lowest triplet state calculated using $T_1(t \text{ fs}) - T_1(20 \text{ fs})$ (d) time traces of (b) at 8677 and 8681 eV.

changes, especially via the $3p \rightarrow 3d$ exchange integral [207]. Indeed, while the transient spectra, shown in Fig. 4.6.a is again dominated by an edge shift. The transient spectra calculated every 20 fs between $\tau=0$ to 500 fs are shown in Fig. 4.6.b. Fig. 4.6.c and d reveal weak transient changes in the T_1 state and the 300 fs oscillatory period of the Cu-N totally symmetry stretch is observed. The magnitude of the changes associated with the wavepacket dynamics corresponds to a $\sim 0.7\%$ spectral change compared to the ground state spectrum, meaning that it has a similar magnitude change as the transient EXAFS signal.

Finally, Fig. 4.7 shows the $K_{\beta_{2,5}}$ XES spectra associated with the femtosecond dynamics in the T_1 state. In contrast to the $K_{\alpha_{1,2}}$ and $K_{\beta_{1,3}}$ XES the stronger effect on the wavepacket dynamics on the transient signal can be clearly observed in Fig. 4.7.c and d. This corresponds to a spectral change of $\sim 5\%$ compared to the ground state spectrum and is about an order of magnitude larger than found for EXAFS, $K_{\alpha_{1,2}}$ and $K_{\beta_{1,3}}$ XES. This highlights the distinct advantage and strong signals associated with directly probing the occupied valence density of states. However, the obvious disadvantage of this technique is, as discussed in the next section, the low cross sections, and therefore photon yields, associated with these transitions.

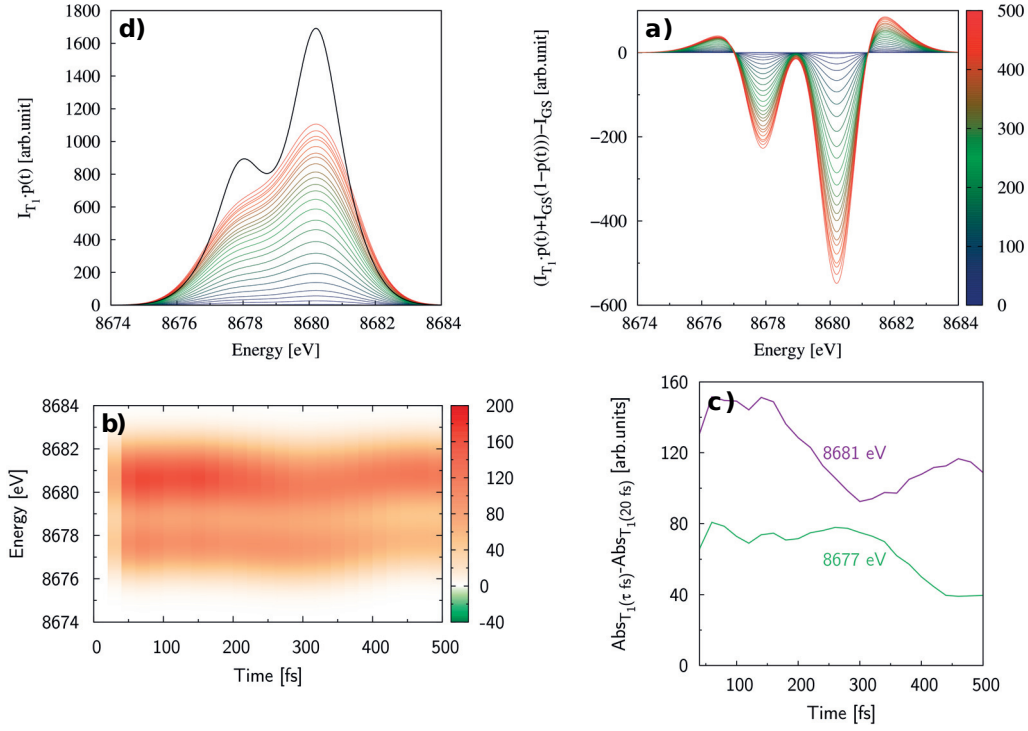


Figure 4.6: The simulated Cu $K_{\beta_{1,3}}$ XES spectra for the dynamics in the lowest triplet T_1 state. (a) The ground state spectrum and b) transient spectrum of the wavepacket in the lowest triplet state from 0 to 500 fs after photoexcitation (c) the transient changes changes in the lowest triplet state calculated using $T_1(t \text{ fs}) - T_1(20 \text{ fs})$ (c) time traces of (d) at 8677 and 8681 eV.

4.3.4 Numerical Examples: Feasibility of Probing Wavepacket Dynamics

In the previous sections we have simulated the femtosecond EXAFS, pre-edge XANES and $K_{\alpha_{1,2}}$, $K_{\beta_{1,3}}$ and $K_{\beta_{2,5}}$ XES spectra of photoexcited $[\text{Cu}(\text{dmp})_2]^+$ using the nuclear wavepacket dynamics reported in the previous Chapter. These have demonstrated that some of the signals (pre-edge XANES, EXAFS, $K_{\beta_{1,3}}$ and $K_{\beta_{2,5}}$) bear characteristics related to the wavepacket dynamics. However, the most crucial aspect of this work, regarding femtosecond laser-pump X-ray-probe experiments being used to investigate such dynamics is the X-ray photon flux required to achieve sufficient sensitivity to resolve these small spectral changes. Many X-ray spectroscopic measurements are performed in fluorescence yield mode. For spectroscopies based upon the detection of scattered (fluorescent) photons, the spectra are formally represented within second order perturbation theory using the Kramers-Heisenberg equation:

$$F(\Omega, \omega) = \sum_f \sum_n \frac{\langle f | \hat{H}_{int} | i \rangle \langle n | \hat{H}_{int} | i \rangle^2}{(E_i - E_n + \hbar\Omega)^2 + \Gamma_f^2/4} \times \frac{\Gamma_f/2\pi}{(E_i - E_n + \hbar\Omega - \hbar\omega)^2 + \Gamma_f^2/4} \quad (4.1)$$

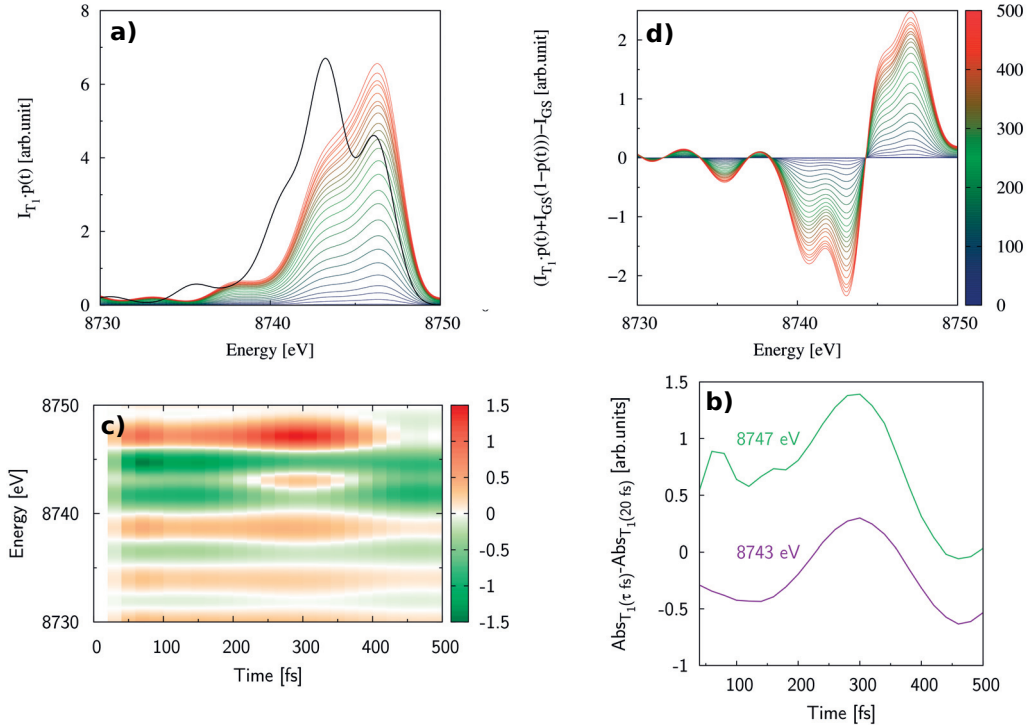


Figure 4.7: The simulated Cu $K\beta_{2.5}$ XES spectra for the dynamics in the lowest triplet T_1 state. (a) The ground state spectrum and (b) transient spectrum of the wavepacket in the lowest triplet state from 0 to 500 fs after photoexcitation (c) the transient changes changes in the lowest triplet state calculated using $T_1(t \text{ fs}) - T_1(20 \text{ fs})$ (c) time traces of (b) at 8743 and 8747 eV.

where $\hbar\Omega$ and $\hbar\omega$ are the incident and emitted photons, respectively and E_i , E_n and E_f are the energies of the initial, intermediate and final states. Γ_n and Γ_f are the lifetime broadening associated with the intermediate and final states. Here, we assume a non-coherent process, in which the absorption matrix elements from initial state i to intermediate state n , mediated by the interaction Hamiltonian \hat{H}_{int} , are weighted by the emission matrix elements [40, 208].

For measurements of the XAS spectra, performed in total fluorescence yield (TFY) mode, the cross section of the absorption matrix element $\langle n | \hat{H}_{int} | i \rangle$ at a particular X-ray incident energy is integrated over all of the emission matrix elements $\langle f | \hat{H}_{int} | i \rangle$. Consequently, as discrimination of the energy of the emitted photons is not required, one can use a point detector, such as silicon photodiode [185]. These can be placed close (15 mm) to the sample, and can, therefore, achieve a larger solid angle. Using the relation:

$$\theta = \frac{\pi r_{APD}^2}{4\pi R^2} \quad (4.2)$$

and assuming that the detector's active radius, $r_{APD}=7\text{mm}$ the solid angle (θ) is $\sim 5\%$. Consequently, given that the efficiency of the fluorescence process at Cu K-edge is $\sim 45\%$ [209]

Chapter 4. Feasibility of ultrafast time-resolved X-ray spectroscopy

and assuming a detector with a quantum efficiency of ~ 0.8 [210], we can combine these 3 components to yield a loss factor (of the photons in vs the photons out) of 2×10^{-2} .

In contrast, detection of the X-ray emission elements is proportional to the cross section of the absorption matrix element ($\langle n | \hat{H}_{int} | i \rangle$) multiplied by the cross section of the emission line of interest ($\langle f | \hat{H}_{int} | i \rangle$), i.e. $K_{\alpha_{1,2}}, K_{\beta_{1,3}}$. Consequently, the photon yield for each spectrum will be significantly lower making it harder to achieve a large signal to noise ratio (SNR) for these photon hungry techniques. In addition, for these experiments the X-ray emission spectrometer is further away from the sample causing additional losses and a smaller solid angle [206, 211]. For each emission line of interest, the fluorescence efficiencies are Cu $K_{\alpha_{1,2}}$ =0.3, Cu $K_{\beta_{1,3}}$ -edge=0.03 and Cu $K_{\beta_{2,5}}$ -edge=0.00001 [211, 209]. Consequently given a reduced solid angle arising from the larger sample detector distance of $\sim 0.04\%$ (~ 5 milliradians) [211, 212], the X-ray attenuation in air due to the larger distance from the detector [41], which is assumed to be 0.3, the total losses are Cu $K_{\alpha_{1,2}}$ -edge= 3.0×10^{-5} , Cu $K_{\beta_{1,3}}$ -edge= 3.0×10^{-9} and Cu $K_{\beta_{2,5}}$ -edge= 9.6×10^{-6} .

Assuming a $100 \mu\text{m}$ thick jet of 25 mM solution, the absorbed fraction of photons, according to the Beer-Lambert law is $\sim 2\%$. It is stressed that this approximation is only strictly valid for solvents containing light elements (e.g., water, acetonitrile, hexane) and may change for heavier solvents, like CCl_4 [31]. With these conditions in mind, given 10^{10} photons per pulse achievable for the monochromatic mode of the LCLS [213], the number of useful photons per pulse detected (see Table 1), i.e. once the loss factors have been included, is: 4×10^6 (TFY), 6×10^3 (Cu $K_{\alpha_{1,2}}$), 6.0×10^2 (Cu $K_{\beta_{1,3}}$) and 2.0×10^0 (Cu $K_{\beta_{2,5}}$).

Table 4.1: The number of X-ray photons (I^{Npho}) and the number (N_{shots}) of X-ray pulses (10^{10} photons per pulse) required to observe the transient $\Delta\chi$ associated with a normal pump-probe signal (signal) and to directly observe the wavepacket dynamics (WP). The photolysis yield f is assumed to be 10% throughout.

	Photons Out Per Pulse	$\Delta\chi$ (Signal)	I^{Npho} (N_{shots})	$\Delta\chi$ (WP)	I^{Npho} (N_{shots})
TFY XANES	4.0×10^6	0.60^1	3.0×10^4 (1)	0.01	1.0×10^8 (25)
TFY EXAFS	4.0×10^6	0.01	1.0×10^8 (25)	0.003	1.0×10^9 (250)
$K_{\alpha_{1,2}}$	6.0×10^3	0.10	1.0×10^6 (170)	-	-
$K_{\beta_{1,3}}$	6.0×10^2	0.20	2.5×10^5 (425)	0.007	2.0×10^8 (3.5×10^5)
$K_{\beta_{2,5}}$	2.0×10^0	0.40	6.3×10^4 (3.2×10^4)	0.050	4.0×10^6 (2.0×10^6)

In an experiment, provided that most of the electronic noise is suppressed, the detection sensitivity can be close to the shot-noise limit. This inherent noise is given as \sqrt{N} , where N is the signal, i.e. the number of photons detected. The signal to noise ratio is therefore given $SNR = N/\sqrt{N}$. Using these boundary conditions, Table 4.1 shows the number of X-ray photons, and consequently of X-ray pulses, required to measure with a $SNR=10$ for i) a transient X-ray spectroscopic signal and ii) the wavepacket dynamics. The number of X-ray

photons (I^{Npho}) required to measure a given signal scales as [31]:

$$I^{Npho} \propto \left[\frac{SNR}{f \cdot \Delta\chi} \right]^2 \quad (4.3)$$

where $\Delta\chi$ is the signal change and f is the photolysis yield assumed to be 10% throughout. $I_0=10^{10}$ is the incoming X-ray intensity (number of photons per pulse), the loss factor (L) and the fraction of absorbed photons (μ_A), we can use Equation 4.3 to estimate the number of X-ray pulses (N_{shots}) required with:

$$N_{shots} = \frac{I^{Npho}}{I_0 \cdot \mu_A \cdot L} \quad (4.4)$$

Using Equations 4.3 and 4.4, Table 4.1 shows that to record a transient signal pump-probe using TFY XANES or TFY EXAFS requires $\sim 3.0 \times 10^4$ and $\sim 1.0 \times 10^8$ photons, respectively. Given that the number of detected photons/pulse detected is 4×10^6 , this makes it plausible for each data point of TFY XANES to be recorded with a SNR=10 within a single X-FEL pulse. TFY EXAFS requires ~ 25 X-ray pulses, however, this still means that each data point can be collected with < 1 s of acquisition time (assuming a 100 Hz repetition rate). In contrast, due to smaller $\Delta\chi$ associated with resolving the spectral fluctuations of wavepacket dynamics a larger number of photons is required. Indeed, to achieve a SNR=10, for TFY XANES and TFY EXAFS each data point would be expected to require ~ 25 and ~ 250 X-ray pulses, respectively. Importantly, this is still achievable within a reasonable data acquisition time (~ 4 s per data point).

Table 4.1 also shows the number of photons required to achieve a transient signal, for $K_{\alpha_{1,2}}$, $K_{\beta_{1,3}}$ and $K_{\beta_{2,5}}$ XES. While these photon hungry techniques are difficult to implement in a time-resolved manner at 3rd generation synchrotrons [206, 212], the increased photon flux associated with the X-FELs makes these feasible in the sub-ps regime. Indeed, in the hardest case, $K_{\beta_{2,5}}$ XES, it is expected that $\sim 3.2 \times 10^4$ X-ray pulses per data point is required. Given the repetition rate of X-FELs (~ 100 Hz), this would require acquisition times of ~ 10 -20 mins per data point. For these experiments the potentially high X-ray fluency and repetition rate of the European X-FEL could make such measurements significantly easier [214]. However, Table 1 shows that while measuring the transient signal is possible even for $K_{\beta_{2,5}}$ XES, the number of X-ray pulses, $\sim 10^{5-6}$ required to achieve sufficient SNR to observe the wavepacket dynamics with these spectroscopies makes them completely unfeasible (~ 6 hours per data point at 100 Hz).

4.4 Conclusions

Ultrafast time-resolved linear and non-linear optical spectroscopies have a strong history of providing important insight into photoexcited dynamics within the femtosecond regime. Owing to the development of the X-FELs, these dynamics can now also be observed in

the short-wavelength regime and provide direct snapshots of interatomic distances and changes in the geometry and charge distribution of molecules. These techniques hold great promise of yielding important new insight into fundamental dynamical processes such as vibrational excitation, bond formation and breaking, relaxation, and time-dependent solvation processes.

In this work we have used wavepacket dynamics simulations to predict femtosecond EXAFS, pre-edge XANES, $K_{\alpha_{1,2}}$, $K_{\beta_{1,3}}$ and $K_{\beta_{2,5}}$ XES spectra. These have demonstrated that for the present system, femtosecond pre-edge XANES, EXAFS, $K_{\beta_{1,3}}$ and $K_{\beta_{2,5}}$ XES spectra all reveal information about the wavepacket dynamics. However using realistic experimental parameters, while it will be possible to record a signal capturing the strongest transient changes for all of the spectroscopies studies herein, we have demonstrated that the wavepacket dynamics can only be observed experimentally within realistic acquisition times for XANES and EXAFS, as the small cross section associated with $K_{\beta_{1,3}}$ and $K_{\beta_{2,5}}$ XES makes the number of photons required unfeasible.

Importantly, in terms of a general feasibility, the transient signals for the present case $[\text{Cu}(\text{dmp})_2]^+$ are dominated by an oxidation shift associated with the charge transfer of an electron from the metal to the ligands upon excitation. As this has no correspondence with the wavepacket dynamics, the changes associated with these vibrational coherences will be a small change on top of the large underlying transient of the edge shift. This means that resolving the wavepacket dynamics for the present system represents a challenging case and, given that, it remains possible, holds significant promise for future experiments in this field. It should be stressed that as the main features in the transient spectrum and the vibrational dynamics are unrelated, the energy region most sensitive to the wavepacket dynamics does not necessarily correspond to the largest changes in the transient spectrum, as shown in Figs. 4.4-4.7, making it important to record the whole spectrum at each time-delay and not just a time scan at one particular energy. For other cases, such as $[\text{Fe}(\text{bpy})_3]^{2+}$ [181, 27, 215, 216, 206], determining the wavepacket dynamics is expected to be easier. In this case, the transient spectrum is not dominated by a feature unrelated to the vibrational coherences. Instead, here the wavepacket dynamics reported by Chergui and co-workers [217] occurs along this Fe-N coordinate, which is also responsible for the principle transient changes in the Fe K-edge XAS spectrum. In this case the wavepacket dynamics would, therefore, be expected to yield larger changes making observing these dynamics easier. This highlights the strong emphasis that should be placed upon fully understanding the dominant contributions to a transient signal at longer times (i.e. using a 3rd generation synchrotrons) before determining if a particular experiment is possible.

5 TSH within QM/MM: a study of the dynamical solvent effects

The non-adiabatic relaxation processes of $[\text{Cu}(\text{dmp})_2]^+$ (dmp = 2,9-dimethyl-1,10-phenanthroline) can also be investigated by using a classical trajectory approach, such as Trajectory Surface Hopping (TSH). In contrast with quantum wavepacket dynamics methods, notably MCTDH, that are based on the reduction of the configuration space through PES-fitting, TSH samples the whole configurational space of the system of interest. In addition, due to a long tradition in the development of ground state classical trajectory dynamics methods, TSH can be easily coupled to the environment using a QM/MM scheme, which describes explicitly the interaction with the solvent. In this chapter, TSH non-adiabatic dynamics is applied to the study of the photophysics of $[\text{Cu}(\text{dmp})_2]^+$, the same system that was previously investigated using the wavepacket dynamics approach (MCTDH dynamics in Chapter 3). This offers the opportunity for an accurate comparison between the two approaches (wavepacket versus trajectory-based) providing important insights about their respective strengths and weaknesses. In addition, this study allows us to compare the nature of the collective modes activated during the TSH dynamics with the normal mode selected for the MCTDH dynamics. Our aim is to complement and generalize the method for the choice of the collective modes used in the wavepacket dynamics by means of a systematic analysis of the TSH trajectories.

5.1 Introduction

As illustrated in Chapters 2 and 3, quantum nuclear wavepacket approaches [110, 56] are based on the time-evolution of a nuclear wavepacket evolving on electronic potential energy surfaces computed *a priori* in a subspace of the complete multidimensional configuration space of the system. The choice of the collective coordinates spanning this subspace can be deduced based on symmetry and physical considerations (see Subsection 2.2.2 and Section 3.2). However, the selection of these variables, in general, relies on empirical *trial and error* approaches, which do not give any guarantee on the quality of the selected configuration space. This can, in principle, lead to severe deficiencies in the dynamics. In addition, in

quantum dynamics methods, solvent is usually treated at the level of a harmonic bath modeled by an ensemble of harmonic oscillators [218, 219]. While this description is in many cases adequate, in others the details of the solute-solvent interaction (hydrogen bonds in particular) [88, 220] is such that a more accurate atomistic representation of the solvent is required.

Classical trajectories non-adiabatic molecular dynamics offer an interesting alternative for the description of the out-of-equilibrium time evolution of the photoexcited system. Notably, the Trajectory Surface Hopping (TSH) [131] approach has met increasing interest in the past years, especially in the Tully scheme flavor [132]. Briefly, in TSH the nuclear wavepacket is replaced with a swarm of classical trajectories, which are free to evolve in the fully unconstrained configuration space of the system. The electronic properties of the system are computed *on-the-fly* at each time step while quantum effects are taken into account through the evaluation of the state amplitudes allowing the system to hop among PESs. Moreover, this method can easily be combined with a QM/MM scheme [25], which treats explicitly the solute/solvent interactions [221]. Despite the mentioned advantages of TSH, there is also a price to pay. In fact, in order to reach statistical convergence a very large number of trajectories is required (in the order of 10^3) limiting, therefore, the applicability of this approach to relatively small molecular systems (with no more than a couple of hundreds of atoms). Furthermore quantum effects, such as quantum decoherence, cannot be captured due to the classical description of the nuclear dynamics and to the fact that the trajectories are not interacting with each others.

The ability of TSH simulations to sample the full-configuration space can also be used to determine the important normal modes that are activated during the dynamics, guiding in this way the selection of degrees of freedom for the model Hamiltonian used in MCTDH quantum dynamics simulations (Chapter 3). To this purpose, principal component analysis (PCA) can be adopted to identify the main vibrational modes of $[\text{Cu}(\text{dmp})_2]^+$ activated during the first few hundreds of femtoseconds following the photoexcitation. This analysis provides important information about the nature of these collective variables and allows us to validate and improve the selection of normal modes used in the MCTDH simulations.

In addition, the combination of the TSH dynamics with the QM/MM scheme allows the investigation of the role played by the solvent during the relaxation process that follows photoexcitation. In particular, we want to explore and elucidate the reasons for the extremely low quantum yield exhibited by Cu(I)-phenanthroline complexes in different solvents. As described in Chapter 1, the quantum yield for $[\text{Cu}(\text{dmp})_2]^+$ in strong donor solvents, such as acetonitrile (MeCN), is $\sim 10^{-4}$ [65, 222], meaning that among 1000 absorbed photons only one is emitted while the rest of the energy is converted into heat and released to the solvent. Understanding the origin of the non-radiative decay mechanisms and exploring new strategies to improve the quantum yield are of prime importance for the design of more efficient dyes for solar energy conversion as well as light-driven catalysis [83].

5.2 Computational details

Non-adiabatic dynamics was performed using the LR-TDDFT-based TSH scheme as implemented in the CPMD code [59, 223]. Electronic states were computed using the PBE exchange and correlation functional [224] and the electronic wavefunction was represented by a plane wave basis set with a cut-off of 85 Ry. Martin-Trouiller pseudopotentials [225] with DCACP corrections to account for the dispersion interactions [226, 227], were used to describe the effects of the core-electrons. For each TSH trajectory, the initial frame was chosen randomly from a ground state Born-Oppenheimer (BO) Molecular Dynamics simulation equilibrated at room temperature (300K) using a Nose-Hoover thermostat [228, 229]. The initial electronic excited state, used to start the TSH dynamics, was selected as the one with the largest oscillator strengths among all the states with energies in the range between 1.5 and 2.6 eV. This energy range was selected according to experimental absorption studies [79, 99], which identify the optical bright $^1\text{MLCT}$ state around 2.6 eV. The non-adiabatic dynamics were carried out with a time step of 5 atomic units (~ 0.12 fs). Nine trajectories were run using the classical TSH algorithm, according to which only transitions between states of the same spin multiplicity (internal conversion) can be described. In our case, since the trajectories were initiated on a photoexcited singlet state, only non-adiabatic transitions between singlet excited states were possible. In order to evaluate ISC probabilities, spin-orbit coupling elements, and Landau-Zener probabilities were calculated at the crossing points between the actual force state (singlet) and all energetically close triplet states (the force state is defined as the electronic state in TSH from which the nuclear forces are derived). To monitor their time evolution, in some cases SOCs were also evaluated along the entire trajectory with a frequency of 1 fs^{-1} . For comparative purposes, one extra trajectory was propagated using the recently implemented TSH/ISC scheme [142], which allows for the *on-the-fly* calculation of the SOCs and corresponding Landau-Zener transition probabilities between states with different spin multiplicities. All molecular dynamics simulations (BO and TSH) were performed within the QM/MM scheme [230] where the $[\text{Cu}(\text{dmp})_2]^+$ complex was described at DFT/TDDFT level while the solvent (acetonitrile) was treated classically with the Amber force field [231]. The electrostatic and van der Waals interactions between the quantum and the classical subsystems were explicitly included as described in [146].

5.3 Trajectory Surface Hopping

Fig. 5.1 shows the singlet running state (red) plotted together with the singlet (blue) and triplet (gray) states energy profiles for three trajectories simulated with the ‘standard’ TSH algorithm as implemented in CPMD [59, 232], which only described non-adiabatic transitions between states with equal spin-multiplicity (singlet states in this case). Upon photoexcitation, all trajectories relax quickly (within 100 fs) into the lowest singlet excited state S_1 , converting potential energy into kinetic energy. This fast relaxation process is made possible by the occurrence of a large number of surface hops within the singlet states manifold (from 5 to 3 hops). Due to the fact that the initial adiabatic electronic state has been selected according

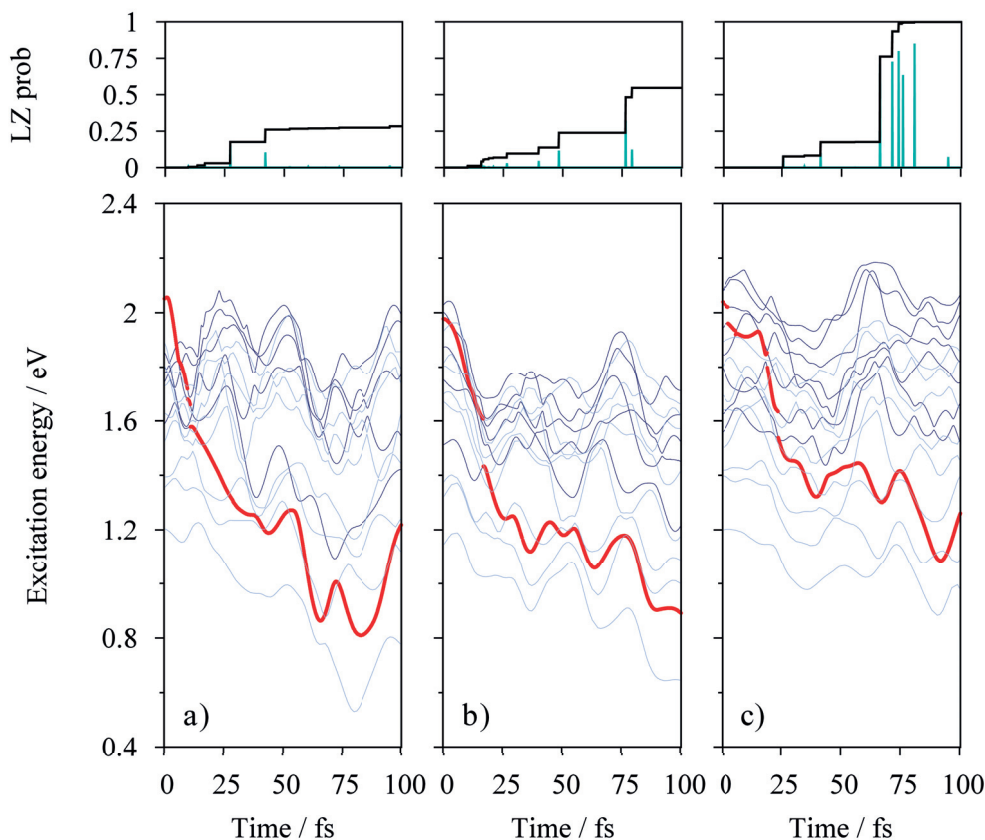


Figure 5.1: Three standard TSH trajectories, with triplet states computed at the end of the dynamics each ~ 1 fs. Color code: singlet states (blue), triplet states (cyan), running state (red). *Top*) Landau-Zener probability (green) and cumulative probability (black) of ISC.

to the value of its oscillator strength, the trajectories are mainly initiated on different states. For the three examples illustrated in Fig. 5.1 these are the S_6 , S_4 , and S_6 adiabatic states, respectively. Table 5.2 reports the initial electronic states for all the nine trajectories. Since the ‘standard’ TSH scheme does not account for transitions between states of different multiplicity, intersystem crossing probabilities were estimated, *a posteriori*, at the crossing points between singlet and triplet states by using the Landau-Zener formula defined in Subsection 2.3.3. The cumulative probability, P , for an ISC event between a singlet and a triplet state to occur along an entire trajectory is computed as

$$P = p_1 + \sum_{i=2}^N p_i \prod_{j=1}^{i-1} (1 - p_j), \quad (5.1)$$

where the indexes i and j run over the number N of crossings between the force state (a singlet) and the manifold of energetically close triplet states. For the three trajectories shown in Fig. 5.1 P corresponds to 28.42 %, 54.73 % and 99.93 %, respectively. The complete set of values of cumulative ISC probabilities is reported in Table 5.2. From this analysis,

we observed that the average cumulative probability is about 53 %, meaning that more than half of the trajectories would undergo at least one ISC event during the first 100 fs of dynamics. The upper panels of Fig. 5.1, shows the Landau-Zener probability for the three plotted trajectories (green lines) together with the cumulative ISC probabilities (black lines).

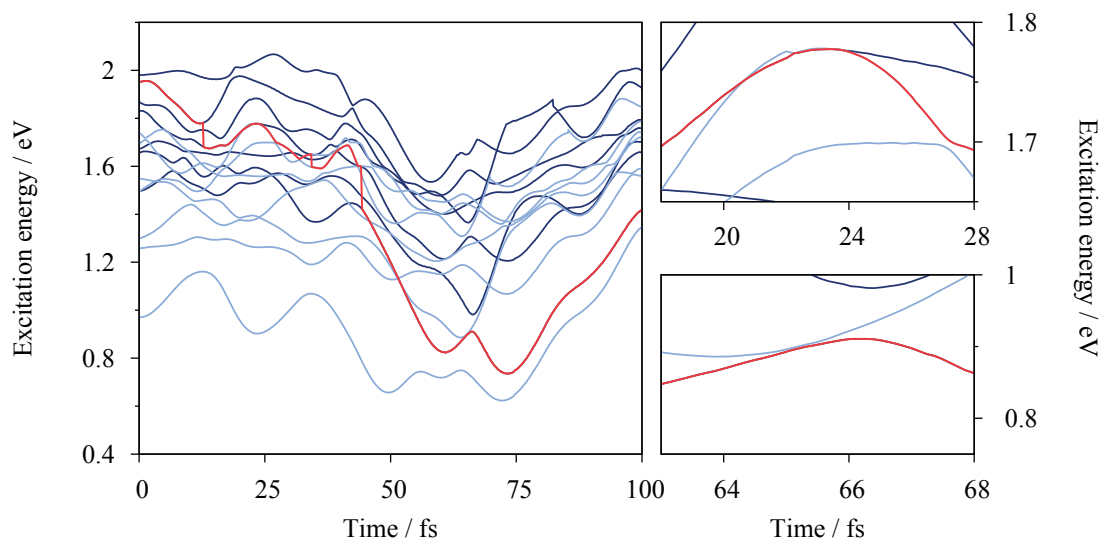


Figure 5.2: TSH/ISC trajectory. Color code: singlet states (blue), triplet states (cyan), running state (red). *Right* Zoom of the trajectory: top) a ISC event, bottom) avoided crossing.

A single trajectory, shown in Fig. 5.2, was carried out using the extended (and computationally more expensive) TSH/ISC scheme [142], which computes *on-the-fly* singlet and triplet excited state energies, spin-orbit couplings between the force state and the two energetically closest electronic states with different spin multiplicity, non-adiabatic Tully's probabilities (for IC events), and Landau-Zener probabilities (for ISC events). Starting from the photoexcited S_6 state, the system relaxes within 100 fs to the lowest excited state S_1 in a series of hops that involve both interlying singlet and triplet states. Notably, at around 13 fs of dynamics, the trajectory first switches into S_4 , followed after 10 fs by an ISC into T_8 (right top zoom in Fig. 5.2) and a subsequent IC into the lower lying triplet state T_7 . Another ISC event occurs at 40 fs, which brings back the system into the manifold of singlet states where the relaxation proceeds, through several further surface hops, until S_1 is reached. At around 65 fs, the force state (S_1) approaches T_2 , however without crossing it (right bottom zoom in Fig. 5.2). Interestingly, in the last 30 fs of dynamics the force state (S_1) and the closest triplet state (T_1) proceed almost in parallel. This is in agreement with static calculations, which show that the lowest singlet and triplet states in $[\text{Cu}(\text{dmp})_2]^+$, at the optimized triplet geometry, have the same character [100] and similar PESs topologies (see cuts of the PESs obtained for the vibronic coupling Hamiltonian illustrated in Chapter 2, Fig. 3.1). Despite this, molecular distortions induced by the relaxation process (which converts roughly 1 eV of photon energy into thermal energy) and by the interaction with the solvent will potentially generate favorable ISC events between S_1 and T_1 in the longer time scale.

5.3.1 Analysis of the electronic state character during the photoexcited dynamics

The analysis of the electronic character of the different states involved in this dynamics allows us to compare in detail the TSH results with the ones obtained using the MCTDH approach. This analysis is hampered by the fact that in the adiabatic representation of the PESs, the electronic character of a given state (numbered according to its energy) can change along the dynamics. On the other end, since the MCTDH dynamics is performed in the diabatic picture, the character of the states is well defined along the entire dynamics.

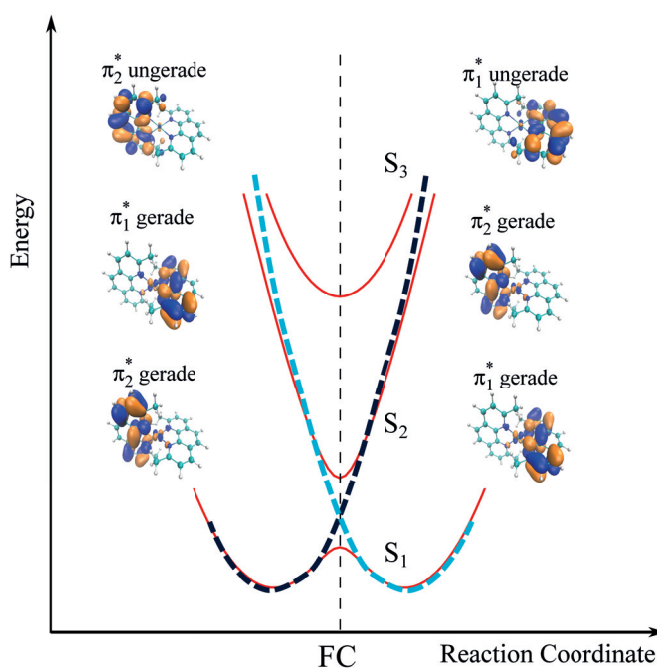


Figure 5.3: Adiabatic singlet potential energy surfaces (solid red lines) along the normal mode ν_{21} as described in Chapter 3. Close to the Frank-Condon region (FC) the excited states have a character arising from mixing of electronic configurations. The ligand-center Π^* antibonding orbitals, discussed in the main text, are shown on the left and right sides. A graphical representation of possible diabatic potential energy surfaces is added with dashed lines.

Fig. 5.3 shows a sketch of the adiabatic and diabatic states along one of the modes selected in the MCTDH dynamics, namely ν_{21} . The solid lines are the adiabatic potential energy lines obtained from single point calculations performed along ν_{21} . In correspondence with the FC structure, the adiabatic photoexcited singlet state, i.e. S_3 has a mixed character derived from the promotion of an electron from the degenerate HOMO (d_{xz}) and HOMO-1 (d_{yz}) orbitals, centered on the central copper atom, to the two degenerate π^* -gerade orbitals, represented in Fig. 3.2 and here indicated, respectively, as π_{g+}^* and π_{g-}^* . Each of these π^* -gerade orbitals is delocalized on both the ligands and their contribution, at the FC geometry, is (almost) the same. As in the case of S_3 , the lowest singlet states, S_1 and S_2 , are obtained from mixed

configurations arising from the photoexcitation of d_{xz} and d_{yz} electrons into the π_{g+}^* and π_{g-}^* orbitals. At the excited state geometry, the character of these lowest singlet adiabatic states changes due to the flattening of the structure. As a result, each state acquires a unique character, that can still be described by the same molecular orbitals. Notably, the lowest singlet state, S_1 , generates from the excitation of an electron from d_{xz} to π_{g+}^* . The same considerations can be used for the other states. It is worth mentioning that S_3 has $d_{xz} \rightarrow \pi_{u+}^*$, where π_{u+}^* is a higher energy π^* molecular orbital with *ungerade* symmetry. Since the system can flatten symmetrically in two opposite directions, the corresponding degenerate configuration gives rise to the equivalent, symmetric transitions where the HOMO is now d_{yz} and the excitations are described by the transitions $d_{yz} \rightarrow \pi_{g-}^*$, $d_{yz} \rightarrow \pi_{g+}^*$ and $d_{yz} \rightarrow \pi_{u-}^*$.

Moving along the normal coordinates, the molecular orbital symmetry breaks and the character of the adiabatic states changes. In particular, moving to the left or the right of the FC point along the collective coordinate ν_{21} , Fig. 5.3, we observe a different localization of the Π^* electron on different ligands. Such delocalization arises from the fact that ν_{21} is a rocking mode and thus, central symmetry is not conserved. To further clarify this observation, we perform a characterization of the first three singlet excited states at the minimum of the S_1 potential energy line along the ν_{21} coordinate, which is located to the right of the FC point (see Fig. 5.3). As reported in Tab. 5.1, the adiabatic states are characterized by excitations from the HOMO (d_{xz}) orbital to the Π^* antibonding orbitals on the ligands. S_1 has a $d_{xz} \rightarrow \pi_{1g}^*$ character, where π_{1g}^* is the π^* -*gerade* orbital centered on one of the two ligands, which here we indicate with the index 1, S_2 has a $d_{xz} \rightarrow \pi_{2g}^*$ character, with π_{2g}^* the π^* -*gerade* orbital centered on the opposite ligand, labeled with 2, and finally S_3 has a $d_{xz} \rightarrow \pi_{1u}^*$ character, where π_{1u}^* is the π^* -*ungerade* orbital centered on ligand 1. As for the excited state geometry, also for the normal mode ν_{21} , which is symmetric respect to the FC geometry, symmetry considerations about the character of the electronic states are valid. Therefore, at the opposite minimum at the left side of Fig.5.3, the adiabatic electronic states have the following characters: $d_{yz} \rightarrow \pi_{2g}^*$, $d_{yz} \rightarrow \pi_{1g}^*$ and $d_{yz} \rightarrow \pi_{2u}^*$.

Table 5.1: Energy and character of the first singlet and triplet electronic excited state at the B3LYP optimized Frank-Condon (FC) (Data from Chapter 3) triplet excited state (Ex.) geometries and minimum of mode ν_{21} .

	FC geometry		Ex.geometry		Minimum ν_{21}	
	Energy (eV)	Character	Energy (eV)	Character	Energy (eV)	Character
S_1	2.44	$d_{xz} \rightarrow \pi_{g+}^*$, $d_{yz} \rightarrow \pi_{g-}^*$	1.88	$d_{xz} \rightarrow \pi_{g+}^*$	2.24	$d_{xz} \rightarrow \pi_{1g}^*$
S_2	2.51	$d_{yz} \rightarrow \pi_{g+}^*$, $d_{xz} \rightarrow \pi_{g-}^*$	1.91	$d_{xz} \rightarrow \pi_{g-}^*$	2.63	$d_{xz} \rightarrow \pi_{2g}^*$
S_3	2.70	$d_{xz} \rightarrow \pi_{g+}^*$, $d_{yz} \rightarrow \pi_{g-}^*$	2.25	$d_{xz} \rightarrow \pi_{u+}^*$	2.71	$d_{xz} \rightarrow \pi_{1u}^*$

The localization of the electronic charge on a Π^* antibonding orbitals localized on a single ligand, is not promoted only by non-centro symmetric vibrations, such as ν_{21} , but also by the solvent reorganization around the photoexcited complex, which can select and stabilize a particular ligand-center orbital [233, 234].

Summarizing, in the diabatic representation each electronic state preserves its own character along the collective coordinate and different diabatic states cross at the FC configuration (dotted lines in Fig. 5.3). The mixed character of the adiabatic states at the FC is therefore reflected in a crossing of different states in the diabatic picture. In the same way, IC processes, which in the adiabatic picture are described by the transfer of wavepacket population (or trajectories in the TSH framework) from S_3 to S_2 and S_1 due to non-adiabatic couplings, translate in the diabatic picture into the relaxation of the nuclear wavepacket along a single diabatic PES that preserve the orbital symmetry.

We now proceed to the analysis of the time evolution of the electronic state characters obtained from the TSH dynamics. As mentioned in Section 5.2, the dynamics is initiated from the singlet state with the largest oscillator strength in the range between 1.5 and 2.5 eV. Due to the conformational distortions induced by the thermal energy, we, therefore, do not expect the initial excited state to correspond exactly to the S_3 state obtained from the optimized static calculations. In particular, the electronic states selected to initialize the 10 trajectories computed in this work lie all between the 4th and the 7th singlet electronic states. The different position of the bright state within the sequence of excited singlet states is a consequence of the high density of states in this interval of energies (from 1.5 to 2.6 eV), which favors state crossings through configurational distortions induced by thermal fluctuations and by interaction with the solvent molecules. In order to compare the two methodologies, we have evaluated and analyzed the character of the force state along the trajectories with a time interval of about 10 fs. Fig. 5.4 reports the character of the different electronic configurations (with the percentages of the different contributing molecular orbitals) for the three trajectories described in Fig. 5.1: triangles refer to transitions from the HOMO manifold (*d* metal-type orbitals) to the π^* orbitals centered on ligand 1, and circles to the π^* orbitals centered on ligand 2. Full (empty) symbols indicate *gerade* (*ungerade*) symmetries, respectively. At $t=0$ fs, most of the trajectories exhibit a mixed character, with the electron delocalized on both ligands. As in the case of transitions computed at the optimized FC geometry, the transitions involve orbitals with *gerade* symmetry. During the relaxation along the singlet states mediated by a series of ICs, the electronic character purifies to a single configuration with the π^* -*gerade* character localized on one of the two ligands. In the diabatic picture, this corresponds to a descent along a well defined diabatic state characterized by the same type of transition. However, it is important to mention that the character of the final state does not always correspond to the predominant state character at $t=0$ fs. This discrepancy is ascribed to the rearrangement of the solvent structure during the first part of the dynamics. Before excitation the solvent structure is optimized for the stabilization of the ground state electronic structure; after photoexcitation the electron is injected into a linear combination of Π^* molecular orbitals localized on both ligands and it is mainly through to solvent fluctuations that localization on one of the two ligands is induced [234, 25]. However, once this selection is done, the electron hops from one ligand to the other become increasingly less probable due to solvent stabilization.

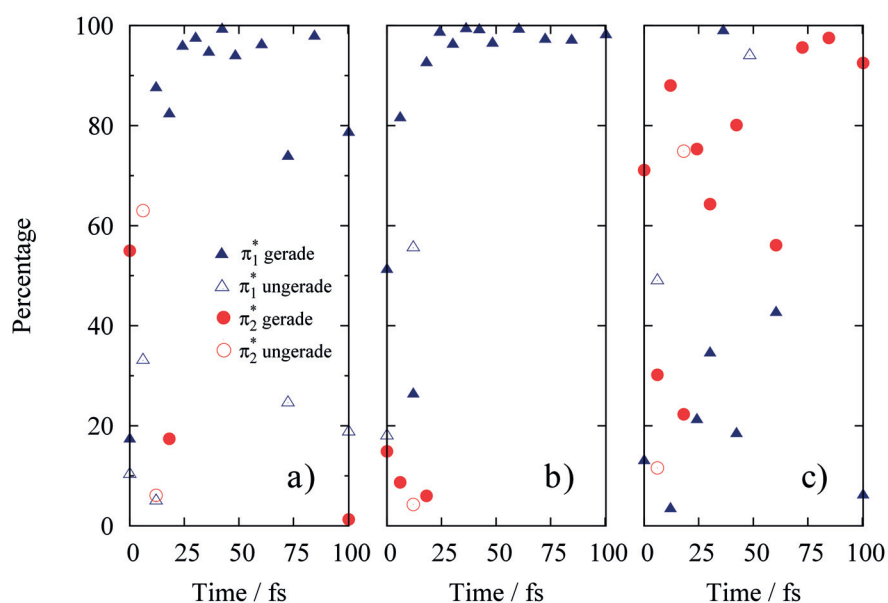


Figure 5.4: Percentage of the electronic configurations of the running singlet state for three trajectories. Triangles represent transitions from the HOMO manifold (d metal-type orbitals) to the π^* orbitals centered on ligand 1, the circles to the π^* orbitals centered on ligand 2. Full and empty dots indicate, respectively, *gerade* and *ungerade* symmetry.

5.3.2 Photophysics of $[\text{Cu}(\text{dmp})_2]^+$: Internal Conversion and Intersystem Crossing dynamics

In this section, we aim at combining the information obtained from the two different, but also complementary, approaches (MCTDH and TSH) that we have used to investigate the photophysics of the Cu(I)-phenanthroline complexes in solution.

Effects of the selection of the xc-functional. A word of caution is order: in comparing the two quantum dynamics approaches we have also to take into account the differences in the level of accuracy applied to the PESs used for the MCTDH and the TSH dynamics. While in MCTDH the required PESs are interpolated along a reduced number of collective vibrational modes, in TSH one needs to compute *on-the-fly* the energies, forces, and couplings at each time step. This implies a very different computational load for the two approaches: for the MCTDH dynamics one can afford the calculation of the excited state electronic properties using hybrid functionals (in our case B3LYP), while for TSH we are forced, because of computational reasons, to select semi-local functionals from the GGA family (PBE in this case). However, for this specific system, the performances of PBE (as well as BLYP) and the hybrid B3LYP are very similar, allowing us to compare directly the results obtained using these two different approximations for the xc functionals. The main difference observed when using GGA functionals is a slight decrease of the energy of the electronic excited states and the energy gaps between them, while keeping the curvatures, and therefore the

forces, almost unchanged. Importantly, the order of the adiabatic states and their electronic character is the same for calculations performed with GGA and hybrid functionals. These differences affect the overall TSH dynamics in two ways. First, due to the underestimation of the states energies, the absorption spectra is usually red shifted. As a consequence, the TSH dynamics using the PBE functional starts at lower energies than in the actual real case, and therefore the initial potential energy of the photoexcited system will be underestimated. Assuming conservation of the total energy, we expect therefore a slower dynamics and longer relaxation times. Second, the small relative shifts between the different PESs observed when comparing PBE with B3LYP calculations will also affect the energy gaps between the states leading to a slightly different transitions probabilities for the state populations (in MCTDH) and the classical trajectories (in TSH).

In conclusion, although the use of GGA functional may overestimate the probability of hops, these effects are small and do not change the physics of the system, as demonstrated by the good agreement between TSH and MCTDH results.

MCTDH/B3LYP sv. TSH/PBE. Summarizing the results obtained with MCTDH, we found an ultrafast IC (in less than 100 fs) that takes part from the initially photoexcited singlet state S_3 to the lowest S_2 and S_1 states; only at this stage we observe sizable ISC-mediated population transferred into the triplet manifold. Due to the strength of the spin-orbit couplings and to the fact that the S_1 , T_2 and T_3 states are almost degenerate in energy, the ISC occurs on a relatively fast time scale (in the sub-picosecond regime). The MCTDH results are in good agreement with previous experimental studies [79, 96]. These also suggest the presence of an additional, slower, time component (with a lifetime of ca.10-20 ps), which, however, cannot be captured by MCTDH since the dynamics is restrained to just the first few ps following photoexcitation.

In TSH, the state population of a given PES (i.e. S_i) is represented by the number of trajectories that at a given time t are driven by the forces computed from that surface (S_i). In the previous subsection, we analyzed the character of the force singlet state of all the trajectories performed using the standard TSH approach that allows just for IC transitions. Within the first 100 fs of dynamics, the initial electronic configuration, that is characterized by a metal-to-ligand-charge-transfer (MLCT) state with one extra electron delocalized over both ligands, evolves towards a new configuration in which the photoelectron becomes mainly localized on a single ligand. This occurs through an ultrafast reorganization of the dipoles of the solvent (without requiring diffusion), which induces a stabilization of the extra electronic charge in the ligand system. The same behaviour was already observed in the case of a Ru(II)-*tris*-bipyridine complex in water, which was extensively studied in Refs. [233, 234]. The final state reached after relaxation along the singlet states manifold corresponds to the lowest adiabatic state S_1 , characterized by the excitation of an electron from a metal d-orbital to a π^* -*gerade* orbital of a single ligand (see also Table 5.2). To summarize, the first ~ 100 fs of dynamics that follows the photoexcitation of complex is characterized, in agreement with

MCTDH, by a MLCT transition followed by a solvent mediated localization of the excited electron on one ligand. This process occurs in concert with the relaxation of the system along a diabatic state (see Fig. 5.3, dashed lines), which is made possible by a series of IC events. We, therefore, do not observe any sign of thermalization within the local minima of the adiabatic PES cuts along the vibrational modes (see Fig. 5.3, solid lines).

Table 5.2: Numbering of the initial (0 fs) and final (100 fs) force singlet states, count of the ISC events, and corresponding cumulative ISC probability (in 100 fs of dynamics) for the nine trajectories carried out with the TSH algorithm. The ISC probabilities are computed *a posteriori* using the Landau-Zener formula

	Force state		no. Crossing points	Cumul. Prob. ISC
	t=0 fs	t=100fs		
a	S ₆	S ₁	10	28.42 %
b	S ₄	S ₁	14	54.73 %
c	S ₆	S ₁	11	99.93 %
d	S ₆	S ₁	14	36.02 %
e	S ₇	S ₁	6	4.30 %
f	S ₇	S ₁	20	98.60 %
g	S ₇	S ₁	15	12.16 %
h	S ₄	S ₁	9	97.56 %
i	S ₇	S ₁	11	46.39 %

The evaluation of an ISC rate is unfortunately not directly accessible using our TSH dynamics scheme since only a single trajectory was computed using the TSH/ISC method, which calculates SOC and LZ probability *on-the-fly*. However, it is possible to make some interesting considerations by further analyzing the trajectories calculated using the standard TSH scheme. As pointed out in the analysis of the MCTDH dynamics, singlet-to-triplet population transfer occurs already during the first sub-picosecond dynamics following photoexcitation. Our TSH trajectories also show multiple crossings between the singlet state that drive the dynamics (the force state) and the manifold of triplet states, from a minimum of six up to twenty (Table 5.2) in about 100 fs. The cumulative probability for ISC evaluated using the LZ formula amounts to more than 90% for three of the nine analyzed trajectories with an average cumulative probability of 53% for the entire ensemble. This means that about half of the trajectories would undergo at least one ISC event during the first 100 fs of dynamics. However, we also note large differences among the different trajectories: three have a cumulative probability smaller than 30%, and one does not make to 5%. The variety of the values of the cumulative probability depends on several factors: i) the number of crossings in the interval of time investigated, ii) the size of the spin-orbit coupling matrix element, and iii) the relative slopes of the PES (single and triplet) at the crossing point. In fact, as described in Section 2.3.3, the Landau-Zener probability is evaluated from the ratio between the SOC matrix element for the two states involved and the absolute value of the energy gap between the same states. In the case of MLCT states, SOCs between singlet and triplet states are in

general large when both transitions (singlet and triplet) involve electron excitations from the same metal d orbital to a different π^* orbital on the ligand system (see Table 5.3), small when they involve different metal d orbitals the equal ligand π^* orbitals, and zero when both transitions involve orbitals with the same characters [13]. As shown in Table 5.3, the largest SOC values occurs when the acceptor π^* -orbitals corresponding to the singlet and triplet transitions are localized on different ligands. For the same reason, no crossings are observed between S_1 and T_1 , since these two states have the same electronic character and the corresponding PES run almost parallel. This is fully consistent with what observed in the MCTDH dynamics. On the other hand, the ISC probabilities between high energy singlet and triplet states may become very large. This allows the occurrence of multiple ISC events along the same trajectories, allowing the system to hop forth and back several times between different singlet and triplet states. Therefore, cumulative probability should be considered as an overestimation of the total effective ISC probability, since in this calculation we do not consider events of higher order that involve back transitions from triplets to singlets. The occurrence of this type of events is clearly shown in the case of trajectory obtained with the TSH/ISC method and shown in Fig. 5.2. In this case, we observe that after a first ISC to T_8 , the system relaxes into T_7 (through an IC) before undergoing another ISC back to a singlet state (S_3). This single trajectory well exemplifies the complexity of the photophysics of this class of metal-complexes, which shows a convoluted sequence of IC and ISC events during the first 100 fs of dynamics after photoexcitation.

Table 5.3: Crossings between singlet and triplet states along the trajectory (a) shown in Fig. 5.1.

Time (fs)	Singlet	Triplet	SOC (cm^{-1})	LZ prob.
9.67 (80)	S_4 (81% $d_{xz} \rightarrow \pi_{1u}^*$)	T_8 (62% $d_{yz} \rightarrow \pi_{2g}^*$)	36.72	0.4 %
13.54 (100)	S_1 (81% $d_{xz} \rightarrow \pi_{1g}^*$)	T_5 (63% $d_{xz} \rightarrow \pi_{1u}^*$)	58.76	1.1 %
16.69 (138)	S_1 (84% $d_{xz} \rightarrow \pi_{1g}^*$)	T_4 (73% $d_{xz} \rightarrow \pi_{1u}^*$)	41.86	1.5 %
27.33 (226)	S_1 (97% $d_{xz} \rightarrow \pi_{1g}^*$)	T_3 (63% $d_{xz} \rightarrow \pi_{2g}^*$)	177.89	15.0 %
42.09 (348)	S_1 (92% $d_{xz} \rightarrow \pi_{1g}^*$)	T_2 (41% $d_{xz} \rightarrow \pi_{2g}^*$) (24% $d_{xz} \rightarrow \pi_{1u}^*$)	114.82	10.4 %
52.37 (430)	S_1 (88% $d_{xz} \rightarrow \pi_{1g}^*$)	T_2 (79% $d_{xz} \rightarrow \pi_{1u}^*$)	36.72	0.8 %
60.11 (496)	S_1 (96% $d_{xz} \rightarrow \pi_{1g}^*$)	T_2 (68% $d_{xz} \rightarrow \pi_{1u}^*$)	28.26	0.4 %
67.37 (556)	S_1 (99% $d_{xz} \rightarrow \pi_{1g}^*$)	T_2 (73% $d_{xz} \rightarrow \pi_{1u}^*$)	18.89	0.1 %
73.17 (606)	S_1 (81% $d_{xz} \rightarrow \pi_{1g}^*$)	T_2 (68% $d_{xz} \rightarrow \pi_{1u}^*$)	32.80	0.4 %
95.06 (784)	S_1 (92% $d_{xz} \rightarrow \pi_{1g}^*$)	T_2 (69% $d_{xz} \rightarrow \pi_{1u}^*$)	31.79	1.4 %

5.3.3 Solvent effects on the dynamics of $[\text{Cu}(\text{dmp})_2]^+$

One of the goals of this study is to investigate if the explicit inclusion of the solvent, within the QM/MM coupling scheme, can help rationalize the extremely low quantum yield that characterizes these complexes. To this end, we studied the TSH dynamics of $[\text{Cu}(\text{dmp})_2]^+$ in

acetonitrile, which gives a luminescence quantum yields is 10^{-4} [222, 65]. This dynamics is compared to another simulation started from exactly the same initial conditions for the coordinates, velocities, and excited state character, but carried out in gas phase. Even though the dynamics is piecewise deterministic, the stochasticity of the surface hopping algorithm introduces randomness in the time evolution, therefore, making a direct comparison of the two trajectories (gas phase and liquid phase) less evident. However, a series of independent runs performed starting from different initial conditions confirmed the overall trends illustrated in Fig. 5.5 and that we will now discuss.

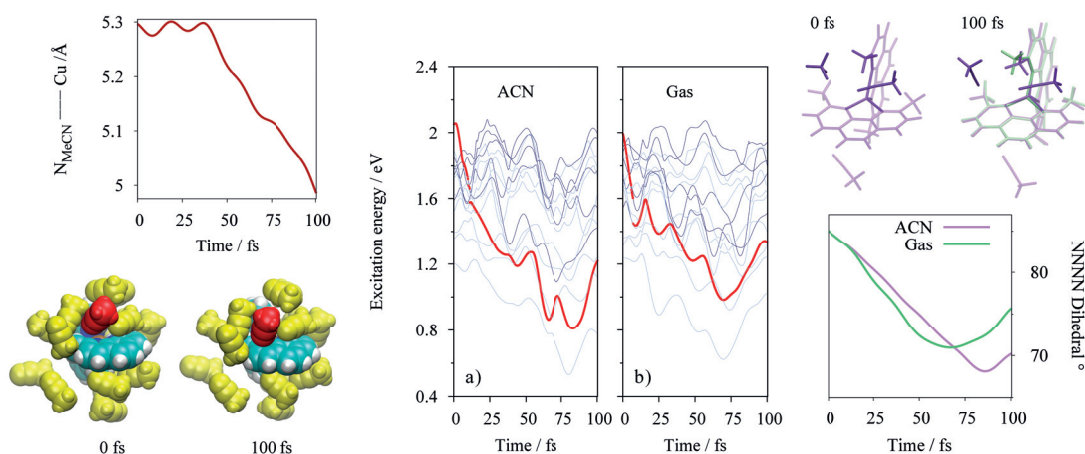


Figure 5.5: *Left-Top*) Distance between the N atom of a close by MeCN molecule (below, highlighted in red) and the central copper atom, as a function of the time. *Left-Bottom*) Solvent structure (yellow) around the complex (cyan, blue and orange) at 0 fs and after 100 fs of dynamics. *Center*) Comparison between a trajectory of $[\text{Cu}(\text{dmp})_2]^+$ in solution and in gas phase. *Right-Top*) Initial and final structures of $[\text{Cu}(\text{dmp})_2]^+$ in solution (violet) and in gas phase (green). *Right-Bottom*) Plot of the NNNN dihedral angle as a function of the time.

The comparison of the energy profiles obtained for the gas phase and liquid phase dynamics is shown in Fig. 5.5-center. For this particular set of initial conditions (but the picture is valid in general) we observe a faster relaxation process in MeCN, which brings the system closer to the ground state. For some other starting configurations we even observed a complete closure of the S_0 - S_1 energy gap in MeCN, while this phenomenon never occurred in the gas phase. Note that the closing of the gap increases the probability of the system to decay into the ground state through a non-radiative channel explaining, therefore, the smaller luminescence quantum yield observed in MeCN.

These effects can both be ascribed to the electrostatic effects induced by the solvent. Even at these ultrafast time scales (< 100 fs) the solvent can produce important stabilization effects through polarization and ultrafast librational relaxation. As in the case of other metal-complexes studied with similar molecular dynamics simulation techniques [233, 234], we also found in this complex an efficient and ultrafast solvent induced stabilization of the

photoexcited complex. In particular, during the relaxation dynamics, one of the MeCN solvent molecules in the first solvation shell of the Cu atoms undergoes a small amplitude rotation that brings its nitrogen atom (which carries a negative partial charge) closer to the metal ion (Fig. 5.5, left panel). The MLCT character of the electronic transition implies, in fact, an oxidation of the Cu atom, which acquires a larger positive charge. The overall effect is, therefore, the stabilization of the photoexcited complex, which relaxes faster and more efficiently towards the ground state (lower energies). It is worth mentioning that, despite the electrostatic attraction between the MeCN molecule and the Cu ion, we do not observe the formation of a real exciplex, as already pointed out in previous publications [88, 220] and discussed in Chapter 6. Finally, collisions between the solute and the solvent molecules can provide additional channels for the dissipation of the excess potential and kinetic energy in the photoexcited system. Looking closer at Fig. 5.5 (on the right panel) we observe that the two structures that were identical at $t=0$ fs become already noticeably different after 100 fs of the dynamics. In particular, the ligand that is reduced in the MLCT transition undergoes a different distortion in solution compared to the gas phase simulation. This is mainly due to collisions with the nearby solvent molecules; on its way to form stabilizing interactions with the metal center, the same MeCN molecule described above collides with the methyl group of the ligand which is therefore displaced into a new, less symmetric, arrangement. This distortion of the overall complex structure can be monitored following the time evolution of the improper dihedral formed by the 4 nitrogen atoms coordinated to the Cu ion (Fig. 5.5, bottom right). In the gas phase, after a fast decay starting at the ground state average value of about 90° the dihedral angle starts oscillating (in a harmonic fashion) around 75° . On the other hand, in solution due to the steric hindrance induced by the intercalating ligand, the angular drift is larger and in the longer time scale, it will induce a further flattening of the complex. This analysis clearly shows that, even at such short time scale, solvent molecules can induce geometric distortions in the complex following the driving force generated by the photoexcitation of the electronic structure.

5.4 Derivation of collective modes for MCTDH dynamics from TSH trajectories

As mentioned in the introduction, one of the advantages of using TSH dynamics is that it can sample the entire (unconstrained) configuration space of the system, without the need of imposing a subset of collective variables for quantum wavepacket dynamics. However, the price to pay is that in order to reach statistical convergence with TSH dynamics a large number of trajectories is needed (in the order of 10^3), making the method unsuited for the simulation of molecular systems with more than 100 atoms. Furthermore, quantum effects, such as decoherence, are not incorporated due to the classical description of the nuclei and to the fact that the trajectories are propagated independently (without coherence).

At present, the best way to investigate the photophysics of complex molecular systems by

5.4. Derivation of collective modes for MCTDH dynamics from TSH trajectories

means of simulations is to combine mixed quantum classical trajectory-based approaches (such as TSH dynamics) with the more accurate but constrained quantum wavepacket dynamics (such as MCTDH).

In this work, we will propose an approach for the automatic determination of the relevant collective variable used to model the MCTDH Hamiltonians by means of TSH simulations performed in the complete, unconstrained, configuration space. The method is based on the principal component analysis (PCA) of the TSH trajectories, which provides a set of collective modes ordered according to their relevance (weights) that can then be projected on the basis of normal modes. In this way, we can automatically select the modes to be used in the MCTDH dynamics.

5.4.1 PCA of the TSH trajectories

PCA is a technique [235, 236, 237], which allows one to identify correlation patterns in a data set of n elements in a d -dimensional space by diagonalizing its covariance matrix.

In molecular quantum dynamics, PCA is based on the diagonalization of the covariant matrix of the nuclear displacements

$$c_{ij} = \langle (R_i(t) - \langle R_i \rangle)(R_j(t) - \langle R_j \rangle) \rangle \quad (5.2)$$

where $R_i(t)$ is the i -th coordinate of the collective position vector $\mathbf{R}(t)$ in the molecular configuration space of dimension $3N_a$ (N_a is the number of atoms), and the parenthesis $\langle \rangle$ represent ensemble averages, which in the case of MD simulations are approximated with time averages. The covariance matrix \mathbf{C} with elements c_{ij} is a square matrix of dimension $3N_a$ and is symmetric with respect to the main diagonal, meaning that it has real eigenvalues and the eigenvectors are orthogonal to each other. The diagonalization of the covariant matrix

$$\mathbf{C}\mathbf{v}_i = \lambda_i \mathbf{v}_i, \quad (5.3)$$

leads a set of eigenvalues λ_i and eigenvectors \mathbf{v}_i ($i = 1, \dots, 3N_a$). Each eigenvalue corresponds to the mean square fluctuation along the corresponding eigenvector or principal component (PC), and describes its contribution to the total fluctuation. The eigenvectors are ordered such that their eigenvalues are in decreasing order, with the first one (the first principal component) corresponding to the largest displacement. By normalizing the sum of all eigenvalues to 1, we can define the number of eigenvalues i_m required to describe 90% of the total dynamics: $\sum_{i=1}^{i_m} \lambda_i = 0.9$. In most cases, the first 10 PCs are often enough to reach this threshold.

The most relevant eigenvectors \mathbf{v}_i ($i = 1, \dots, i_m$) can be used to select the vibrational modes that are relevant for the description of the dynamics in the excited state. Using the projection

between the PC \mathbf{v}_i and the normal mode \mathbf{d}_k

$$p_{i,k} = (\mathbf{v}_i \cdot \mathbf{d}_k). \quad (5.4)$$

the relevant normal modes are the ones which have the largest overlap with the relevant PCs (we use the standard scalar product in the Euclidean $3N$ space).

In order to visualize the different PCs, it is possible to associate to each of them a meta-trajectory obtained through the projection of the original trajectory $\mathbf{R}(t)$

$$\mathbf{R}_{[i]}^m(t) = (\mathbf{v}_i \cdot \mathbf{R}(t)). \quad (5.5)$$

5.4.2 Application to the MCTDH dynamics of $[\text{Cu}(\text{dmp})_2]^+$

By applying PCA to our data set, the single trajectories performed within TSH, we can retrieve information about the vibrational normal modes activated during the photorelaxation dynamics of $[\text{Cu}(\text{dmp})_2]^+$.

However, a PCA performed on the entire set of atoms composing the dye will inevitably assign large intensities (weights) to all the collective, low frequency, fluctuations involving the bulky ligands. On the other hand, the MCTDH dynamics is mainly focused on the short time, high frequency modes, that can be sampled with a few hundreds of fs. For instance, the ligand displacement illustrated in Fig. 5.5 (right panel) is induced by a steric repulsion that follows the relaxation of the solvent molecules in the first solvation shell of the Cu atom; this effect is clearly out of reach for MCTDH, which is based on an implicit treatment of the solvent effects. The structural fluctuations (or collective molecular modes) relevant for MCTDH are mainly associated those associated with Cu-N bond length or distortions of the ligand geometry at the metal center. We, therefore, decided to restrict the PCA, described in the previous section, to the first eight neighboring atoms of the Cu: four nitrogen and four carbon atoms as shown in Fig. 5.6 (right). This relatively small set of atoms is capable of capturing all relevant molecular modes activated during the first ultrafast dynamics following photoexcitation, neglecting the effects of the low frequency modes associated to the thermal oscillations of the bulky ligands.

For each TSH trajectory, the first two eigenvectors were projected onto the normal modes, computed for the optimized ground state structure of $[\text{Cu}(\text{dmp})_2]^+$ (see Chapter 3), and the projections were multiplied by the corresponding PCA eigenvalue. Fig. 5.6 (Left) shows the relative weights corresponding to the first 60 normal modes of $[\text{Cu}(\text{dmp})_2]^+$ obtained from three TSH trajectories; the labels *a*, *b*, and *c* refer to the same trajectories plotted in Fig. 5.1. Different colours correspond to different symmetries. Despite the simplifications introduced in this analysis, in particular, the consideration of just a few PC modes and the analysis of only three trajectories, we observe that the PCA of the TSH dynamics is able to capture essentially all modes used in the definition of our previous vibrational Hamiltonian

5.4. Derivation of collective modes for MCTDH dynamics from TSH trajectories

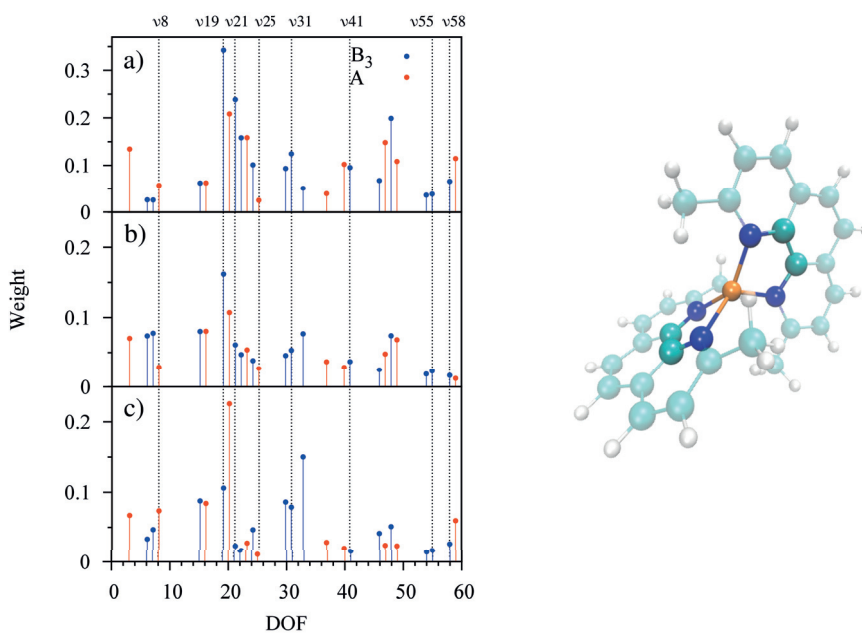


Figure 5.6: *Left*) Projection of the first 2 eigenvalues of the PCA onto the first 60 normal modes. *Right*) Representation of $[\text{Cu}(\text{dmp})_2]^+$ (transparent) and of the selected region (opaque) used for performing PCA.

for the $[\text{Cu}(\text{dmp})_2]^+$ complex [238].

According to symmetry considerations relating the normal modes to the relevant electronic transitions important for the photodynamics, only total symmetric and B_3 -symmetric modes were considered in the construction of the MCTDH Hamiltonian [238].

The top panel of Fig. 5.6, shows the eight modes used for the MCTDH dynamics reported in ref. [238]. We observe that the set of important modes selected by our PCA analysis matches the one used in the quantum dynamics simulations, confirming the quality of our *a priori* choice of the relevant configuration *subspace*. Nonetheless, there are additional modes, emerging from our analysis, that were not included in the MCTDH dynamics. However, while potentially important, the effect of these modes on the dynamics of the $[\text{Cu}(\text{dmp})_2]^+$ has still to be investigated. Notably, the total symmetric ν_{20} has a large weight in all trajectories considered, and in some cases, Fig. 5.6.c, it is even the dominant one. This mode corresponds to a symmetric change of the angles defined by the nitrogen atoms of one ligand and the central copper: when one angle decreases, the corresponding one increases, and vice-versa.

In order to test the relevance of this additional mode in the description of the non-adiabatic relaxation of $[\text{Cu}(\text{dmp})_2]^+$ in MCTDH, we built a new vibronic coupling Hamiltonian that includes this mode. A cut of the PES (only singlet states) along ν_{20} is shown on the right hand side of Fig. 5.7. This mode is fitted with a Morse potential, whose parameters are given in Table 5.4. In Table 5.5 we report the first and second order on-diagonal coupling

terms; off-diagonal terms outcoming from the fit are vanishing. This Hamiltonian was used for a quantum dynamics within the singlet states manifold (triplet states were not included since the PCA was performed on TSH trajectories evolving on singlet states only). Fig. 5.7 (Left) shows the population decay of the photoexcited singlet state, S_3 , simulated using different model Hamiltonians: the original one, used in Chapter 3, was built using the 8 vibrational modes selected using symmetry considerations from the pool of ground state modes, while the second Hamiltonian was obtained by adding the additional ν_{20} mode to previous configurational subspace, for a total of 9 collective modes. As shown in Fig. 5.7, the population decay simulated with both Hamiltonian is very similar. However, slight differences can be observed after ~ 250 fs of dynamics, when we observe a slowing down of the population decay in the dynamics performed with the 9 modes Hamiltonian. In fact, mode ν_{20} is thought to be activated by the interaction with the bath modes (solvent) [119], playing little role during the first instants following photoexcitation. Instead, this mode contributes substantially to the vibronic cooling of the system through the coupling with the bath, a process that occurs in the picoseconds time scale. We can also draw a general conclusion about the inclusion of additional modes in the MCTDH dynamics. When these modes couple to the other vibrational modes used to build the quantum Hamiltonian, they contribute to the spreading of the nuclear wavepacket, which tend to overdiffuse and decohere. This is a similar effect to the one observed in TSH in the full configuration space, which needs a very large number of trajectories in order to converge properties and rates at long time scales.

One can also use PCA to select the minimal set of relevant normal modes to be used in MCTDH dynamics. This approach can help to rationalize the photophysics of the system of interest, providing a reasonable description of the dynamics in the minimal configuration sub-space possible. In addition, this ‘dimensional reduction’ procedure will improve the efficiency of the MCTDH calculations.

From the analysis of the PCs of the TSH dynamics, we noticed that the weights of the vibrational modes ν_{19} and ν_{21} (Fig. 5.6, left panel) are among the largest for most of the trajectories (these modes are present in all Hamiltonians studies so far). To test the possibility to reduce the number of relevant modes for the MCTDH dynamics we generated two more vibronic Hamiltonians: one just composed by the two modes ν_{19} and ν_{21} , and another one built on the 8-mode Hamiltonian to which we removed the same two modes. The quality of the dynamics computed for the different vibronic Hamiltonian is judged by looking at the population dynamics of the photoexcited singlet state (see Fig. 5.7, left panel). We observe that while these two modes (ν_{19} and ν_{21}) are not able to capture the correct decay, their inclusion in the Hamiltonian is essential. In fact, the 6-mode Hamiltonian (build without modes ν_{19} and ν_{21}) gives also an unsatisfactory, unconverged, picture of the relaxation process. We conclude therefore that, in order to be effective these two modes need to be coupled to the remaining modes, which – despite their small amplitude – are essential to describe the non-adiabatic dynamics of the system.

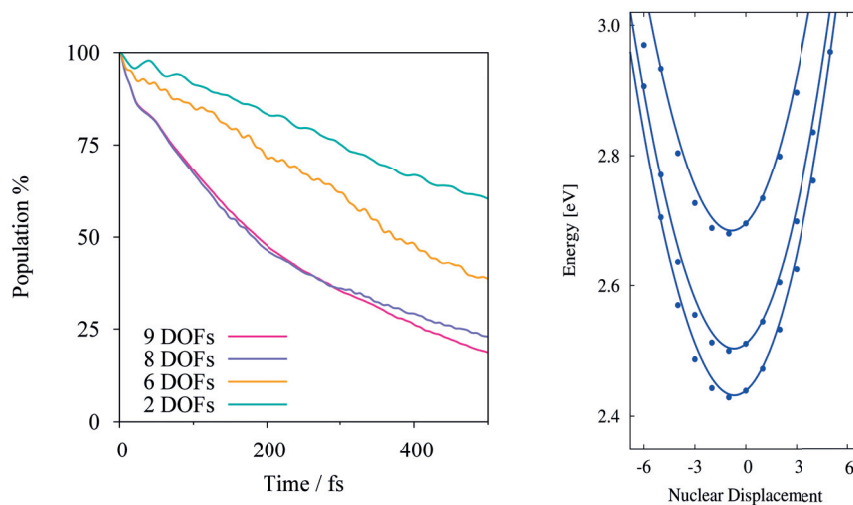


Figure 5.7: *Left*) Population decay of the photoexcited singlet state using a model Hamiltonian with 8 degrees of freedom (as described in Chapter 3), with 6 degrees of freedom (not considering ν_{19} and ν_{21} , with two degrees of freedom (considering only ν_{19} and ν_{21}). *Right*) Cut through the PES along mode ν_{20} . The dots corresponds to quantum chemistry calculation, the lines to the fit from which the expansion coefficients are determined.

Table 5.4: Morse parameters for the additional normal mode ν_{20} .

	D_0 (eV)	$k \cdot 10^{-4}$ (a.u.)	Q_0
S ₁	99.051	60.793	-0.678
S ₂	99.978	57.675	-0.701
S ₃	98.094	60.162	-0.845

Table 5.5: First and second order on-diagonal coupling constants in eV of mode ν_{20} .

κ_{S_1}	κ_{S_2}	κ_{S_3}
0.0208	0.0213	0.0260
γ_{S_1}	γ_{S_2}	γ_{S_3}
0.0061	-	0.0058

5.5 Discussion and Conclusions

In conclusion, in this work, we applied TSH dynamics to the study of the non-adiabatic dynamics of the photoexcited metal complex $[\text{Cu}(\text{dmp})_2]^+$ and compared the results with previous calculations performed with the quantum dynamics package MCTDH. The main difference between these two diverse but complementary approaches are: the dimensions of the sampled configuration space, which is confined to less than 10 dimensions in MCTDH,

and the nature of the dynamics, which in TSH is approximated with an ensemble of classical trajectories that can undergo non-adiabatic transitions (ICs and ISCs) among the different electronic states.

Despite these differences, we found that both IC and ISC rates obtained with TSH agree with those described using the MCTDH approach. This points to a robustness of the quantum dynamics, which in the case of the observables of interest for our study does not seem to depend crucially on the nature of the propagation schemes. More specifically, classical trajectories provide a good description of the dynamics far from the regions of strong coupling, while the surface hopping algorithm is able to capture most of the quantum effects at the avoided crossings. In particular, the missing quantum coherence of the TSH trajectories (due to the independent trajectory approximation) does not seem to affect the spreading of the trajectory ensemble significantly, at least in the subpicosecond timescale. On the other hand, the confinement of the MCTDH dynamics to a subspace of the full molecular configuration space is not introducing important biases, when the correct, and complete set of collective vibrational modes are selected, as we have shown through the PCA.

Both approaches, TSH and MCTDH, agree with the following picture of the photodynamics of $[\text{Cu}(\text{dmp})_2]^+$: upon photoexcitation into the optically bright singlet states, which is made of a combination of electron excitations from d to π^* -gerade orbitals, the system quickly loses potential energy and relaxes into a singlet state characterized by the localization of the MLCT electron on a single ligand. The selection of the ligand depends mainly on the reorganization of the solvent molecules in the first solvation shell of the metal ion. This process occurs in less than 100 fs in both TSH and MCTDH dynamics. Intersystem crossing events can take place all along the relaxation path before the system reaches the lowest singlet state manifold. Spin orbit couplings, and thus ISC probabilities depend strongly on the character of the electronic state configurations, and favours transitions between singlet and triplet states (in both directions) among high energy PESs. In fact, only a few transitions between S_1 and T_1 are observed. As a consequence, ISCs mainly occur in a sub-picosecond scale before the full relaxation of the system into S_1 , or at longer time-scale (not covered by the present simulations) since transitions between S_1 and the high energy triplet states are still possible, even though with very low probabilities due to the small SOCs.

The extremely low quantum yield, 10^{-4} , is also a consequence of the solvent effect. By taking advantage of the QM/MM scheme, which allows us to describe the solvent explicitly within classical mechanics, we could observe an ultrafast solvent reorganization process in the first solvation shell of the metal center, which leads to the formation of attractive interactions with the positively charged Cu ion and therefore to an overall energy stabilization of the complex. In some cases, we even observed a complete closure of the gap between the ground state and S_1 , opening up a channel for non-radiative decay. It is worth stressing that this type of analysis is only possible in the framework of TSH dynamics, which can be coupled to an explicit representation (classical or QM) of the solvent. The combination of MCTDH with an explicit solvent model is highly desirable, however, its implementation is hampered by

the difficulty to parametrize a coupling Hamiltonian able to describe the loosely bound and often anharmonic solvent modes.

As already mentioned, MCTDH can produce an accurate description of the quantum dynamics when there is an appropriate selection of the relevant active vibrational modes to include in the vibronic coupling Hamiltonian. Unfortunately, up to now there is no systematic approach for the calculation of these collective coordinates, and, therefore, their choice is made by inspection of the ground state normal modes and is guided by qualitative arguments based on their symmetry. In this work, we addressed the issue of selecting the relevant normal mode to use in the quantum dynamics by means of a Principal Component Analysis carried out on the excited states TSH trajectories. By projecting the first most representative PCs onto the ground state normal modes, we were able to identify most of the modes previously selected for the simulation of the quantum dynamics of $[\text{Cu}(\text{dmp})_2]^+$ with MCTDH (Chapter 3). However, it is important to mention that there is not necessarily a correlation between the weights of the different PC modes (which are measured in terms of the size of the corresponding eigenvalues) and their relevance for the quantum dynamics; it is well possible that there are PC modes that only participate marginally to the overall TSH dynamics, while being essential for the quantum dynamics, especially for the description of the small amplitude ultrafast component. In particular, by applying PCA to the TSH trajectories and projecting the corresponding eigenvectors into the normal modes of the system, we were able to identify an additional mode, ν_{20} , that contributes in an important way to the description of the TSH dynamics and that was not considered in the MCTDH dynamics reported in Chapter 3. Our analysis confirmed that this mode was not essential for the dynamics, but it can be considered a 'bath mode' that is activated by the solvent interaction (which is explicit in TSH dynamics) but which does not influence the quantum dynamics at least in the sub-ps time scale. We showed that PCA can become a powerful tool for the identification of the normal modes to include in the relevant subspace to use in MCTDH dynamics. However, in the present form, it cannot yet be fully automatized and replace the selection based on chemical intuition

6 Study of the emission properties of Cu(I)-phenanthroline complexes

The luminescence quenching observed in all studied Cu(I)-phenanthroline complexes have puzzled researchers for more than 30 years. The exciplex model, proposed in 1985 by McMillin [68], was not confirmed by recent X-ray absorption measurements [88]. Herein, we use density functional theory (DFT) and time-dependent DFT (TDDFT), classical and quantum mechanics/molecular mechanics (QM/MM) molecular dynamics (MD) simulations to elucidate a full understanding of the role of the geometric and electronic structure, spin orbit coupling, single-triplet gap and the solvent environment on the emission properties of ten copper(I)-phenanthroline complexes. Our quantum chemistry calculations reveal clear trends in the electronic properties, such as the single-triplet gap strongly responsible for the emission properties, allowing us to rationalize the role of specific structural modifications. The classical and QM/MM MD simulations show, in agreement with recent experimental observations, that the lifetime shortening of the excited state in donor solvents (acetonitrile) is not due to an exciplex. Instead, the solute-solvent interaction is transient and arises from a solvent structure already present in the electronic ground state.

The results presented in this chapter are published in the following papers:

“Solvent-induced luminescence quenching: static and time-resolved x-ray absorption spectroscopy of a copper (I) phenanthroline complex”, T. J. Penfold, S. Karlsson, G. Capano, F. A. Lima, J. Rittmann, M. Reinhard, MH Rittmann-Frank, O. Bräm, E. Baranoff, R. Abela, I. Tavernelli, U. Röthlisberger, C. J. Milne, M. Chergui, *J. Phys. Chem. A*, 117, 22, (2013)

“Theoretical Rationalization of the Emission Properties of Prototypical Cu(I)-Phenanthroline Complexes”, G. Capano, U. Röthlisberger, I. Tavernelli and T. J. Penfold, *J. Phys. Chem. A*, 119, 27, (2015).

6.1 Introduction

Owing to their luminescence properties and versatility, transition metal complexes have been subjected to an extensive research effort aimed towards a wide range of possible applications. Among these, the archetypal luminescent transition metal complex is tris-(bipyridyl) ruthenium(II), $[\text{Ru}(\text{bpy})_3]^{2+}$ [158, 17, 159]. Here, the amalgamation of a relatively easily oxidised d^6 metal ion and the electron accepting bipyridine ligands means that the low lying excited states exhibit metal-to-ligand charge transfer (MLCT) character. Once populated, by either photo- or electrical excitation, the participation of the metal ion in these excited states not only facilitates large spin-orbit coupling (SOC) and permits ultrafast intersystem crossing (ISC) [19, 25], but also promotes a strong $T_1 \rightarrow S_0$ radiative transition that has a lifetime of ~ 500 ns and a high quantum yield [66]. In addition, it is a stable molecule and for this reason is considered a good candidate as emitter. However, high cost, low abundance, and toxicity make ruthenium derived complexes unappealing for commercial applications.

Similar complexes based on 1st row transition metal ions, such as $[\text{Fe}(\text{bpy})_3]^{2+}$ [239, 27], have a smaller d-d crystal field splitting and consequently suffer from the presence of low-lying non-emissive metal centred transitions that quench the excited state emission. While these problems can be overcome, to a certain extent, using structural modifications of the ligands to destabilise the metal-centred states [240, 241] this places a large restriction on the structural modifications that can be performed to fine tune their photophysical properties. Consequently, one of the most attractive methods is to simply remove the metal centred states by adopting a complex based upon d^{10} metal ions, such as Cu(I), Ag(I), Au(I), Zn(II) and Cd(II) [242, 243]. Among the most popular are those containing Cu(I) ions [65], especially those complexed with phenanthroline ligands [244].

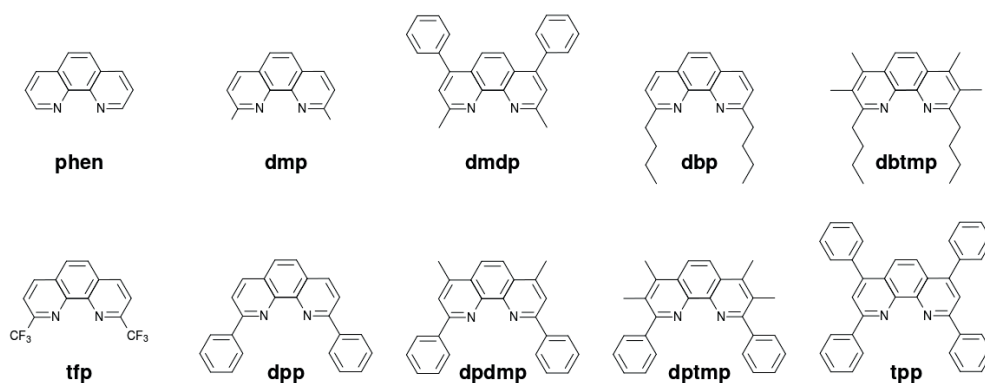


Figure 6.1: A schematic representation of the ten ligands and their abbreviated name studied herein.

As extensively described in Sec. 1.3, several groups have investigated the photophysical properties of the Cu(I)-phenanthroline complexes. After photon absorption into the optically bright $^1\text{MLCT}$ the complex undergoes relaxation, through internal conversion, structural

distortion, associated with the pseudo Jahn-Teller (PJT) instability of the Cu(II) ion, and intersystem crossing (ISC), to the lowest triplet state in few picoseconds. These processes are concluded within a few tens of picoseconds and are similar for all Cu(I)-phenanthroline complexes. Therefore, these dynamics do not have a significant impact on the potential application of these compounds.

However, the same cannot be said for the longer time (picoseconds to microseconds) dynamics associated with the emission from the low-lying excited states. Indeed, it was demonstrated [65, 68, 74, 245, 222] that the emission lifetime of these complexes is strongly dependent upon both structural modifications to the phenanthroline ligands and the environment within which the complex is embedded, especially in the case of solutions (see Subsec. 1.3.2). For the first it was observed that, in general, complexes with cumbersome substituents, such as aryl or large alkyl groups at the positions 2,9 of the phenanthroline (see Fig. 6.2 for the number nomenclature of the ligands), have stronger emission and longer luminescence lifetime. For the latter, they found that emission lifetimes can be significantly shortened in donating solvents (i.e., those behaving as Lewis bases), such as acetonitrile (MeCN) [70], compared to the case for nondonating solvents, such as dichloromethane (DCM). They attributed this quenching to complexation of a solvent molecule (exciplex) that most likely occurs at the metal center, during which the interaction between the Cu(II) atom and the electron-rich donor molecule is thought to stabilize the excited state relative to the ground state, reducing the energy gap and, therefore, increasing the rate of nonradiative decay [81]. This interpretation applies also the relationship between structural modification and emission properties: large substituents, in fact, can prevent solvent molecule, to approach the metal center and to form an exciplex. However, a recent time-resolved X-ray absorption spectroscopy study [88] has demonstrated that the transient XAS spectrum is the same for $[\text{Cu}(\text{dmp})_2]^+$ (dmp = 2,9-dimethyl-1,10-phenanthroline) in MeCN and DCM. Given the sensitivity of XAS to the coordination number and the structure around the absorbing atom [40, 246], this makes complexation of a solvent molecule very unlikely and, therefore, the exact nature of the solute-solvent interaction and the role of the geometric configuration remain undetermined.

Finally, as described in Subsec. 1.3.1, besides the role of the environment, also the temperature affects the radiative properties of these complexes [76]. Indeed, owing to a relatively small energy gap between the emitting singlet and triplet states, the thermal motion is able to promote reverse intersystem crossing (rISC) from the T_1 to S_1 increasing the contribution of the S_1 state to the total radiative decay.

These previous works have demonstrated both the importance and interest for understanding the excited state properties of Cu(I)-phenanthroline molecules. especially the role of the geometric and electronic structure and the solvent. Consequently, in this contribution we use DFT and TDDFT, classical and QM/MM MD simulations to provide a thorough description of the ground and excited state properties of ten Cu(I)-phenanthroline complexes, namely $[\text{Cu}(\text{phen})_2]^+$, $[\text{Cu}(\text{dmp})_2]^+$, $[\text{Cu}(\text{tfp})_2]^+$, $[\text{Cu}(\text{dmdp})_2]^+$, $[\text{Cu}(\text{dpp})_2]^+$, $[\text{Cu}(\text{dpdmp})_2]^+$,

$[\text{Cu}(\text{dptmp})_2]^+$, $[\text{Cu}(\text{tpp})_2]^+$, $[\text{Cu}(\text{dbp})_2]^+$ and $[\text{Cu}(\text{dbtmp})_2]^+$ (see Fig. 6.1). Our quantum chemistry calculations reproduce the trends observed experimentally and permit us to rationalize the lifetime of these complexes in terms of the geometric and geometric structure, spin orbit coupling structural distortions, providing important information towards engineering new complexes aimed at improved properties for a particular application. Using the molecular dynamics simulations, we find, contrary to previous work, that the excited state of none of these complexes exhibits the formation of an exciplex. Instead the solvent-solute interaction is transient and arises from a solvent configuration already present in the ground state.

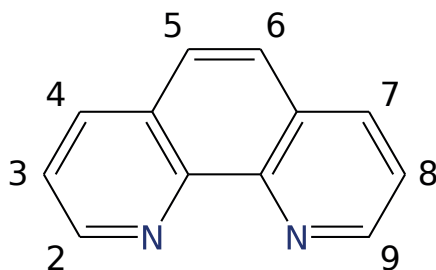


Figure 6.2: The number nomenclature for the phenanthroline ligands.

6.2 Computational Details

6.2.1 Electronic structure calculations

The structure of the electronic ground state and lowest triplet states of the ten Cu(I)-phenanthroline complexes were optimised at DFT(BLYP) [196, 247] and DFT(B3LYP) [248] level using Gaussian09 [160]. The effect of the weak $\pi-\pi$ interactions were accounted for during the optimisations using the Grimme's D2 dispersion correction [249]. A triple- ζ (Cu) and double- ζ (F, N, C and H) basis sets were used for all of the electronic structure calculations.

The excited state energies were computed using linear response time-dependent density functional theory (LR-TDDFT) with the approximation of the B3LYP exchange and correlation functional as implemented within Amsterdam Density Functional (ADF) [250, 164, 251]. The SOC matrix elements were computed with the perturbative approach developed by Wang and Ziegler [162]. A TZP basis set was used for all atoms and scalar relativistic effects were accounted for using the zeroth order relativistic approximation (ZORA) [166, 252].

Finally, it is noted that throughout this work we have computed all emission properties from the optimized T_1 geometry. Though direct comparison with the experimental data also requires the emission to the calculated relaxed S_1 geometry, previous studies [96, 98, 253, 238] have demonstrated its similarity to the T_1 state. In addition, due to the weak exchange interaction between the S_1 and T_1 states, which leads to the small $\Delta E_{S_1-T_1}$, the energy gap between these states, $\Delta E_{S_1-T_1}$, is expected to be independent of geometry and, therefore,

close to constant for all nuclear configurations [254].

6.2.2 Molecular dynamics simulations

Classical MD simulations of the ten Cu(I)-phenanthroline complexes were performed using the Amber12 package [231]. The standard force field implemented in Amber12 was augmented with additional parameters describing the bonds, angles and dihedrals involving the copper atom. The bonding parameters (equilibrium bond lengths and angles as well as the corresponding force constants and dihedral potentials) and force constants of these additional parameters were obtained using DFT(B3LYP) as implemented in Gaussian09 [160]. Calculation of the Hessian matrix provided the force constants for bonds and angles. The charges were calculated with the Restricted Electrostatic Potential (RESP) [255] method fixing the charge of Cu with the one obtained applying the Mulliken method. The classical simulations were performed with a time step of 1 fs and the trajectories were printed each 200 time step. The data were collected after 1 ns of equilibration, for a total of 15 ns.

The classical MD simulations have been supplemented with Car-Parrinello [152] QM/MM [146, 256] MD simulations that were performed for four of the complexes, $[\text{Cu}(\text{phen})_2]^+$, $[\text{Cu}(\text{dmp})_2]^+$, $[\text{Cu}(\text{dbp})_2]^+$ and $[\text{Cu}(\text{dpp})_2]^+$. Starting from an equilibrated configuration from the classical MD trajectory, the systems were thermalised for 2 ps controlling by scaling the temperature of the ions. Subsequently, the systems were equilibrated for a further picosecond using two Nose-Hoover thermostats [228, 229] (one on the quantum region and one for the classical region) with a coupling frequency of 2000 cm^{-1} . Finally, the MD was run for ~ 20 ps from which all of the properties were calculated. In all cases a fictitious electron mass of 600 a.u. and a time step of 0.01 fs was used. The quantum part, which incorporated the Cu(I)-Phenanthroline complex only, was computed with DFT(BLYP) using a Troullier-Martin pseudopotential [225] to describe the core-electron. The plane-wave cut-off was 85 Ry. To effect of weak $\pi - \pi$ interactions, were also included during the calculations using the Dispersion-Corrected Atom-Centered Potential (DCACP) method [226, 257, 227].

6.3 Results

In this contribution, we aim to provide a complete description of the photophysical properties of ten Cu(I)-phenanthroline complexes in terms of their electronic and geometric structure, their SOC and solvent environment. Towards this goal, we use quantum chemistry and molecular dynamics simulations as described above. In the proceeding section, we initially focus on the gas phase structures, absorption and emission properties and SOC, before in the final section describing the structure and the effect of the solvation shell.

6.3.1 Quantum chemistry: The geometric and electronic structure and contribution of spin orbit coupling

	Method	Ground State			³ MLCT		
		Cu-N (Å)	∠ NCuN _{intra} (°)	∠ dha(°)	Cu-N (Å)	∠ NCuN _{intra} (°)	∠ dha(°)
[Cu(phen) ₂] ⁺	BLYP	2.05	83	90	2.01	83	39
	B3LYP	2.06	82	90	2.00	84	39
[Cu(dmp) ₂] ⁺	BLYP	2.04	81	90	2.00	83	68
	B3LYP	2.05	81	90	2.02	83	70
[Cu(tfp) ₂] ⁺	BLYP	2.03	83	90	1.99	84	76
					2.02		
	B3LYP	2.05	83	90	1.97	84	74
				2.02			
[Cu(dmdp) ₂] ⁺	BLYP	2.04	82	87	2.00	83	59
	B3LYP	2.05	81	88	1.98	84	58
				1.99			
[Cu(dpp) ₂] ⁺	BLYP	2.05	83	54	2.02	84	53
	B3LYP	2.06	83	55	2.01	84	53
[Cu(dpdp) ₂] ⁺	BLYP	2.04	83	54	2.02	84	51
	B3LYP	2.05	82	54	1.99	83	53
				2.03	85		
[Cu(dptmp) ₂] ⁺	BLYP	2.05	83	65	2.01	84	58
					2.02		
	B3LYP	2.05	82	65	1.99	84	61
[Cu(tpp) ₂] ⁺	BLYP	2.04	83	51	2.00	84	50
	B3LYP	2.05	83	50	1.99	84	50
[Cu(dbp) ₂] ⁺	BLYP	2.05	82	86	2.00	83	75
			83		2.03	84	
	B3LYP	2.07	82	86	2.00	83	75
				2.03	84		
[Cu(dbtmp) ₂] ⁺	BLYP	2.04	82	84	2.00	83	70
		2.06	83			84	
	B3LYP	2.04	81	83	2.01	84	70
		2.06	82				

Table 6.1: The DFT(B3LYP) and DFT(BLYP) optimised geometry of the electronic ground state and lowest triplet state of the ten Cu(I)-phenanthroline complexes. In each case the effect of the weak $\pi - \pi$ interactions were accounted for during the optimisations using the D2 Grimme's dispersion correction [249].

The geometric structure Table 6.1 summarises the main structural parameters for the DFT(B3LYP) and DFT(BLYP) optimised geometries of the ten Cu(I)-phenanthrolines complexes. The corresponding geometries optimised at DFT(BLYP) are in close agreement throughout, indicating that the inclusion of Hartree-Fock exchange does not have a significant effect on the geometry. These latter geometric parameters are included only to permit a closer comparison with the QM/MM MD simulations presented in Subsection 6.3.2.

In the ground state, we observe that the Cu-N bond lengths are almost constant for each of the complexes (2.04-2.07 Å) and do not adjust to compensate for changes in steric hindrance associated with bulky substituents in the positions 2,9. Instead, this is achieved solely through changes to the dihedral angle between the ligands. While for small (CH₃, CF₃)

or no substituents in the positions 2,9 the dihedral angle between the ligands is $\sim 90^\circ$, we observe a small reduction ($\sim 80^\circ$) upon the addition of the n-butyl groups ($[\text{Cu}(\text{dbp})_2]^+$, $[\text{Cu}(\text{dbtmp})_2]^+$).

However, while bulky, the n-butyl substituents are rather flexible and instead the largest distortions are observed upon the addition of phenyl ligands. For $[\text{Cu}(\text{dpp})_2]^+$ a dihedral angle of 55° is found. It is worth noting that this is $\sim 15^\circ$ smaller than recently reported [258]. This is because for the phenyl substituted complexes, we have found that the dihedral angle of the optimised geometry is rather sensitive to the weak $\pi - \pi$ interactions. For all of these optimisations we have used the D2 Grimme's dispersion correction [249], which appears to overestimate the dihedral angle. Interestingly, this is not the case for the QM/MM MD simulations presented below where these interactions were addressed using the DCACP method. However, although this does have a slight effect on the lower vibronic band in the absorption spectra present below, these differences do not change the qualitative interpretation of the results as discussed.

Substituents in the positions 3,8 also affect the dihedral angle, in agreement with experimental conclusions drawn by comparing the profile of the absorption spectra [69]. For $[\text{Cu}(\text{dptmp})_2]^+$, methyl substituents in the positions 3,8 lead to a dihedral angle slightly closer to perpendicular. This arises because steric hindrance that can occur between these additional methyl groups and the substituents in the positions 2,9 that prevent the flattening distortion. Interestingly, this effect is only observed for the $[\text{Cu}(\text{dptmp})_2]^+$, due to the flexible n-butyl substituents.

In agreement with recent experimental observations [88, 258], there are two principle structural changes in the lowest triplet state; firstly a contraction of the Cu-N bond distance. This change induces a small strain into the ligands, which is compensated for by an increase in $\angle \text{NCuN}_{\text{intra}}$. These changes are consistent with the removal of a $d\pi$ anti-bonding electron from the metal atom. For some of the complexes we observe that in the excited state the photoexcited electron is localised principally on one of the ligands in agreement with Raman spectroscopic studies [259]. As a consequence, the two ligands can be subjected to different distortions with a different contraction of the Cu-N bond distances (for example for $[\text{Cu}(\text{tfp})_2]^+$ a contraction of 0.4 \AA and 0.1 \AA for different ligands). Here, it is important to note that although this is only observed for some of the complexes, upon the inclusion of finite temperature, the symmetry breaking associated with thermal motion means that this localisation would be expected to occur for all of the complexes [234, 260].

The second structural change is the well-documented decrease in the dihedral angle associated with generation of a Cu(II) d^9 configuration and proceeding PJT distortion [222]. As expected, the largest change in the dihedral angle is observed for sterically unhindered phenanthroline ligands. For $[\text{Cu}(\text{phen})_2]^+$ the dihedral reduced to 39° . Following the trends observed in the ground state, smaller changes are observed for complexes with bulky substituents, indeed $[\text{Cu}(\text{dpp})_2]^+$, $[\text{Cu}(\text{dpdmp})_2]^+$, $[\text{Cu}(\text{dptmp})_2]^+$ and $[\text{Cu}(\text{tpp})_2]^+$ all exhibit

changes $<5^\circ$.

Table 6.2: Room temperature absorption data for the ten Cu(I)-phenanthroline complexes in DCM compared to values calculated using LR-TDDFT as implemented within ADF. *a* [98], *b* [78], *c* [69], *d* [261] *e* [262].

	Exp. (nm)	Calculated eV (nm)	<i>f</i>	Transition	dha($^\circ$)
[Cu(phen) ₂] ⁺ <i>a</i>	458	2.59 (478.7)	0.1232	S ₀ → S ₃	90
[Cu(dmp) ₂] ⁺ <i>b</i>	454	2.66 (465.2)	0.1542	S ₀ → S ₃	90
[Cu(tfp) ₂] ⁺ <i>d</i>	462	2.54 (488.1)	0.2100	S ₀ → S ₇	90
[Cu(dmdp) ₂] ⁺ <i>b</i>	495	2.48 (499.9)	0.3986	S ₀ → S ₃	88
[Cu(dpp) ₂] ⁺ <i>b</i>	560	1.91 (649.1)	0.0305	S ₀ → S ₁	55
		2.06 (601.9)	0.0122	S ₀ → S ₂	
		2.09 (593.2)	0.0218	S ₀ → S ₃	
	436	2.74 (452.5)	0.0341	S ₀ → S ₅	
		2.83 (438.1)	0.0190	S ₀ → S ₆	
[Cu(dpdmp) ₂] ⁺ <i>c</i>	550	1.94 (639.0)	0.0120	S ₀ → S ₁	54
		1.96 (632.6)	0.0372	S ₀ → S ₂	
		1.98 (626.2)	0.0232	S ₀ → S ₃	
	440	2.71 (457.5)	0.0233	S ₀ → S ₅	
[Cu(dptmp) ₂] ⁺ <i>c</i>		1.98 (632.6)	0.0380	S ₀ → S ₁	65
		1.99 (632.6)	0.0160	S ₀ → S ₂	
		2.00 (632.6)	0.0112	S ₀ → S ₃	
	467	2.67 (464.3)	0.0678	S ₀ → S ₇	
[Cu(tpp) ₂] ⁺ <i>b</i>	590	1.87 (663.0)	0.0701	S ₀ → S ₁	50
		1.99 (623.0)	0.0159	S ₀ → S ₂	
		2.02 (613.8)	0.0401	S ₀ → S ₃	
	460	2.67 (464.3)	0.0901	S ₀ → S ₅	
[Cu(dbp) ₂] ⁺ <i>c</i>	457	2.52 (492.0)	0.1481	S ₀ → S ₃	86
[Cu(dbtmp) ₂] ⁺ <i>c</i>	453	2.61 (475.0)	0.1536	S ₀ → S ₅	83

The electronic properties:absorption Table 6.2 shows the experimental and computed absorption energies. Previous characterisations have shown that the absorption spectra of these complexes can be split into two distinct classes, which is largely dependent on the dihedral angle between the ligands in the ground state [69]. For complexes that have a dihedral angle close to 90° , one broad MLCT absorption band centered around ~ 400 - 500 nm is observed. However, for complexes distorted from the perpendicular ligand arrangement a shoulder at lower energies (~ 550 nm) is observed. These transitions arise from vibronic transitions into lower states, which are dipole forbidden at the D_{2d} symmetry, but become allowed due to the dihedral distortion.

For [Cu(phen)₂]⁺ the calculated transition is in good agreement with the main experimental absorption. The first allowed excitation occurs to the S₃ state and corresponds to a HOMO→LUMO (45%) and HOMO-1→LUMO+1 (44%) transition. For [Cu(tfp)₂]⁺, [Cu(dbp)₂]⁺ and [Cu(dbtmp)₂]⁺, the substituents have quite small effects on the main absorption and it appears at a similar energy to [Cu(phen)₂]⁺. Indeed for [Cu(tfp)₂]⁺ only a slight lowering

of the absorption band is observed, which is associated with electron withdrawing effect of the CF_3 group. In contrast, the inductive effect of the alkyl substituents leads to a slight increase in the maximum of the absorption band. Interestingly, while the energy of the main absorption band does not change, the state which is populated does, in fact for $[\text{Cu}(\text{tfp})_2]^+$ the optically bright states is S_7 . However, this would only be expected to change the ultrafast dynamics associated with non-adiabatic relaxation and as these initial steps are completed within a few tens of picoseconds, one would not expect this should not have a significant impact on emission properties.

Compared to the previous systems, those complexes with phenyl substituents in the positions 2,9 exhibits an additional absorption bands, which occurs at lower energies than the main band and is due to vibronic transitions, which becomes allowed by breaking the perpendicular D_{2d} symmetry. As expected, we observe that these calculated transitions are lower than those observed experimentally, which as discussed in the previous section is due to the description of the weak $\pi - \pi$ interactions. As observed experimentally, the oscillator strength for these absorption bands is significantly less than for the other complexes. This is a consequence of the pushing effect of the phenyl substituents in the positions 2,9 on the π system towards the metal centre. This decreases the transition dipole length and, therefore, the oscillator strength of the transition [263]. As expected, this effect is somewhat reduced for $[\text{Cu}(\text{tpp})_2]^+$, for which phenyl substituents in the positions 4,7 counteract the effect of those in the positions 2,9, increasing the oscillator strength [263].

Table 6.3: Room temperature emission data for the ten Cu(I)-phenanthroline complexes in MeCN or DCM compared to values calculated using LR-TDDFT as implemented within ADF [78], b [69], c [261], d [262].

	in MeCN		in DCM		Calculated				dha(°)
	Exp. (nm/eV)	τ (ns)	Exp. (nm/eV)	τ (ns)	T_1 (eV)	S_1 (eV)	f_{S_1}	$\Delta S_1/T_1$ (eV)	
$[\text{Cu}(\text{phen})_2]^+$ ^d	-	-	-	< 20	0.62	1.22	0.057	0.6	39
$[\text{Cu}(\text{dmp})_2]^+$ ^c	700/1.71	<2	690/1.74	90	1.29	1.77	0.041	0.48	69
$[\text{Cu}(\text{tfp})_2]^+$ ^c	-	-	665/1.86	165	1.34	1.73	0.038	0.39	74
$[\text{Cu}(\text{dmdp})_2]^+$ ^a	-	-	770/1.61	80	1.04	1.60	0.123	0.56	58
$[\text{Cu}(\text{dpp})_2]^+$ ^a	735/1.69	180	710/1.75	280	1.43	1.66	0.036	0.23	53
$[\text{Cu}(\text{dpdmp})_2]^+$ ^b	-	-	720/1.72	310	1.31	1.65	0.023	0.34	53
$[\text{Cu}(\text{dptmp})_2]^+$ ^b	735/1.69	260	715/1.73	480	1.25	1.66	0.044	0.41	61
$[\text{Cu}(\text{tpp})_2]^+$ ^a	765/1.62	120	745/1.66	230	1.30	1.61	0.080	0.31	50
$[\text{Cu}(\text{dbp})_2]^+$ ^b	730/1.70	35	715/1.73	150	1.36	1.69	0.036	0.33	75
$[\text{Cu}(\text{dbtmp})_2]^+$ ^b	690/1.78	440	670/1.85	920	1.38	1.73	0.045	0.35	70

The electronic properties: emission Table 6.3 shows the experimental and computed emission energies for each of the complexes. Experimentally, the emission bands are featureless and rather broad, overlapping with both the computed S_1 and T_1 energies. However, the peak of the emission spectra, highlighted in Table 6.3, is closer to that of the S_1 energy. This is indicative of the luminescence mechanism known as thermally activated delayed fluorescence (TADF), well documented for these complexes [13]. Here, depending on the size

of the SOC matrix elements and the energy separation ($\Delta E_{S_1-T_1}$) between the S_1 and T_1 state, the emission of the former becomes increasingly dominant in the emission spectrum at ambient temperatures as this state is thermally populated [76]. In this case, the contribution of each state to the emission spectrum is governed by a Boltzmann distribution according to:

$$\frac{\text{Int}(S_1 \rightarrow S_0)}{\text{Int}(T_1 \rightarrow S_0)} = \frac{k^r(S_1 \rightarrow S_0)}{k^r(T_1 \rightarrow S_0)} \cdot \exp\left(-\frac{\Delta E_{S_1-T_1}}{k_B T}\right) \quad (6.1)$$

Here $\text{Int}(S_1 \rightarrow S_0)$ and $\text{Int}(T_1 \rightarrow S_0)$, $k^r(S_1 \rightarrow S_0)$ and $k^r(T_1 \rightarrow S_0)$ represent the fluorescence and phosphorescence intensities and the corresponding radiative rates, respectively, k_B is the Boltzmann constant and T the absolute temperature [13].

For $[\text{Cu}(\text{phen})_2]^+$ we find a very small energy gap due to its large structural distortion in the excited state. This explains its very short lifetime (~ 2 ps in acetonitrile) [262], which is dominated by a large contribution of non-radiative decay [81]. For $[\text{Cu}(\text{dmp})_2]^+$, $[\text{Cu}(\text{dmdp})_2]^+$ and $[\text{Cu}(\text{tfp})_2]^+$ we observe a large emission energy and a longer emission lifetime, as expected due to the smaller structural distortion. Of these three, $[\text{Cu}(\text{dmdp})_2]^+$ exhibits the shorter lifetime due to the smaller energy gap ($S_1 \rightarrow S_0$) and large oscillator strength. The latter is due to the phenyl substituents in the positions 4,7, which extend the π system away from the metal centre and increase the transition dipole length and, therefore, the oscillator strength of the transition [263].

The inclusion of larger substituents (phenyl and n-butyl) onto the positions 2,9 has a significant effect on the lifetime. Despite the smaller energy gap with the ground state, $[\text{Cu}(\text{dpp})_2]^+$ has a lifetime (in DCM), which is almost a factor of two longer than $[\text{Cu}(\text{tfp})_2]^+$ and a factor of four larger than $[\text{Cu}(\text{dmdp})_2]^+$. The phenyl substituents in the positions 2,9 bring the π system towards from the metal centre and decrease the transition dipole length [263] and, therefore, a large decrease in the oscillator strength is observed. For the latter, the large dihedral angle of $[\text{Cu}(\text{dpp})_2]^+$ leads to the smaller SOC coupling, and, therefore, mixing of the S_1 and T_1 states at the triplet geometry. As the radiative rate of the triplet state is expressed

$$k^r(T_1 \rightarrow S_0) = \frac{64\pi^2 \nu^3}{3\hbar c^3} \left| \frac{\langle S_1 | \hat{H}_{SO} | T_1 \rangle}{\Delta E_{S_1-T_1}} \cdot \langle S_0 | e\mathbf{r} | S_1 \rangle \right|^2 \quad (6.2)$$

the reduction in SOC reduces the mixing of the S_1 and T_1 states, thus extending the lifetime of the triplet state.

The role of the $\Delta E_{S_1-T_1}$ energy gap in the TADF mechanism is exemplified by comparison between $[\text{Cu}(\text{dpp})_2]^+$, $[\text{Cu}(\text{dpdmp})_2]^+$ and $[\text{Cu}(\text{dptmp})_2]^+$. Indeed all three have similar emission bands entered at similar energies (~ 1.70 eV), however their lifetime in DCM varies by almost factor of two, due to an increasing $\Delta E_{S_1-T_1}$ energy gap because the inductive effect of the methyl substituents increase the interactions between the unpaired electrons is largely due to the smaller spatial separation from the metal centred d-orbitals. For these

complexes, the inductive effect of the methyl substituents at the positions 3,4,7,8 of the phenanthroline ligands pushes the electron density towards the copper ions. This increases the interaction between the unpaired electron on the ligands with the one on the metal centered d-orbitals, due to the smaller spatial separation. As a consequence, we observe a decrease of the contribution of the S_1 fluorescence to the overall radiative emission (Eq. 6.1). In addition, a reduction of the mixing of the singlet and triplet state (Eq. 6.2) reduces $k^r(T_1)$, which, therefore, contributes to the extension of the lifetime of the excited state. $[\text{Cu}(\text{tpp})_2]^+$ does not follow this trend, because the phenyl substituents in the positions 4,7 not only reduce interactions between the unpaired electrons but also, by extending the π system away from the metal d-orbital, increase the dipole length and consequently the oscillator strength, giving rise to a shorter lifetime.

Finally, in terms of the emission lifetime, perhaps the most intriguing complexes are $[\text{Cu}(\text{dbp})_2]^+$ and $[\text{Cu}(\text{dbtmp})_2]^+$, which offer strongly contrasting lifetimes. Indeed, the similarity of the solvent environment and SOC matrix elements (discussed below) lead us to rules of these are the main factors contributing to this significant change. Instead, we assign this simply to the exponential energy gap law, when compared between for the experimental emission spectra, in agreement with a similar effect recently observed in Ref. [82]. Indeed, for the latter, the methyl groups donate electrons to the conjugated core, raising the energy of the low lying π^* orbitals and increasing the energy of the low lying emitting states. Due to the inductive effect of the alkyl groups in the 2,9 position, this effect is largest for $[\text{Cu}(\text{dbtmp})_2]^+$.

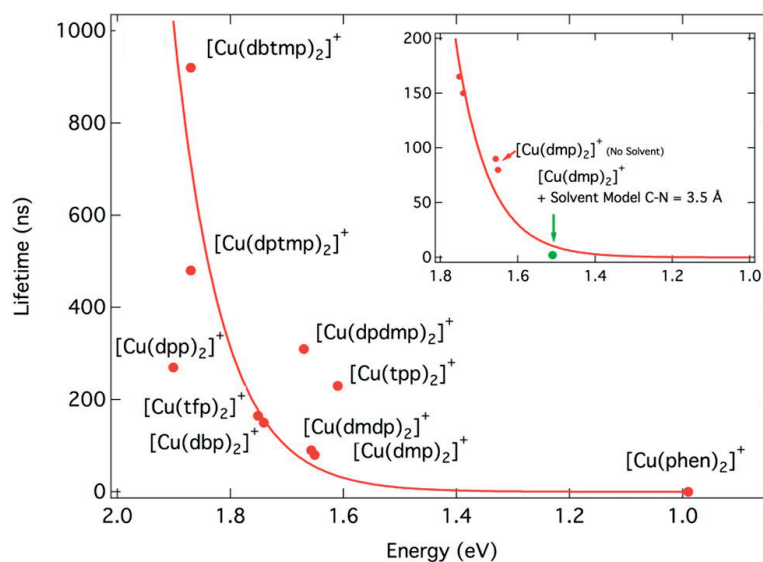


Figure 6.3: Luminescence lifetime in DMC versus the calculated LR-TDDFT T_1 energy for the 10 Cu(I)-phenanthroline complexes studied here. In the insert, zoom of the complexes with the shortest lifetime, including the experimental lifetime of $[\text{Cu}(\text{dmp})_2]^+$ in MeCN and the calculated LR-TDDFT T_1 energy of $[\text{Cu}(\text{dmp})_2]^+$ +MeCN (see Fig. 6.11)

Fig. 6.3 shows a graphical summary of the luminescence lifetime as a function of the cal-

culated T_1 energy (reported in Table 6.3), here discussed. The relationship, as expected by the energy gap law [81], is exponential. However, although the majority of the complexes follow this curve, there are three exceptions: $[\text{Cu}(\text{dpp})_2]^+$, $[\text{Cu}(\text{dpdmp})_2]^+$, $[\text{Cu}(\text{tpp})_2]^+$. For the first, $[\text{Cu}(\text{dpp})_2]^+$, this discrepancy, as already discussed, can be rationalized in terms of the energy gap between S_1 and T_1 . In fact, in this case, the energy gap is smaller to other complexes, increasing the radiative rate of the triplet state. For $[\text{Cu}(\text{dpdmp})_2]^+$, $[\text{Cu}(\text{tpp})_2]^+$, energy gap is similar to other complexes and, therefore, the reason for such long lifetime, should be found elsewhere. By analyzing the emission data, one can observe that for these complexes, the emission radiative rate is reduced by the small oscillator strengths of the state S_1 .

Spin orbit coupling: As previously discussed, large SOC not only permits ultrafast inter-system crossing (ISC), which promotes a strong $T_1 \rightarrow S_0$ radiative transition, but also plays an important role in the TADF fluorescence mechanism. Consequently, understanding the SOC at both the ground and triplet states geometries plays an important role in determining the lifetime and fluorescence mechanism of these complexes. The first study into the SOC of Cu(I)-phenanthrolines was performed by Nozaki and co-workers [100] on $[\text{Cu}(\text{dmp})_2]^+$. Using a semi-quantitative approach, which assumed only the Cu 3d electrons contribute significantly to ISC, they reported that the SOC matrix elements were strongly dependent on the dihedral angles between the two ligands, which they used to explain the slow ISC rate observed at the flattened PJT geometry.

In calculating the SOC matrix elements, they assumed a one-electron one-center approximation for the SOC operator:

$$H_{SO} = \zeta \sum_i^{N_{el}} l_i s_i \quad (6.3)$$

where l_i is the angular momentum of electron i , and s_i is the spin operator of electron i . ζ is the spin-orbit coupling constant, proportional to the atomic number and inversely proportional to the mean cubic radial distribution (r^{-3}) of the electron and is, therefore, responsible for the so-called *heavy atom effect*. However, besides the effect of heavy atoms, one must also consider the integral over the two states involved:

$$[H_{SO}]_{ij} = \langle \Psi_{S_i} | H_{SO} | \Psi_{T_j} \rangle \quad (6.4)$$

This integral, sometimes referred to as the internal effect, depends principally on the character of the states involved, as outlined for organic systems by El-Sayed [264]. In his work, El-Sayed highlighted that to achieve effective SOC, any change in spin must be accompanied by a corresponding change in angular momentum, so that total angular momentum is conserved. For the MLCT states involved here, both the $^3d\pi^*$ and $^1d\pi^*$ should involve the same π^* orbital because the SOC of π electrons is small. Furthermore, as any atomic angular

momenta in low-symmetry transition metal complexes are quenched, the spin-orbit coupling of the d electron works between the $d\pi^*$ configurations involving different d orbitals. Consequently, under the assumption of one-centre spin-orbit integrals, the $^3d\pi^*$ electronic configuration in the lowest state is effectively coupled with the specific $^1d\pi^*$ configurations involving the d orbital with a different orientation and having a common π^* orbital. For this reason, it has previously been identified [265], that despite the heavy atom effect, Au(I) complexes generally exhibit smaller SOC matrix elements than Cu(I) complexes, due to the smaller contribution of d -orbitals in the excited state.

Table 6.4: The main ($>10 \text{ cm}^{-1}$) spin orbit coupling matrix elements (in cm^{-1}) between the low lying (singlet, triplet) states of the ten Cu(I)-phenanthroline complexes at the Franck-Condon and flattened geometries

	$\langle \Psi_{S_n} H_{SO} \Psi_{T_m} \rangle$ (n,m)		
	Ground state		$^3\text{MLCT}$
$[\text{Cu}(\text{phen})_2]^+$	86 (1,1)	33 (2,3)	13 (1,1)
	266 (1,2)	306 (2,4)	
$[\text{Cu}(\text{dmp})_2]^+$	237 (1,1)	210 (2,3)	43 (1,1)
	169 (1,2)	244 (2,4)	
$[\text{Cu}(\text{tfp})_2]^+$	280 (1,1)	317 (2,4)	50 (1,1)
	44 (1,2)		
$[\text{Cu}(\text{dmdp})_2]^+$	263 (1,1)	26 (2,2)	25 (1,1)
	32 (1,2)	210 (2,3)	32 (1,2)
	15 (1,3)	205 (2,4)	
$[\text{Cu}(\text{dpp})_2]^+$	29 (1,1)	16 (2,4)	21 (1,1)
$[\text{Cu}(\text{dpdmp})_2]^+$	38 (1,1)		28 (1,1)
			20 (1,2)
			13 (1,3)
$[\text{Cu}(\text{dptmp})_2]^+$	39 (1,1)	16 (2,4)	23 (1,1)
$[\text{Cu}(\text{tpp})_2]^+$	26 (1,1)		19 (1,1)
$[\text{Cu}(\text{dbp})_2]^+$	143 (1,1)	182 (2,2)	37 (1,1)
	15 (1,2)	237 (2,4)	
	232 (1,3)		
$[\text{Cu}(\text{dbtmp})_2]^+$	125 (1,1)	19 (2,1)	34 (1,1)
	232 (1,3)	177 (2,2)	
	40 (1,4)	25 (2,3)	
		227 (2,4)	

Table 6.4 shows the significant ($>10 \text{ cm}^{-1}$) SOC matrix elements for the ten Cu(I)-phenanthroline complexes at both the Franck-Condon and lowest triplet state geometries. At the Franck-Condon geometry, the complexes that exhibit no dihedral distortion show significant SOC matrix elements ($>10 \text{ cm}^{-1}$) between the S_1 , S_2 states and the triplet manifold. Indeed, $[\text{Cu}(\text{dmdp})_2]^+$ exhibits very similar spin orbit coupling characteristics as described by Nozaki and co-workers [100] for $[\text{Cu}(\text{dmp})_2]^+$, showing in contrast to the oscillator strengths reported

in the previous section, the phenyl substituent in the positions 4,7, which contain only light elements, do not have a large impact on the magnitude of the SOC matrix elements. At the equilibrium geometry, the main coupling is between the S_1 and T_1 , which is 263 cm^{-1} . This arises from the spin orbit integrals between the two main configurations, which each contribution $\sim 40\%$ to the excited state wavefunction, of namely:

$$\langle \Psi_{S_1} | H_{SO} | \Psi_{T_1} \rangle = \frac{1}{2} \langle d_{yz} \rightarrow \pi_1^* | H_{SO} | d_{xz} \rightarrow \pi_1^* \rangle + \quad (6.5)$$

$$\frac{1}{2} \langle d_{xz} \rightarrow \pi_2^* | H_{SO} | d_{yz} \rightarrow \pi_2^* \rangle \quad (6.6)$$

where d_{yz} is the HOMO, d_{xz} is the HOMO-1, π_1^* and π_2^* are the LUMO and LUMO+1, respectively. For the reasons discussed above the $\frac{1}{2} \langle d_{yz} \rightarrow \pi_1^* | H_{SO} | d_{yz} \rightarrow \pi_2^* \rangle$ and $\frac{1}{2} \langle d_{xz} \rightarrow \pi_1^* | H_{SO} | d_{xz} \rightarrow \pi_2^* \rangle$ integrals do not contribute.

In terms of the role of sub picosecond ISC for these complexes, in Chapter 3 we have seen, for $[\text{Cu}(\text{dmp})_2]^+$, that efficient ISC occurs along the flattening coordinate where the S_1 state becomes degenerate with the T_2 , T_3 and T_4 states. This is a clear example of the Landau-Zener formalism, used for spin crossings in molecular systems, when the rate of ISC is not only dependent on the SOC matrix elements, but the gap between the two coupled states. To assess this for $[\text{Cu}(\text{dmdp})_2]^+$, Fig. 6.4 shows the excited states and SOC matrix elements along its flattening coordinate. Importantly, the T_3 and T_4 states cross S_1 and S_2 , and in company with the significant coupling at the corresponding crossing points, one could expect bifurcation of the wavepacket and ultrafast ISC as shown in Chapter 3 for $[\text{Cu}(\text{dmp})_2]^+$.

For complexes, in both the ground and lowest triplet states, which exhibit a broken symmetry and a flattened dihedral angle, the SOC matrix elements are significantly reduced to $< 50 \text{ cm}^{-1}$. This is because the main configurations for both the S_1 and T_1 states correspond to the $d_{yz} \rightarrow \pi_1^*$ transitions. Therefore, SOC integrals work between ligand-centered MOs instead of metal-centered MOs, which do not offer the change in orbital angular momentum upon the change of spin.

Finally in the ground state geometry, substitution of alkyl chains into the positions 2,9 ($[\text{Cu}(\text{dbp})_2]^+$ and $[\text{Cu}(\text{dbtmp})_2]^+$) on the phenanthroline ligands reduces the SOC between the S_1 and T_1 , but increases it for S_1 and S_2 with T_3 and T_4 . This is because the d-orbitals are slightly more split leading to purer excitations. Since probability of hopping is not zero only at the crossing points between the S_1 and S_2 surfaces with T_3 and T_4 , Cu(I)-phenanthroline with alkyl substituents are more likely to have a faster intersystem crossing.

6.3.2 Molecular dynamics

In the previous sections, we have focused on the role of the electronic and structure properties of these complexes on the emission characteristics. However, it is well-documented that

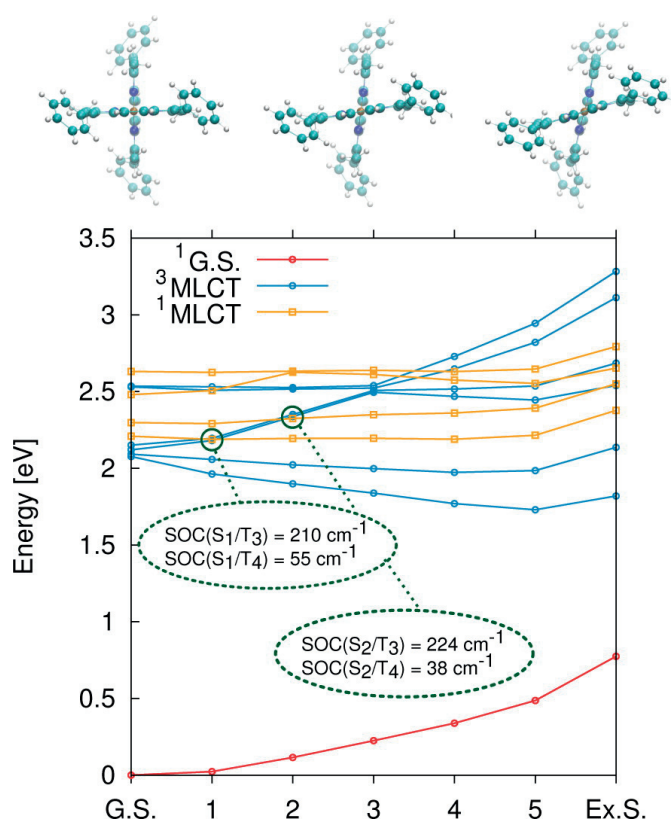


Figure 6.4: Energy, in eV, of the ground state (red) singlet (orange) and triplet (green) MLCT excited state of $[\text{Cu}(\text{dmdp})_2]^+$ along the direct coordinate that connects the ground with the excited state geometry. Spin orbit coupling elements, in cm^{-1} between S_1 and S_2 with T_3 and T_4 is shown as well. Zero energy corresponds to the binding energy of the ground state configuration.

molecular environment, especially the solvent, also plays a crucial role in its lifetime. Indeed, as outlined in the introduction, extensive characterisation of McMillin and co-workers [68] has demonstrated that the emission lifetimes of Cu(I)-phenanthrolines can be significantly shortened in donating solvents (i.e. those behaving as Lewis bases), such as MeCN [70]. They attributed this quenching to complexation of a solvent molecule (exciplex) that most likely occurs at the metal centre. The interaction between the Cu(II) atom and the electron-rich donor molecule is thought to stabilise the excited state relative to the ground state, reducing the energy gap and, therefore, increasing the rate of nonradiative decay [81]. However, a recent time-resolved X-ray absorption spectroscopy study [88] has demonstrated that the transient XAS spectrum is the same for $[\text{Cu}(\text{dmp})_2]^+$ in MeCN and DCM. This means that at all present, complexation with a solvent molecule at the metal atom is not visible on the transient XAS spectra. Consequently, despite the extensive measurements, the exact nature of the solute-solvent interaction is still undetermined.

Computationally the most expedient way of addressing this is to use molecular dynamics, which makes it possible to study the dynamics of these complexes with an explicit description

Chapter 6. Study of the emission properties of Cu(I)-phenanthroline complexes

of the solvent. Hybrid quantum-classical methods, such as QM/MM, offer a way of accurately treating the electronic structure of the solute while explicitly including the effects of the solvent. While useful, for the size of the systems considered herein, the time scale accessible for QM/MM simulations is of a few picoseconds. As an accurate statistical analysis of the solvent structure requires longer simulations, we supplement these simulations with purely classical simulations.

Classical vs QM/MM Structural: The mean values and standard deviations of the main structural parameters obtained from the QM/MM and classical MD simulations are shown in Table 6.7.

The additional parameters for the force-field were obtained by calculating the Hessian matrix for the Cu(I)-phenanthroline shown in Fig. 6.1, in both the ground singlet state, $^1\text{MLCT}$, and the triplet state, $^3\text{MLCT}$. We employed, in fact, for simulating the dynamics of the molecule in the ground and in the excited triplet state two different sets of force fields due to the important structural changes of the photoexcited system. As an example, we report and discuss here the $[\text{Cu}(\text{dmp})_2]^+$ force field, Tables 6.5 and 6.6, keeping in mind that similar considerations can be done for the other complexes. As reported in Table 6.5, the equilibrium distance between the central copper and the close N atoms decreases in the triplet excited states (from 2.11 Å to 2.02 Å). Such shortening arises from the charge transfer, in the excited state, from copper to a ligand-centered π^* orbital (see Fig. 3.2 for a representation of these orbitals). As a consequence, the force constant that describes this bond increases fourfold (from 57 to 202 Kcal mol $^{-1}$). Moreover, the flattening of the molecule, in the triplet state, leads to a change of the equilibrium value of the angles and dihedrals defined by the central copper and the neighbor atoms. Notably, the pseudo-Jahn-Teller distortion changes the angle between the ligands, for $[\text{Cu}(\text{dmp})_2]^+$, from 90° to 77°. This value depends, as described in the next sections, on the substituents attached to the phenanthroline ligands.

Force constants and the barrier potential of the dihedral angles calculated for $[\text{Cu}(\text{dmp})_2]^+$ were used for all the other complexes, changing, of course, the equilibrium values. $[\text{Cu}(\text{dpp})_2]^+$, $[\text{Cu}(\text{tpp})_2]^+$ and $[\text{Cu}(\text{dbp})_2]^+$ represent an exception: force constants parameters, for Cu-N and N-Cu-N angles, calculated for $^3\text{MLCT}$ were applied also to the ground state case.

The validity of the classical MD force fields was assessed by comparing average value and standard deviation of some relevant structural parameters with the ones obtained by Car-Parrinello (CP) QM/MM MD simulations. Fig. 6.5 shows such comparison for $[\text{Cu}(\text{dmp})_2]^+$, for both the ground and the lowest triplet excited state. All the characteristic geometrical features are well represented by our parametrization. The only exceptions are the NCuN cis and trans angles, in the excited states, that in the classical description have a narrower distribution, meaning that these angles are more rigid than in the CP simulation.

The mean values and standard deviations of the main structural parameters obtained from

Table 6.5: Parameters used for $[\text{Cu}(\text{dmp})_2]^+$ in Classical MD for the ground state $^1\text{MLCT}$ and the first excited $^3\text{MLCT}$ structure: K_{bond} (Kcal mol^{-1}), K_θ ($\text{Kcal mol}^{-1} \text{rad}^{-1}$) and $V_\gamma/2$ (Kcal mol^{-1}). The parameters for the other complexes can be found in [231]

Bond	$^1\text{MLCT}$		$^3\text{MLCT}$			
	R_{eq}	K_{bond}	R_{eq}	K_{bond}		
Cu-N	2.11	57	2.02	202		
Angle	θ_{eq}	K_θ	θ_{eq}	K_θ		
N-Cu-N (intra)	80.6	10	83.4	58		
N-Cu-N (cis)	125.5	3.3	110.6	58		
N-Cu-N (trans)	125.5	3.3	139.6	58		
Cu-N-CA	129.0	40	129.4	158		
Cu-N-CB	111.6	26	110.8	158		
N-CA-CA	121.2	54	120.7	54		
N-CB-CB	127.7	70	117.7	70		
N-CA-CT	118.7	64	118.7	64		
CB-CB-CH	119.3	43	120.0	43		
Dihedral	γ_{eq}	$V_\gamma/2$	n	γ_{eq}	$V_\gamma/2$	n
N-Cu-N-CB (intra)	0	4.4	1	-1	4.4	1
N-Cu-N-CB (cis)	-127	4.4	2	-141	4.4	3
N-Cu-N-CB (trans)	127	4.4	2	113	4.4	3
N-Cu-N-CA (intra)	180	4.4	1	-173	4.4	1
N-Cu-N-CA (cis)	-53	4.4	2	-60	4.4	3
N-Cu-N-CA (trans)	53	4.4	2	46	4.4	3
Cu-N-CB-CB	180	3.4	2	2	1.0	3
Cu-N-CA-CA	180	4.8	2	-4	1.0	3

Table 6.6: Charges, calculated with the RESP method, used for $[\text{Cu}(\text{dmp})_2]^+$ in Classical MD for the ground state $^1\text{MLCT}$ and the first excited $^3\text{MLCT}$ structure.

Atom	$^1\text{MLCT}$	$^3\text{MLCT}$
Cu	0.53	0.74
N	-0.38	-0.49
C1	0.38	0.44
C2	-0.24	-0.32
C3	-0.11	-0.08
C4	0.08	0.03
C5	-0.19	-0.20
C6	0.15	0.21
CT	-0.43	-0.48
H2	0.16	0.18
H3	0.16	0.16
H5	0.16	0.17
HC	0.14	0.15

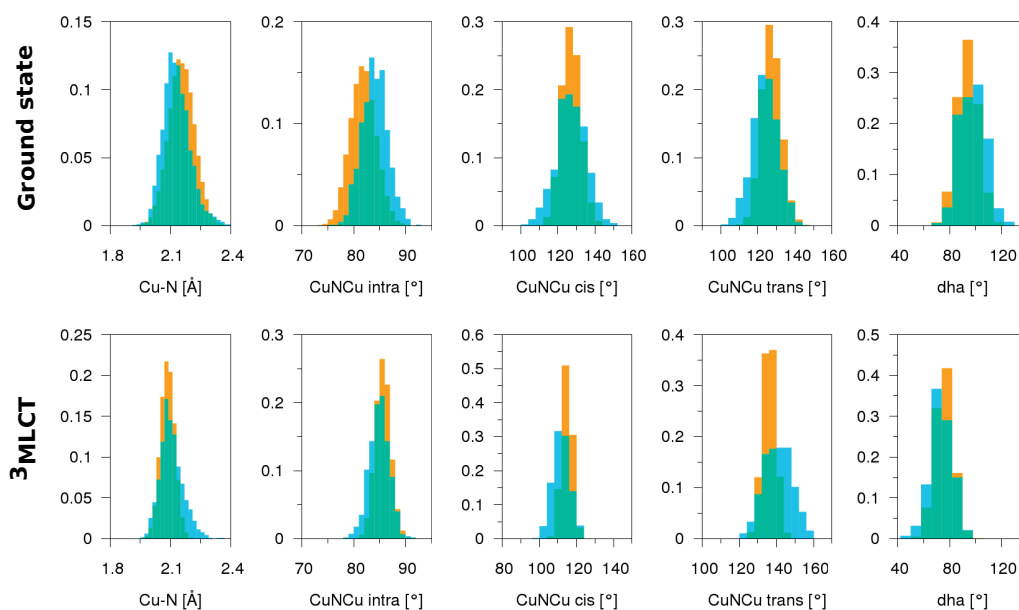


Figure 6.5: Distribution obtained by Classical (*orange*) and QM/MM (*blue*) MD simulation of the bond Cu-N, the angles N-Cu-N and the dihedral angle describing the distortion between the ligand planes for the ground state of $[\text{Cu}(\text{dmp})_2]^+$

the QM/MM and classical MD simulations for all complexes are shown in Table 6.7. Also for the other systems computed with both methods ($[\text{Cu}(\text{phen})_2]^+$, $[\text{Cu}(\text{dpp})_2]^+$, $[\text{Cu}(\text{dbp})_2]^+$), we find close agreement, verifying the validity of the force-fields. However, there is one notable exception, namely the dihedral angle between the ligands of $[\text{Cu}(\text{dpp})_2]^+$ in both the ground and excited states. This is because, as previously noted, for the phenyl substituted complexes the dihedral angle is quite sensitive to the DFT functional and the description of weak $\pi-\pi$ interactions. For this complex, the force field is parameterised using DFT(BLYP) and incorporated the effect of the weak $\pi-\pi$ interactions through the D2 Grimme's dispersion correction [249]. In contrast, during the QM/MM simulations, these interactions were addressed using the Dispersion-Corrected Atom-Centered Potential (DCACP) [226, 227] method. This results in a larger dihedral angle in the case of the latter, which is in better agreement with previous experimental observations [258, 87]. Importantly, an additional gas phase geometry optimisation performed within CPMD using DCACP demonstrated that the difference arises solely from the description of these weak $\pi-\pi$ interactions and is not a structural change induced by the solvent shell. However, this difference in the dihedral angle does not have a significant effect on the structure of the first solvation shell in the ground state. While, as a consequence of this large dihedral angle in the classical MD simulations, a slightly stronger solute-solvent interaction is observed in the excited state (see Fig. 6.5), this does not change the qualitative interpretation of the results as discussed below.

Finally, an additional check was performed comparing the radial distribution function $g(r)$ and the integrated radial distribution function $N(r)$ of MeCN nitrogen around the copper of

$[\text{Cu}(\text{dmp})_2]^+$, $[\text{Cu}(\text{phen})_2]^+$, $[\text{Cu}(\text{dpp})_2]^+$ and $[\text{Cu}(\text{dbp})_2]^+$ obtained from the classical and the CP simulations, shown in Fig. 6.6. One of the differences between the two methodologies is the amount of noise in the CP simulations. This arises from the fact that, due to the larger computational cost, CP simulations can not reach statistical convergency (the data were extracted from a 2 ps long dynamics, in contrast to the 15 ns long dynamic with classical parametrization). Notably, this is the case of $[\text{Cu}(\text{dpp})_2]^+$. The classical radial distribution function of this complex, in the triplet state, exhibit a peak that is not present in the CP simulations. This lack is produced by a flip of the flattening distortion from one configuration to the opposite one, in the middle of the dynamics. This leads to a subsequent reorganization of the solvent, especially that region that, due to the sudden change of structure, has been pushed away from its previous location. However, since the dynamics is run only for 2 ps, the solvent has not enough time for readjusting and this is reflected in the non-equilibrated CP radial distribution function. On the other hand, CP simulations can better describe the electronic distribution of the quantum system and thus the interaction with the solvent. This can be clearly observed in the case of $[\text{Cu}(\text{phen})_2]^+$. Here, CP distributions are shifted to smaller distances (0.3 Å), meaning that the MeCN nitrogens strongly interact with the central copper.

Table 6.7: Mean Values for Selected Geometrical Features with Corresponding Standard Deviations (σ) from the QM/MM and Classical Simulations.

	Method	Ground State			³ MLCT		
		Cu-N (Å)	$\angle \text{NCuN}_{\text{intra}}$ (°)	$\angle \text{dha}$ (°)	Cu-N (Å)	$\angle \text{NCuN}_{\text{intra}}$ (°)	$\angle \text{dha}$ (°)
$[\text{Cu}(\text{phen})_2]^+$	CMD	2.00 (0.066)	83 (2.6)	90 (9)	1.98 (0.035)	85 (1.4)	48 (7)
	QMMM	2.03 (0.075)	83 (2.5)	82 (20)	2.01 (0.073)	83 (3.4)	41 (9)
$[\text{Cu}(\text{dmp})_2]^+$	CMD	2.03 (0.07)	84 (2.5)	94 (10)	1.99 (0.03)	85 (2.00)	70 (7)
	QMMM	2.034 (0.06)	81 (2.5)	90 (8)	2.00 (0.07)	85 (1.5)	70 (8)
$[\text{Cu}(\text{tfp})_2]^+$	CMD	2.08 (0.062)	81 (2.5)	90 (7)	2.02 (0.036)	85 (1.5)	75 (7)
$[\text{Cu}(\text{dmdp})_2]^+$	CMD	2.00 (0.065)	81 (2.6)	94 (11)	1.98 (0.036)	84 (1.6)	76 (7)
$[\text{Cu}(\text{dpp})_2]^+$	CMD	2.02 (0.036)	85 (1.5)	55 (7)	4.95 (0.035)	89 (1.6)	51 (7)
	QMMM	2.08 (0.091)	83 (2.8)	67 (9)	2.04 (0.086)	84 (3.1)	64 (12)
$[\text{Cu}(\text{dpdmp})_2]^+$	CMD	2.01 (0.036)	85 (1.5)	54 (7)	2.01 (0.080)	88 (1.6)	52 (7)
$[\text{Cu}(\text{dptmp})_2]^+$	CMD	2.01 (0.036)	85 (1.5)	65 (7)	1.95 (0.036)	88 (1.5)	65 (7)
$[\text{Cu}(\text{tpp})_2]^+$	CMD	2.05 (0.036)	84 (1.5)	53 (7)	1.94 (0.036)	88 (1.6)	51 (7)
$[\text{Cu}(\text{dbp})_2]^+$	CMD	2.04 (0.056)	81 (1.4)	87 (6)	2.02 (0.036)	83 (1.6)	74 (7)
					1.98 (0.036)	84 (1.6)	
	QMMM	2.05 (0.087)	83 (2.7)	95 (10)	2.02 (0.081)	85 (2.7)	78 (11)
$[\text{Cu}(\text{dbtmp})_2]^+$	CMD	2.05 (0.062)	81 (2.5)	90 (7)	2.00 (0.072)		
					2.02 (0.035)	84 (1.5)	77 (7)

Analysis of the Solvation Structure: Figures 6.7, 6.8 and 6.9 show the Cu- N_{MeCN} and Cu- Cl_{DCM} radial distribution functions (RDF) and distance dependent coordination number $N(r)$ for both the ground and excited states extracted from the classical MD simulations. For $[\text{Cu}(\text{phen})_2]^+$, $[\text{Cu}(\text{dmp})_2]^+$, $[\text{Cu}(\text{dpp})_2]^+$ and $[\text{Cu}(\text{dbp})_2]^+$ these are compared to the RDFs obtained from the QM/MM MD configurations in Fig. 6.6.

The red trace in Fig. 6.7 corresponds to the solvation structure for $[\text{Cu}(\text{phen})_2]^+$. As this

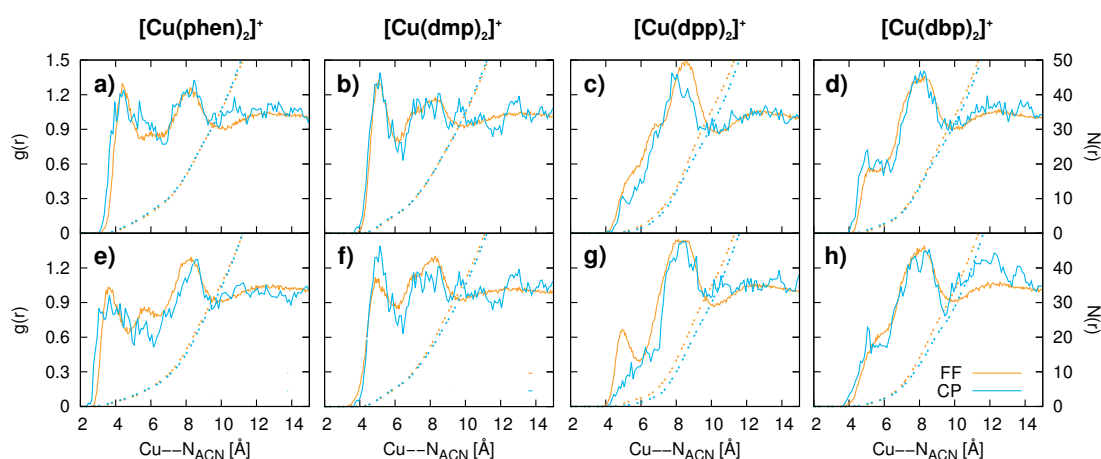


Figure 6.6: Comparison between Classical and QM/MM MD's radial distribution function $g(r)$ (solid line) and integrated radial distribution function $N(r)$ (dashed line) of $[\text{Cu}(\text{phen})_2]^+$, $[\text{Cu}(\text{dmp})_2]^+$, $[\text{Cu}(\text{dpp})_2]^+$ and $[\text{Cu}(\text{dbp})_2]^+$ in the ground state (a-d) and in the the lowest triplet excited state (e-h).

complex has no substituents on the phenanthroline ligands it is expected to exhibit the largest interaction with the solvent and indeed, this is observed in both the ground and excited states. For MeCN, the first Cu-N_{MeCN} solvation shell in both the ground and excited states is observed at ~ 4 Å. However, importantly in both case it is not a distinct structure separated from the bulk solvent, and the RDF indicates continual exchange between the first solvation shell and the bulk. Indeed, this is actually accentuated in the excited state, and demonstrates that while, due to the large flattening angle there is likely to be a solvent interaction at the Cu atom, it is weak ($r > 3$ Å) and, therefore, is transient in nature meaning it cannot be classified as an exciplex. Interestingly, the RDF for the complex dissolved in DCM shows that the solvent molecule are able to come slightly close to the copper atom. In this case, the very large dihedral angle in the excited state, introduces no steric hindrance for either the chlorine or nitrogen atoms and, therefore, this observation arises purely from electrostatic considerations.

This observation would appear to rule out the possibility of a distinct solvent effect on the lifetime of $[\text{Cu}(\text{phen})_2]^+$, which was recently shown experimentally by Hua *et al.* [266]. They reported that the excited state decay dynamics of $[\text{Cu}(\text{phen})_2]^+$ is dominated by 2 distinct timescales, 0.2 ps and 1.8 ps. The first, which was assigned to the flattening of the ligands is 0.1 ps in MeCN due to the lower viscosity of this solvent. The latter time constant (1.8 ps) was assigned to the lifetime of the S₁ state. This was reported to be 1.4 ps in MeCN, and this slight shortening was assigned to the stabilisation of the charge- transfer character state in a more polar solvent. Interestingly, the difference in the total lifetime reported by Chen *et al.* [85] is because a small portion of ISC to the triplet occurs for the complex in DCM and not MeCN. However, this is not a solvent effect, but arises from a small portion of the wavepacket that enters the T₁. While, due to the lifetime this cannot occur at the flattened state, this must

occur along the flattening coordinate where the low lying triplets are degenerate with the S_1 state, as proposed to be the reason for sub picosecond ISC in $[\text{Cu}(\text{dmp})_2]^+$. The residence time at the closest distance was estimated, for $[\text{Cu}(\text{dmp})_2]^+$, to be $\sim 100 - 200$ fs, before returning to the bulk.

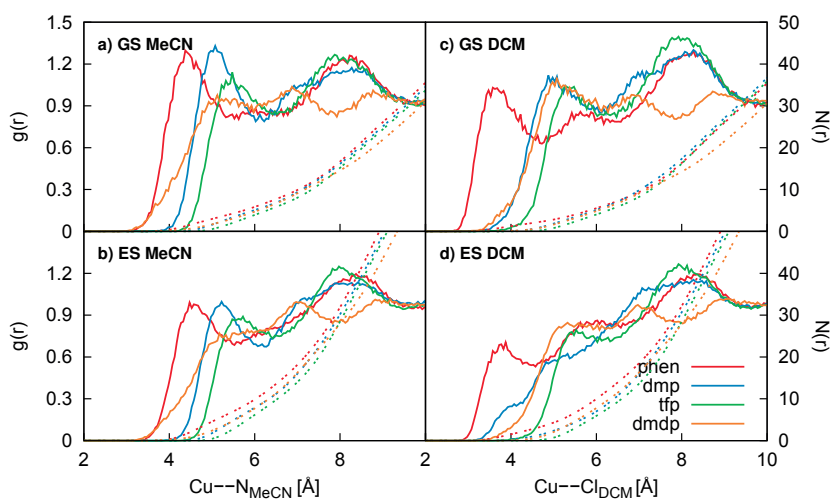


Figure 6.7: Comparison between Classical and QM/MM MD's radial distribution function $g(r)$ (solid line) and integrated radial distribution function $N(r)$ (dashed line) of $[\text{Cu}(\text{dmp})_2]^+$, $[\text{Cu}(\text{tfp})_2]^+$ and $[\text{Cu}(\text{dmdp})_2]^+$ in a,c) the ground and b,d) the lowest triplet excited states in MeCN and DCM.

The effect of the addition of small substituents, CF_3 ($[\text{Cu}(\text{tfp})_2]^+$) and CH_3 ($[\text{Cu}(\text{dmp})_2]^+$ and $[\text{Cu}(\text{dmdp})_2]^+$) in the positions 2,9 are shown in Fig.6.7. In both cases the first solvation shell shifts further away from Cu, as expected. However, while the peaks of the first solvation shells appear at the similar distances, the additional steric hindrance of the fluorine atoms, in comparisons to the hydrogens, means that there is a smaller probability of solvent molecules coming to shorter ($<4 \text{ \AA}$) distances.

Fig. 6.8 shows the effect of adding phenyl ligands in the positions 2,9 of the phenanthroline ligands. In comparison to those complexes with only small substituents, the effect, as expected is quite stark. While there is the appearance of a weak first solvation shell around $\sim 5 \text{ \AA}$, the probability of finding solvent molecules here is significantly reduced. Indeed the main feature in the RDF does not occur until between 8-10 \AA away from the copper. We also observe much smaller changes between the ground and the excited state solvent structures, consistent with small changes in the structure of the solute. This confirms that, while a weak solvent effect is still observed for these complexes, it does not arise from an excited state

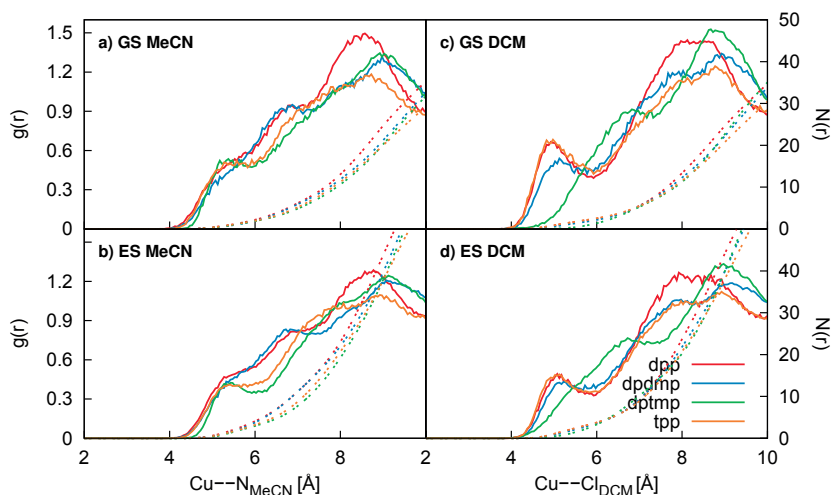


Figure 6.8: Comparison between Classical and QM/MM MD's radial distribution function $g(r)$ (solid line) and integrated radial distribution function $N(r)$ (dashed line) of $[\text{Cu}(\text{dpp})_2]^+$, $[\text{Cu}(\text{dpdm})_2]^+$ and $[\text{Cu}(\text{dptmp})_2]^+$ in a,c) the ground and b,d) the lowest triplet excited states in MeCN and DCM.

effect, rather from a particular solvent structure that is also present in the electronic ground state.

Finally, Fig. 6.9 shows the effect of adding alkyl substituents in the positions 2,9 of the phenanthroline ligands. Like the phenyl substituents, these significantly reduce the magnitude of the first solvation shell. Again the substituents on the backs of the ligands have only a very small effect at short distances ($< \sim 6 \text{ \AA}$). This effect is larger at ($> \sim 6 \text{ \AA}$) and are associated with the second solvation shell being shifted backwards. Although this will reduce the interaction between the solvent and the complex, it is expected to have very little effect on the lifetime arising from solvent interactions.

While useful, the RDFs presented in the previous section do not contain information about the angular distribution of the solvent shell. Fig. 6.10 shows the solvent density around the $[\text{Cu}(\text{phen})_2]^+$, $[\text{Cu}(\text{dpp})_2]^+$ and $[\text{Cu}(\text{dbp})_2]^+$. For $[\text{Cu}(\text{phen})_2]^+$, this shows an ordered first solvation shell, which follows and intercalates along the lines of the phenanthroline ligands in a manner similar to that reported for $[\text{Ru}(\text{bpy})_3]^{2+}$ [233, 234] and $[\text{Fe}(\text{bpy})_3]^{2+}$ [267, 216]. Importantly, as indicated by the RDFs, the solvent structure does not change significantly in the excited state, indicating that while a weak solvent effect is present in the excited state, it does not arise from an excited state effect, but rather from a particular solvent

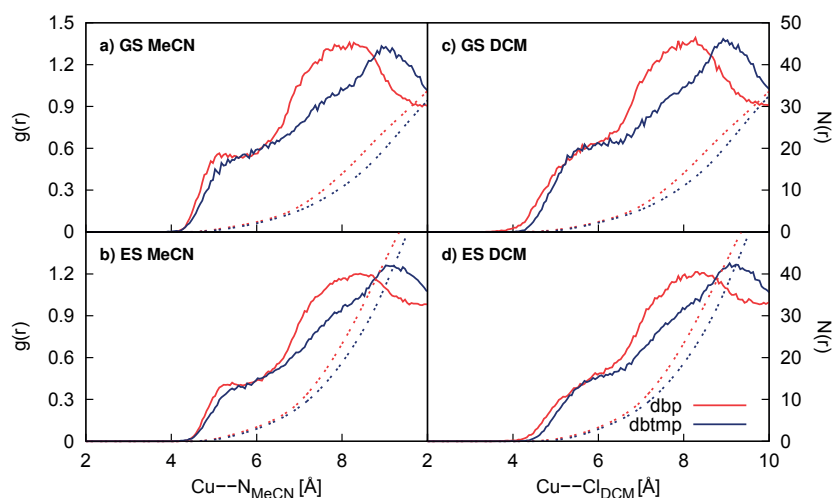


Figure 6.9: Comparison between Classical and QM/MM MD's radial distribution function $g(r)$ (solid line) and integrated radial distribution function $N(r)$ (dashed line) of $[\text{Cu}(\text{dbp})_2]^+$ and $[\text{Cu}(\text{dbtmp})_2]^+$ in a,c) the ground and b,d) the lowest triplet excited states in MeCN and DCM.

structure that is also present in the electronic ground state.

Upon addition of substituents in the positions 2,9 ($[\text{Cu}(\text{dpp})_2]^+$ and $[\text{Cu}(\text{dbp})_2]^+$), the order is slightly reduced due to the disruption of these

In order to confirm that no exciplex are formed, we calculated the ground state (DFT) and the excited states (TDDFT) potential energy surfaces of the system composed by $[\text{Cu}(\text{dmp})_2]^+$ and a molecule of MeCN as a function of the $\text{Cu}-\text{N}_{\text{MeCN}}$ distance (see Fig. 6.11). We found that the equilibrium distance starts at around 4.2 Å, in agreement with the radial distribution functions shown in Fig. 6.7 that show that the probability of the solvent to approach the copper atom within 3.5-4.00 Å, is small. Plotting the T_1 -ground state energy gap (1.55 eV) and associated experimental lifetime on the exponential curve, Fig. 6.3, we observe that this stabilization largely accounts for the quenching of the luminescence. It is interesting to note that for our calculation of the energy gap, excluding the solvent, the experimental lifetime lies just above the exponential curve, while for the $[\text{Cu}(\text{dmp})_2]^+ + \text{MeCN}$ model lies below it. This is because although the solvent molecule reduces the energy gap between T_1 and the ground state, it also slightly reduces the gap between T_1 and S_1 , especially when $\text{Cu}-\text{N}_{\text{MeCN}}$ is less than 4.0 Å. This will increase the mixing of the state and, therefore, increase the phosphorescence rate.

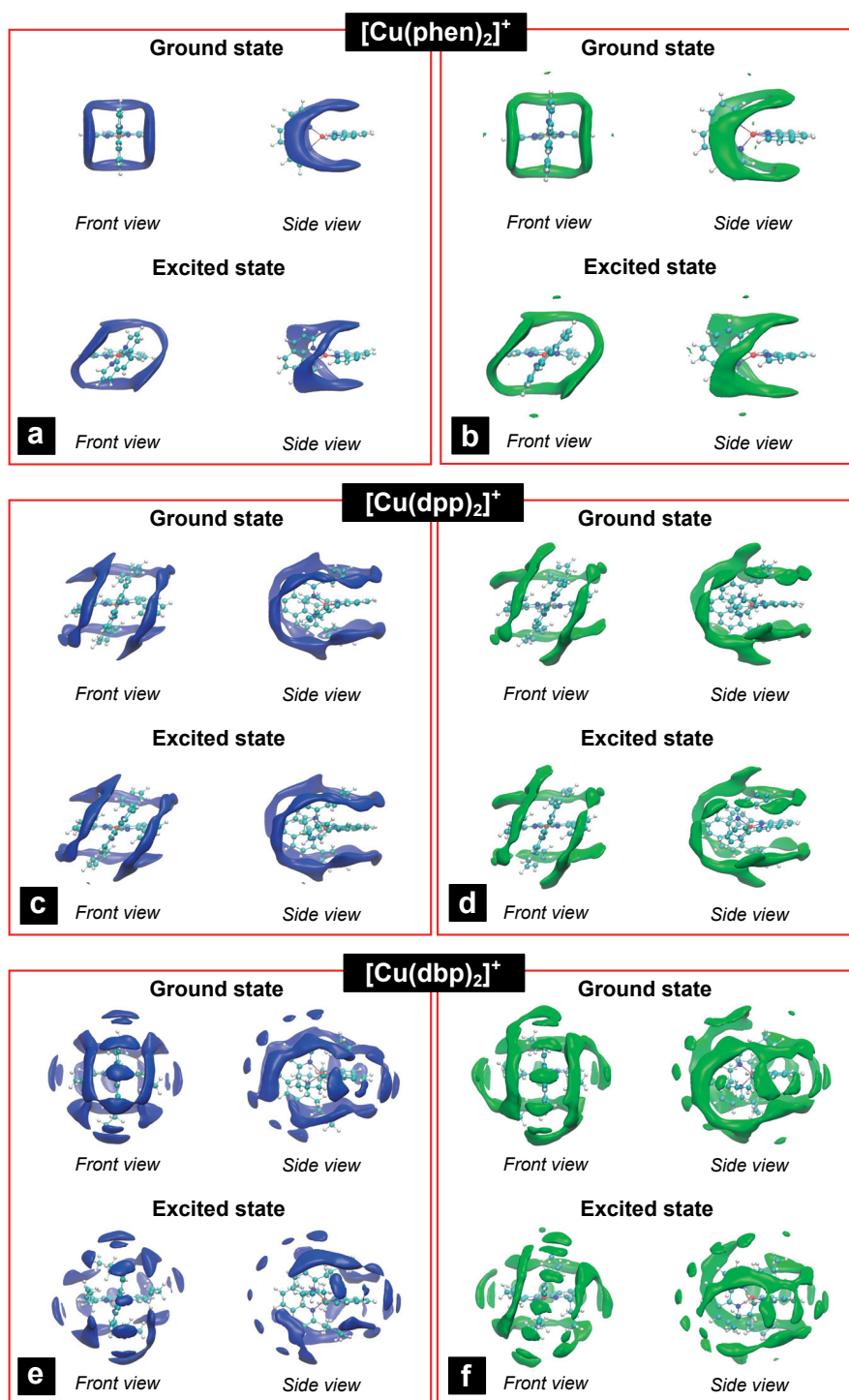


Figure 6.10: Solvent density of MeCN (blue) and DCM (green) around $[\text{Cu}(\text{phen})_2]^+$, $[\text{Cu}(\text{dpp})_2]^+$ and $[\text{Cu}(\text{dbp})_2]^+$, in both the ground and $^3\text{MLCT}$ state.

6.4 Discussions

The photophysical properties of Cu(I)-phenanthroline complexes have drawn significant attention owing to a range of possible applications. However, so far the applications of these

complexes have been prohibited by strong solvent and structure dependent lifetime, which has made understanding, let alone predicting their photophysical properties a significant challenge. In the previous sections, we have presented detailed simulations studying the role of the electronic and geometric structure, the SOC and the solvent environment in the excited state properties. In this section, we discuss the implications of these results and possible pathways to further develop their applicability.

Importantly, the timescale associated with understanding the photophysical properties of these complexes can be split into two distinct classes. The first includes processes that occur within the femtosecond domain and that are dominated by non-adiabatic phenomena. Importantly, these initial steps are completed within a few tens of picoseconds and are broadly equivalent for all of the complexes. Consequently, one would expect that these dynamics should not have a significant impact on the potential application of these complexes. The second class is processes that occur on the pico- to microsecond timescales, strongly associated with the radiative and non-radiative emission. As these are strongly affected by structural, electronic and solvent modifications, it is these that have been the focus of this present work. In the following paragraphs we outline the ingredients for designing a long live and high quantum yield complex.

As demonstrated by McMillin and co-workers, the solvent has a significant effect on the lifetime of the excited state. However, contrary to the previous conclusion and in agreement with a recent time-resolved XAS study [88], our classical and QM/MM MD simulations demonstrate that exciplex formation does not occur for these Cu(I)-phenanthroline complexes. Although the open structure of the complex in the excited state does lead to increased solute-solvent interactions, this is a transient mechanism which arises from a solvent structure which is already present in the ground state. In terms of extending the lifetime it is clear that reducing the effect on the solvent environment is highly desirable. Our MD simulations have demonstrated that the solvent-solute interaction is more or less comparable for any substituent in the positions 2,9, which is bulkier than CH₃ or CF₃. In addition, substituent in the positions 3,4,7 and 8, push the first solvation shell back slightly further reducing the effect of the solvent. However, one must remain mindful of the electronic effect of additional substituents, which we have found are dominant. Indeed, this is epitomised by [Cu(dpp)₂]⁺, [Cu(dpdpmp)₂]⁺ and [Cu(dptmp)₂]⁺. These complexes all exhibit similar solvation shell structures and quenching, but the variation in their lifetimes are dominated by the $\Delta E(S_1-T_1)$.

Electronically, our simulations, in agreement with previous experimental observations demonstrate that the absorption spectrum is only strongly dependent on the dihedral angle between the ligands. In the case of structures distorted from the equilibrium, a strong vibronic band (550 nm) is observed at energies lower than the main MLCT absorption band (400-500 nm). This is, happily not the case for the emission properties, which demonstrate that substituents effects can have a strong effect on the luminescent properties providing the opportunity to fine tune their properties for a particular application. Firstly, any sub-

stituents in the positions 2,9 increases the emission energy compared to $[\text{Cu}(\text{phen})_2]^+$. This is simply due to the smaller dihedral angle. Indeed, as demonstrated with $[\text{Cu}(\text{tfp})_2]^+$, the main way to tune the emission energy is through the dihedral angle. As a general rule, the larger the dihedral the smaller the emission energy, the smaller the lifetime and the smaller the quantum yield and non radiative effects contribute. Addition effects of fine tuning the ligands can be achieved using groups in the positions 3,4,7 and 8, which exhibit an inductive effect. This is demonstrated in the complexes with methyl substituents, as they increase the energy of the emitting state and, by increasing the spatial overlap between the orbitals involved in the excited states increase the $\Delta E(S_1-T_1)$.

Tuning the $\Delta E(S_1-T_1)$ also helps control the emission lifetime. Indeed, this is usually smaller for states of MLCT character than for states, which are mainly localised at the ligands, i.e. ligand centred (LC) states [13] because for the former case, the interactions between the unpaired electrons are smaller due to the larger spatial separation of the involved orbitals. Consequently, groups in the positions 3,4,6,7 that extend the π -network, such as phenyl, further reduce this interaction and, therefore, reduce $\Delta E(S_1-T_1)$, while electron donating groups, such as methyl increase this gap, increasing the lifetime, as demonstrated for $[\text{Cu}(\text{dpdmp})_2]^+$ and $[\text{Cu}(\text{dptmp})_2]^+$ compared to $[\text{Cu}(\text{dpp})_2]^+$ and $[\text{Cu}(\text{dbtmp})_2]^+$ compared to $[\text{Cu}(\text{dbp})_2]^+$. In going from a phenyl to alkyl substituent, this effect is reduced.

The quantum yield of these complexes is enhanced by perpendicular structures. Therefore, phenyl groups are not much better than methyl substituents. This means that alkyl substituents are the best, recently demonstrate Ref. [82], which reports a Cu(I)-phenanthroline complex with a lifetime and quantum yield comparable to $[\text{Ru}(\text{bpy})_3]^{2+}$.

6.5 Conclusions

Herein we have presented a detailed theoretical investigation of the emission properties of ten Cu(I)-phenanthroline complexes. These simulations allow us to draw the following conclusions; i) The MD simulations in the excited state of none of these complexes exhibit the formation of an exciplex. Instead, the solvent-solute interaction is transient and arises from a solvent configuration already present in the ground state. Importantly, although for no or small substituents in the positions 2,9 solvent quenching is a significant problem, for substituent larger than CH_3 , the strongest effect on the lifetime of the complex is the substituents influence on the electronic and geometric structure of the complex, rather than its ability to hinder the solvent interaction. ii) The complexes that exhibit the longest lifetime and highest quantum yield are those which exhibit a dihedral angle closest to 90° in the excited state, which during the present study is $[\text{Cu}(\text{dbp})_2]^+$ and $[\text{Cu}(\text{dbtmp})_2]^+$. This is because reducing the flattening angle maintains a significant energy gap between the ground and lower excited states, reducing non-radiative decay. iii) The addition of methyl groups in the positions 3,4,7 and 8 have a strong effect on the lifetime of the complexes, due to the reduction of the dihedral flattening.

Besides these homoleptic complexes, there has been a significant recent development in a wide range of heteroleptic and bimetallic complexes. These studies demonstrated that while it has taken some time, in terms of solar energy conversion schemes, Cu complexes present one exciting method for reducing the cost and overall environmental impact of new and existing solar energy technologies, for which it is hoped that these present results will help towards this goal.

7 Unravelling the photophysics of two long-living Cu(I)-phenanthrolines

In this final chapter, the emission properties of other two Cu(I)-phenanthroline complexes, $[\text{Cu}(\text{dsbp})_2]^+$ and $[\text{Cu}(\text{dsbptmp})_2]^+$, are investigated. Synthesized for the first time in 2014, such molecules thrilled the inorganic chemistry community thanks to their astonishing emission properties (long-lived emitting states, of the order of μs , and large quantum yield of 1.9%-6.3%), which finally makes this class of complexes a realistic candidate for solar applications.

By using the quantum mechanical tools presented in the previous chapter, a complete analysis of the interplay between geometry, electronic structure, and solvent effects is performed in order to identify what makes exceptional these complexes.

7.1 Introduction

The increasing energy demand is pressing to find an environmentally clean alternative to the traditional energy sources. Metal-organic complexes have emerged as building block for solar energy harvesting devices. As an example, Ru(II)-tris-bipyridine [158, 17, 159, 268], has been proposed as sensitizer for solar cells and photocatalytic systems. The success of this complex is due to its photophysical properties: it absorbs in the visible region of the spectrum, has a long living emitting state (MLCT) that can transfer electrons to titania nanoparticles, is chemically stable and exhibits reversible electrochemical behaviour. However, Ru is a rare earth element and its high cost, combined with its toxicity prevent it to be an environmentally sustainable and economical affordable system.

The research of a cheaper and environment friendly replacement have pushed the investigation on first-row metal complexes. Cu(I)-phenanthrolines are among the possible alternative [65, 269, 222, 270] but realistic applications of these compounds is limited by the short lifetime of the emitting states. The lowest triplet MLCT state decays rapidly to the ground state with a small quantum yield (for $[\text{Cu}(\text{dmp})_2]^+$ in acetonitrile it is 10^{-4} [69]). Quantum yield is the ratio between emitted and absorbed photons and, therefore, is a measure for eval-

Chapter 7. Unravelling the photophysics of two long-living Cu(I)-phenanthrolines

uating how many electrons the system can transfer to an active system, such as TiO_2 [269]. In order to build efficient dye-sensitized-solar-cells (DSSCs) or photocatalytic devices, one needs the highest possible quantum yield (the theoretical limit is 1). Such a low quantum yield is ascribed to large non-radiative decay rates. As we have seen in the previous chapter, the non-radiative rate depends on the energy gap between excited states and ground state (the smaller the gap, the larger the rate) and the electrostatic interaction with the solvent. The former, in addition, is contingent upon the extension of the pseudo-Jahn-Teller (PJT) distortion, which can further reduce the energy gap. However, several studies performed on different Cu(I)-phenanthroline [69, 70, 78, 82, 270, 271], have shown that it is very easy to tune the photophysics by changing the substituents group of the phenanthroline ligands. Notably, complexes with bulky alkyls substituents, such as $[\text{Cu}(\text{dbp})_2]^+$ and $[\text{Cu}(\text{dbtmp})_2]^+$ (see Chapter 6), are more likely to retain the ground state structure and prevent the PJT reorganization, leading to a larger quantum yield and longer emission lifetime.

Following this indication, in 2014 Castellano and co-workers [82] synthesized and characterized two Cu(I)-phenanthroline complexes with branched *sec*-butyl at the positions 2,9 (see Fig. 7.1). They found for $[\text{Cu}(\text{dsbp})_2]^+$ (dsbp =2.9-di-(*sec*-butyl-1,10-phenanthroline)) and for $[\text{Cu}(\text{dsbptm})_2]^+$ (dsbptm =2.9-di-(*sec*-butyl-3,4,7,8,-tetramethyl-1,10-phenanthroline)) very long luminescence lifetimes, of the order of μs , one order of magnitude longer than $[\text{Cu}(\text{dptmp})_2]^+$, and large photoluminescence quantum yield, respectively, 1.9% and 6.3%.

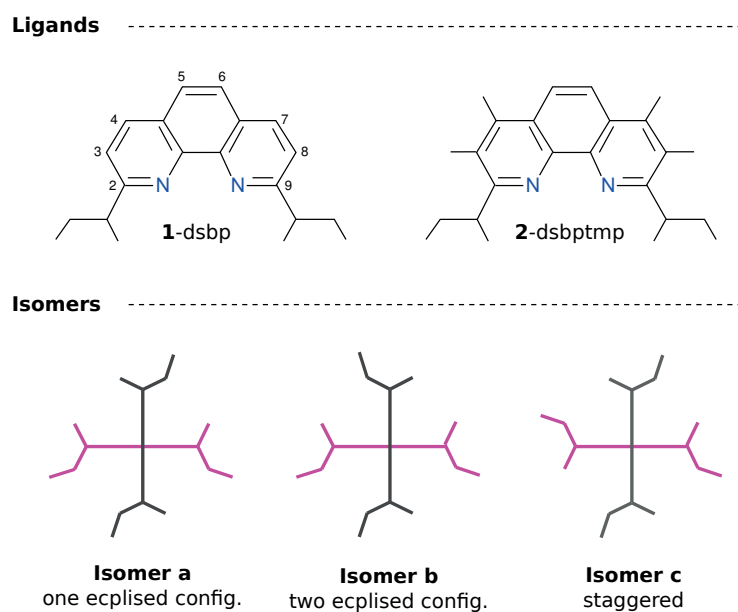


Figure 7.1: *Top.* : Phenanthroline ligands of the complexes studied in this work. *Bottom:* Different orientations of the *sec*-butyl substituents respect to the phenanthroline ligands, one depicted in grey and one in purple.

In order to understand the underlying factors behind these remarkable photophysical prop-

erties, we performed DFT and LR-TDDFT calculations of the geometric and electronic structures. Moreover, for analyzing the effects of the solvent, classical molecular dynamics (MD) simulations, combined with Car-Parrinello quantum mechanical/molecular mechanic (QM/MM) MD, were performed in both the ground state and the ³MLCT lowest excited state. We show that the exceptional photoluminescence properties of [Cu(dsbp)₂]⁺ and [Cu(dbptmp)₂]⁺ in solution are determined by their electronic and geometric features. The cumbersome *sec*-butyl substituents at the positions 2,9 of the phenanthroline ligands prevent the molecule, in the excited state, to be susceptible to large PJT distortions. As a consequence, ISC, which occurs principally when the molecule has a structure close to that of the ground state, is faster, leading to a rapid population of the long-lived triplet state. In addition, the interaction with the solvent is weak because the bulky structure of the complex pushes it to large distances, reducing the excited state stabilization effect.

7.2 Computational details

The preparation of the force field is described in details in the previous Chapter 6. Briefly, force constants and equilibrium values were computed by gas phase calculations with the Gaussian09 code [160] using the B3LYP [196, 247, 272, 248] exchange and correlation functional. Electronic wavefunction is described by a triple- ζ basis set (Cu) and double- ζ basis set (F, N, C and H). Charges were obtained with the Restricted Electrostatic Potential (RESP) [146] fixing the copper charges using the Mullikan definition. Classical molecular dynamics were carried out for 15 ns after equilibration.

QM/MM molecular dynamics were simulated using the CPMD code [273] in the Car-Parrinello fashion [152], using BLYP [196, 247] functional, including DCACP correction [226, 227, 257], and Martin-Trouiller pseudopotential [225] with a cut-off of 85 Ry. Each QM/MM MD was run for 20 ps after equilibration.

Excited state energies, from the optimized ground state and triplet excited state structures computed with Gaussian09, were calculated with the ADF package [250, 251] using B3LYP functional and the TZVP basis set for all atoms. Spin orbit coupling perturbation was included within the Wang-Ziegler formalism [162].

7.3 Results

Geometric structure Fig. 7.1-*Top* shows a scheme of the ligands composing the two Cu(I)-phenanthroline complexes presented in this chapter, [Cu(dsbp)₂]⁺ and [Cu(dsbptm)₂]⁺. Herein the molecules will be called respectively [Cu(**1**)₂]⁺ and [Cu(**2**)₂]⁺. The phenanthroline ligands of the two copper complexes differ only in the methyl groups present in the dsbptmp ligand at the positions 3,4,7 and 8. Importantly, the presence of the *sec*-butyl at the positions 2,9 means that these complexes can exist in three possible isomers shown in Fig 7.1-*Bottom*.

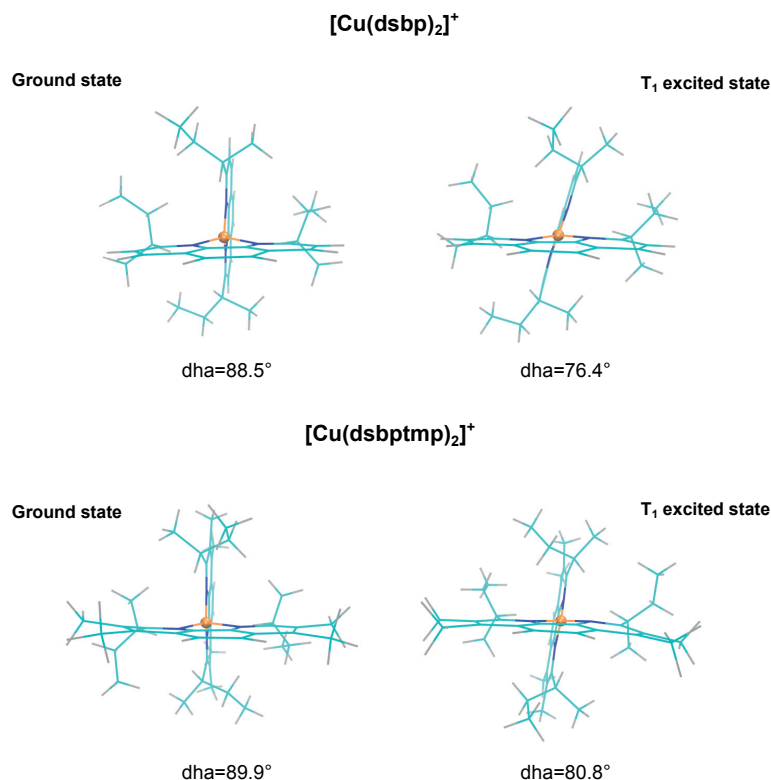


Figure 7.2: Ground state and excited state optimized geometries of [Cu(1)₂]⁺ and [Cu(2)₂]⁺

The isomers identified with the label *a* are the most stable for both [Cu(1)₂]⁺ and [Cu(2)₂]⁺ by respectively 0.08 eV and 0.07 eV (B3LYP gas phase calculation). Some relevant structural parameters for the optimized geometry of the isomers *a*, computed at DFT(BLYP) and at DFT(B3LYP) level of theory are reported in Table 7.1. These are largely in agreement, indicating only minor effects upon the inclusion of exact exchange. In the ground state, the two ligands of [Cu(1)₂]⁺ and [Cu(2)₂]⁺ are perpendicular in both cases and exhibit Cu-N distance of ~2.1 Å, slightly longer than reported for other related Cu(I)-phenanthroline complexes (see Table 6.1). The long-lived lowest excited state T₁ state exhibits a shorter Cu-N bond length and a smaller angle between the ligands. This flattening is smaller for [Cu(2)₂]⁺ as the additional steric hindrance caused by the methyl substituents in the positions 3,4,7 and 8 reduced the flattening distortion (Fig. 7.2). The ground state structural parameters of the isomers *b* and *c* of both complexes are similar to their more stable counterpart *a* and, for this reason, they are not reported here. The same is valid for the excited state structures of the isomers of [Cu(dsbptm)₂]⁺. On the other hand, in the excited state, the less stable isomers of [Cu(dsbp)₂]⁺ exhibit a larger angle between the ligands (BLYP: *a*=80.0, *b*=82.7, *c*=81.7; B3LYP: *a*=76.4, *b*=80.3, *c*=79.3). This asymmetry between [Cu(1)₂]⁺ and [Cu(2)₂]⁺ isomers can be explained in terms of steric impediment. The maximum amplitude of the flattening is determined by the size of the substituents at the positions 2,9 and their relative

orientations. However, the presence of methyl groups in the positions 3,4,7, and 8 adds a constraint to the conformational space of the molecule. As a consequence, the three isomers of $[\text{Cu}(\mathbf{2})_2]^+$ and the isomers *b* and *c* of $[\text{Cu}(\mathbf{1})_2]^+$ show the same flattening in the excited state while the stable isomer *a* of $[\text{Cu}(\mathbf{1})_2]^+$, due the more favorable rotational configuration of the *sec*-butyl substituents, exhibits a larger distortion.

Table 7.1: The DFT(B3LYP), DFT(BLYP) optimized geometries and the average structure obtained from classical and QM/MM MD simulations of the electronic ground state and lowest triplet state of the $[\text{Cu}(\text{dsbp})_2]^+$ (**1**) and $[\text{Cu}(\text{dsbptm})_2]^+$ (**2**).

	Method	Ground State			³ MLCT		
		Cu-N (Å)	∠ NCuN (°)	∠ lig-Cu-lig(°)	Cu-N (Å)	∠ NCuN (°)	∠ lig-Cu-lig(°)
$[\text{Cu}(\mathbf{1})_2]^+$	BLYP	2.09/2.12	81.9	87.8	2.01	83.7	80.0
	B3LYP	2.10/2.14	80.9	88.5	2.00	83.9	76.4
	QM/MM	2.05±0.08	83.5±2.5	87.5±10.9	2.01±0.08	84.3±2.7	75.0±11.11
	CMD	2.04±0.06	81.9±1.4	89.8±6.0	2.01±0.04	84.8±1.5	73.9±7.1
$[\text{Cu}(\mathbf{2})_2]^+$	BLYP	2.09/2.12	81.7	89.9	2.05/2.07	83.5	77.6
	B3LYP	2.10/2.14	80.9	89.9	1.97/2.13	80.9/85.6	80.8
	CMD	2.07±0.05	81.1±1.4	89.8±7.6	2.05±0.04	83.6±1.5	67.9±8.0

Table 7.2: ADF calculations of the singlet excited state. For each isomer of $[\text{Cu}(\mathbf{1})_2]^+$ and $[\text{Cu}(\mathbf{2})_2]^+$ energy (eV) and oscillator strength of the transitions are reported. Experimental values are obtained from Ref. [82]

	Exp. (nm)	Transition	Isomer a		Isomer b		Isomer c	
			E (eV)	<i>f</i>	E (eV)	<i>f</i>	E (eV)	<i>f</i>
$[\text{Cu}(\mathbf{1})_2]^+$	455 ^α (2.72)	S ₀ → S ₁	2.37	0.0010	2.37	0.0003	2.38	0.0010
		S ₀ → S ₂	2.43	0.0002	2.45	0.0001	2.45	0.0002
		S ₀ → S ₃	2.56	0.1060	2.59	0.1185	2.59	0.1186
$[\text{Cu}(\mathbf{2})_2]^+$	445 ^β (2.78)	S ₀ → S ₁	2.53	0.0000	2.51	0.0006	2.50	0.0018
		S ₀ → S ₂	2.59	0.0000	2.56	0.0000	2.56	0.0000
		S ₀ → S ₃	2.68	0.0002	2.64	0.0003	2.64	0.0019
		S ₀ → S ₄	2.69	0.0013	2.67	0.0003	2.69	0.0006
		S ₀ → S ₅	2.73	0.1393	2.69	0.1233	2.74	0.1266

Absorption Properties The absorption spectra have been computed for all the isomers of $[\text{Cu}(\mathbf{1})_2]^+$ and $[\text{Cu}(\mathbf{2})_2]^+$. The calculations have been performed in gas phase using the B3LYP exchange and correlation functional. The absorption energy and oscillator strength of the lowest excited singlet states are reported in Table 7.2 and compared with the experimental maximum absorption in dimethylchloride at room temperature [70, 83]. Previous characterizations have shown that the absorption spectra of these complexes can be split in two distinct classes, which are largely dependent on the dihedral angle between the ligands in the ground state [69]. Complexes with a dihedral angle (dha) of about 90° exhibit a single strong absorption band, which corresponds to the population of a metal-to-ligand charge transfer (MLCT) state. On the other hand complexes with a smaller dihedral angle show an

absorption shoulder at smaller excitation energies. The breaking of the symmetry changes the transitions rules allowing transition that are forbidden in the higher symmetry structure ($d_{\text{h}}=90^\circ$). As both $[\text{Cu}(\mathbf{1})_2]^+$ and $[\text{Cu}(\mathbf{2})_2]^+$ have a dihedral angle close to 90° , one broad absorption band centered at ~ 450 nm is observed. For $[\text{Cu}(\mathbf{1})_2]^+$, the first optically bright transition is $S_0 \rightarrow S_3$ and occurs at 2.72 eV, in good agreement with experimental observations [83]. For $[\text{Cu}(\mathbf{2})_2]^+$, the inductive effect of the additional methyl substituents shifts this transition to higher energies, 2.78 eV. In this case, the transition is $S_0 \rightarrow S_5$.

Table 7.3: Character of the principal transition of $[\text{Cu}(\mathbf{1})_2]^+$ and $[\text{Cu}(\mathbf{2})_2]^+$.

Transition	Isomer A		Isomer B		Isomer C	
	Character		Character		Character	
$[\text{Cu}(\mathbf{1})_2]^+$ $S_0 \rightarrow S_3$	HOMO-1 \rightarrow LUMO+1	39%	HOMO-1 \rightarrow LUMO	43%	HOMO-1 \rightarrow LUMO	41%
	HOMO \rightarrow LUMO	26%	HOMO \rightarrow LUMO+1	35%	HOMO \rightarrow LUMO+1	29%
	HOMO-1 \rightarrow LUMO	20%	HOMO-1 \rightarrow LUMO+1	13%	HOMO-1 \rightarrow LUMO+1	18%
	HOMO \rightarrow LUMO+1	13%	HOMO \rightarrow LUMO	7%	HOMO \rightarrow LUMO	10%
$[\text{Cu}(\mathbf{2})_2]^+$ $S_0 \rightarrow S_5$	HOMO \rightarrow LUMO+3	29%	HOMO \rightarrow LUMO+3	36%	HOMO-1 \rightarrow LUMO+3	46%
	HOMO-1 \rightarrow LUMO+4	20%	HOMO-1 \rightarrow LUMO+4	34%	HOMO \rightarrow LUMO+4	24%
	HOMO \rightarrow LUMO+4	16%	HOMO \rightarrow LUMO+4	12%	HOMO-1 \rightarrow LUMO+4	10%
	HOMO-1 \rightarrow LUMO+3	15%	HOMO-1 \rightarrow LUMO+3	9%	HOMO \rightarrow LUMO+3	7%
	HOMO01 \rightarrow LUMO+1	10%				
	HOMO-1 \rightarrow LUMO	7%				

As expected, in both cases the system is photoexcited into the metal-to-ligand charge transfer (MLCT) states. The S_3 and the S_5 states, for respectively $[\text{Cu}(\mathbf{1})_2]^+$ and $[\text{Cu}(\mathbf{2})_2]^+$, arise from the promotion of a d electron to a π^* orbital centered on the ligands. Table 7.3 reports the most important contribution for these transitions. The Kohn-Sham orbitals of the two complexes in the ground state are shown in Fig. 7.3. Because the orbitals of the isomers b and c are the same, they are not displayed here. The HOMO and HOMO-1 orbitals of $[\text{Cu}(\mathbf{1})_2]^+$ and $[\text{Cu}(\mathbf{2})_2]^+$ have principally d character and are almost degenerate. In $[\text{Cu}(\mathbf{1})_2]^+$ LUMO and LUMO+1 correspond to the π^* *gerade* orbitals localized on different ligands and, as HOMO and HOMO-1, are almost degenerate. For this reason, the S_3 excitation arises from four different contributions. The methyl groups at the positions 3,4,7,8 of $[\text{Cu}(\mathbf{2})_2]^+$ destabilize the π^* *gerade* orbitals (LUMO+3 and LUMO+4) and stabilize the π^* *ungerade* orbitals (LUMO and LUMO+1). As a consequence, the absorption peak is shifted to higher energy.

Emission Properties The emission of Cu(I)-phenanthroline complexes is characterized by an ultrafast (less than 1 ps) [99, 79] and a slow component, whose lifetime depends on the nature of the complex and on the solvent. The fast component was assigned to emission from the lowest singlet state S_1 while the long-lived component to emission from the lowest triplet state T_1 at the relaxed excited state geometry. During the relaxation process, as already

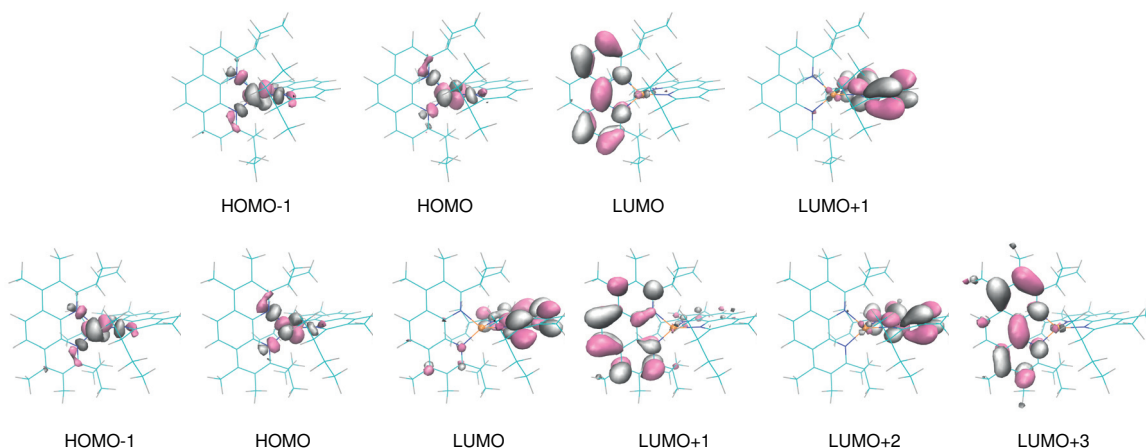


Figure 7.3: Frontier orbitals of the *a* isomers of $[\text{Cu}(\text{dsbp})_2]^+$ (first line) and $[\text{Cu}(\text{dsbtmp})_2]^+$ (second line). Isovalues:0.035

mentioned, the molecule flattens and relaxes into one of the minima of the lowest triplet state. Since $[\text{Cu}(\mathbf{1})_2]^+$ and $[\text{Cu}(\mathbf{2})_2]^+$ are homoleptic complexes possessing a D_2 symmetry, the potential energy surface of the lowest singlet and triplet state are characterized by a double-minimum structure [96, 253]. The population of the lowest triplet states, through ISC, occurs along all the relaxation coordinates but principally at geometric configurations close to that of the ground state [79, 99, 238].

Table 7.4: Room temperature emission data for $[\text{Cu}(\mathbf{1})_2]^+$ and $[\text{Cu}(\mathbf{2})_2]^+$ in acetonitrile (MeCN) and dimethylchloride (DCM). α [70], β [82]

	in MeCN		in DCM	
	Exp. (nm/eV)	τ (μs)	Exp. (nm/eV)	τ (μs)
$[\text{Cu}(\mathbf{1})_2]^+$	700 (1.77)	0.13	690 ^{α} (1.80)	0.40
$[\text{Cu}(\mathbf{2})_2]^+$	649 (1.91)	1.46	621 ^{β} (2.00)	2.8

Table 7.5 reports the emission data of the two complexes. In both case, due to the small structural reorganization in the excited state, we find a relatively large $T_1 \rightarrow S_0$ energy gap. This reduces the contribution of non-radiative decay and consequently is responsible for the higher emission quantum yields observed for these complexes in comparison to related complexes [70]. The intrinsic luminescence lifetime of these complexes are determined by three principal characteristics, as shown by the expression for the radiative rate of the lowest triplet state:

$$k^r(T_1) = \frac{64\pi^2 \nu^3}{3hc^3} \left| \frac{\langle S_1 | \hat{H}_{so} | T_1 \rangle}{\Delta E_{S_1-T_1}} \cdot \langle S_0 | e\mathbf{r} | S_1 \rangle \right|^2 \quad (7.1)$$

where ν is the frequency of the emitted light. The intrinsic lifetime of the emission, that is

Chapter 7. Unravelling the photophysics of two long-living Cu(I)-phenanthrolines

Table 7.5: Phosphorescence (decay from T_1) emission, fluorescence emission (decay from S_1), oscillator strength of the fluorescence, spin-orbit coupling matrix element between T_1 and S_1 , radiative rate and intrinsic lifetime of the lowest emitting state.

	G.S. geometry						T ₁ geometry					
	T ₁ eV	S ₁ eV	f _{S1} 10 ⁻³	[\hat{H}_{SO}] ₁₁ cm ⁻¹	k _r 10 ⁻¹¹	τ 10 ¹⁰ s	T ₁ eV	S ₁ eV	f _{S1} 10 ⁻²	[\hat{H}_{SO}] ₁₁ cm ⁻¹	k _r 10 ⁻¹¹	τ 10 ¹⁰ s
[Cu(1) ₂] ⁺ <i>a</i>	2.30	2.41	1.10	74	7.0240	1.424	1.53	1.84	3.58	37	68.922	0.1451
<i>b</i>	2.26	2.37	0.30	94	0.7996	79.96	1.55	1.84	1.56	63	52.000	0.1922
<i>c</i>	2.26	2.38	0.90	115	10.771	0.928	1.56	1.84	1.95	60	69.266	0.1431
[Cu(2) ₂] ⁺ <i>a</i>	2.42	2.53	0.07	32	0.0064	1614	1.66	1.85	0.39	61	0.0756	132.31
<i>b</i>	2.40	2.50	0.56	63	1.4616	6.841	1.62	1.82	0.39	60	0.0613	163.01
<i>c</i>	2.38	2.50	1.81	118	45.012	0.222	1.63	1.82	0.45	64	0.1048	95.35

defined as the reciprocal of the radiative rate, is determined by the magnitude of $S_1 \rightarrow S_0$ oscillator strength ($\langle S_0 | e\mathbf{r} | S_1 \rangle$), by the mixing between the S_1 and T_1 states as described by the spin orbit coupling matrix elements ($\langle S_1 | \hat{H}_{SO} | T_1 \rangle$) and by the energy gap between the two states ($\Delta E_{S_1-T_1}$). For the latter, the inductive characteristic of the *sec*-butyl and methyl groups (for [Cu(2)₂]⁺) decreases the spatial separation of the unpaired electron on the ligands and the one on the metal d-orbitals. This increases the exchange interaction in the excited state causing a larger separation between the S_1 and T_1 states ($\Delta E_{S_1-T_1}$) with respect to other Cu(I)-phenanthroline complexes. As a consequence the rate of delayed fluorescence to the total radiative emission [11] is reduced. As the T_1 state is a much purer spin state, the $T_1 \rightarrow S_0$ is much weaker leading to a longer lifetime. This is emphasized in [Cu(dsbptmp)₂]⁺ where the methyl groups push the electron density towards the metal 3d ions reducing the transition dipole size and, therefore, the oscillator strength [263]. The lifetime is, therefore, further lengthened (see Table. 7.5).

Finally, the mixing of the spin states depends on the magnitude of the spin orbit coupling constants. As demonstrated in Sec. 6.3.1, this is almost exclusively determined by the contribution of the d-orbitals to the excited states. For [Cu(dsbp)₂]⁺ and [Cu(dsbptmp)₂]⁺ we observe exactly the same trends. However, due to the structural rigidity of the complex, and the small distortion in the excited state the spin orbit coupling matrix elements between the ground and excited states remain similar.

Solvent effect Fig. 7.4 shows the Cu-N_{MeCN} and Cu-Cl_{DCM} radial distribution functions (RDF) and integrated radial distribution function, N(r), for both the ground (GS) and excited states (ES) extracted from the classical MD simulations. In both cases, the *sec*-butyl ligands in the positions 2,9 of the phenanthroline ligands ensure that no solvent molecules are able to come close than ~ 4 Å to the copper. The RDF of [Cu(1)₂]⁺ exhibits a peak at ~ 8 Å for both MeCN and DCM, which corresponds to the first shell of molecules surrounding the *sec*-butyl

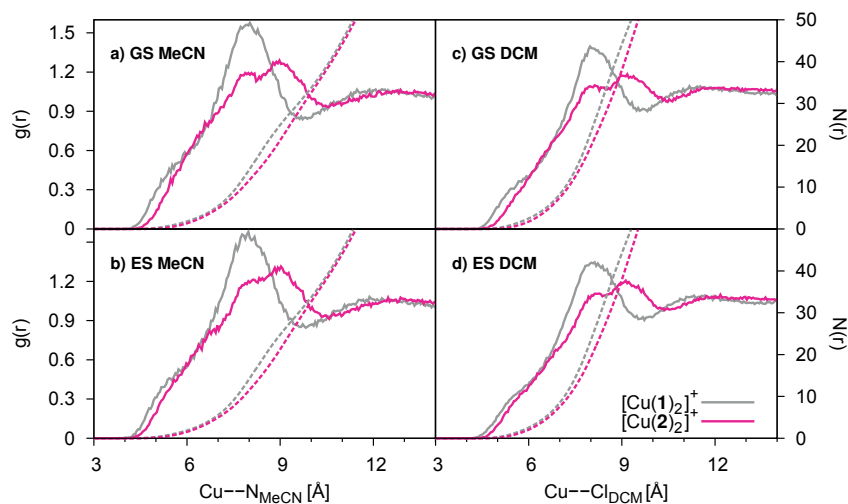


Figure 7.4: Comparison between Classical and QM/MM MD's radial distribution function $g(r)$ (solid line) and integrated radial distribution function $N(r)$ (dashed line) of $[\text{Cu}(\text{dsbp})_2]^+$ and $[\text{Cu}(\text{dsbtmp})_2]^+$ in a,c) the ground and b,d) the lowest triplet excited states in MeCN and DCM.

groups and the external part of the phenanthroline ligand. At similar distance the RDF of $[\text{Cu}(\mathbf{2})_2]^+$ shows two peaks: the first, at 8 Å as for $[\text{Cu}(\mathbf{1})_2]^+$, indicates the solvent in the *sec*-butyl region, the second, at a distance of 10 Å, due to the pushing effect of the external methyl groups, arises from the outward region. This relatively weak solvent interaction that is present in the ground state, combined with the small structural changes means that we observe only small changes between the ground and the excited state solvent structures. Indeed, this is emphasized in Fig. 7.5, which shows the angular distribution of solvent molecules around the complex. As highlighted in the figure, by blue and green colors, the most internal shell is composed by solvent molecules that wrap the phenanthroline ligands, while the external one, more diffuse, spreads in the space wiped out by the *sec*-butyl substituents.

As observed also for $[\text{Cu}(\text{dbp})_2]^+$ and $[\text{Cu}(\text{dbtmp})_2]^+$, the additional presence of methyl groups at 3,4,7,8 position, further push the solvent on the external part of the complex.

7.4 Discussion and conclusion

Unravelling the role of geometry, electronic structure, solvent interaction, in tuning the photophysical properties is of primary importance for guiding the design of efficient metal-

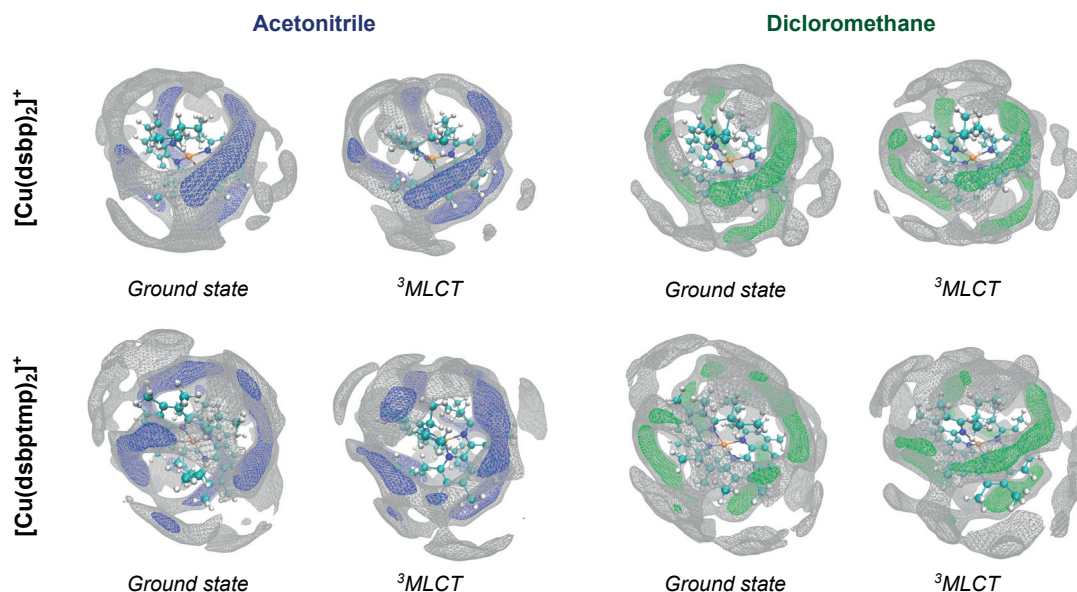


Figure 7.5: Solvent density. Isovalues in acetonitrile: 12000 (grey), 8500 (blue). Isovalues in dimethylchloride: 11000 (grey), 8000 (green).

organic complexes. Here, we have studied the emission of two Cu(I)-phenanthroline complexes, $[\text{Cu}(\text{dsbp})_2]^+$ and $[\text{Cu}(\text{dsbtmp})_2]^+$, which exhibit long luminescence lifetime.

As discussed in Chapter 6, the absorption and emission properties of these complexes can be tuned changing substituents. Notably, cumbersome alkyl groups at positions 2,9 prevent the PJT distortion of the molecule upon photoexcitation. This is also the case of $[\text{Cu}(\text{dsbp})_2]^+$ and $[\text{Cu}(\text{dsbtmp})_2]^+$ that are characterized by a branched substituents, *sec*-butyl. The optimized ground state structure of $[\text{Cu}(\text{dsbp})_2]^+$ is slightly distorted from the equilibrium geometry, that has D_2 symmetry, distortion that is not present for $[\text{Cu}(\text{dsbtmp})_2]^+$ due to the stabilization effect of the methyl groups at position 3,4,7,8. Our electronic structure calculations have revealed that the methyl groups also influence the electronic structure of the system. Indeed, the inductive effect of the methyl substituents destabilizes the π^* -gerade orbitals leading to a blue shift (~ 0.06 eV) of the optically bright $^1\text{MLCT}$ state. The combined effect of *sec*-butyl and methyl substituents is even larger in the lowest triplet excited state. Both $[\text{Cu}(\text{dsbp})_2]^+$ and $[\text{Cu}(\text{dsbtmp})_2]^+$ do not undergo a large flattening due to the steric impediment induced by *sec*-butyl groups and the electronic stabilization produced by the methyl groups. The consequences of this small distortion are diverse.

First, PJT distortion, by breaking the symmetry and removing the degeneracy of frontier orbitals, lowers the energy of a system. Preventing such a distortion, the energy gap between the emitting triplet state T_1 and the ground state remains large. This effect is particularly pronounced in $[\text{Cu}(\text{dsbp})_2]^+$ and $[\text{Cu}(\text{dsbtmp})_2]^+$. As reported in the previous chapter, the majority of Cu(I)-phenanthroline have an emission wavelength larger than 700 nm (with

the exception of $[\text{Cu}(\text{dbtmp})_2]^+$). In the case of $[\text{Cu}(\text{dsbp})_2]^+$ and $[\text{Cu}(\text{dsbptmp})_2]^+$, this is smaller than 700 nm. As a consequence, the non-radiative decay rate, that is inversely proportional to the energy gap, is smaller than the one of similar complexes.

Second, Cu(I)-phenanthroline complexes are characterized by large spin-orbit couplings (SOCs) between S_1 and low lying triplet states at nuclear configurations that correspond to the ground state geometry. Moving along the relaxation coordinates, SOC decreases and, in the case of $[\text{Cu}(\text{dmp})_2]^+$, they reduce by about one order of magnitude at the optimized excited state geometry. $[\text{Cu}(\text{dsbp})_2]^+$ and $[\text{Cu}(\text{dsbptmp})_2]^+$, retaining the ground state geometry and do not exhibit relevant changes in the value of SOC. This has important repercussions. In fact, ISC, as extensively investigated in Chapter 3, occurs from the singlet to the triplet states principally at the ground state geometry. Fast ISC means that population is quickly transferred to a triplet state, that in contrast to singlet excited states, has a smaller radiative decay to the singlet ground state.

The small distortion also affects the radiative decay of T_1 . This depends on T_1-S_0 energy gap, which, as we have seen, is large for both $[\text{Cu}(\text{dsbp})_2]^+$ and $[\text{Cu}(\text{dsbptmp})_2]^+$. In addition, it depends on the SOC between S_1 and T_1 that for all Cu(I)-phenanthroline is small, the energy gap between S_1 and T_1 and the oscillator strength of the $S_1 \rightarrow S_0$ transition. At the optimized ground state structure, this transition is optically forbidden, but, due to the break of the symmetry, it starts to be allowed moving along the relaxation path. The retention of the initial geometry leads to a smaller oscillator strength compared to the other systems, and thus to a smaller radiative decay rate. This can be even reduced by an enlargement of the gap between S_1 and T_1 . This is the case of $[\text{Cu}(\text{dsbptmp})_2]^+$: methyl groups, by pushing the electronic distribution in the excited states towards the copper, increases the exchange interaction causing a larger separation between S_1 and T_1 .

Finally, our classical MD and QM/MM molecular dynamics have shown that the interaction between solute and solvent is very weak. The steric impediment generated by the *sec*-butyl wipe out the solvent from the metal center reducing the energy stabilization of the electronic excited states.

In conclusion, we have investigated the photophysics of two Cu(I)-phenanthroline complexes with very long emission lifetime, rationalizing the role of the geometric structure in determining electronic properties. We found that the long lived emissions and large quantum yields of $[\text{Cu}(\text{dsbp})_2]^+$ and $[\text{Cu}(\text{dsbptmp})_2]^+$ are associated with the presence of cumbersome substituents at the positions 2,9 that prevent PJT distortion and thus increase the energy gap between the emitting triplet state and the ground state. The addition of methyl groups at the positions 3,4,7,8, helps retain the ground state structure and, due to the electronic inductive effect, reduces the radiative triplet decay rate.

Conclusions

In this thesis project I studied the photophysical properties of Cu(I)-phenanthroline complexes in solution, in firm connection with optical and X-ray spectroscopy investigations.

These systems are very promising for energy-conversion and photo-catalysis applications. In order to shed light on the processes that rule their photophysical and photochemical properties, different computational techniques were applied in these studies. The first steps of relaxation, upon photoexcitation, occur on an ultrafast time scale (less than 1 ps) and are a fingerprint of the quantum nuclear nature of the system.

By applying wavepacket quantum dynamics (MCTDH) to a prototypical Cu(I)-phenanthroline molecule, $[\text{Cu}(\text{dmp})_2]^+$, we found, in agreement with ultrafast transient absorption and fluorescence up-conversion spectroscopy [79, 99, 96] that, upon excitation, the system relaxes in a *subpicosecond* time scale, through internal conversion, to the lowest excited singlet state. The initial stages of the intersystem crossing occur principally at the Franck-Condon region where spin-orbit coupling is maximum (300 cm^{-1}) [100] while the pseudo-Jahn-Teller distortion takes place in a much longer timescale (10–100 ps) [79]. Non-adiabatic molecular dynamics methods, such as Trajectory Surface Hopping, may be used as complementary techniques for the investigation of these phenomena. In contrast to MCTDH, that is based on the reduction of the configurational space by selecting a *sub*-space of the normal modes of the system, TSH can span it freely. This offers the opportunity, by analyzing the collective variables activated during the dynamics, to guide the choice of the *sub*-space. We proposed Principal Component Analysis as identification tool for the normal modes to include in the MCTDH *sub*-space.

Ultrafast X-ray spectroscopies provides direct observation of the electronic and structural changes occurring upon photoexcitation in the *subpicosecond* time scale. The time resolution required by these techniques can be achieved with the new-generation X-ray Free Electron Laser. Using wavepacket dynamics, we interrogated the feasibility of EXAFS, pre-edge XANES, $K_{\alpha_{1,2}}$, $K_{\beta_{1,3}}$ and $K_{\beta_{2,5}}$ XES spectra. We found that, due to the weak signal, the wavepacket dynamics of $[\text{Cu}(\text{dmp})_2]^+$ can be observed in realistic experimental conditions for EXAFS and pre-edge XANES.

Cu(I)-phenanthroline complexes are characterized by a long-lived luminescence of which

Chapter 7. Unravelling the photophysics of two long-living Cu(I)-phenanthrolines

lifetime and quantum yields can be tuned by the solvent and by the architecture of the ligands. Combining transient X-ray absorption spectroscopy and Molecular Dynamics simulations, we were able to rationalize the nature of the quenching of the luminescence observed in strong donating solvent. In contrast with the previously accepted model [68], which was based on the formation of an exciplex (a species formed by two molecules, one in the excited state and one in the ground state), we showed that no stable exciplexes are formed and the quenching is due to electrostatic solute-solvent interactions. In a further systematic study we investigated the effect of different ligands in tuning the emission properties of Cu(I)-phenanthroline complexes. This research has high impact in determining the structural and electronic features in order to guide the synthesis of complexes with the desired physical properties.

A Electronic structure

In order to determine the electronic structure of a molecular system, we need to solve the electronic time-independent Schrödinger equation (TISE) ¹ for a given nuclear configuration:

$$\hat{H}_{el}\Psi_{el}(\mathbf{r}; \mathbf{R}) = E_{el}\Psi_{el}(\mathbf{r}; \mathbf{R}). \quad (\text{A.1})$$

The electronic wavefunction Ψ_{el} is a many-body function, which depends on $3N$ coordinates, where N is the number of electrons of the system. In principle, the equation may be solved by representing Ψ_{el} in a convenient basis set and diagonalizing the Hamiltonian. However, the computational cost increases exponentially with the number of electrons and it is feasible only for small systems (few atoms). Different methods have been developed in order to determine approximate solutions of the TISE. In the Hartree-Fock method, the electronic wavefunction is approximated by a single Slater determinant. Following versions, classified under the name of post-Hartree-Fock methods, have been developed in order to improve the weakness of Hartree-Fock but the computational cost of these approximated schemes remains prohibitive for the majority of the systems. A revolution started in 1964 when Hohenberg and Kohn published in their seminal paper [274] the two foundation theorems of the Density Functional Theory (DFT), followed by a second publication [275], in 1965, by Kohn and Sham in which an operative solution to the functional problem was proposed.

A.1 The Hohenberg-Kohn theorems

Density Functional Theory (DFT) is an exact theory of many-body systems. In this formulation, proposed by Hohenberg and Kohn [274], any property of a many interacting particles system can be expressed as a functional of the ground state density. In the specific case of a system composed of electrons and clamped nuclei, the Hamiltonian is expressed as:

$$\hat{H}_{el} = \hat{T}_e + \hat{V}_{ee} + \hat{V}_{ext}(\mathbf{r}_i) \quad (\text{A.2})$$

¹Let's suppose that the relativistic effects are not taken into account.

Appendix A. Electronic structure

where, as defined in Chapter 2, \hat{T}_e is the kinetic energy of the electrons, \hat{V}_{ee} is the Coulomb interaction between electrons and V_{ext} is the external potential generated by the nuclei.

The first theorem states:

For any system of interacting particles, the external potential $V_{ext}(\mathbf{r})$, except for a constant, is a unique functional of the nondegenerate² ground state density.

As a consequence, since $V_{ext}(\mathbf{r})$ fixes the Hamiltonian, this latter is a functional of the electronic ground state density $n_0(\mathbf{r})$. It follows, that, all properties of the system, included the many-body wavefunctions, are determined by $n_0(\mathbf{r})$:

$$V_{ext}(\mathbf{r}) \xrightarrow{H_e|\Psi=E_e|\Psi} \Psi(r) \xrightarrow{|\Psi_0(r)|^2} n_0(\mathbf{r}). \quad (\text{A.3})$$

The second theorem states:

For any external potential $V_{ext}(\mathbf{r})$ can be defined an universal functional of the ground state density for the energy $E[n(\mathbf{r})]$:

$$E[n(\mathbf{r})] = T[n(\mathbf{r})] + V_{ee}[n(\mathbf{r})] + \int d\mathbf{r} V_{ext}(\mathbf{r})n(\mathbf{r}). \quad (\text{A.4})$$

The minimum of $E[n(\mathbf{r})]$ corresponds to the expectation value of the Hamiltonian in the ground state and the density that minimize the functional is the exact ground state density:

$$E_{min\Psi}[n(\mathbf{r})] = \langle \Psi_0 | \hat{H} | \Psi_0 \rangle = E[n_0(\mathbf{r})]. \quad (\text{A.5})$$

In the DFT formalism the density has a key role and from there one can determine the properties of an electronic system without using the many-body wavefunction. Despite this achievement, there are still many practical problems because, for example, we don't know how to compute the external potential of a many-body interacting system.

The astute solution proposed by Kohn and Sham (KS) [275] was to substitute the complicate many-body system with an auxiliary non-interacting system. This replacement is possible under the condition that the two systems have the same density:

$$n_0(\mathbf{r}) = n_0^{KS}(\mathbf{r}) = \sum_i^{occ} |\phi_i^{KS}|^2. \quad (\text{A.6})$$

²This restriction was eliminated by the alternative definitions of functional proposed by Levy and Lieb[276, 277, 278].

In the previous equation ϕ_i^{KS} are the one-electron KS orbitals, solution of the DFT KS-equation

$$\left[-\frac{1}{2}\nabla^2 + V_{eff}^{KS}(\mathbf{r}) \right] \phi_i^{KS}(\mathbf{r}) = \epsilon_i \phi_i^{KS}(\mathbf{r}) \quad (\text{A.7})$$

where the static KS effective potential is defined as

$$V_{eff}^{KS}[n(\mathbf{r})] = V_{ext}(\mathbf{r}) + V_H[n(\mathbf{r})] + V_{xc}[n(\mathbf{r})] \quad (\text{A.8})$$

in which $V_{ext}(\mathbf{r})$ is the external potential (the nuclei-electron electrostatic interaction). The electron-electron interaction \hat{V}_{ee} is partitioned in two contributions: $V_H(\mathbf{r})$ is the Hartree potential, the classical Coulomb e-e repulsion and $V_{xc}(\mathbf{r})$ is the exchange and correlation potential. The non-interacting wavefunction is a single Slater determinant of N occupied Kohn-Sham (KS) orbitals. Following from the Hohenberg-Kohn theorem, if V_{eff}^{KS} exists, it is unique. As a consequence, the total energy is a unique functional of the density:

$$E[n(\mathbf{r})] = T^{KS}[n(\mathbf{r})] + E_H[n(\mathbf{r})] + E_{xc}[n(\mathbf{r})] + \int d\mathbf{r} V_{ext}(\mathbf{r})n(\mathbf{r}) \quad (\text{A.9})$$

where $T^{KS}[n(\mathbf{r})]$ is easily computed from the KS orbitals

$$T^{KS}[n(\mathbf{r})] = \sum_i^N \epsilon_i - \int d\mathbf{r} V_{eff}(\mathbf{r})n(\mathbf{r}). \quad (\text{A.10})$$

The convenience of the KS scheme lies in using the orbitals energies ϵ_i , which are cheap to compute, to calculate the total energy. The only missing step at this point is to find an expression for $E_{xc}[n(\mathbf{r})]$. Comparing the KS functional (Eq. A.9) with the HK functional (Eq. A.4) the exchange and correlation functional can be expressed as

$$E_{xc}[n(\mathbf{r})] = (T[n(\mathbf{r})] - T^{KS}[n(\mathbf{r})]) + V_{ee}[n(\mathbf{r})] - E_H[n(\mathbf{r})] \quad (\text{A.11})$$

whence one can show that $E_{xc}[n(\mathbf{r})]$ is equal to the difference of the kinetic and interaction energy of the real many-body system from those of the fictitious Kohn-Sham system in which the electron-electron interaction is replaced by the Hartree potential.

A.2 Exchange-correlation functionals

In order to make operative the Kohn-Sham scheme, we need to define the exchange and correlation potential $E_{xc}[n(\mathbf{r})]$. Many approximations have been proposed but in this appendix only the most common are discussed.

Appendix A. Electronic structure

Local Density Approximation Exchange and correlation functional can be approximated as a local functional of the density, namely

$$E_{xc}^{LDA}[n(\mathbf{r})] = \int d\mathbf{r} \epsilon_{xc}[n(\mathbf{r}), \mathbf{r}] n(\mathbf{r}) \quad (\text{A.12})$$

where $\epsilon_{xc}[n(\mathbf{r}), \mathbf{r}]$ is the exchange and correlation density energy. In a spin-polarized system, a similar version, the local spin-density approximation (LSDA) is obtained in the same manner. Since LDA is exact for a homogeneous electron gas, it is a good approximation for systems in which the electron density does not vary rapidly. The most common parametrization adopted makes use for the exchange energy density of the analytical expression deduced by Dirac [279]:

$$\epsilon_x[n(\mathbf{r})] = -\frac{3}{4\pi} \left(\frac{9\pi}{4} \right)^{1/3} \frac{1}{r_s} \quad r_s = \left(\frac{3}{4\pi n_0(\mathbf{r})} \right)^{1/3} \quad (\text{A.13})$$

and for the correlation density energy, in the limit of high density and low density, the following expression:

$$\epsilon_c = \begin{cases} A \ln r_s + B + r_s (C \ln r_s + D) & r_s \leq 1, \text{ for high density} \\ \frac{1}{2} \left(\frac{g_0}{r_s} + \frac{g_1}{r_s^{3/2}} + \frac{g_2}{r_s^2} + \dots \right) & r_s > 1, \text{ for low density} \end{cases} \quad (\text{A.14})$$

At intermediate densities, the correlation density energy is described by the Perdew and Wang parametrization [280] obtained from the quantum Monte Carlo results of Ceperley and Alder [281].

Generalized Gradient Approximation The natural extension of the LDA approach is a semi-local approximation, which includes the gradient of the density. The original ‘‘gradient’’ expansion was already proposed by Kohn and Sham in their seminal paper [275]. The Generalized Gradient Approximation (GGA) refers to a collection of formulations. As in the LDA, GGAs does not contain empirical parameters. The general form of the functional is [282]:

$$E_{xc}^{GGA}[n(\mathbf{r})] = \int d\mathbf{r} \epsilon_{xc}[n(\mathbf{r}), \mathbf{r}] n(\mathbf{r}) + \int d\mathbf{r} F_{xc}[\nabla n(\mathbf{r}), n(\mathbf{r}), \mathbf{r}] \quad (\text{A.15})$$

where the function F_{xc} has to be built in such a way to satisfy a number of conditions including the exchange-correlation hole sum rule. Numerous form of GGA’s functionals have been proposed, among them the BLYP (Becke’s formulation for the exchange [196] and Lee-Yang-Parr correlation [247, 283] functional) and the PBE (Perdew-Burke-Enzerhod) [224] functionals.

A.2. Exchange-correlation functionals

The BLYP functional has the following analytical expression:

$$\text{Becke 88 exchange} \quad \epsilon_x^{LDA} \left(1 - \frac{\beta}{2^{1/3} A_x} \frac{x^2}{1 + 6\beta x \sinh^{-1}(x)} \right) \quad (\text{A.16})$$

for $x = 2(6\pi^2)^{1/3}$, $s = 2^{1/3} |\Delta n(\mathbf{r})|/n(\mathbf{r})^{4/3}$, $A_x = (3/4)(3/\pi)^{1/3}$, $\beta = 0.0042$.

$$\text{LYP correlation} \quad \epsilon_c = -a \frac{1}{1 + d n(\mathbf{r})^{-1/3}} \left[n(\mathbf{r}) + b n(\mathbf{r})^{2/3} \left(C_F n(\mathbf{r})^{5/3} - 2t_W + \frac{1}{9} (t_W + \frac{1}{2} \nabla^2 n(\mathbf{r})) e^{-cn(\mathbf{r})^{-1/3}} \right) \right] \quad (\text{A.17})$$

for $C_F = 3/10(3\pi^2)^{2/3}$, $a = 0.04918$, $b = 0.132$, $c = 0.2533$, $d = 0.349$ and

$$t_W = \frac{1}{8} \left(\frac{|\nabla n(\mathbf{r})|^2}{n(\mathbf{r})} - \nabla^2 n(\mathbf{r}) \right). \quad (\text{A.18})$$

Such functional have been used for computing the electronic structure of a series of Cu-phenanthroline complexes (see Chapter 6 and 7).

The PBE functional is defined as:

$$F_x(s) = 1 + k - \frac{k}{1 + \mu s^2/k}, \quad s = \frac{\nabla n(\mathbf{r})}{n(\mathbf{r})^{4/3}} \quad (\text{A.19})$$

with $\mu = 0.21951$, $k = 0.804$

$$F_c(r_s, \eta, t) = \gamma \phi^3 \ln \left[1 + \frac{\beta}{\gamma} t^2 \frac{1 + At^2}{1 + At^2 + A^2 t^4} \right] \quad (\text{A.20})$$

where

$$A(r_s, \eta) = \frac{\beta}{\gamma} \frac{1}{e^{-\epsilon_c^{LDA}/\gamma\phi^3} - 1}, \quad \phi(\eta) = \frac{1}{2} [(1 + \eta)^{2/3} + (1 - \eta)^{2/3}] \quad (\text{A.21})$$

$$\eta = \frac{1 - \ln 2}{\pi^2}, \quad r_s = \left[\frac{3}{2\pi n(\mathbf{r})} \right]^{1/3}, \quad t(\mathbf{r}) = \frac{|\nabla n(\mathbf{r})|}{2\phi k_s n(\mathbf{r})}, \quad k_s = \sqrt{4k_F/\pi} \quad (\text{A.22})$$

The PBE functional was used in Chapter 4 for describing the electronic structure of $[Cu(\text{dmp})_2]^+$.

Hybrid functionals LDAs and GGAs functionals suffer from the wrong asymptotic behaviour as $r \rightarrow \infty$, due to the approximate exchange within the xc-functionals [284]. The potential decays as $-1/r$ but in the LDA/GGA approach it decreases exponentially. This failure is associated with the self-interaction error [45], which is, on the other hand, exactly removed by the non-local Hartree-Fock (HF) method. In order to reduce this problem, hybrid

Appendix A. Electronic structure

functionals were developed. The idea behind lies in adding a fraction of exact HF exchange to the common GGA functionals.

The expression for B3LYP [248] functional, the hybrid version of BLYP, is

$$E_{xc} = c_1 E_x^{LDA} + c_2 E_x^{B88} + c_3 E_x^{HF} + C_4 E_C^{LYP} + (1 - c_4) E^{VWN} \quad (\text{A.23})$$

where E_x^{LDA} is the LDA exchange, E_x^{B88} is Becke's gradient correction for the exchange [196], E_x^{HF} is the Hartree-Fock exchange energy, E_C^{LYP} [247] and E_C^{VWN} [272] are respectively the LYP and VWN correlation energies. The parameters are adjustable and obtained usually by fitting the energies of a set of "test molecules". In the standard version they are $c_1=0.80$, $c_2=0.72$, $c_3=0.20$ and $c_4=0.81$. The HF exchange is computed from the following equation, employing the Kohn-Sham orbitals:

$$E_x^{HF} = \sum_{i,j} \iint \frac{\phi_i(\mathbf{r})\phi_j(\mathbf{r})\phi_i^*(\mathbf{r}')\phi_j^*(\mathbf{r}')}{|\mathbf{r}-\mathbf{r}'|} d\mathbf{r}d\mathbf{r}'. \quad (\text{A.24})$$

Calculation of the non-local E_x^{HF} is expensive, limiting the use of these functional to molecular systems.

B3LYP functional have been employed for determining the electronic structure of the Cu(I)-phenanthroline studied in this thesis.

A.3 Basis sets and Pseudopotential

The last ingredient we need for characterizing a system is a basis set for expanding the electronic wavefunctions. The choice of the basis set depends on the studied system. Usually, they are grouped into two classes: atomic basis functions and plane waves.

The former are more suitable for molecular systems because basis functions are centered on atoms [285]. Common choices are Gaussians [286, 287] or Slater [288] functions. Integrals with localized basis functions are easier to compute and less computational resources are required. For this reason, the use of these basis sets allows us to carried out all-electron calculations. On the other hand, since atomic basis sets do not constitute an orthonormalized basis set, the wavefunction is not variational. This leads to a disadvantage for *ab-initio* MD where the forces can not be computed within the Hellmann-Feynman theorem [289, 290] making the calculations more expensive [291]³.

³Forces are computed by the gradient of the electronic energy:

$$\begin{aligned} F &= -\nabla E = -\nabla \langle \Psi_{el} | \hat{H}_{el} | \Psi_{el} \rangle \\ &= \langle \Psi_{el} | \nabla \hat{H}_{el} | \Psi_{el} \rangle + 2 \langle \nabla \Psi_{el} | \hat{H}_{el} | \Psi_{el} \rangle \end{aligned}$$

In Hellmann-Feynman, the second term vanishes and only the first element has to be computed.

Plane waves are commonly used when periodic boundary conditions are applied. Moreover, they are a complete basis set and this allows to easily test the converge of the results by simply increasing the expansion cut-off. Since plane waves satisfy the orthonormality condition, they are specially suited for performing *ab-initio* MD because the calculation of the forces can be done within the Hellman-Feynman scheme and they are independent of the nuclear coordinates [292]. However, the number of planes needed for describing the wavefunction near the nuclei is considerable, due to the large kinetic energy of the valence electron in this region. The atomic wavefunctions are eigenstate of the atomic Hamiltonian; valence and core electrons must be mutually orthogonal but, since the core states are localized in the vicinity of the nuclei, the valence states have rapid oscillations. Since core electrons do not participate in the chemical properties of the system, they can be replaced by an effective pseudopotential [293] that acts on the valence electrons. The valence electrons wavefunction is replaced by a pseudowavefunction that is smoother nearby the atoms and, beyond a certain radius, corresponds to the 'true' wavefunction. Importantly, the pseudowavefunction has to reproduce the properties of the all-electron calculation. Different schemes for the construction of pseudopotential have been developed. One of the most used leads to the so-called 'norm-conservative' pseudopotential, such as the Martin-Trouiller pseudopotential [225], used in this thesis.

B TDDFT in a Nutshell

B.1 The foundation theorems

Time-Dependent Density Functional Theory (TDDFT) allows one to describe the behaviour of a system that is not in the ground state or in an equilibrium state. TDDFT lays its foundations in two theorems.

The first one, the Runge-Gross theorem, proposed in 1984 [294] and equivalent to the Hohenberg-Kohn theorem for DFT, states that there is a unique, one-to-one correspondence between time-dependent electronic density and external potential for any given initial fixed many-body state $\Psi(t=0)$:

$$v_{ext}(\mathbf{r}, t) \xrightarrow[\Psi(t=0)]{-i\hbar\partial\Psi/\partial t = \mathcal{H}(t)\Psi} \Psi(t) \xrightarrow{|\Psi(t)|^2} \rho(\mathbf{r}, t). \quad (\text{B.1})$$

The application of an external potential, $v_{ext}(\mathbf{r}, t)$ produces a time-dependent wave function $\Psi(t)$ for a given initial condition $\Psi(t=0)$ via the time dependent Schrödinger equation; the same wavefunction determines uniquely the electronic density $n(\mathbf{r}, t)$. The Runge-Gross theorem is valid only for potentials that are Taylor-expandable around $t=0$.

The second one, the Leeuwen theorem [295], is equivalent to the Kohn-Sham theorem and it guarantees that the time-dependent density $n(\mathbf{r}, t)$ of a many-body system evolving from an initial many-body state $\Psi(t=0)$ under the influence of an external potential $v_{ext}(\mathbf{r}, t)$ can be reproduced by a different initial state $\Psi'(t=0)$ with a different external potential $v'_{ext}(\mathbf{r}, t)$. Thus, the Leeuwen theorem allows describing the evolution of an interacting system replacing it with a non-interacting (KS) system.

B.2 Linear response TDDFT

Linear response TDDFT (LR-TDDFT) is an alternative approach [296] developed for studying systems subjected to a weak external potential. In molecular spectroscopy the perturbation

Appendix B. TDDFT in a Nutshell

can be generated by a laser beam and LR-TDDFT can be helpful for determining the excitation energies. Supposing a time-dependent perturbation $v_1(\mathbf{r}, t)$ is switch on at t_0 . The total external potential is thus

$$v_{ext}(\mathbf{r}, t) = v_0(\mathbf{r}) + v_1(\mathbf{r}, t)\theta(t - t_0) \quad (\text{B.2})$$

where v_0 is the static external potential and $\theta(t - t_0)$ is a step function. The initial electronic density n_0 is affected by the perturbation ($n(t)$). The difference between the time-dependent density and the initial static density takes the name of density response and can be expanded in powers of the perturbation:

$$n(t) - n_0 = n_1(t) + n_2(t) + n_3(t) + \dots \quad (\text{B.3})$$

The first term is the linear response of the density and represents one of the key quantities in LR-TDDFT. It can be expressed as

$$n_1(t) = \int d\mathbf{r}' \int dt \chi(\mathbf{r}, t, \mathbf{r}', t') v_1(\mathbf{r}', t') \quad (\text{B.4})$$

in which $\chi(\mathbf{r}, t, \mathbf{r}', t')$ is the density-density response function defined as

$$\chi(\mathbf{r}, t, \mathbf{r}', t') = \left. \frac{\delta n[v_{ext}](\mathbf{r}, t)}{\delta v_{ext}(\mathbf{r}', t')} \right|_{v_0(\mathbf{r})}. \quad (\text{B.5})$$

The Runge-Gross theorem allows calculating the perturbing potential from the density-density response

$$v_1(\mathbf{r}, t) = \int d\mathbf{r}' \int dt \chi^1(\mathbf{r}, t, \mathbf{r}', t') n_1(\mathbf{r}', t'). \quad (\text{B.6})$$

Similarly, we can derivate the corresponding equations for a time-dependent KS system with an effective potential

$$n_{s1}(t) = \int d\mathbf{r}' \int dt \chi_s(\mathbf{r}, t, \mathbf{r}', t') v_{s1}(\mathbf{r}', t') \quad (\text{B.7})$$

with

$$\chi_s(\mathbf{r}, t, \mathbf{r}', t') = \left. \frac{\delta n_s[v_s](\mathbf{r}, t)}{\delta v_s(\mathbf{r}', t')} \right|_{v_{s0}(\mathbf{r})} \quad (\text{B.8})$$

and the linearized effective potential

$$v_{s1}(\mathbf{r}, t) = v_1(\mathbf{r}, t) + \int d\mathbf{r}' \frac{\rho_1(\mathbf{r}', t)}{|\mathbf{r} - \mathbf{r}'|} + v_{xc1}(\mathbf{r}, t). \quad (\text{B.9})$$

The first two terms are respectively the external perturbation, $v_1(\mathbf{r}, t)$, and the linearized response of the Hartree potential; the third term is the linearized xc potential which is, after functional Taylor expansion

$$v_{xc1}(\mathbf{r}, t) = \int d\mathbf{r}' \int dt \underbrace{\frac{\delta v_{xc}[n](\mathbf{r}, t)}{\delta n}}_{f_{xc}(\mathbf{r}, t, \mathbf{r}', t')} \Big|_{n_0(\mathbf{r})} n_1(\mathbf{r}', t') \quad (\text{B.10})$$

where $f_{xc}(\mathbf{r}, t, \mathbf{r}', t')$ is the time-dependent xc kernel. Generally, the adiabatic approximation is applied:

$$f_{xc}(\mathbf{r}, t, \mathbf{r}', t') = \delta(t - t') \frac{\delta v_{xc}(\mathbf{r})}{\delta n(\mathbf{r}')} [n_0]. \quad (\text{B.11})$$

Using the Leeuwen theorem one can write

$$n_1 = n_{s1}, \quad (\text{B.12})$$

which leads to the following expression for the density-density response function:

$$\chi(\mathbf{r}, t, \mathbf{r}', t') = \chi_s(\mathbf{r}, t, \mathbf{r}', t') - \int d\mathbf{r} d\mathbf{r}' \int dt dt' \chi_s(\mathbf{r}, t, \mathbf{r}', t') \left(\frac{\delta(t - t')}{|\mathbf{r} - \mathbf{r}'|} + f_{xc}(\mathbf{r}, t, \mathbf{r}', t') \right) \chi(\mathbf{r}, t, \mathbf{r}', t'). \quad (\text{B.13})$$

In order to extract information about the excitation energies, it is useful to work in the frequency space through Fourier transformations. The frequency-dependent non-interacting KS density-density response function (Eq. B.8) can be written as

$$\chi_s(\mathbf{r}, \mathbf{r}', \omega) = \sum_{j,k=1}^{\infty} (n_j - n_k) \frac{\phi_j^0(\mathbf{r}) \phi_k^{0*}(\mathbf{r}) \phi_k^0(\mathbf{r}') \phi_j^{0*}(\mathbf{r}')}{\omega - \omega_{jk} + i\eta} \quad (\text{B.14})$$

where n_j and n_k are the occupation number of the KS orbitals and ϕ_i^0 the static KS orbitals. The response function has poles at frequencies $\omega_{jk} = \epsilon_j - \epsilon_k$ which correspond to the excitation energies of the KS system. Solving Eq. B.13 and applying Fourier transform at the time variable $(t - t')$ finally one gets

$$\chi^{-1}(\mathbf{r}, \mathbf{r}', \omega) = \chi_s^{-1}(\mathbf{r}, \mathbf{r}', \omega) - \frac{1}{|\mathbf{r} - \mathbf{r}'|} - f_{xc}(\mathbf{r}, \mathbf{r}', \omega), \quad (\text{B.15})$$

whose poles are the excitation of the interacting system. Of particular interest in molecular spectroscopy is the computation of the dynamic dipole polarizability. The linear photoreponse induced by an electronic dipole polarization is

$$p_1(t) = \int dt' \alpha(t - t') \mathbf{E}(t'), \quad (\text{B.16})$$

Appendix B. TDDFT in a Nutshell

that in the frequency space is translated as

$$p_1(\omega) = \int dt' \alpha(\omega) \mathbf{E}(\omega) \quad (\text{B.17})$$

where \mathbf{E} is the time-dependent and spatial-independent electric field and α is the dynamics polarization tensor, defined as

$$\alpha_{\mu\nu} = \int d\mathbf{r} n_{1\nu}(\mathbf{r}, t) \hat{r}_\mu. \quad (\text{B.18})$$

We can note that dynamic polarizability and response function have poles at the same position in the frequency space. Thus the poles ω_n of the mean polarizability

$$\bar{\alpha}(\omega) = \frac{1}{3} \text{tr} \alpha(\omega) = \sum_{n=1}^{\infty} \frac{f_n}{\omega_n^2 - \omega^2} \quad (\text{B.19})$$

are the excitation energies and the residue, f_n , are the dimensionless absorption oscillator strength.

B.3 Casida formalism

As we have seen previously, the excitation energies are computed from the density-density response function when a perturbation is applied. However, the presence of an external perturbation is not strictly required because the system can maintain a finite response at its excitation frequencies [45].

In the Casida formalism, the response function in the frequency domain is expressed in the basis of KS orbitals $\{\phi_i(\mathbf{r})\}$

$$\chi(\mathbf{r}, \mathbf{r}', \omega) = \sum_{ij,kl} \phi_i(\mathbf{r}) \phi_j^*(\mathbf{r}) \phi_k(\mathbf{r}') \phi_l^*(\mathbf{r}') \chi_{ij,kl}(\omega). \quad (\text{B.20})$$

This leads to a set of coupled equations [297] that are expressed in the following matrix form

$$\begin{pmatrix} A & B \\ B^* & A^* \end{pmatrix} \begin{pmatrix} X \\ Y \end{pmatrix} = \omega \begin{pmatrix} -1 & 0 \\ 0 & 1 \end{pmatrix} \begin{pmatrix} X \\ Y \end{pmatrix} \quad (\text{B.21})$$

in which

$$A_{ia,jb} = \delta_{ij} \delta_{ab} (\epsilon_a - \epsilon_i) + 2 \int d\mathbf{r} \int d\mathbf{r}' \phi_q^*(\mathbf{r}) f_{Hxc}(\mathbf{r}, \mathbf{r}') \phi_{q'}(\mathbf{r}') \quad (\text{B.22})$$

$$B_{ia,jb} = 2 \int d\mathbf{r} \int d\mathbf{r}' \phi_q^*(\mathbf{r}) f_{Hxc}(\mathbf{r}, \mathbf{r}') \phi_{-q'}(\mathbf{r}'). \quad (\text{B.23})$$

Tamm-Dancoff approximation Casida's equations describe both excitation and de-excitation (stimulated emission) processes. In the Tamm-Dancoff approximation (TDA)[151], the latter are neglected and equations are simplified to the following expression:

$$AX = \omega X. \quad (\text{B.24})$$

Although TDA violates the oscillator strength sum-rule, it has been shown that in certain cases it provides better results [298, 151] than full LR-TDDFT.

B.4 Sternheimer formalism

The Sternheimer formalism [299, 300, 301, 302] provides an alternative scheme for computing LR-TDDT energies and properties. In this approach, the calculation of the unoccupied KS orbitals is not required as in the case of Casida's equations. For each occupied KS orbital a one response orbital $\{\phi_{n,i}^{\{\pm\}}(\mathbf{r})\}$ is computed:

$$\phi_{n,i}^{\{\pm\}} = \sum_{j=1} \int d\mathbf{r}' \frac{\phi_j(\mathbf{r})\phi_j^*(\mathbf{r}')\phi_n(\mathbf{r}')}{\omega - \omega_{jn} + i\eta} \left[v_1(\mathbf{r}', \omega) + \int d\mathbf{r} f_{xc}(\mathbf{r}', \mathbf{r}, \omega) n_1(\mathbf{r}, \omega) \right]; \quad (\text{B.25})$$

the linear response orbitals are usually chosen orthogonal to the subspace of the KS orbitals $\langle \phi_{n,i}^{\{\pm\}} | \phi_i \rangle$. Frequency-dependent density response, Eq. B.4, is written in the following way:

$$n_1(\mathbf{r}, \pm\omega) = \sum_i^{N_{el}} \phi_i(\mathbf{r}) \phi_{n,i}^{\{\pm\}*}(\mathbf{r}) + \phi_{n,i}^{\{\pm\}}(\mathbf{r}) \phi_i^*(\mathbf{r}). \quad (\text{B.26})$$

Let's consider the simple case of a harmonic perturbation of frequency ω ,

$$v_{ext}^{(1)}(\mathbf{r}, t) = v_{ext}^+(\mathbf{r})e^{i\omega t} + v_{ext}^-(\mathbf{r})e^{-i\omega t}, \quad (\text{B.27})$$

whose effect on the system is described as

$$\delta v_{eff} = v_{ext}^{(1)}(\mathbf{r}, t) + \delta v_{SCF} \quad (\text{B.28})$$

where δv_{SCF} is the linear response of the self-consistent-field response

$$\delta v_{n,SCF}(\pm\omega) = \int d\mathbf{r}' \left(\frac{1}{|r-r'|} + \frac{\delta^2 E_{xc}}{\delta n(r)\delta n(r')} \Big|_{\rho=\rho_0} \right). \quad (\text{B.29})$$

Excitation energies are the solution of the following equations for the perturbed LR KS orbitals

$$\sum_j^{N_{el}} (\mathcal{H}_{KS}^{(0)} \delta_{ij} - \epsilon_{ij}) |\phi_{n,j}^{\{\pm\}}\rangle + \mathcal{Q} \delta v_{n,SCF}(\pm\omega) |\phi_i\rangle = \mp \omega_n |\phi_{n,j}^{\{\pm\}}\rangle \quad (\text{B.30})$$

Appendix B. TDDFT in a Nutshell

where $\mathcal{H}_{KS}^{(0)}$ is the ground state KS Hamiltonian, ϵ_{ij} is the Lagrange multiplier which ensures the orthogonality of the ground-state orbitals and $\mathcal{Q} = 1 - \sum_i^{N_{el}} |\phi_i\rangle\langle\phi_i|$ is the projector on the subspace of unperturbed unoccupied states. Solving Eq. B.30 requires knowing only the occupied KS orbitals and their corresponding linear response functions, decreasing the number of states used for the calculation. When implemented in real space, the method scales as N^2 and its advantage is clear when high-energy excited states are required. Expanding the ground state KS orbital $\{\phi_i(\mathbf{r})\}$ and the LR orbitals $\{\phi_{n,i}^{\{\pm\}}(\mathbf{r})\}$ in an orthogonal basis set $\{\kappa_p(\mathbf{r})\}$,

$$\phi_i(\mathbf{r}) = \sum_{p=1}^M c_{pi}^0 \kappa_p(\mathbf{r}) \quad \phi_i^{\{\pm\}}(\mathbf{r}) = \sum_{p=1}^M c_{pi}^{\{\pm\}} \kappa_p(\mathbf{r}), \quad (\text{B.31})$$

the response kernel is expressed as [147]

$$\mathcal{K}_{pu,qv} = \int d\mathbf{r} d\mathbf{r}' \kappa_p^*(\mathbf{r}) \kappa_p(\mathbf{r}) \left[\frac{1}{|r-r'|} + \frac{\delta^2 E_{xc}}{\delta\rho(\mathbf{r})\delta\rho(\mathbf{r}')} \Big|_{\rho=\rho_0} \right] \kappa_p^*(\mathbf{r}') \kappa_p(\mathbf{r}'). \quad (\text{B.32})$$

Within the Sternheimer formalism, the TDA is recovered setting $c_{p,i}^{\{\pm\}} = 0$.

Bibliography

- [1] Stallmann, O. Use of metal complexes in organic dyes and pigments. *J. Chem. Educ.* 37, 220 (1960).
- [2] Kolar, J., Štolfa, A., Strlič, M., Pompe, M., Pihlar, B., Budnar, M., Simčič, J., and Reissland, B. Historical iron gall ink containing documents — Properties affecting their condition. *Analytica Chimica Acta* 555, 167 (2006).
- [3] History of Organometallic Chemistry. In *Organometallic Chemistry and Catalysis* pages 5–20. Springer Berlin Heidelberg (2007).
- [4] Kalyanasundaram, K. and Grätzel, M. Applications of functionalized transition metal complexes in photonic and optoelectronic devices. *Coordination chemistry reviews* 177, 347 (1998).
- [5] Xu, H., Chen, R., Sun, Q., Lai, W., Su, Q., Huang, W., and Liu, X. Recent progress in metal–organic complexes for optoelectronic applications. *Chemical Society Reviews* 43, 3259 (2014).
- [6] An, Z., Zheng, C., Tao, Y., Chen, R., Shi, H., Chen, T., Wang, Z., Li, H., Deng, R., Liu, X., and Huang, W. Stabilizing triplet excited states for ultralong organic phosphorescence. *Nat Mater* 14, 685 (2015).
- [7] Chergui, M. Ultrafast Photophysics of Transition Metal Complexes. *Acc. Chem. Res.* 48, 801 (2015).
- [8] Prier, C. K., Rankic, D. A., and MacMillan, D. W. C. Visible Light Photoredox Catalysis with Transition Metal Complexes: Applications in Organic Synthesis. *Chem. Rev.* 113, 5322 (2013).
- [9] Kumar, S. G. and Devi, L. G. Review on Modified TiO₂ Photocatalysis under UV/Visible Light: Selected Results and Related Mechanisms on Interfacial Charge Carrier Transfer Dynamics. *J. Phys. Chem. A* 115, 13211 (2011).
- [10] O'Regan, B. and Graetzel, M. A low-cost, high-efficiency solar cell based on dye-sensitized colloidal TiO₂ films. *Nature* 353, 737 (1991).
- [11] Czerwieńiec, R., Yu, J., and Yersin, H. Blue-Light Emission of Cu(I) Complexes and Singlet Harvesting. *Inorg. Chem.* 50, 8293 (2011).
- [12] Hashimoto, M., Igawa, S., Yashima, M., Kawata, I., Hoshino, M., and Osawa, M. Highly Efficient Green Organic Light-Emitting Diodes Containing Luminescent Three-Coordinate Copper(I) Complexes. *J. Am. Chem. Soc.* 133, 10348 (2011).
- [13] Yersin, H., Rausch, A. F., Czerwieńiec, R., Hofbeck, T., and Fischer, T. The triplet state of organo-transition metal compounds. Triplet harvesting and singlet harvesting for efficient OLEDs. *Coordination Chemistry Reviews* 255, 2622 (2011).
- [14] Franck, J. and Dymond, E. G. Elementary processes of photochemical reactions. *Trans. Faraday Soc.* 21, 536 (1926).
- [15] Condon, E. Minutes of the Stanford Meeting, March 6, 1926. *Phys. Rev.* 27, 637 (1926).
- [16] Stratt, R. M. and Maroncelli, M. Nonreactive Dynamics in Solution: The Emerging Molecular View of Solvation Dynamics and Vibrational Relaxation. *J. Phys. Chem.* 100, 12981 (1996).
- [17] Yeh, A. T., Shank, C. V., and McCusker, J. K. Ultrafast Electron Localization Dynamics Following Photo-Induced Charge Transfer. *Science* 289, 935 (2000).

Bibliography

- [18] Gawelda, W., Cannizzo, A., Pham, V.-T., van Mourik, F., Bressler, C., and Chergui, M. Ultrafast Nonadiabatic Dynamics of $[\text{FeII}(\text{bpy})_3]^{2+}$ in Solution. *J. Am. Chem. Soc.* 129, 8199 (2007).
- [19] Cannizzo, A., van Mourik, F., Gawelda, W., Zgrablic, G., Bressler, C., and Chergui, M. Broadband femtosecond fluorescence spectroscopy of $[\text{Ru}(\text{bpy})_3]^{2+}$. *Angew. Chem. Int. Ed. Engl.* 45, 3174 (2006).
- [20] van der Veen, R. M., Cannizzo, A., van Mourik, F., Vlcek, A., and Chergui, M. Vibrational Relaxation and Intersystem Crossing of Binuclear Metal Complexes in Solution. *J. Am. Chem. Soc.* 133, 305 (2011).
- [21] Jablonsky, A. Efficiency of Anti-Stokes Fluorescence in Dyes. *Nature* 131, 839 (1933).
- [22] Domcke, W. and Yarkony, D. R. Role of Conical Intersections in Molecular Spectroscopy and Photoinduced Chemical Dynamics. *Annual Review of Physical Chemistry* 63, 325 (2012).
- [23] Cannizzo, A., Blanco-Rodríguez, A. M., El Nahhas, A., Sebera, J., Zálíš, S., Vlček, Jr, A., and Chergui, M. Femtosecond Fluorescence and Intersystem Crossing in Rhenium (I) Carbonyl- Bipyridine Complexes. *Journal of the American Chemical Society* 130, 8967 (2008).
- [24] Braem, O., Messina, F., Baranoff, E., Cannizzo, A., Nazeeruddin, M. K., and Chergui, M. Ultrafast Relaxation Dynamics of Osmium-Polypyridine Complexes in Solution. *J. Phys. Chem. C* 117, 15958 (2013).
- [25] Tavernelli, I., Curchod, B. F. E., and Rothlisberger, U. Nonadiabatic molecular dynamics with solvent effects: A LR-TDDFT QM/MM study of ruthenium (II) tris (bipyridine) in water. *Chemical Physics* 391, 101 (2011).
- [26] Zewail, A. H. Femtochemistry: Atomic-Scale Dynamics of the Chemical Bond. *J. Phys. Chem. A* 104, 5660 (2000).
- [27] Cannizzo, A., Milne, C. J., Consani, C., Gawelda, W., Bressler, C., van Mourik, F., and Chergui, M. Light-induced spin crossover in Fe(II)-based complexes: The full photocycle unraveled by ultrafast optical and X-ray spectroscopies. *Coordination Chemistry Reviews* 254, 2677 (2010).
- [28] Berera, R., van Grondelle, R., and Kennis, J. T. M. Ultrafast transient absorption spectroscopy: principles and application to photosynthetic systems. *Photosynth Res* 101, 105 (2009).
- [29] Xu, J. and Knutson, J. R. Ultrafast Fluorescence Spectroscopy via Upconversion: Applications to Biophysics. *Methods Enzymol* 450, 159 (2008).
- [30] Chergui, M. and Zewail, A. H. Electron and X-Ray Methods of Ultrafast Structural Dynamics: Advances and Applications. *ChemPhysChem* 10, 28 (2009).
- [31] Bressler, C. and Chergui, M. Ultrafast X-ray Absorption Spectroscopy. *Chem. Rev.* 104, 1781 (2004).
- [32] Chen, L. X., Jaeger, W. J., Jennings, G., Gosztola, D. J., Munkholm, A., and Hessler, J. P. Capturing a photoexcited molecular structure through time-domain x-ray absorption fine structure. *Science* 292, 262 (2001).
- [33] Huang, Z. and Kim, K.-J. Review of x-ray free-electron laser theory. *Phys. Rev. ST Accel. Beams* 10, 034801 (2007).
- [34] Kim, K. H., Kim, J. G., Nozawa, S., Sato, T., Oang, K. Y., Kim, T. W., Ki, H., Jo, J., Park, S., Song, C., Sato, T., Ogawa, K., Togashi, T., Tono, K., Yabashi, M., Ishikawa, T., Kim, J., Ryoo, R., Kim, J., Ihee, H., and Adachi, S.-i. Direct observation of bond formation in solution with femtosecond X-ray scattering. *Nature* 518, 385 (2015).
- [35] McFarland, B. K., Farrell, J. P., Miyabe, S., Tarantelli, F., Aguilar, A., Berrah, N., Bostedt, C., Bozek, J. D., Bucksbaum, P. H., Castagna, J. C., Coffee, R. N., Cryan, J. P., Fang, L., Feifel, R., Gaffney, K. J., Glowacki, J. M., Martinez, T. J., Mucke, M., Murphy, B., Natan, A., Osipov, T., Petrovic, V. S., Schorb, S., Schultz, T., Spector, L. S., Swiggers, M., Tenney, I., Wang, S., White, J. L., White, W., and Gühr, M. Ultrafast X-ray Auger probing of photoexcited molecular dynamics. *Nat Commun* 5 (2014).
- [36] Barty, A., Kuepper, J., and Chapman, H. N. Molecular imaging using X-ray free-electron lasers. *Annu Rev Phys Chem* 64, 415 (2013).

- [37] Capano, G., Penfold, T. J., Besley, N. A., Milne, C. J., Reinhard, M., Rittmann-Frank, H., Glatzel, P., Abela, R., Rothlisberger, U., Chergui, M., and Tavernelli, I. The role of Hartree Fock exchange in the simulation of X-ray absorption spectra: A study of photoexcited. *Chemical Physics Letters* 580, 179 (2013).
- [38] Rehr, J. J. and Albers, R. C. Theoretical approaches to x-ray absorption fine structure. *Rev. Mod. Phys.* 72, 621 (2000).
- [39] Szlachetko, J., Cotte, M., Morse, J., Salome, M., Jagodzinski, P., Dousse, J.-C., Hoszowska, J., Kayser, Y., and Susini, J. Wavelength-dispersive spectrometer for X-ray microfluorescence analysis at the X-ray microscopy beamline ID21 (ESRF). *Journal of Synchrotron Radiation* 17, 400 (2010).
- [40] Milne, C. J., Penfold, T. J., and Chergui, M. Recent experimental and theoretical developments in time-resolved X-ray spectroscopies. *Coordination Chemistry Reviews* pages 44–68 (2014).
- [41] Bergmann, U. and Glatzel, P. X-ray emission spectroscopy. *Photosynth Res* 102, 255 (2009).
- [42] Sayers, D. E., Stern, E. A., and Lytle, F. W. New Technique for Investigating Noncrystalline Structures: Fourier Analysis of the Extended X-Ray Absorption Fine Structure. *Phys. Rev. Lett.* 27, 1204 (1971).
- [43] Kimball, G. E. and Shortley, G. H. The Numerical Solution of Schrödinger's Equation. *Phys. Rev.* 45, 815 (1934).
- [44] Joly, Y. X-ray absorption near-edge structure calculations beyond the muffin-tin approximation. *Phys. Rev. B* 63, 125120 (2001).
- [45] Ullrich, C. *Time-Dependent Density-Functional Theory: Concepts and Applications*. OUP Oxford (2012).
- [46] Wang, F., Ziegler, T., van Lenthe, E., van Gisbergen, S., and Baerends, E. J. The calculation of excitation energies based on the relativistic two-component zeroth-order regular approximation and time-dependent density-functional with full use of symmetry. *J Chem Phys* 122, 204103 (2005).
- [47] Wang, F. and Ziegler, T. Theoretical study of the electronic spectra of square-planar platinum (II) complexes based on the two-component relativistic time-dependent density-functional theory. *The Journal of Chemical Physics* 123, 194102 (2005).
- [48] Fronzoni, G., Stener, M., Decleva, P., Wang, F., Ziegler, T., van Lenthe, E., and Baerends, E. J. Spin-orbit relativistic time dependent density functional theory calculations for the description of core electron excitations: TiCl₄ case study. *Chemical Physics Letters* 416, 56 (2005).
- [49] Neese, F. The ORCA program system. *WIREs Comput Mol Sci* 2, 73 (2012).
- [50] Josefsson, I., Kunnus, K., Schreck, S., Foehlich, A., de Groot, E., Wernet, P., and Odelius, M. Ab Initio Calculations of X-ray Spectra: Atomic Multiplet and Molecular Orbital Effects in a Multiconfigurational SCF Approach to the L-Edge Spectra of Transition Metal Complexes. *J. Phys. Chem. Lett.* 3, 3565 (2012).
- [51] Autschbach, J. and Ziegler, T. Nuclear spin-spin coupling constants from regular approximate relativistic density functional calculations. I. Formalism and scalar relativistic results for heavy metal compounds. *The Journal of Chemical Physics* 113, 936 (2000).
- [52] Autschbach, J. and Ziegler, T. Nuclear spin-spin coupling constants from regular approximate relativistic density functional calculations. II. Spin-orbit coupling effects and anisotropies. *The Journal of Chemical Physics* 113, 9410 (2000).
- [53] Lee, N., Petrenko, T., Bergmann, U., Neese, F., and DeBeer, S. Probing Valence Orbital Composition with Iron K X-ray Emission Spectroscopy. *J. Am. Chem. Soc.* 132, 9715 (2010).
- [54] Beckwith, M. A., Roemelt, M., Collomb, M.-N., DuBoc, C., Weng, T.-C., Bergmann, U., Glatzel, P., Neese, F., and DeBeer, S. Manganese K β X-ray Emission Spectroscopy As a Probe of Metal-Ligand Interactions. *Inorg. Chem.* 50, 8397 (2011).
- [55] Koeppe, H., Domcke, W., and Cederbaum, L. S. Multimode Molecular Dynamics Beyond the Born-Oppenheimer Approximation. In Prigogine, I. and Rice, S. A., editors, *Advances in Chemical Physics* pages 59–246. John Wiley & Sons, Inc. (1984).
- [56] Worth, G. A. and Cederbaum, L. S. BEYOND BORN-OPPENHEIMER: Molecular Dynamics Through a Conical Intersection. *Annual Review of Physical Chemistry* 55, 127 (2004).

Bibliography

- [57] Beck, M. H., Jaeckle, A., Worth, G. A., and Meyer, H. D. The multiconfiguration time-dependent Hartree (MCTDH) method: a highly efficient algorithm for propagating wavepackets. *Physics Reports* 324, 1 (2000).
- [58] Tully, J. C. Mixed quantum–classical dynamics. *Faraday Discuss.* 110, 407 (1998).
- [59] Tapavicza, E., Tavernelli, I., and Rothlisberger, U. Trajectory Surface Hopping within Linear Response Time-Dependent Density-Functional Theory. *Phys. Rev. Lett.* 98, 023001 (2007).
- [60] Linsebigler, A. L., Lu, G., and Yates Jr, J. T. Photocatalysis on TiO₂ surfaces: principles, mechanisms, and selected results. *Chemical reviews* 95, 735 (1995).
- [61] Fujishima, A., Rao, T. N., and Tryk, D. A. Titanium dioxide photocatalysis. *Journal of Photochemistry and Photobiology C: Photochemistry Reviews* 1, 1 (2000).
- [62] Roy, S. C., Varghese, O. K., Paulose, M., and Grimes, C. A. Toward solar fuels: photocatalytic conversion of carbon dioxide to hydrocarbons. *ACS Nano* 4, 1259 (2010).
- [63] Duan, L., Bozoglian, F., Mandal, S., Stewart, B., Privalov, T., Llobet, A., and Sun, L. A molecular ruthenium catalyst with water-oxidation activity comparable to that of photosystem II. *Nature Chemistry* 4, 418 (2012).
- [64] Yin, Q., Tan, J. M., Besson, C., Geletii, Y. V., Musaev, D. G., Kuznetsov, A. E., Luo, Z., Hardcastle, K. I., and Hill, C. L. A fast soluble carbon-free molecular water oxidation catalyst based on abundant metals. *Science* 328, 342 (2010).
- [65] Armaroli, N. Photoactive mono- and polynuclear Cu(I)–phenanthrolines. A viable alternative to Ru(II)–polypyridines? *Chem. Soc. Rev.* 30, 113 (2001).
- [66] Juris, A., Balzani, V., Barigelletti, F., Campagna, S., Belser, P., and Zelewsky, A. v. Ru(II) polypyridine complexes: photophysics, photochemistry, electrochemistry, and chemiluminescence. *Coordination Chemistry Reviews* 84, 85 (1988).
- [67] Zgierski, M. Z. Cu(I)-2,9-dimethyl-1,10-phenanthroline: Density functional study of the structure, vibrational force-field, and excited electronic states. *J. Chem. Phys.* 118, 4045 (2003).
- [68] McMillin, D. R., Kirchhoff, J. R., and Goodwin, K. V. Exciplex quenching of photo-excited copper complexes. *Coordination Chemistry Reviews* 64, 83 (1985).
- [69] Cunningham, C. T., Cunningham, K. L. H., Michalec, J. F., and McMillin, D. R. Cooperative Substituent Effects on the Excited States of Copper Phenanthrolines. *Inorganic Chemistry* 38, 4388 (1999).
- [70] Eggleston, M. K., McMillin, D. R., Koenig, K. S., and Pallenberg, A. J. Steric effects in the ground and excited states of Cu (NN) 2+ systems. *Inorganic Chemistry* 36, 172 (1997).
- [71] Eggleston, M. K., Fanwick, P. E., Pallenberg, A. J., and McMillin, D. R. A Twist on the Copper Center in the Crystal Structure of [Cu(dnpp)₂]PF₆ and the Charge-Transfer Excited State? (dnpp = 2,9-Dineopentyl-1,10-phenanthroline). *Inorg. Chem.* 36, 4007 (1997).
- [72] Ahn, B.-T. and McMillin, D. R. Studies of photoinduced electron transfer from bis(2,9-dimethyl-1,10-phenanthroline)copper(I). *Inorg. Chem.* 17, 2253 (1978).
- [73] Buckner, M. T., Matthews, T. G., Lytle, F. E., and McMillin, D. R. Simultaneous emissions including intraligand emission and charge-transfer emission from [bis(triphenylphosphine)(phenanthroline)copper](I+). *J. Am. Chem. Soc.* 101, 5846 (1979).
- [74] Blaskie, M. W. and McMillin, D. R. Photostudies of copper(I) systems. 6. Room-temperature emission and quenching studies of bis(2,9-dimethyl-1,10-phenanthroline)copper(I). *Inorg. Chem.* 19, 3519 (1980).
- [75] Blasse, G. and McMillin, D. R. On the luminescence of bis (triphenylphosphine) phenanthroline copper (I). *Chemical Physics Letters* 70, 1 (1980).
- [76] Kirchhoff, J. R., Gamache, R. E., Blaskie, M. W., Del Paggio, A. A., Lengel, R. K., and McMillin, D. R. Temperature dependence of luminescence from Cu(NN)₂+ systems in fluid solution. Evidence for the participation of two excited states. *Inorg. Chem.* 22, 2380 (1983).

- [77] Everly, R. M. and McMillin, D. R. Reinvestigation of the absorbing and emitting charge-transfer excited states of $[\text{Cu}(\text{NN})_2]^+$ systems. *J. Phys. Chem.* 95, 9071 (1991).
- [78] Ichinaga, A. K., Kirchhoff, J. R., McMillin, D. R., Dietrich-Buchecker, C. O., Marnot, P. A., and Sauvage, J. P. Charge-transfer absorption and emission of $\text{Cu}(\text{NN})_2^+$ systems. *Inorg. Chem.* 26, 4290 (1987).
- [79] Shaw, G. B., Grant, C. D., Shirota, H., Castner, E. W., Meyer, G. J., and Chen, L. X. Ultrafast Structural Rearrangements in the MLCT Excited State for Copper(I) bis-Phenanthrolines in Solution. *J. Am. Chem. Soc.* 129, 2147 (2007).
- [80] Palmer, C. E. A., McMillin, D. R., Kirmaier, C., and Holten, D. Flash photolysis and quenching studies of copper(I) systems in the presence of Lewis bases: inorganic exciplexes? *Inorg. Chem.* 26, 3167 (1987).
- [81] Englman, R. and Jortner, J. The energy gap law for radiationless transitions in large molecules. *Molecular Physics* 18, 145 (1970).
- [82] McCusker, C. E. and Castellano, F. N. Design of a Long-Lifetime, Earth-Abundant, Aqueous Compatible Cu(I) Photosensitizer Using Cooperative Steric Effects. *Inorganic Chemistry* 52, 8114 (2013).
- [83] Khnayzer, R. S., McCusker, C. E., Olaiya, B. S., and Castellano, F. N. Robust Cuprous Phenanthroline Sensitizer for Solar Hydrogen Photocatalysis. *J. Am. Chem. Soc.* 135, 14068 (2013).
- [84] Gothard, N. A., Mara, M. W., Huang, J., Szarko, J. M., Rolczynski, B., Lockard, J. V., and Chen, L. X. Strong Steric Hindrance Effect on Excited State Structural Dynamics of Cu(I) Diimine Complexes. *J. Phys. Chem. A* 116, 1984 (2012).
- [85] Lockard, J. V., Kabehie, S., Zink, J. I., Smolentsev, G., Soldatov, A., and Chen, L. X. Influence of Ligand Substitution on Excited State Structural Dynamics in Cu(I) Bisphenanthroline Complexes†. *J. Phys. Chem. B* 114, 14521 (2010).
- [86] Armaroli, N. Electronic Excited-State Engineering. *ChemPhysChem* 9, 371 (2008).
- [87] Cunningham, C. T., Moore, J. J., Cunningham, K. L. H., Fanwick, P. E., and McMillin, D. R. Structural and Photophysical Studies of $\text{Cu}(\text{NN})_2^+$ Systems in the Solid State. Emission at Last from Complexes with Simple 1,10-Phenanthroline Ligands. *Inorganic Chemistry* 39, 3638 (2000).
- [88] Penfold, T. J., Karlsson, S., Capano, G., Lima, F. A., Rittmann, J., Reinhard, M., Rittmann-Frank, M. H., Braem, O., Baranoff, E., Abela, R., Tavernelli, I., Rothlisberger, U., Milne, C. J., and Chergui, M. Solvent-Induced Luminescence Quenching: Static and Time-Resolved X-Ray Absorption Spectroscopy of a Copper(I) Phenanthroline Complex. *J. Phys. Chem. A* 117, 4591 (2013).
- [89] Iwamura, M., Takeuchi, S., and Tahara, T. Ultrafast Excited-State Dynamics of Copper(I) Complexes. *Acc. Chem. Res.* 48, 782 (2015).
- [90] Kau, L. S., Spira-Solomon, D. J., Penner-Hahn, J. E., Hodgson, K. O., and Solomon, E. I. X-ray absorption edge determination of the oxidation state and coordination number of copper. Application to the type 3 site in *Rhus vernicifera* laccase and its reaction with oxygen. *J. Am. Chem. Soc.* 109, 6433 (1987).
- [91] Chen, L. X., Shaw, G. B., Novozhilova, I., Liu, T., Jennings, G., Attenkofer, K., Meyer, G. J., and Coppens, P. MLCT State Structure and Dynamics of a Copper(I) Diimine Complex Characterized by PumpProbe X-ray and Laser Spectroscopies and DFT Calculations. *J. Am. Chem. Soc.* 125, 7022 (2003).
- [92] Chen, L. X., Jennings, G., Liu, T., Gosztola, D. J., Hessler, J. P., Scaltrito, D. V., and Meyer, G. J. Rapid Excited-State Structural Reorganization Captured by Pulsed X-rays. *J. Am. Chem. Soc.* 124, 10861 (2002).
- [93] Smolentsev, G., Soldatov, A. V., and Chen, L. X. Three-Dimensional Local Structure of Photoexcited Cu Diimine Complex Refined by Quantitative XANES Analysis. *J. Phys. Chem. A* 112, 5363 (2008).
- [94] Smolentsev, G., Sukharina, G., Soldatov, A. V., and Chen, L. X. Application of XANES spectroscopy to study local structure of photoexcited Cu complex. *Nuclear Instruments and Methods in Physics Research Section A: Accelerators, Spectrometers, Detectors and Associated Equipment* 603, 122 (2009).
- [95] Iwamura, M., Ishii, K., Takeuchi, S., and Tahara, T. The Hollow on the Excited-State Potential for Photo-induced 'Jahn-Teller' Distortion of Copper Complexes Revealed by Ultrafast Spectroscopy. In *Conference on Lasers and Electro-Optics - Pacific Rim, 2007. CLEO/Pacific Rim 2007* pages 1–2 (2007).

Bibliography

- [96] Iwamura, M., Watanabe, H., Ishii, K., Takeuchi, S., and Tahara, T. Coherent Nuclear Dynamics in Ultrafast Photoinduced Structural Change of Bis(diimine)copper(I) Complex. *J. Am. Chem. Soc.* 133, 7728 (2011).
- [97] L. X. Chen, X. Zhang, J. V. Lockard, A. B. Stickrath, K. Attenkofer, G. Jennings and D.-J. Liu. Excited-state molecular structures captured by X-ray transient absorption spectroscopy: a decade and beyond. *Acta Cryst.* A66, 240 (2010).
- [98] Iwamura, M., Takeuchi, S., and Tahara, T. Substituent effect on the photoinduced structural change of Cu(I) complexes observed by femtosecond emission spectroscopy. *Physical Chemistry Chemical Physics* 16, 4143 (2014).
- [99] Iwamura, M., Takeuchi, S., and Tahara, T. Real-Time Observation of the Photoinduced Structural Change of Bis(2,9-dimethyl-1,10-phenanthroline)copper(I) by Femtosecond Fluorescence Spectroscopy: A Realistic Potential Curve of the JahnTeller Distortion. *J. Am. Chem. Soc.* 129, 5248 (2007).
- [100] Siddique, Z. A., Yamamoto, Y., Ohno, T., and Nozaki, K. Structure-Dependent Photophysical Properties of Singlet and Triplet Metal-to-Ligand Charge Transfer States in Copper(I) Bis(diimine) Compounds. *Inorg. Chem.* 42, 6366 (2003).
- [101] Schroedinger, E. An Undulatory Theory of the Mechanics of Atoms and Molecules. *Phys. Rev.* 28, 1049 (1926).
- [102] Born, M. *Kopplung der Elektronen- und Kernbewegung in Molekeln und Kristallen*. Vandenhoeck & Ruprecht, Goettingen (1951).
- [103] Born, M. and Huang, K. *Dynamical Theory of Crystal Lattices*. Clarendon Press (1954).
- [104] Yarkony, D. R. Nuclear dynamics near conical intersections in the adiabatic representation: I. The effects of local topography on interstate transitions. *The Journal of Chemical Physics* 114, 2601 (2001).
- [105] Yarkony, D. R. Nonadiabatic Quantum Chemistry - Past, Present, and Future. *Chem. Rev.* 112, 481 (2012).
- [106] Smith, F. T. Diabatic and Adiabatic Representations for Atomic Collision Problems. *Phys. Rev.* 179, 111 (1969).
- [107] Mead, C. A. and Truhlar, D. G. Conditions for the definition of a strictly diabatic electronic basis for molecular systems. *The Journal of Chemical Physics* 77, 6090 (1982).
- [108] Born, M. and Oppenheimer, R. Zur Quantentheorie der Molekeln. *Ann. Phys.* 389, 457 (1927).
- [109] Meyer, H.-D., Gatti, F., and Worth, G. A., editors. *Multidimensional Quantum Dynamics*. Wiley-VCH Verlag GmbH & Co. KGaA, Weinheim, Germany (2009).
- [110] Kosloff, R. Time-dependent quantum-mechanical methods for molecular dynamics. *J. Phys. Chem.* 92, 2087 (1988).
- [111] Meyer, H.-D., Manthe, U., and Cederbaum, L. The multi-configurational time-dependent Hartree approach. *Chemical Physics Letters* 165, 73 (1990).
- [112] Manthe, U. On the integration of the multi-configurational time-dependent Hartree (MCTDH) equations of motion. *Chemical Physics* 329, 168 (2006).
- [113] Worth, G. A., Meyer, H.-D., Koeppel, H., Cederbaum, L. S., and Burghardt, I. Using the MCTDH wavepacket propagation method to describe multimode non-adiabatic dynamics. *International Reviews in Physical Chemistry* 27, 569 (2008).
- [114] Dirac, P. a. M. Note on Exchange Phenomena in the Thomas Atom. *Mathematical Proceedings of the Cambridge Philosophical Society* 26, 376 (1930).
- [115] Frenkel, J. *Wave mechanics: Advanced General Theory*. Oxford: Clarendon Press (1934).
- [116] Penfold, T. J. and Worth, G. A. A model Hamiltonian to simulate the complex photochemistry of benzene II. *The Journal of Chemical Physics* 131, 064303 (2009).
- [117] Fontana, P. R. and Meath, W. J. One and Two-Center Expansions of the BreitPauli Hamiltonian. *Journal of Mathematical Physics* 9, 1357 (1968).

- [118] Penfold, T. J. and Worth, G. A. The effect of molecular distortions on spin-orbit coupling in simple hydrocarbons. *Chemical Physics* 375, 58 (2010).
- [119] Lasorne, B., Sicilia, F., Bearpark, M. J., Robb, M. A., Worth, G. A., and Blancafort, L. Automatic generation of active coordinates for quantum dynamics calculations: Application to the dynamics of benzene photochemistry. *The Journal of Chemical Physics* 128, 124307 (2008).
- [120] Ben-Nun, M. and Martinez, T. J. Nonadiabatic molecular dynamics: Validation of the multiple spawning method for a multidimensional problem. *The Journal of Chemical Physics* 108, 7244 (1998).
- [121] Ben-Nun, M., Quenneville, J., and Martinez, T. J. Ab Initio Multiple Spawning: Photochemistry from First Principles Quantum Molecular Dynamics. *J. Phys. Chem. A* 104, 5161 (2000).
- [122] Martínez, T. J. Insights for Light-Driven Molecular Devices from Ab Initio Multiple Spawning Excited-State Dynamics of Organic and Biological Chromophores. *Acc. Chem. Res.* 39, 119 (2006).
- [123] Lasorne, B., Bearpark, M. J., Robb, M. A., and Worth, G. A. Direct quantum dynamics using variational multi-configuration Gaussian wavepackets. *Chemical Physics Letters* 432, 604 (2006).
- [124] Lasorne, B., Robb, M. A., and Worth, G. A. Direct quantum dynamics using variational multi-configuration Gaussian wavepackets. Implementation details and test case. *Phys. Chem. Chem. Phys.* 9, 3210 (2007).
- [125] Mendive-Tapia, D., Lasorne, B., Worth, G. A., Robb, M. A., and Bearpark, M. J. Towards converging non-adiabatic direct dynamics calculations using frozen-width variational Gaussian product basis functions. *The Journal of Chemical Physics* 137, 22A548 (2012).
- [126] Roemer, S., Ruckebauer, M., and Burghardt, I. Gaussian-based multiconfiguration time-dependent Hartree: A two-layer approach. I. Theory. *The Journal of Chemical Physics* 138, 064106 (2013).
- [127] Aoki, H., Tsuji, N., Eckstein, M., Kollar, M., Oka, T., and Werner, P. Nonequilibrium dynamical mean-field theory and its applications. *Rev. Mod. Phys.* 86, 779 (2014).
- [128] Barbatti, M. Nonadiabatic dynamics with trajectory surface hopping method. *Wiley Interdisciplinary Reviews: Computational Molecular Science* 1, 620 (2011).
- [129] Tully, J. C. Perspective: Nonadiabatic dynamics theory. *The Journal of Chemical Physics* 137, 22A301 (2012).
- [130] Fang, J.-Y. and Hammes-Schiffer, S. Comparison of surface hopping and mean field approaches for model proton transfer reactions. *The Journal of Chemical Physics* 110, 11166 (1999).
- [131] Tully, J. C. and Preston, R. K. Trajectory Surface Hopping Approach to Nonadiabatic Molecular Collisions: The Reaction of H⁺ with D₂. *The Journal of Chemical Physics* 55, 562 (1971).
- [132] Tully, J. C. Molecular dynamics with electronic transitions. *The Journal of Chemical Physics* 93, 1061 (1990).
- [133] Morelli, J. and Hammes-Schiffer, S. Surface hopping and fully quantum dynamical wavepacket propagation on multiple coupled adiabatic potential surfaces for proton transfer reactions. *Chemical Physics Letters* 269, 161 (1997).
- [134] Hammes-Schiffer, S. and Tully, J. C. Proton transfer in solution: Molecular dynamics with quantum transitions. *The Journal of Chemical Physics* 101, 4657 (1994).
- [135] Mueller, U. and Stock, G. Surface-hopping modeling of photoinduced relaxation dynamics on coupled potential-energy surfaces. *The Journal of Chemical Physics* 107, 6230 (1997).
- [136] Fang, J.-Y. and Hammes-Schiffer, S. Improvement of the Internal Consistency in Trajectory Surface Hopping. *J. Phys. Chem. A* 103, 9399 (1999).
- [137] Granucci, G., Persico, M., and Zocante, A. Including quantum decoherence in surface hopping. *The Journal of Chemical Physics* 133, 134111 (2010).
- [138] Jasper, A. W., Stechmann, S. N., and Truhlar, D. G. Fewest-switches with time uncertainty: A modified trajectory surface-hopping algorithm with better accuracy for classically forbidden electronic transitions. *The Journal of Chemical Physics* 116, 5424 (2002).

Bibliography

- [139] Shenvi, N., Subotnik, J. E., and Yang, W. Simultaneous-trajectory surface hopping: A parameter-free algorithm for implementing decoherence in nonadiabatic dynamics. *The Journal of Chemical Physics* 134, 144102 (2011).
- [140] Warshel, A. and Karplus, M. Semiclassical trajectory approach to photoisomerization. *Chemical Physics Letters* 32, 11 (1975).
- [141] Freitag, L. and González, L. Theoretical Spectroscopy and Photodynamics of a Ruthenium Nitrosyl Complex. *Inorg. Chem.* 53, 6415 (2014).
- [142] Carvalho, F. F. d. and Tavernelli, I. Nonadiabatic dynamics with intersystem crossings: A time-dependent density functional theory implementation. *The Journal of Chemical Physics* 143, 224105 (2015).
- [143] Granucci, G., Persico, M., and Spighi, G. Surface hopping trajectory simulations with spin-orbit and dynamical couplings. *The Journal of Chemical Physics* 137, 22A501 (2012).
- [144] Warshel, A. and Levitt, M. Theoretical studies of enzymic reactions: Dielectric, electrostatic and steric stabilization of the carbonium ion in the reaction of lysozyme. *Journal of Molecular Biology* 103, 227 (1976).
- [145] Rothlisberger, U. and Carloni, P. Drug-Target Binding Investigated by Quantum Mechanical/Molecular Mechanical (QM/MM) Methods. In Professor, M. F., Professor, G. C., and Professor, K. B., editors, *Computer Simulations in Condensed Matter Systems: From Materials to Chemical Biology Volume 2* number 704 in Lecture Notes in Physics pages 449–479. Springer Berlin Heidelberg (2006).
- [146] Laio, A., VandeVondele, J., and Rothlisberger, U. A Hamiltonian electrostatic coupling scheme for hybrid Car–Parrinello molecular dynamics simulations. *The Journal of Chemical Physics* 116, 6941 (2002).
- [147] Hutter, J. Excited state nuclear forces from the Tamm-Dancoff approximation to time-dependent density functional theory within the plane wave basis set framework. *The Journal of Chemical Physics* 118, 3928 (2003).
- [148] Furche, F. and Ahlrichs, R. Adiabatic time-dependent density functional methods for excited state properties. *The Journal of Chemical Physics* 117, 7433 (2002).
- [149] Doltsinis, N. L. and Kosov, D. S. Plane wave/pseudopotential implementation of excited state gradients in density functional linear response theory: A new route via implicit differentiation. *The Journal of Chemical Physics* 122, 144101 (2005).
- [150] Casida, M. E. Generalization of the optimized-effective-potential model to include electron correlation: A variational derivation of the Sham-Schlüter equation for the exact exchange-correlation potential. *Phys. Rev. A* 51, 2005 (1995).
- [151] Hirata, S. and Head-Gordon, M. Time-dependent density functional theory within the Tamm-Dancoff approximation. *Chemical Physics Letters* 314, 291 (1999).
- [152] Car, R. and Parrinello, M. Unified Approach for Molecular Dynamics and Density-Functional Theory. *Phys. Rev. Lett.* 55, 2471 (1985).
- [153] Pastore, G., Smargiassi, E., and Buda, F. Theory of ab initio molecular-dynamics calculations. *Phys. Rev. A* 44, 6334 (1991).
- [154] Tangney, P. and Scandolo, S. How well do Car–Parrinello simulations reproduce the Born–Oppenheimer surface? Theory and examples. *The Journal of Chemical Physics* 116, 14 (2002).
- [155] Tangney, P. On the theory underlying the Car-Parrinello method and the role of the fictitious mass parameter. *The Journal of Chemical Physics* 124, 044111 (2006).
- [156] Case, D. A., Cheatham, T. E., Darden, T., Gohlke, H., Luo, R., Merz, K. M., Onufriev, A., Simmerling, C., Wang, B., and Woods, R. J. The Amber biomolecular simulation programs. *J. Comput. Chem.* 26, 1668 (2005).
- [157] Salomon-Ferrer, R., Case, D. A., and Walker, R. C. An overview of the Amber biomolecular simulation package. *WIREs Comput Mol Sci* 3, 198 (2013).

- [158] Damrauer, N. H., Cerullo, G., Yeh, A., Boussie, T. R., Shank, C. V., and McCusker, J. K. Femtosecond Dynamics of Excited-State Evolution in $[\text{Ru}(\text{bpy})_3]^{2+}$. *Science* 275, 54 (1997).
- [159] Bhasikuttan, A. C., Suzuki, M., Nakashima, S., and Okada, T. Ultrafast Fluorescence Detection in Tris(2,2'-bipyridine)ruthenium(II) Complex in Solution: Relaxation Dynamics Involving Higher Excited States. *J. Am. Chem. Soc.* 124, 8398 (2002).
- [160] Frisch, M. J., Trucks, G. W., Schlegel, H. B., Scuseria, G. E., Robb, M. A., Cheeseman, J. R., Scalmani, G., Barone, V., Mennucci, B., Petersson, G. A., Nakatsuji, H., Caricato, M., Li, X., Hratchian, H. P., Izmaylov, A. F., Bloino, J., Zheng, G., Sonnenberg, J. L., Hada, M., Ehara, M., Toyota, K., Fukuda, R., Hasegawa, J., Ishida, M., Nakajima, T., Honda, Y., Kitao, O., Nakai, H., Vreven, T., Montgomery, Jr., J. A., Peralta, J. E., Ogliaro, F., Bearpark, M., Heyd, J. J., Brothers, E., Kudin, K. N., Staroverov, V. N., Kobayashi, R., Normand, J., Raghavachari, K., Rendell, A., Burant, J. C., Iyengar, S. S., Tomasi, J., Cossi, M., Rega, N., Millam, J. M., Klene, M., Knox, J. E., Cross, J. B., Bakken, V., Adamo, C., Jaramillo, J., Gomperts, R., Stratmann, R. E., Yazyev, O., Austin, A. J., Cammi, R., Pomelli, C., Ochterski, J. W., Martin, R. L., Morokuma, K., Zakrzewski, V. G., Voth, G. A., Salvador, P., Dannenberg, J. J., Dapprich, S., Daniels, A. D., Farkas, , Foresman, J. B., Ortiz, J. V., Cioslowski, J., and Fox, D. J. Gaussian 09 Revision A.1 (2009). Gaussian Inc. Wallingford CT 2009.
- [161] Zhao, Y. and Truhlar, D. G. The M06 suite of density functionals for main group thermochemistry, thermochemical kinetics, noncovalent interactions, excited states, and transition elements: two new functionals and systematic testing of four M06-class functionals and 12 other functionals. *Theor Chem Account* 120, 215 (2007).
- [162] Wang, F. and Ziegler, T. A simplified relativistic time-dependent density-functional theory formalism for the calculations of excitation energies including spin-orbit coupling effect. *The Journal of Chemical Physics* 123, 154102 (2005).
- [163] Guerra, C. F., Snijders, J. G., Velde, G. t., and Baerends, E. J. Towards an order-N DFT method. *Theor Chem Acc* 99, 391 (1998).
- [164] van Gisbergen, S. J. A., Snijders, J. G., and Baerends, E. J. Implementation of time-dependent density functional response equations. *Computer Physics Communications* 118, 119 (1999).
- [165] adf. ADF2009.01; Scientific Computation and Modelling: Amsterdam (2010).
- [166] Lenthe, E. v., Baerends, E. J., and Snijders, J. G. Relativistic regular twocomponent Hamiltonians. *The Journal of Chemical Physics* 99, 4597 (1993).
- [167] Lenthe, E. v., Baerends, E. J., and Snijders, J. G. Relativistic total energy using regular approximations. *The Journal of Chemical Physics* 101, 9783 (1994).
- [168] Huang, J., Buyukcakir, O., Mara, M. W., Coskun, A., Dimitrijevic, N. M., Barin, G., Kokhan, O., Stickrath, A. B., Ruppert, R., Tiede, D. M., Stoddart, J. F., Sauvage, J.-P., and Chen, L. X. Highly Efficient Ultrafast Electron Injection from the Singlet MLCT Excited State of Copper(I) Diimine Complexes to TiO₂ Nanoparticles. *Angewandte Chemie International Edition* 51, 12711 (2012).
- [169] Zewail, A. H. Laser Femtochemistry. *Science* 242, 1645 (1988).
- [170] Mukamel, S. *Principles of Nonlinear Optical Spectroscopy*. Oxford University Press (1999).
- [171] Reis, D. A. and Lindenberg, A. M. Ultrafast X-Ray Scattering in Solids. In Cardona, M. and Merlin, R., editors, *Light Scattering in Solid IX* number 108 in Topics in Applied Physics pages 371–422. Springer Berlin Heidelberg (2006).
- [172] Elsaesser, T. and Woerner, M. Photoinduced structural dynamics of polar solids studied by femtosecond X-ray diffraction. *Acta Cryst. A* 66, 168 (2010).
- [173] Johnson, S. L., Beaud, P., Vorobeve, E., Milne, C. J., E. D. Murray, Fahy, S., and Ingold, G. Non-equilibrium phonon dynamics studied by grazing-incidence femtosecond X-ray crystallography. *Acta Cryst. A* 66, 157 (2010).
- [174] Sciaini, G. and Miller, R. J. D. Femtosecond electron diffraction: heralding the era of atomically resolved dynamics. *Rep. Prog. Phys.* 74, 096101 (2011).

Bibliography

- [175] Penfold, T. J., Milne, C. J., and Chergui, M. Recent Advances in Ultrafast X-Ray Absorption Spectroscopy of Solutions. In Rice, S. A. and Dinner, A. R., editors, *Advances in Chemical Physics* pages 1–41. John Wiley & Sons, Inc. (2013).
- [176] Bressler, C. and Chergui, M. Molecular Structural Dynamics Probed by Ultrafast X-Ray Absorption Spectroscopy. *Annual Review of Physical Chemistry* 61, 263 (2010).
- [177] Chen, L. Probing transient molecular structures with time-resolved pump/probe XAFS using synchrotron X-ray sources. *Journal of Electron Spectroscopy and Related Phenomena* 119, 161 (2001).
- [178] Zewail, A. H. 4d Ultrafast Electron Diffraction, Crystallography, and Microscopy. *Annual Review of Physical Chemistry* 57, 65 (2006).
- [179] Veen, R. M. v. d., Penfold, T. J., and Zewail, A. H. Ultrafast core-loss spectroscopy in four-dimensional electron microscopy. *Structural Dynamics* 2, 024302 (2015).
- [180] Schoenlein, R. W., Chattopadhyay, S., Chong, H. H. W., Glover, T. E., Heimann, P. A., Shank, C. V., Zholents, A. A., and Zolotarev, M. S. Generation of Femtosecond Pulses of Synchrotron Radiation. *Science* 287, 2237 (2000).
- [181] Bressler, C., Milne, C., Pham, V.-T., ElNahhas, A., Veen, R. M. v. d., Gawelda, W., Johnson, S., Beaud, P., Grolimund, D., Kaiser, M., Borca, C. N., Ingold, G., Abela, R., and Chergui, M. Femtosecond XANES Study of the Light-Induced Spin Crossover Dynamics in an Iron(II) Complex. *Science* 323, 489 (2009).
- [182] Huse, N., Cho, H., Hong, K., Jamula, L., de Groot, F. M. F., Kim, T. K., McCusker, J. K., and Schoenlein, R. W. Femtosecond Soft X-ray Spectroscopy of Solvated Transition-Metal Complexes: Deciphering the Interplay of Electronic and Structural Dynamics. *J. Phys. Chem. Lett.* 2, 880 (2011).
- [183] Pham, V.-T., Penfold, T. J., van der Veen, R. M., Lima, F., El Nahhas, A., Johnson, S. L., Beaud, P., Abela, R., Bressler, C., Tavernelli, I., Milne, C. J., and Chergui, M. Probing the Transition from Hydrophilic to Hydrophobic Solvation with Atomic Scale Resolution. *J. Am. Chem. Soc.* 133, 12740 (2011).
- [184] Khan, S. Free-electron lasers. *Journal of Modern Optics* 55, 3469 (2008).
- [185] Lemke, H. T., Bressler, C., Chen, L. X., Fritz, D. M., Gaffney, K. J., Galler, A., Gawelda, W., Haldrup, K., Hartsock, R. W., Ihee, H., Kim, J., Kim, K. H., Lee, J. H., Nielsen, M. M., Stickrath, A. B., Zhang, W., Zhu, D., and Cammarata, M. Femtosecond X-ray Absorption Spectroscopy at a Hard X-ray Free Electron Laser: Application to Spin Crossover Dynamics. *J. Phys. Chem. A* 117, 735 (2013).
- [186] Zhang, W., Alonso-Mori, R., Bergmann, U., Bressler, C., Chollet, M., Galler, A., Gawelda, W., Hadt, R. G., Hartsock, R. W., Kroll, T., Kjær, K. S., Kubicek, K., Lemke, H. T., Liang, H. W., Meyer, D. A., Nielsen, M. M., Purser, C., Robinson, J. S., Solomon, E. I., Sun, Z., Sokaras, D., van Driel, T. B., Vanko, G., Weng, T.-C., Zhu, D., and Gaffney, K. J. Tracking excited-state charge and spin dynamics in iron coordination complexes. *Nature* 509, 345 (2014).
- [187] Cammarata, M., Bertoni, R., Lorenc, M., Cailleau, H., Di Matteo, S., Mauriac, C., Matar, S. F., Lemke, H., Chollet, M., Ravy, S., Laulhe, C., Letard, J.-F., and Collet, E. Sequential Activation of Molecular Breathing and Bending during Spin-Crossover Photoswitching Revealed by Femtosecond Optical and X-Ray Absorption Spectroscopy. *Phys. Rev. Lett.* 113, 227402 (2014).
- [188] Ogi, Y., Obara, Y., Katayama, T., Suzuki, Y.-I., Liu, S. Y., Bartlett, N. C.-M., Kurahashi, N., Karashima, S., Togashi, T., Inubushi, Y., Ogawa, K., Owada, S., Rubesova, M., Yabashi, M., Misawa, K., Slavicek, P., and Suzuki, T. Ultraviolet photochemical reaction of [Fe(III)(C₂O₄)₃]³⁻ in aqueous solutions studied by femtosecond time-resolved X-ray absorption spectroscopy using an X-ray free electron laser. *Structural Dynamics* 2, 034901 (2015).
- [189] Wernet, P., Kunnus, K., Josefsson, I., Rajkovic, I., Quevedo, W., Beye, M., Schreck, S., Grübel, S., Scholz, M., Nordlund, D., Zhang, W., Hartsock, R. W., Schlotter, W. F., Turner, J. J., Kennedy, B., Hennies, F., de Groot, F. M. F., Gaffney, K. J., Techert, S., Odelius, M., and Foehlich, A. Orbital-specific mapping of the ligand exchange dynamics of Fe(CO)₅ in solution. *Nature* 520, 78 (2015).
- [190] Stolow, A., Bragg, A. E., and Neumark, D. M. Femtosecond Time-Resolved Photoelectron Spectroscopy. *Chem. Rev.* 104, 1719 (2004).

- [191] Mukamel, S. Femtosecond Optical Spectroscopy: A Direct Look at Elementary Chemical Events. *Annual Review of Physical Chemistry* 41, 647 (1990).
- [192] H.-D. Meyer, U. Manthe, L.S. Cederbaum. The multi-configurational time-dependent Hartree approach. *Chemical Physics Letters* 165, 73 (1990).
- [193] Kouppel, H., Domcke, W., and Cederbaum, L. S. Multimode Molecular Dynamics Beyond the Born-Oppenheimer Approximation. In Prigogine, I. and Rice, S. A., editors, *Advances in Chemical Physics* pages 59–246. John Wiley & Sons, Inc. (1984).
- [194] Besley, N. A., Gilbert, A. T. B., and Gill, P. M. W. Self-consistent-field calculations of core excited states. *The Journal of Chemical Physics* 130, 124308 (2009).
- [195] Rehr, J. J., Kas, J. J., Prange, M. P., Sorini, A. P., Takimoto, Y., and Vila, F. Ab initio theory and calculations of X-ray spectra. *Comptes Rendus Physique* 10, 548 (2009).
- [196] Becke, A. D. Density-functional exchange-energy approximation with correct asymptotic behavior. *Phys. Rev. A* 38, 3098 (1988).
- [197] Perdew, J. P. Density-functional approximation for the correlation energy of the inhomogeneous electron gas. *Phys. Rev. B* 33, 8822 (1986).
- [198] Schaefer, A., Horn, H., and Ahlrichs, R. Fully optimized contracted Gaussian basis sets for atoms Li to Kr. *The Journal of Chemical Physics* 97, 2571 (1992).
- [199] Weigend, F. and Ahlrichs, R. Balanced basis sets of split valence, triple zeta valence and quadruple zeta valence quality for H to Rn: Design and assessment of accuracy. *Phys. Chem. Chem. Phys.* 7, 3297 (2005).
- [200] Hess, B. A., Marian, C. M., Wahlgren, U., and Gropen, O. A mean-field spin-orbit method applicable to correlated wavefunctions. *Chemical Physics Letters* 251, 365 (1996).
- [201] Stener, M., Fronzoni, G., and de Simone, M. Time dependent density functional theory of core electrons excitations. *Chemical Physics Letters* 373, 115 (2003).
- [202] DeBeer George, S., Petrenko, T., and Neese, F. Prediction of Iron K-Edge Absorption Spectra Using Time-Dependent Density Functional Theory†. *J. Phys. Chem. A* 112, 12936 (2008).
- [203] Jackson, B. and Metiu, H. Examination of the use of wave packets for the calculation of atom diffraction by surfaces. *The Journal of Chemical Physics* 82, 5707 (1985).
- [204] Koningsberger, D. C., Mojet, B. L., Dorssen, G. E. v., and Ramaker, D. E. XAFS spectroscopy; fundamental principles and data analysis. *Topics in Catalysis* 10, 143 (2000).
- [205] Penfold, T. J., Tavernelli, I., Milne, C. J., Reinhard, M., Nahhas, A. E., Abela, R., Rothlisberger, U., and Chergui, M. A wavelet analysis for the X-ray absorption spectra of molecules. *The Journal of Chemical Physics* 138, 014104 (2013).
- [206] Vanko, G., Bordage, A., Glatzel, P., Gallo, E., Rovezzi, M., Gawelda, W., Galler, A., Bressler, C., Doumy, G., March, A. M., Kanter, E. P., Young, L., Southworth, S. H., Canton, S. E., Uhlig, J., Smolentsev, G., Sundstroem, V., Haldrup, K., van Driel, T. B., Nielsen, M. M., Kjaer, K. S., and Lemke, H. T. Spin-state studies with XES and RIXS: From static to ultrafast. *Journal of Electron Spectroscopy and Related Phenomena* 188, 166 (2013).
- [207] de Groot, F. High-Resolution X-ray Emission and X-ray Absorption Spectroscopy. *Chem. Rev.* 101, 1779 (2001).
- [208] F. De Groot and A. Kotani. *Core Level Spectroscopy of Solids*. CRC Press Book (2008).
- [209] Krause, M. O. Natural widths of atomic K and L levels, Ka X-ray lines and several KLL Auger lines. *Journal of Physical and Chemical Reference Data* 8 (1979).
- [210] W. Gawelda. *Time-resolved x-ray absorption spectroscopy of transition metal complexes*. EPFL Thesis (2006).
- [211] Szlachetko, J., Nachtegaal, M., Boni, E. d., Willmann, M., Safonova, O., Sa, J., Smolentsev, G., Szlachetko, M., Bokhoven, J. A. v., Dousse, J.-C., Hoszowska, J., Kayser, Y., Jagodzinski, P., Bergamaschi, A., Schmitt, B., David, C., and Luecke, A. A von Hamos x-ray spectrometer based on a segmented-type diffraction crystal for single-shot x-ray emission spectroscopy and time-resolved resonant inelastic x-ray scattering studies. *Review of Scientific Instruments* 83, 103105 (2012).

Bibliography

- [212] March, A. M., Assefa, T. A., Bressler, C., Doumy, G., Galler, A., Gawelda, W., Kanter, E. P., Nemeth, Z., Papai, M., Southworth, S. H., Young, L., and Vanko, G. Feasibility of Valence-to-Core X-ray Emission Spectroscopy for Tracking Transient Species. *J. Phys. Chem. C* 119, 14571 (2015).
- [213] Bozek, J. D. AMO instrumentation for the LCLS X-ray FEL. *Eur. Phys. J. Spec. Top.* 169, 129 (2009).
- [214] M. Altarelli, R. Brinkmann, M. Chergui, W. Decking, B. Dobson, S. Duesterer, G. Gruebel, W. Graeff, H. Graafsma, and J. Hajdu. The european x-ray free-electron laser. *Technical Design Report, DESY 97* (2006).
- [215] Gawelda, W., Pham, V.-T., van der Veen, R. M., Grolimund, D., Abela, R., Chergui, M., and Bressler, C. Structural analysis of ultrafast extended x-ray absorption fine structure with subpicometer spatial resolution: Application to spin crossover complexes. *The Journal of Chemical Physics* 130, 124520 (2009).
- [216] Haldrup, K., Vanko, G., Gawelda, W., Galler, A., Doumy, G., March, A. M., Kanter, E. P., Bordage, A., Dohn, A., van Driel, T. B., Kjaer, K. S., Lemke, H. T., Canton, S. E., Uhlig, J., Sundstroem, V., Young, L., Southworth, S. H., Nielsen, M. M., and Bressler, C. Guest Host Interactions Investigated by Time-Resolved X-ray Spectroscopies and Scattering at MHz Rates: Solvation Dynamics and Photoinduced Spin Transition in Aqueous Fe(bipy)₃²⁺. *J. Phys. Chem. A* 116, 9878 (2012).
- [217] Consani, C., Premont Schwarz, M., ElNahhas, A., Bressler, C., van Mourik, F., Cannizzo, A., and Chergui, M. Vibrational Coherences and Relaxation in the High Spin State of Aqueous [FeII(bpy)₃]²⁺. *Angewandte Chemie International Edition* 48, 7184 (2009).
- [218] Makri, N. and Miller, W. H. Time-dependent self-consistent field (TDSCF) approximation for a reaction coordinate coupled to a harmonic bath: Single and multiple configuration treatments. *The Journal of Chemical Physics* 87, 5781 (1987).
- [219] Kapral, R. Progress in the Theory of Mixed Quantum-Classical Dynamics. *Annual Review of Physical Chemistry* 57, 129 (2006).
- [220] Capano, G., Rothlisberger, U., Tavernelli, I., and Penfold, T. J. Theoretical Rationalization of the Emission Properties of Prototypical Cu(I)-Phenanthroline Complexes. *J. Phys. Chem. A* 119, 7026 (2015).
- [221] Tavernelli, I. Nonadiabatic Molecular Dynamics Simulations: Synergies between Theory and Experiments. *Acc. Chem. Res.* 48, 792 (2015).
- [222] Scaltrito, D. V., Thompson, D. W., O'Callaghan, J. A., and Meyer, G. J. MLCT excited states of cuprous bis-phenanthroline coordination compounds. *Coordination Chemistry Reviews* 208, 243 (2000).
- [223] Tavernelli, I., Curchod, B. F. E., Laktionov, A., and Rothlisberger, U. Nonadiabatic coupling vectors for excited states within time-dependent density functional theory in the Tamm-Dancoff approximation and beyond. *The Journal of Chemical Physics* 133, 194104 (2010).
- [224] Perdew, J. P., Burke, K., and Ernzerhof, M. Generalized Gradient Approximation Made Simple. *Phys. Rev. Lett.* 77, 3865 (1996).
- [225] Troullier, N. and Martins, J. L. Efficient pseudopotentials for plane-wave calculations. *Phys. Rev. B* 43, 1993 (1991).
- [226] von Lilienfeld, O. A., Tavernelli, I., Rothlisberger, U., and Sebastiani, D. Optimization of Effective Atom Centered Potentials for London Dispersion Forces in Density Functional Theory. *Phys. Rev. Lett.* 93, 153004 (2004).
- [227] Lin, I.-C., Coutinho-Neto, M. D., Felsenheimer, C., von Lilienfeld, O. A., Tavernelli, I., and Rothlisberger, U. Library of dispersion-corrected atom-centered potentials for generalized gradient approximation functionals: Elements H, C, N, O, He, Ne, Ar, and Kr. *Phys. Rev. B* 75, 205131 (2007).
- [228] Nose, S. A unified formulation of the constant temperature molecular-dynamics methods. *J. Chem. Phys.* 81, 512 (1984).
- [229] Hoover, W. Canonical dynamics: Equilibrium phase-space distributions. *Phys. Rev. A* 31, 1695 (1985).
- [230] Lin, H. and Truhlar, D. G. QM/MM: what have we learned, where are we, and where do we go from here? *Theor Chem Acc* 117, 185 (2006).

- [231] Case, D. A., Pearlman, D. A., Caldwell, J. W., Cheatham, T. E., Wang, J., Ross, W. S., Simmerling, C. L., Darden, T. A., Merz, K. M., Stanton, R. V., Cheng, A. L., Vincent, J. J., Crowley, M., Tsui, V., Gohlke, H., Radmer, R. J., Duan, Y., Pitera, J., Massova, I., Seibel, G. L., Singh, U. C., Weiner, U. K., and A, K. P. *AMBER 12 University of California, San Francisco*. (2012).
- [232] Tavernelli, I., Tapavicza, E., and Rothlisberger, U. Non-adiabatic dynamics using time-dependent density functional theory: Assessing the coupling strengths. *Journal of Molecular Structure: THEOCHEM* 914, 22 (2009).
- [233] Moret, M.-E., Tavernelli, I., and Rothlisberger, U. Combined QM/MM and Classical Molecular Dynamics Study of [Ru(bpy)₃]²⁺ in Water. *J. Phys. Chem. B* 113, 7737 (2009).
- [234] Moret, M.-E., Tavernelli, I., Chergui, M., and Rothlisberger, U. Electron Localization Dynamics in the Triplet Excited State of [Ru(bpy)₃]⁽³⁾(²⁺) in Aqueous Solution. *Chemistry-A European Journal* 16, 5889 (2010).
- [235] Pearson, K. LIII. On lines and planes of closest fit to systems of points in space. *Philosophical Magazine Series 6* 2, 559 (1901).
- [236] Hotelling, H. Analysis of a complex of statistical variables into principal components. *Journal of Educational Psychology* 24, 417 (1933).
- [237] Hotelling, H. Relations Between Two Sets of Variates. *Biometrika* 28, 321 (1936).
- [238] Capano, G., Chergui, M., Rothlisberger, U., Tavernelli, I., and Penfold, T. J. A Quantum Dynamics Study of the Ultrafast Relaxation in a Prototypical Cu(I)-Phenanthroline. *J. Phys. Chem. A* 118, 9861 (2014).
- [239] Lawthers, I. and McGarvey, J. J. Spin-state relaxation dynamics in iron (III) complexes: photochemical perturbation of the 2t. d₁₀ spin equilibrium by pulsed-laser irradiation in the ligand-to-metal charge-transfer absorption band. *Journal of the American Chemical Society* 106, 4280 (1984).
- [240] Fredin, L. A., Pápai, M., Rozsályi, E., Vanko, G., Wärnmark, K., Sundström, V., and Persson, P. Exceptional Excited-State Lifetime of an Iron(II)-N-Heterocyclic Carbene Complex Explained. *The Journal of Physical Chemistry Letters* pages 2066–2071 (2014).
- [241] Visbal, R. and Gimeno, M. C. N-heterocyclic carbene metal complexes: photoluminescence and applications. *Chemical Society Reviews* 43, 3551 (2014).
- [242] Mathew, S., Yella, A., Gao, P., Humphry-Baker, R., Curchod, B. F., Ashari-Astani, N., Tavernelli, I., Rothlisberger, U., Nazeeruddin, M. K., and Grätzel, M. Dye-sensitized solar cells with 13% efficiency achieved through the molecular engineering of porphyrin sensitizers. *Nature chemistry* (2014).
- [243] Barbieri, A., Accorsi, G., and Armaroli, N. Luminescent complexes beyond the platinum group: the d₁₀ avenue. *Chemical Communications* page 2185 (2008).
- [244] Lazorski, M. S. and Castellano, F. N. Advances in the light conversion properties of Cu (I)-based photosensitizers. *Polyhedron* (2014).
- [245] Del Paggio, A. A. and McMillin, D. R. Substituent effects and the photoluminescence of Cu(PPh₃)₂(NN)⁺ systems. *Inorg. Chem.* 22, 691 (1983).
- [246] Reinhard, M., Penfold, T. J., Lima, F. A., Rittmann, J., Rittmann-Frank, M. H., Abela, R., Tavernelli, I., Rothlisberger, U., Milne, C. J., and Chergui, M. Photooxidation and photoaquation of iron hexacyanide in aqueous solution: A picosecond X-ray absorption study. *Structural Dynamics* 1, 024901 (2014).
- [247] Lee, C., Yang, W., and Parr, R. G. Development of the Colle-Salvetti correlation-energy formula into a functional of the electron density. *Phys. Rev. B* 37, 785 (1988).
- [248] Stephens, P. J., Devlin, F. J., Chabalowski, C. F., and Frisch, M. J. Ab Initio Calculation of Vibrational Absorption and Circular Dichroism Spectra Using Density Functional Force Fields. *J. Phys. Chem.* 98, 11623 (1994).
- [249] Grimme, S. Semiempirical gga-type density functional constructed with a long-range dispersion correction. *The Journal of Computational Chemistry* 27, 1787 (2006).

Bibliography

- [250] Fonseca Guerra, C., Snijders, J. G., Te Velde, G., and Baerends, E. J. Towards an order- N DFT method. *Theoretical Chemistry Accounts* 99, 391 (1998).
- [251] ADF2009.01, SCM, *Theoretical Chemistry, Vrije Universiteit, Amsterdam, The Netherlands*. Scientifici Computation and Modelling (2010). [Http://www.scm.com/](http://www.scm.com/).
- [252] van Lenthe, E., Baerends, E. J., and Snijders, J. G. Relativistic total energy using regular approximations. *The Journal of Chemical Physics* 101, 9783 (1994).
- [253] Capano, G., Penfold, T. J., Rothlisberger, U., and Tavernelli, I. A Vibronic Coupling Hamiltonian to Describe the Ultrafast Excited State Dynamics of a Cu(I)-Phenanthroline Complex. *CHIMIA International Journal for Chemistry* 68, 227 (2014).
- [254] Penfold, T. J. On Predicting the Excited-State Properties of Thermally Activated Delayed Fluorescence Emitters. *J. Phys. Chem. C* 119, 13535 (2015).
- [255] Bayly, C. I., Cieplak, P., Cornell, W., and Kollman, P. A. A well-behaved electrostatic potential based method using charge restraints for deriving atomic charges: the RESP model. *The Journal of Physical Chemistry* 97, 10269 (1993).
- [256] Laio, A., VandeVondele, J., and Rothlisberger, U. D-RESP: Dynamically Generated Electrostatic Potential Derived Charges from Quantum Mechanics/Molecular Mechanics Simulations. *J. Phys. Chem. B* 106, 7300 (2002).
- [257] von Lilienfeld, O., Tavernelli, I., Rothlisberger, U., and Sebastiani, D. Performance of optimized atom-centered potentials for weakly bonded systems using density functional theory. *Phys. Rev. B* 71, 195119 (2005).
- [258] Mara, M. W., Jackson, N. E., Huang, J., Stickrath, A. B., Zhang, X., Gothard, N. A., Ratner, M. A., and Chen, L. X. Effects of Electronic and Nuclear Interactions on the Excited-State Properties and Structural Dynamics of Copper(I) Diimine Complexes. *J. Phys. Chem. B* 117, 1921 (2013).
- [259] Gordon, K. C. and McGarvey, J. J. Time-resolved resonance Raman spectroscopy of bis (2, 9-dimethyl-1, 10-phenanthroline) copper (1+) in solution. *Inorganic Chemistry* 30, 2986 (1991).
- [260] Domingo, A., Sousa, C., and de Graaf, C. The effect of thermal motion on the electron localization in metal-to-ligand charge transfer excitations in [Fe(bpy) 3] 2+. *Dalton Transactions* (2014).
- [261] Miller, M. T., Gantzel, P. K., and Karpishin, T. B. A Photoluminescent Copper (I) Complex with an Exceptionally High CuII/CuI Redox Potential:[Cu (bfp) 2]+(bfp= 2, 9-bis (trifluoromethyl)-1, 10-phenanthroline). *Angewandte Chemie International Edition* 37, 1556 (1998).
- [262] Ruthkosky, M., Castellano, F. N., and Meyer, G. J. Photodriven Electron and Energy Transfer from Copper Phenanthroline Excited States. *Inorganic Chemistry* 35, 6406 (1996).
- [263] Phifer, C. C. and McMillin, D. R. The basis of aryl substituent effects on charge-transfer absorption intensities. *Inorganic Chemistry* 25, 1329 (1986).
- [264] ElSayed, M. A. Spin—Orbit Coupling and the Radiationless Processes in Nitrogen Heterocyclics. *The Journal of Chemical Physics* 38, 2834 (1963).
- [265] Hsu, C.-W., Lin, C.-C., Chung, M.-W., Chi, Y., Lee, G.-H., Chou, P.-T., Chang, C.-H., and Chen, P.-Y. Systematic Investigation of the Metal-Structure–Photophysics Relationship of Emissive d10-Complexes of Group 11 Elements: The Prospect of Application in Organic Light Emitting Devices. *Journal of the American Chemical Society* 133, 12085 (2011).
- [266] Hua, L., Iwamura, M., Takeuchi, S., and Tahara, T. The substituent effect on the MLCT excited state dynamics of Cu(i) complexes studied by femtosecond time-resolved absorption and observation of coherent nuclear wavepacket motion. *Phys. Chem. Chem. Phys.* pages – (2015).
- [267] Lawson Daku, L. and Hauser, A. Ab Initio Molecular Dynamics Study of an Aqueous Solution of [Fe (bpy) 3](Cl) 2 in the Low-Spin and in the High-Spin States. *The Journal of Physical Chemistry Letters* 1, 1830 (2010).

- [268] Altobello, S., Argazzi, R., Caramori, S., Contado, C., Da Fré, S., Rubino, P., Choné, C., Larramona, G., and Bignozzi, C. A. Sensitization of Nanocrystalline TiO₂ with Black Absorbers Based on Os and Ru Polypyridine Complexes. *Journal of the American Chemical Society* 127, 15342 (2005).
- [269] Mara, M. W., Bowman, D. N., Buyukcakir, O., Shelby, M. L., Haldrup, K., Huang, J., Harpham, M. R., Stickrath, A. B., Zhang, X., Stoddart, J. E., Coskun, A., Jakubikova, E., and Chen, L. X. Electron Injection from Copper Diimine Sensitizers into TiO₂: Structural Effects and Their Implications for Solar Energy Conversion Devices. *J. Am. Chem. Soc.* 137, 9670 (2015).
- [270] Accorsi, G., Armaroli, N., Duhayon, C., Saquet, A., Delavaux-Nicot, B., Welter, R., Moudam, O., Holler, M., and Nierengarten, J.-F. Synthesis and Photophysical Properties of Copper(I) Complexes Obtained from 1,10-Phenanthroline Ligands with Increasingly Bulky 2,9-Substituents. *European Journal of Inorganic Chemistry* 2010, 164 (2010).
- [271] Garakyaraghi, S., Danilov, E. O., McCusker, C. E., and Castellano, F. N. Transient Absorption Dynamics of Sterically Congested Cu(I) MLCT Excited States. *J. Phys. Chem. A* 119, 3181 (2015).
- [272] Vosko, S. H., Wilk, L., and Nusair, M. Accurate spin-dependent electron liquid correlation energies for local spin density calculations: a critical analysis. *Can. J. Phys.* 58, 1200 (1980).
- [273] Andreoni, W. and Curioni, A. New advances in chemistry and materials science with CPMD and parallel computing. *Parallel Computing* 26, 819 (2000).
- [274] Hohenberg, P. Inhomogeneous Electron Gas. *Phys. Rev.* 136, B864 (1964).
- [275] Kohn, W. and Sham, L. J. Self-Consistent Equations Including Exchange and Correlation Effects. *Phys. Rev.* 140, A1133 (1965).
- [276] Levy, M. Universal variational functionals of electron densities, first-order density matrices, and natural spin-orbitals and solution of the *v*-representability problem. *PNAS* 76, 6062 (1979).
- [277] Levy, M. Electron densities in search of Hamiltonians. *Phys. Rev. A* 26, 1200 (1982).
- [278] Lieb, E. H. Density functionals for coulomb systems. *Int. J. Quantum Chem.* 24, 243 (1983).
- [279] Mahan, G. D. *Many-Particle Physics*. Springer Science & Business Media (2013).
- [280] Perdew, J. P. and Zunger, A. Self-interaction correction to density-functional approximations for many-electron systems. *Phys. Rev. B* 23, 5048 (1981).
- [281] Ceperley, D. M. and Alder, B. J. Ground State of the Electron Gas by a Stochastic Method. *Phys. Rev. Lett.* 45, 566 (1980).
- [282] Perdew, J. P. and Burke, K. Comparison shopping for a gradient-corrected density functional. *Int. J. Quantum Chem.* 57, 309 (1996).
- [283] Colle, R. and Salvetti, O. Approximate calculation of the correlation energy for the closed shells. *Theoretica chimica acta* 37, 329 (1975).
- [284] van Leeuwen, R. and Baerends, E. J. Exchange-correlation potential with correct asymptotic behavior. *Phys. Rev. A* 49, 2421 (1994).
- [285] Jensen, F. J. *Introduction to Computational Chemistry*. Wiley, Chichester (1999).
- [286] Davidson, E. R. and Feller, D. Basis set selection for molecular calculations. *Chem. Rev.* 86, 681 (1986).
- [287] Briddon, P. and Jones, R. LDA Calculations Using a Basis of Gaussian Orbitals. *phys. stat. sol. (b)* 217, 131 (2000).
- [288] Chong, D. P., Van Lenthe, E., Van Gisbergen, S., and Baerends, E. J. Even-tempered slater-type orbitals revisited: From hydrogen to krypton. *J. Comput. Chem.* 25, 1030 (2004).
- [289] Hellmann, H. *Einfuehrung in die Quantenchemie*. Deuticke, Leipzig (1937).
- [290] Feynman, R. P. Forces in Molecules. *Phys. Rev.* 56, 340 (1939).
- [291] Pulay, P. Ab initio calculation of force constants and equilibrium geometries in polyatomic molecules. *Molecular Physics* 17, 197 (1969).

Bibliography

- [292] Martin, R. M. *Electronic Structure: Basic Theory and Practical Methods*. Cambridge University Press (2004).
- [293] Schwerdtfeger, P. The Pseudopotential Approximation in Electronic Structure Theory. *ChemPhysChem* 12, 3143 (2011).
- [294] Runge, E. and Gross, E. K. U. Density-Functional Theory for Time-Dependent Systems. *Phys. Rev. Lett.* 52, 997 (1984).
- [295] van Leeuwen, R. Mapping from Densities to Potentials in Time-Dependent Density-Functional Theory. *Phys. Rev. Lett.* 82, 3863 (1999).
- [296] Gross, E. K. U. and Kohn, W. Local density-functional theory of frequency-dependent linear response. *Phys. Rev. Lett.* 55, 2850 (1985).
- [297] Casida, M. E. *Recent Advances in Density Functional Methods*. World Scientific (1995).
- [298] Casida, M. E., Gutierrez, F., Guan, J., Gadea, F.-X., Salahub, D., and Daudey, J.-P. Charge-transfer correction for improved time-dependent local density approximation excited-state potential energy curves: Analysis within the two-level model with illustration for H₂ and LiH. *The Journal of Chemical Physics* 113, 7062 (2000).
- [299] Sternheimer, R. M. Electronic Polarizabilities of Ions from the Hartree-Fock Wave Functions. *Phys. Rev.* 96, 951 (1954).
- [300] Mahan, G. D. and Subbaswamy, K. R. *Local Density Theory of Polarizability*. Springer Science & Business Media (1990).
- [301] Yabana, K., Nakatsukasa, T., Iwata, J.-I., and Bertsch, G. F. Real-time, real-space implementation of the linear response time-dependent density-functional theory. *phys. stat. sol. (b)* 243, 1121 (2006).
- [302] Andrade, X., Botti, S., Marques, M. A. L., and Rubio, A. Time-dependent density functional theory scheme for efficient calculations of dynamic (hyper)polarizabilities. *The Journal of Chemical Physics* 126, 184106 (2007).

GLORIA CAPANO

PERSONAL INFORMATION

Date of Birth Milano, 05 December 1987
email capano.gloria@gmail.com
phone (office) +41 21 6930365 · (personal) +41 78 6758244
Address Boulevard de la Fôret 35, 1009, Pully, Switzerland

WORK EXPERIENCE

January 2012–Present Ph.D. Assistant
Laboratory of Computational Chemistry and Biochemistry (LCBC)
Laboratory of Ultrafast Spectroscopy (LSU)
École polytechnique fédérale de Lausanne - Lausanne (Switzerland)

Classical and QM/MM Molecular Dynamics calculations of metallorganic complexes in solution combined with X-Ray absorption fine spectroscopy simulations in collaboration with the Paul Scherrer Institute in Villigen (Switzerland). Quantum dynamics calculations using the MCTDH package for ultrafast dynamics of metallorganic complexes. Trajectory surface hopping approach based on linear response time-dependent-functional theory (LR-TDDFT) in the quantum mechanical/molecular dynamics (QM/MM) scheme for metallorganic complexes with optical interest. *Supervisors:* Dr. Ivano Tavernelli, Prof. Majed Chergui

Courses:

- Molecular quantum dynamics
- Computational methods for quantum dynamics

Student assistant for the following courses:

- Introduction to electronic structure methods
- Molecular dynamics e Monte-Carlo simulations
- Computational methods for quantum dynamics

EDUCATION

2009-2011 Master degree in Material Science, 110/110.
Department of Material Science, University of Milano-Bicocca (Italy)

Thesis: *Ab-initio* calculations with the density functional theory (DFT) method in generalized gradient approximation (GGA) of silica ultrathin film on Ru(0001). *Supervisors:* Prof. Gianfranco Pacchioni, Dr. Livia Giordano

Courses:

- Solid State Physics
- Surface Physics
- Surface Chemistry
- Surface Microscopy
- Nanotechnology (Chemical and Physical Properties)

• Semiconductor Physics

2006-2009 Bachelor degree in Material Science, 110/110 cum laude.
Department of Material Science, University of Milano-Bicocca (Italy)

Thesis: Investigation of the optical properties of rubrene molecular crystal and tetracene ultrathin film on rubrene(001) using time resolved-fluorescence spectroscopy. *Supervisors*: Prof. Franco Meinardi, Prof. Riccardo Tubino

PUBLICATIONS

G. Capano, M. Chergui, U. Röthlisberger, I. Tavernelli, T. J. Penfold
"A quantum dynamics study of the ultrafast relaxation in a prototypical Cu(I)-phenanthroline."
The Journal of Physical Chemistry A **118** (42), 98619869 (2014)

G. Capano, T. J. Penfold, U. Röthlisberger and I. Tavernelli
"A Vibronic Coupling Hamiltonian to describe the ultrafast excited state dynamics of a Cu(I)-phenanthroline complex."
Chimia **68** (4), 227-230 (2014) ‡
‡: **Invited article for presentation award in the Swiss Chemical Society Meeting.**

G. Capano, T.J. Penfold, N.A. Besley, C.J. Milne, M. Reinhard, H. Rittmann-Frank, P. Glatzel, R. Abela, U. Rothlisberger, M. Chergui and I. Tavernelli
"The role of Hartree-Fock exchange in the simulation of X-ray absorption spectra: A study of photoexcited $[\text{Fe}(\text{bpy})_3]^{2+}$."
Chemical Physical Letter. **580**, 179-184 (2013).

T. J. Penfold, S. Karlsson, G. Capano F.A Lima, M. Reinhard, M.H. Rittmann-Frank, J. Rittmann, O. Braem, R. Abela, E. Baranoff, I. Tavernelli, U. Rothlisberger, C.J. Milne and M. Chergui.
"Solvent induced luminescence quenching: Static and time-resolved X-ray absorption spectroscopy of a Copper(I) phenanthroline complex."
The Journal of Physical Chemistry A. **117**, 4591-4601 (2013)

COMPUTER SKILLS

In experience with computational chemistry softwares:

- Gaussian
- ORCA
- Amsterdam Density Functional (ADF)
- Vienna Ab-initio Simulation Package (VASP)
- Car-Parrinello Molecular Dynamics (CPMD)
- PW Quantum Espresso
- FEFF and FDMNES (packages for the simulation of X-ray fine structure spectra)

Graphic programs: XCrysden, Molekel, Molddraw, VMD, Gmolden.

High familiarity with MS Office / Libre Office programs suite and Latex. Good knowledge of programming languages Fortran and C+.

COMMUNICATION SKILLS

Very good presentation skills developed by posters and conferences talks.
Experience in performing on a stage due to music performances.

SOCIAL SKILLS

174 Organised and responsible person, with a good problem-solving attitude.
Ability for synthetic and global view over concrete situations.
Very good teamworking skill.

OTHER INFORMATION

- Awards* 2013 · Metrohm Awards for the best oral presentations - Swiss Chemical Society Fall Meeting
- Invited Talk* 2014 · Cecam workshop: "Recent progress in adiabatic and non-adiabatic methods in quantum dynamics" Lausanne, Switzerland
- Languages* ITALIAN · Mother tongue
 ENGLISH · Advanced (C1)
 FRENCH · Advanced (C1)
 PORTUGUESE · Intermediate (B1-B2)
 SPANISH · Basic (B1)
- Interests* I studied piano at the Conservatory of Music 'G. Verdi' Of Milan where I obtained the *Diploma di Compimento Inferiore*. I participated in musical activities of the Bicocca University Chorus and of the Chamber Music Association of École Polytechnique Fédérale de Lausanne. In 2006, I was part of the young jury at the International Venice Movie Festival (63th edition) as winner of a National Movie Competition.

April 8, 2016